TRIBOLOGICAL AND MECHANICAL PROPERTIES IMPROVEMENT THROUGH REINFORCEMENT BY USING FRICTION STIR PROCESSING

A Thesis submitted to the Delhi Technological University, Delhi in fulfillment of the requirements for the award of the degree of

DOCTOR OF PHILOSOPHY

IN

MECHANICAL ENGINEERING

By

SUMIT JAIN

(2K16/Ph.D/ME/34)

UNDER THE SUPERVISION OF

Prof. R. S. MISHRA

(Professor)

Department of Mechanical Engineering,

Delhi Technological University

DEPARTMENT OF MECHANICAL ENGINEERING DELHI TECHNOLOGICAL UNIVERSITY
NEW DELHI-110042, INDIA

DECLARATION

I hereby declare that the research work presented in this thesis, entitled **"TRIBOLOGICAL AND MECHANICAL PROPERTIES IMPROVEMENT THROUGH REINFORCEMENT BY USING FRICTION STIR PROCESSING"** is an original work carried out by me under the supervision of Prof. R.S. Mishra, Professor, Department of Mechanical Engineering, Delhi Technological University, Delhi. This thesis has been prepared in conformity with the rules and regulations of the Delhi Technological University, Delhi. The research work reported and results presented in the thesis have not been submitted either in part or full to any other university or institute for the award of any other degree or diploma.

SUMIT JAIN
(2K16/Ph.D/ME/34)
Research Scholar
Department of Mechanical Engineering
Delhi Technological University, Delhi

CERTIFICATE

This is to certify that the thesis entitled, **"TRIBOLOGICAL AND MECHANICAL PROPERTIES IMPROVEMENT THROUGH REINFORCEMENT BY USING FRICTION STIR PROCESSING"** submitted by **Sumit Jain, (Roll No. 2K16/Ph.D/ME/34)** in partial fulfillment of requirements for the award of degree of **DOCTOR OF PHILOSOPHY** in **Mechanical Engineering** is a bonafide record of original research work carried by him under my supervision.

This is also certified that this work has not been submitted to any other institute or university for the award of any other diploma or degree.

Prof. (Dr.) R. S. Mishra
Professor
Department of Mechanical Engineering
Delhi Technological University, Delhi

ACKNOWLEDGEMENT

The work presented here would not have been possible without the help of many talented and learned people. First and foremost, I would like to thank my supervisor Prof. R.S. Mishra, Department of Mechanical Engineering, Delhi Technological University, Delhi, for extending his full support and encouragement. I deeply value the invaluable suggestions and creative freedom, he provided to me. I also greatly benefitted from his experience and skills, which he shared with me with utmost generosity. I highly appreciate the personal attention and interest, which he showed towards my research work. I had the privilege to learn from him not just lessons of engineering but of life. I am thankful to the supervisor to help me to get access to all the necessary facilities in DTU including welding laboratory.

I would like to express, a sincere gratitude to Prof. S. K. Garg, Chairman, DRC, and Head of the Department, Mechanical Engineering, Delhi Technological University, for their valuable help, motivation and extending all the necessary processing and experimental facilities during my research work.

My sincere thanks to all the faculty and staff members of Department of Mechanical Engineering (DTU), who supported me during my entire course work and research work. I am grateful to Mr. Girish Anand for their technical and experimental support.

I would like to express my sincere thanks to my friend Dr. Husain Mehdi, Assistant professor, MIET, Meerut and Mr. Rajat Gupta, Assistant professor, ADGITM, Delhi for their help and support throughout my research work.

I am short of words to express my sincere gratitude to my parents. Whatever I have achieved in my life; it is because of them. I can't express in words their efforts to nurture me. I am grateful to my wife Mrs. Geeta Jain for her support and encouragement during my overall research work.

SUMIT JAIN

ABSTRACT

This research work focuses on a comparative study on weld quality of dissimilar aluminum alloys incorporated with three different volume fractions and two different sizes of reinforcement particles using friction stir processing (FSP) technique. Aluminum alloys AA7075 and AA6061 plates of thickness 6 mm were used as base materials to fabricate dissimilar FSPed composite joints and, micro and nano-sized Al_2O_3 particles were used as reinforcing candidates. Tool rotational speed (700-1100 rpm), traverse speed (40-60 mm/min) and different volume fraction of reinforcement particles (4-10%) were used as input process parameters for response output such as, tensile strength, %elongation, micro-hardness and wear behavior. Central composite face-centered design (CCFCD) under response surface methodology (RSM) is employed to develop the design matrix for conducting the experiments. Microstructural characterization is carried out using optical microscopy and scanning electron microscope (SEM) equipped with energy-dispersive X-ray spectroscopy (EDS). Tensile fractured surfaces were also examined by SEM. Multi-response mathematical model is established for prediction of response parameters. This model is proficient to forecast the main effects and interactive effects of three levels of the opted process parameters. Results show that increasing the tool rotational speed and decreasing the traverse speed, leads to improve the dispersion pattern of reinforcing particles of Al_2O_3 (micro and nano) in the stir zone of FSPed composite joints. The large dimples and quasi cleavage with a sharp edge and various depths were found on the fractured tensile specimen surface of low tool rotational speed whereas fine dimples were found at high tool rotational speed of FSP composite joints. The maximum tensile strength (241.35 MPa), microhardness (157.5 HV) and minimum wear weight loss (10.3 mg) for FSPed composite joints incorporated with Al_2O_3 microparticles were observed at rotational speed of 1100 rpm, traverse speed of 40 mm/min with 10% volume fraction of Al_2O_3 particles. The optimized value of tensile strength, % elongation, micro-hardness and wear (weight loss) at the stir zone are 227.80 MPa, 19.31, 147.97 HV and 10.474 mg respectively, whereas the optimized value of tool rotational speed, traverse speed and volume fraction of Al_2O_3 particles are 1096.76 rpm, 55.59 mm/min and 8.64 % respectively was found for Al_2O_3 microparticles.

The maximum tensile strength (254.9 MPa) and microhardness (169.1 HV) for FSPed composite joint incorporated with Al_2O_3 nanoparticles were observed at rotational speed of 1100 rpm, traverse speed of 40 mm/min with 10% volume fraction of Al_2O_3 particles. Whereas, minimum wear weight loss (8.97 mg) for FSPed composite joint incorporated

with Al_2O_3 particles was observed at rotational speed of 1100 rpm, traverse speed of 60 mm/min with 10% volume fraction of Al_2O_3 particles. The optimized value of tensile strength, %elongation, micro-hardness and wear (weight loss) at stir zone are 240.45 MPa, 24.95%, 157.89 HV, and 9.17 mg, respectively, whereas the optimized value of tool rotational speed, traverse speed and volume fraction of Al_2O_3 particles are 1089.40 rpm, 58.09 mm/min, and 8.74% respectively was found for Al_2O_3 nanoparticles.

TABLE OF CONTENTS

LIST OF FIGURES

LIST OF TABLES

CHAPTER-1
INTRODUCTION

1.1 WELDING

Welding is a fusion technique of joining two similar or dissimilar metals with or without the use of pressure and filler metals. To fuse metals, heat is needed, which can originate from a variety of sources including an electric arc, chemical reaction, electric resistance, friction, or radiant radiation etc.

1.2 CLASSIFICATION OF WELDING

In general, welding is basically classified into two categories:

1. Fusion welding
2. Forge/Solid state welding

1.2.1 Fusion welding

It refers to the welding technique that uses melting to fuse materials with comparable compositions and melting temperatures. A heat-affected zone is developed in the material as a consequence of the high phase transformations characteristic in these processes. The following are the commonly used fusion welding:

- Arc welding
- Electric resistance welding
- Gas welding
- Thermit welding

1.2.2 Forge/Solid state welding

Solid state welding is a type of welding in which the parent material is welded at a temperature below its melting point. Diffusion is responsible for the bonding that takes place.

The following are the commonly used solid-state welding techniques:

- Friction stir welding
- Cold welding

- Diffusion welding
- Explosive welding

1.3 FRICTION STIR WELDING (INTRODUCTION)

The Welding Institute (TWI) is an organization in the UK, which specializes in materials joining technologies, invented an extremely new and world-beating welding technique in late 1991 [1]. Friction stir welding (FSW) is a good term for this technique. FSW is a solid-state method, which means that the joining materials do not melt during the process. It is utilized when the original qualities of metal must be preserved to the greatest extent feasible. This is due to the mechanically intermixing the two metal pieces, which allows them to be fused by softening them with mechanical pressure.

In friction stir welding a revolving tool of cylindrical shape is used, which moves along the parting line of two metal plates. Frictional heat is generated owing to the friction between the workpiece and he rotating tool, allowing the material to soften without melting under mechanical pressure. The weld is generated when the material is deformed at temperatures less than the melting point. The traverse and rotation speed of the FSW tool generates a distinctive imbalance between the neighbouring surfaces throughout the welding process. The advancing side is where the tool rotation aligns welding tool translation, whereas the retreating side is where the two motions, rotation and translation, oppose each other.

1.3.1 Working principle

In FSW, the cylindrical tool is mounted on the friction stir welding machine's rotating spindle. Furthermore, the work piece plates must be firmly secured on a fixture in such a way that the base plate faces are not driven apart. The revolving tool is then lowered gradually between the separating lines of the two plates to be welded [2]. Frictional heat is generated owing to friction between the work piece and rotating tool, softening the material without melting it. During welding, the friction heat also assists the tool in moving along the parting line of the base plates. The high temperature achieved is on the order of 0.8 times the material's melting point. The plasticized material is transported to the tool pin's trailing edge and forged by the tool shoulder's close contact with the pin profile. The process is categorized as a solid-phase keyhole welding approach because

a hole to admit the pin is produced and may be filled throughout the welding operation. Fig. 1.1 depicts the friction stir welding principle in action.

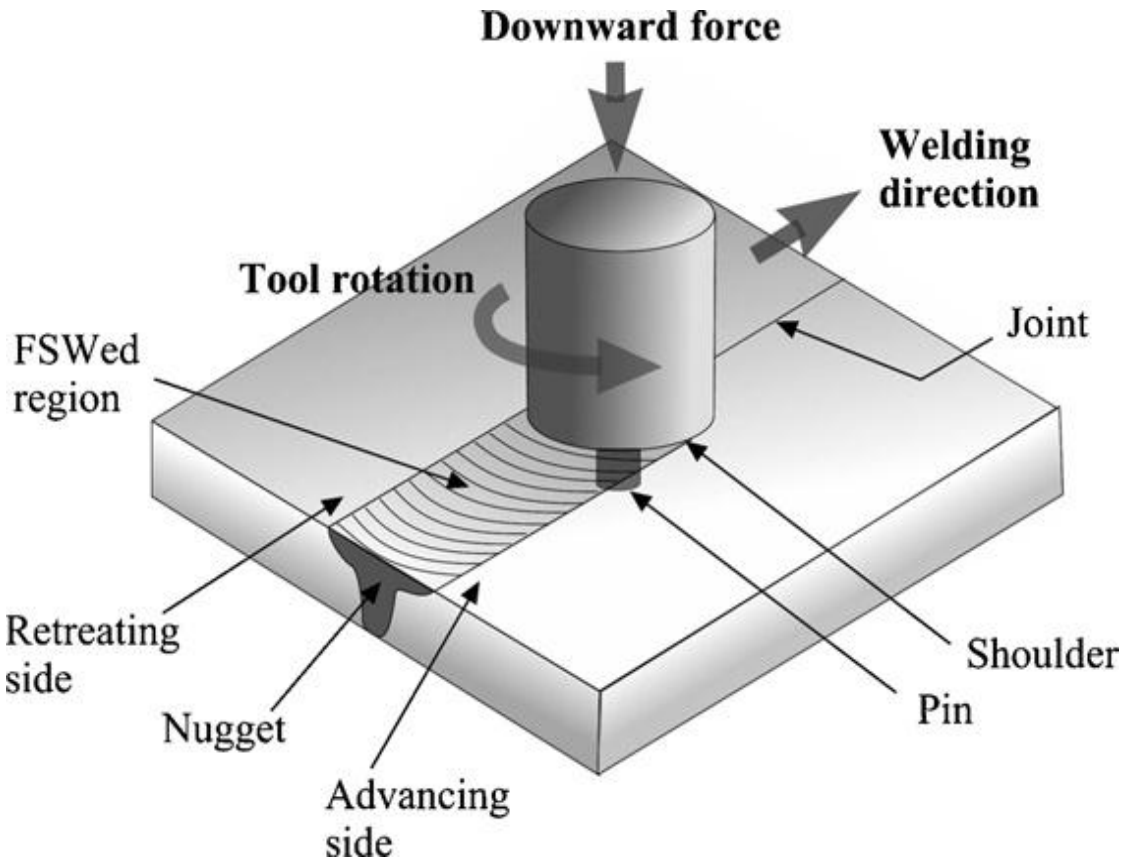

Figure 1.1: Schematic representation of FSW principle [3]

1.3.2 Advantages of FSW

This is a clean and environmentally friendly method because there are no bad issues such as arc production, which might cause an industrial hazard, radiation, the release of poisonous gas, or a dangerous laser beam for human eyes. The following are some additional benefits:

- There are no fumes or splatter produced, and no shielding gas is required, making the process environmentally pleasant.
- The tool used is of non-consumable type.
- As the weld is produced in the solid state, gravity has no effect, and the operation may be performed in any situation (horizontal, vertical, overhead or orbital).
- There is no need for grinding, pickling or brushing.

- Since this procedure is carried out at a low temperature, shrinkage during solidification is minimal.
- There is no need of filler materials.
- Unlike fusion welding, no oxide treatment is required.
- The weld produced is of high quality, with outstanding mechanical qualities and a fine microstructure.
- The method is cost-effective because it eliminates the need for mechanical forming after welding.
- Welding of different metals is possible.
- Automation is a viable option.

1.3.3 Applications

1.3.3.1 Marine industries

The marine industries were among the first to use the technology for commercial purposes. The following applications are suited for the process:

- Panels for bulkheads.
- extrusions.
- Superstructures and Hulls.
- Transport and Marine structures.
- Sailing boats.

1.3.3.2 Aerospace industry

At the meantime, the aerospace sector uses FSW to join space vehicle elements. Friction stir welded and successfully tested circumferential lap welds and longitudinal butt welds of Aluminum alloys fuel tanks for space vehicles. As a result, FSW procedure can be utilized for:

- Fuselages.
- Scientific and Military rockets.
- Cryogenic fuel tanks.
- External throwaway tanks.
- Fuel tanks.

1.3.3.3 Rail-way industry

The first commercial manufacture of high-speed trains consisting of aluminum extrusions that can be linked via FSW has been declared. The following are some examples of applications:

- High-speed trains.
- Railway tankers and rolling stock.
- Underground carriages.
- Container bodies.

1.3.3.4 Land transportation

Several automobile businesses and suppliers to this industry are now experimenting with the FSW technology for commercial use. The following are examples of possible applications:

- Truck bodies
- Engine and chassis cradles
- Tail lifts for lorries
- Wheel rims
- Mobile cranes
- Airfield transportation vehicles and Buses
- Fuel tankers
- Bicycle and Motorcycle frames

1.3.3.5 Construction industry

It is feasible to employ portable FSW equipment for the following purposes:

- Window frames
- Aluminum bridges
- Facade panels
- Fabrication of Pipes
- Pipelines of aluminum
- Air conditioners and heat exchangers
- power plants reactors

1.3.3.6 Electrical industry

FSW is becoming increasingly utilized in the electrical sector for:

- Electrical connectors
- Electric motor housings
- Encapsulation of electronics
- Bus bars

1.3.3.7 Other industries

FSW is also a feasible alternative for:

- Gas cylinders.
- Joining of copper or aluminum coils.
- Refrigeration panels.
- Cooking equipment.

1.3.4 Disadvantages

- Welding rates are considerably slower.
- Work pieces must be tightly fastened.
- Each weld must have a keyhole.
- When welding materials of various thickness, different length pin tools are required.

1.4 FRICTION STIR PROCESSING (FSP)

FSP is considered a variant of the FSW method. FSW is used to weld materials in solid-state, particularly those with low melting points, such as aluminum alloys. The term "friction stir processing" was first used as a keyword in the study of Mishra et al. [4] in 1999. It was suggested in 2003 that FSP may be used to successfully manufacture light metal alloy surface composites (SCs) [5]. After this accomplishment, FSP became known as a surface modification and grain refinement approach, and it became a key milestone in solid-state material processing techniques. The working concept of FSP is similar to that of FSW, excluding that FSP is used for the processing of the base materials to improve desirable features such as grain refinement, mechanical and surface properties enhancement, and so on, whilst FSW is used to combine multiple plates/sheets. FSP employs an indestructible tool with a specifically developed shoulder and pin that rotates and plunges into base material and traverses in a specified direction

to cover up the required area, as illustrated in Fig. 1.2. Apart from composite manufacturing, contemporary FSP uses include microstructural modification of metal matrix composites (MMCs), homogenizing alloys derived by powdered metallurgy, easing casting flaws, secondary particle dissolution, generating functionally graded composites, metallic foams, and so on [6-9]. Finding a material with specific properties is one of the most important issues in many industrial applications, especially in the aerospace and transportation industries. So there is a need of designing material with the desired properties. However, there are many limitations in terms of cost and time of production with conventional processing techniques like powder metallurgy technique and stir casting . High strength accompanied by high ductility is possible with materials having fine and homogenous grain structures. Friction stir processing is the technique that would produce a material with small grain size that satisfies the requirements of strength and ductility [10]. In this study, the fabrication of composites in the joining of dissimilar aluminum alloys was discussed.

1.5 MECHANISM OF COMPOSITE FABRICATION USING FSP

Composite fabrication is accomplished by adding reinforcing particles to the base material matrix from the outside and then executing FSP. There are two steps to composite manufacturing using FSP. The incorporation of reinforcing particles (RPs) into the base material-matrix is the first stage, and the FSP of the RPs incorporated base matrix is the second stage. RPs (also known as reinforcement approaches) can be pre-placed in a variety of ways. Groove techniques, Direct pasting of RPs, spray techniques, and other approaches are among them [11]. Each technique of reinforcement preplacement has its own set of stages and advantages and disadvantages. The approach of direct pasting RPs onto the base matrix was used to begin the production of SCs. It is a rapid procedure that does not require any preparation stages such as drilling holes or grooves, but it has a substantial problem of RP waste during FSP [12]. During the process, a small percentage of RPs sputters out, resulting in RP waste. To avoid sputtering during FSP, various reinforcement schemes have been developed. The groove method, spray technique, hole technique, and hollow tool technique are examples of these. The groove method is the most popular. The groove method entails machining a groove on the surface of plate with predetermined dimensions [13-14]. The RPs are then poured into the groove and squeezed. The groove entrance is sealed with a pinless tool after the RPs are packed. FSP is then conducted using a specifically

developed instrument with a pin. Fig. 1.2 depicts the typical stages involved in the groove approach. However, the groove can be covered with a thin sheet or piece of tape to avoid having to seal the groove. The hole technique entails drilling holes of appropriate diameters in the base material [16]. Half of the tool shoulder was proposed to covers the next hole ahead of the hole. The spray technique is another approach for eliminating the closing phase. The base plate does not even need to be machined. A slurry of reinforcing particles is sprayed on surface of base plate using plasma spray, and other methods, followed by FSP.

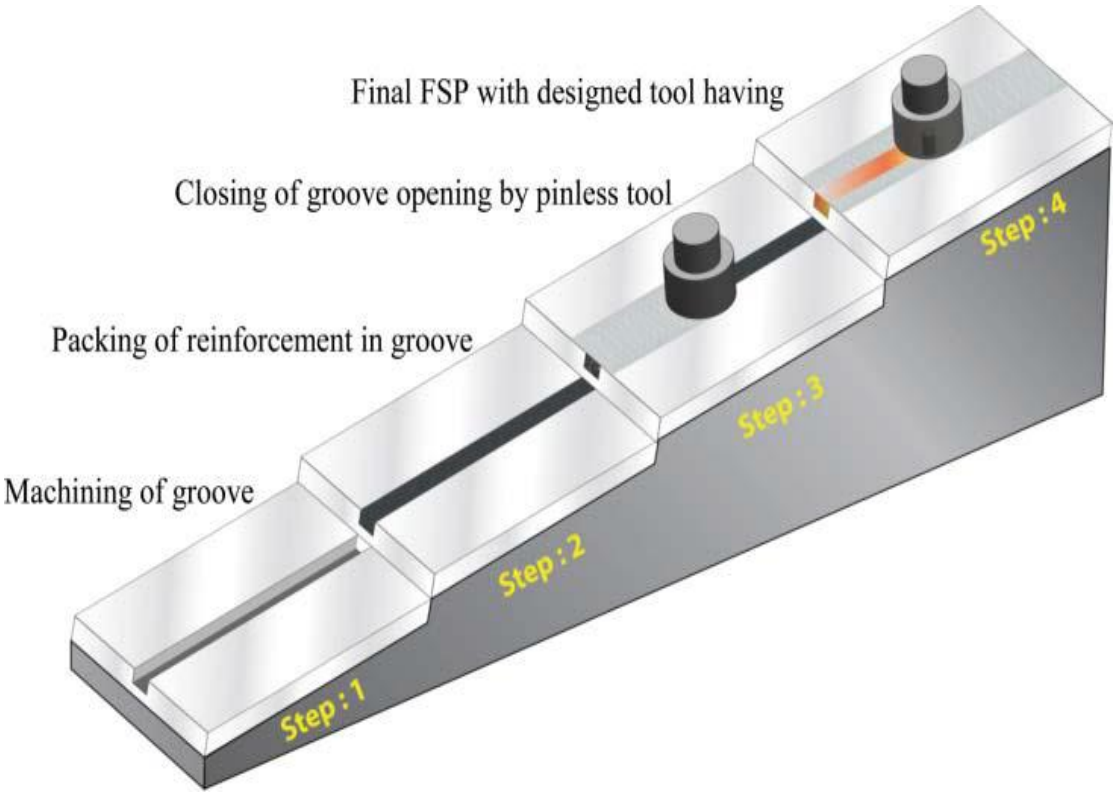

Figure 1.2: Steps in composite fabrication via groove method [15]

Reinforcing particles are formerly immersed in the hollow tool, which is then flowed out to penetrate the area limited between the shoulder of the tool and deformed zone in the hollow tool process. As the rotating tool moves longitudinally, these RPs compress into the workpiece. However, a deeper SCs layer requires more work in this manner. As a consequence, it can be determined that a variety of reinforcing techniques are in use, each of which leads in a different RP dispersion and developed different composite characteristics.

In a comparative analysis, Rathee et al. [17] found that direct pasting of reinforcing particles is a simpler approach but produces less homogeneous surface composites than the hole and groove method.

Furthermore, as compared with the blind hole approach, the groove with tool-offset approach produces more uniform composites. To generate defect-free, sound, and uniform ex-situ surface composites, an appropriate reinforcing procedure should be used. The following is a summary of the composite manufacturing mechanism utilizing FSP. The development of friction heat across the region joining the revolving tool and the work material resulting in softening and plasticization of the workpiece material during FSP [18,19].

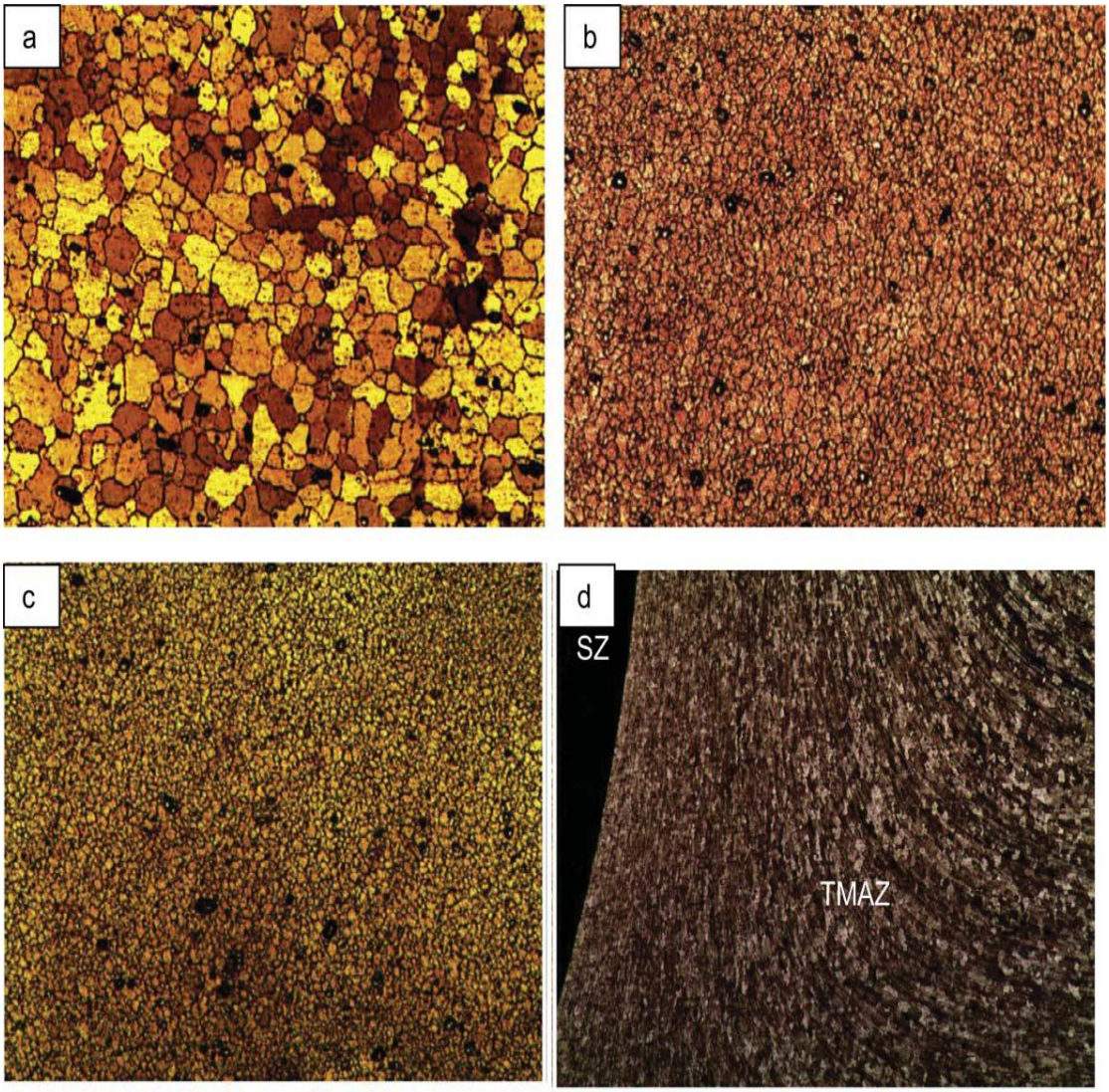

Figure 1.3: Microscopic graphs of: (a) Parent material, (b) FSPed without RPs, (c) FSPed with RPs of CNT, (d) Upward flow pattern of composite interface [20]

The microstructure of as received AA5083 with 21 µm grain size as depicted in Fig. 1.3 a. the grain size was decreased to 6.31 µm after employing FSP without RPs as depicted in Fig. 1.3 b. On addition of RPs of CNT, the size of grains was further

decreased to 3.98 µm as revealed in Fig. 1.3 c [20]. So, the study revealed that the degree of grain size reduction mainly depends on base material, type and size of reinforcing particles, number of FSP passes and selection of optimum process parameters.

1.6 FACTORS AFFECTING WELD QUALITY VIA FSP

Improvements in composite microstructure and mechanical characteristics are entirely dependent on how reinforcing particles are dispersed in the base matrix, which changes depending on the reinforcing technique used and the variable combinations used in composite production.

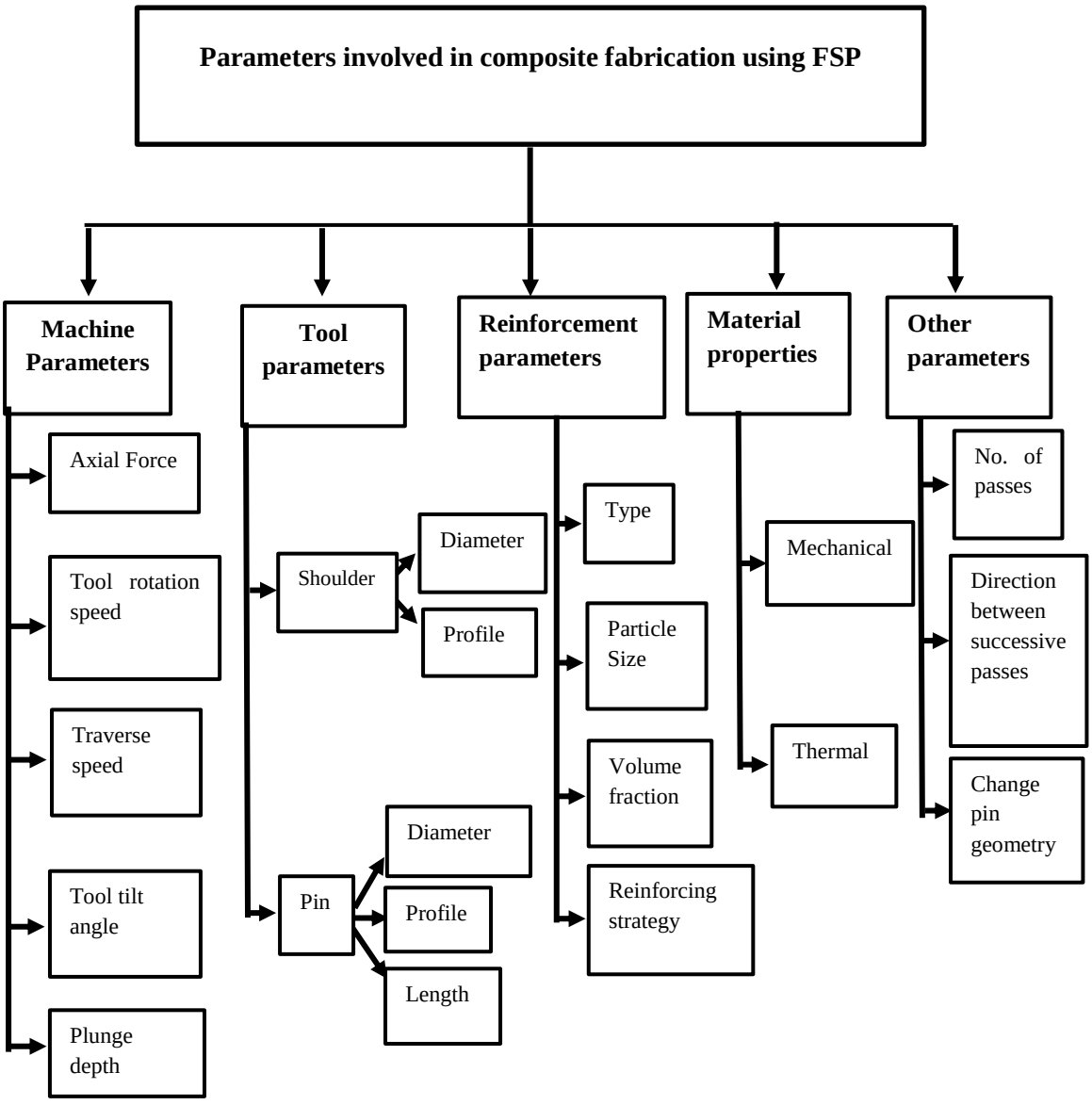

Figure 1.4: Various parameters involved in composite fabrication

Figure 1.4 is an illustration of the many elements involved in composite production. These parameters may be categorized into five categories according on their impact on SC properties: machine particular, tool particular, reinforcement particular, material property precise, and other strategies. When compared to other factors, some contribute more to property enhancement.

1.6.1 Tool rotation speed (RS)

The rate at which the tool revolves around its axis is known as the tool rotation speed. It is an essential factor in FSP/FSW. The heat input in the workpiece during welding is also affected by tool rotation speed. It is expressed in rpm.

1.6.2 Traverse speed of the tool

The tool's traverse speed influences the joint properties as well. This refers to the rate at which the revolving tool moves forward on the workpiece. During processing/welding, the variation of the heat input in the workpiece depending on the tool traverse speed.

1.6.3 Axial force applied by the tool

In FSP/FSW the download force employed between the tool and the work piece is also an essential element. The downward force is used to keep the tool in contact with the surface of parent material.

1.6.4 Tool Tilt angle

During friction stir processing/welding, the weld quality is also depending on the angle of tool with respect to the workpiece.

The angle is usually 90^0, however it can vary up to 3^0 in special circumstances.

1.6.5 Plunge depth

The link between plunging depth and tool inclination is substantial. Tilt inclinations and plunging depths may be modified concurrently to produce desired tool-work piece contact areas. Increased tilt inclinations while keeping constant plunge depths result in reduced heat production because there is less contact surface between the workpiece surface and the shoulder of tool. Higher tool penetration depths are required to

compensate for the loss in surface contact and consequently the quantity of heat produced.

1.6.6 Shoulder diameter

The shoulder diameter of tool is utilized to generate more heat during processing/welding and to cap the plasticized material when it is "stirred." The weld quality is also impacted by the tool shoulder diameter. The weld zone will be larger as the tool shoulder diameter increases.

1.6.7 Tool pin length

This is a crucial consideration for determining joint properties. The length of pin should be slightly lesser than the workpiece thickness. As a result, the tool pin length might be regarded a critical parameter in friction stir processing/welding.

1.6.8 Tool pin diameter

The diameter of the tool pin is utilized to generate friction heat and agitate the material during welding. In FSP/FSP, the tool pin diameter is a critical parameter. Friction heat in the treated zone will increase as the tool pin diameter increases.

1.6.9 Tool pin profile

During FSP/FSW, many tool pin profiles can be employed. The quality of the weld junction is also affected by the tool form.

Cylindrical, cylindrical with threads, square, hexagonal and trapezoidal are some of the most common tool pin forms.

1.6.10 Reinforcement particles type, size, and volume percent

The characteristics of manufactured composites are also influenced by the type and size of RPs. Various types of reinforcing particles such as silicon carbide (SiC), tungsten carbide (WC), carbon nanotubes, graphite, boron carbide (B_4C), aluminum oxide (Al_2O_3), and others have been used to fabricate SCs utilizing FSP. Several researchers created hybrid composites employing two or more RPs at varying ratios of hybrid, in addition to mono composites.

1.6.11 Other parameters

The dispersion of reinforcing particles improves with the enhancement in the number of passes during composite manufacture through friction stir processing, as does the change in direction and pin shape. The following factors are being combined in order to better regulate the process, which is currently being researched.

1.7 TYPES OF REINFORCEMENT PARTICLES

Despite their wide range of technical uses and exceptional features, Al alloys have limited yield strength, stiffness, and wear resistance in some applications. Their strengthening is required to make them appropriate for certain technical applications. The young' modulus, yield strength and wear resistance of ceramic particles incorporated in Aluminum matrix rises. AMMCs are gaining prominence in the aerospace, defense, car, and marine industries as a result of their enhanced characteristics. To take advantage of their hard character, a variety of reinforcement particles have been introduced to aluminum-matrix utilizing FSP. Ceramic particle forms of reinforcements are described in this section. Silicon carbide (SiC), graphite, titanium carbide (TiC), titanium diboride (TiB_2), boron carbide (B_4C), aluminum oxide (Al_2O_3), carbon nanotubes, and other reinforcing particles are often employed. In addition to process factors, MMC characteristics are influenced by the type, size, volume percentage, and spatial orientation of RPs [21]. Here, the characteristics of various RPs, as well as their fabrication challenges and applications, are examined.

Silicon carbide (SiC)

One of the most common reinforcements used in AMMC is silicon carbide (SiC). It has a low density (3.20 g/cm^3) and melting temperature (2700 ºC). High variations in thermal expansion coefficients between two constituent components (SiC and Al) generate problems during solidification, which is a common concern when synthesizing Al–SiC composites using standard composite production processes. FSP overcomes these issues because it is a solid-state method [22].

Boron carbide (B_4C)

Boron carbide is another prominent reinforcing material. It has a low density (nearly 2.52 g/cm^3) and hardness of about 2800 kg/mm^2 [22]. It has a melting temperature of 2,763 ºC. Composites of Al/B_4C are useful for nuclear power reactors as neutron

absorbers. The particles of boron carbide are also utilized to improve the aluminum alloys' ballistic performance. These composites are commonly utilized in the construction of bicycle frames, ballistic jackets, armour vehicles and tanks, car parts, and other items due to higher hardness, remarkable bonding capability, and strong thermal and chemical stability [23].

Titanium diboride

Titanium diboride (TiB_2) is a high-density material with a density of 4.52 g/cm^3, a hardness of about 2,500 kg/mm^2, and a melting temperature of 3,225 ºC [24]. It is thermally stable and has a high Young's modulus (about 565 GPa). Because of its considerable hardness, and excellent thermal stability, it is being used in MMCs. In standard liquid state composite manufacturing approaches, however, mixing the particles of TiB_2 necessitates additional effort due to TiB_2 particles settling down due to its higher density and low wettability differential than aluminum alloys [25]. FSP/FSW overcomes these issues because it is a solid-state approach.

Carbon nano tubes (CNTs)

CNTs are another essential reinforcing candidate that has been demonstrated to be useful in the production of MMCs. These are graphitic carbon materials that are tube-shaped and have a high modulus of elasticity (up to 1 TPa) and stiffness (up to 63GPa). These have excellent thermal and electrical properties in addition to excellent mechanical characteristics. These can be metallic or semiconductor depending on their shape and size [26].

AMMCs reinforced with carbon nanotubes are becoming more popular in a range of structural applications. However, CNTs' ability to tolerate severe plastic deformation at higher temperatures is a serious drawback. High shear stresses cause CNTs to fail, and they turn into fine spheres, as in the ball milling [27]. When CNT walls are broken, new structures such as carbon onions may form. CNTs, on the other hand, have been shown to withstand a variety of SPD processes, including equal channel angular processing, accumulative roll bonding, and so on.

A single FSP pass was used to establish CNT survival in MMCs [28]. To increase the homogeneity of CNTs in MMCs like those seen in Fig. 5a and 5b, traditional FSP requires many passes. Fig. 1.5a depicts nonuniformity in CNT distribution after two

FSP runs, whereas Fig. 1.5b depicts homogeneity after three passes. After two FSP runs, some tube-shaped structures became visible, indicating that the CNTs had withstood the second FSP run, as seen in Fig. 1.5c. Furthermore, as shown in Fig. 1.5d [29], In contrast to the initial CNTs, this resulted in a shortening of the CNTs and the formation of particular circular formations.

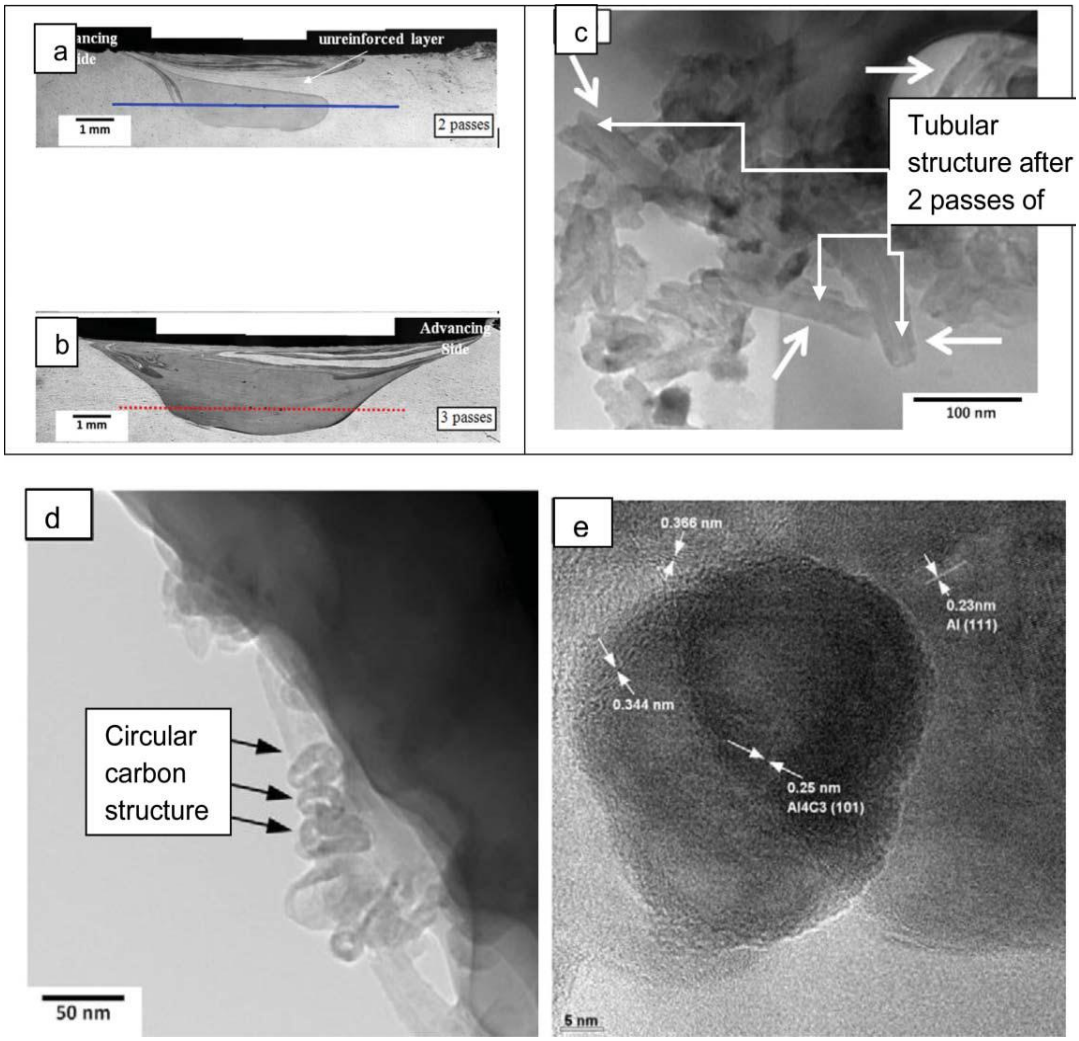

Figure 1.5: Micrograph of Al5059+CNT composites after: (a) 2-FSP passes; (b) 3-FSP pass; (c, d) 2-FSP pass TEM photograph; (e, f) after 3-FSP pass HRTEM photograph [29]

Titanium carbide (TiC)

Titanium carbide (TiC) has such a high melting temperature of 3067 ºC and a density of 4. 91g/cm^3. TiC has a high elastic modulus and the grain refining capability when compared to aluminum alloys. Al/TiC composites are challenging to produce due to TiC's high density, poor wettability, and substantial CTE discrepancy between Al and TiC.

Cerium oxide (CeO_2)

Cerium oxide (CeO_2) seems to be another significant reinforcement that is gaining popularity in aluminum-based MMCs for sectors such as the shipping sector, where corrosion resistance is critical. In general, the addition of RPs (especially SiC) lowers the corrosion resistance of aluminum-based MMCs [30]. CeO_2 is commonly used as a corrosion protection promoter because it serves as a cathodic blocker, slowing down cathode activities. [31].

Aluminum oxide (Al_2O_3)

Aluminum oxide is another essential reinforcing candidate used in the production of MMCs. It has a low melting point of roughly 2,050 ° C. and a high density (4.08 g/cm^3). Because of their superior wettability, low melting point, and inexpensive cost, they are becoming increasingly popular.

In the FSP manufacturing of surface composites, some researchers used micro and nano-sized Al_2O_3 particles. Zarghani et al. [32] created Al6082/ Al_2O_3 surface composites. The introduction of nano-sized Al_2O_3 particles increased microhardness by 168 % and increased wear resistance by two to thrice. Particles dispersion consistency, wear resistance and microhardness all improved as FSP passes increased. Raaft et al. [33] discussed the synthesis of monocomposites of A356 with graphite and Al_2O_3 particles. In terms of wear and mechanical properties, the scientists discovered that A356/ Al_2O_3 based composites beat A356/ graphite-based composites. A maximum improvement in microhardness of 82 percent was also observed in Al_2O_3-based composites.

Therefore, in the present study, micro and nano-sized particles of Al_2O_3 are used as reinforcing candidates.

1.8 DECSRIPTION OF THE ROTATING TOOL

The tool has two essential elements, the shoulder and pin as depicted in Fig. 1.6. The pin has generally a cylindrical form that projects from the shoulder surface and a longitudinal axis that is parallel to the shoulder longitudinal axis. During welding, the pin creates heat and stirs the material. At working temperatures, the pin must be big enough to keep above the plastic stress level. The weld quality is also affected by the profiles of tool pin. Cylindrical, cylindrical threaded, trapezoidal, square, and other pin profiles are available. The tool shoulder has two purposes: to produce more heat at the

work-piece/ tool frictional contact and to cap the "stirred" plasticized material. The plasticized material during FSW tends to extrude from the tool's leading to the trailing side, but is restrained by tool shoulder, resulting in a smooth surface finish.

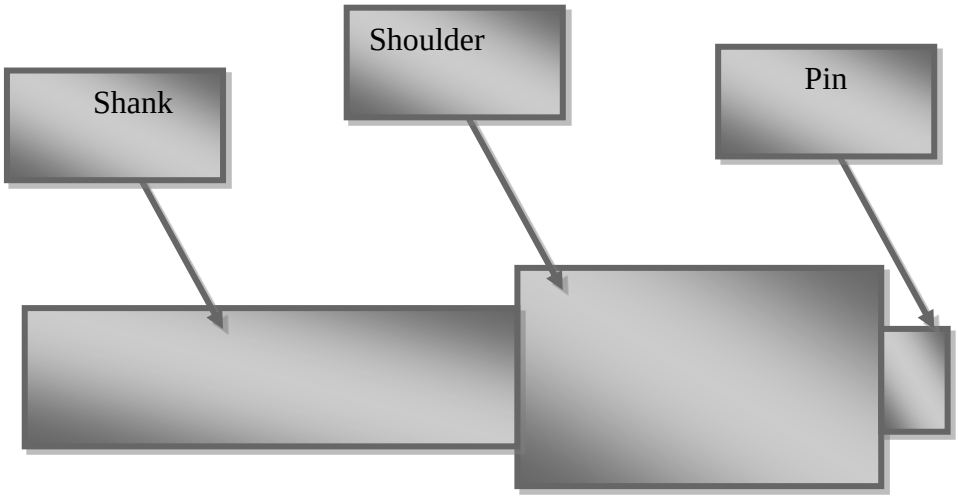

Figure 1.6: Tool outline for FSW

1.9 TOOL MATERIAL

Friction stir welding/ processing, is carried out by thermomechanical deformation in which the tool temperature approaching base metal's solidus temperature. Welding/processing takes place at temperatures between 70 and 90 percent of the base metal's melting temperature, thus the material of tool should be enough strong enough to sustain twisting and breaking at this temperature. As a result, having a tool that loses dimensional stability, the intended characteristics, fractures are undesired [34].

The following factors must be considered while selecting a tool material:

- Strength at ambient and elevated temperature
- Tool reactivity
- Machinability
- Fractural toughness
- Wear resistance
- thermal expansion coefficient
- Elevated temperature stability.

An FSW/FSP tool used may be made of various materials such as H13 tool steel, tungsten-based, Ni-alloys, polycrystalline-cubic boron nitride (PCBN), and other materials. A tool composed of H13 tool steel that has been heat treated and oil quenched was employed in this study.

1.9.1 Tool Steel

Tool steel like H13 is very common tool material which is used in FSW/FSP for magnesium alloy, aluminum alloy, and copper alloy. The advantages of tool steel include easy machinability and availability, low cost and have excellent mechanical properties. The tool steel H13 can be used for similar or dissimilar aluminum alloy. H13 tool steel have a resistance to damage from deformation and abrasion in the FSW of aluminum alloys.

1.9.2 Nickel Cobalt base alloy

The Nickel cobalt-based alloys are fabricated to reveal high strength and excellent corrosion protection. The operating temperature should be less than the precipitation temperature ranges from 600-800°C to prevent the dissolution and precipitate over-aging. Nickel cobalt base alloy tool is mainly designed for aircraft engine components.

1.9.3 Refractory Metals

The refractory metals such as tungsten, tantalum and molybdenum are used for high temperatures and high densities parent materials for friction stir welding. These metals are the strongest alloy having melting point from 1000-1500^{0}C. The refractory metals tools are mainly design for welding of aluminum alloy, copper, steels and tungsten base alloy, but the main drawback of refractory metals is high cost, long lead time and difficult to machining.

1.9.4 Carbides and Metal matrix composite

Because of superior mechanical and physical properties (i.e. fracture toughness, wear resistance and ambient temperature) of carbide they are mainly used as machining tools. Friction stir welding tool such as tungsten carbide is reported to have fine and uniform welded surface with or without pin thread. Tungsten carbide is brittle in nature and have very high strength due to bonding between tungsten and carbide atoms. Tis bonding also leads to have high melting point about 2800^{0}C. This tool is mainly used for copper, steel and aluminum alloy welding.

1.10 TOOLS DESIGN

A good tool design and correct material selection may change the weld characteristics and reduce the void size. A good quality and perfect designed tool may prevent the surface tears and reduce the flashing. The tool shoulder diameter and pin diameter design may play some significant roles in the welded joint. Additionally, tool pin can reduce tool stresses and provide better flow along the direction of welding. There are different types of tool design including shoulder design and pin design which are given below.

1.10.1 Shoulder design

The tool geometry is the essential element which control the flow of material during FSW/FSP. The tool shoulder is also responsible for the frictional heat generation and facilitating of material movement around the tool pin. The tool shoulder also produces downward force for consolidation of weldment. The FSW/FSP technique employs a variety of shoulders, including the ones listed below.

1.10.1.1 Concave shoulder

The concave shoulder is the most common and standard design for FSW because they produce good quality welds, easily machined, and simple design. The small angle from 6 to10^0 produced between the pin and the shoulder edge. During the FSW process, the displaced base plate material is inserted into the shoulder's cavity. The shoulder may have to increase material distortion amount created by the tool shoulder, resulting in an increase in the proper mixing of base material and high-quality weld. As the feed rate increases, the concave shoulder has a tendency to lift away the work piece surface, and when concave shoulder replaces by the scrolled shoulder then they reduce the tool lift and increase the welding speed.

1.10.1.2 Convex Shoulder

Another type of friction stir welding tool is the convex shoulder. Generally, this type of shoulder is not used because parent material pushed away from the pin by convex shape. This type of shoulder is reported successfully for a very thin plate approximately 0.45 mm with tool shoulder diameter of 6 mm. The tool shoulder may have engaged at any position with the workpiece but the tool's outer edge is not engaged with

workpiece, this is the main advantage of convex shape tool. There are two types of the profile may be used of convex shoulder either tapered or curved profile.

1.10.2 Pin Design

The FSW/FSP tool pin is used for enhance the mechanical properties of work-piece and obtained the heat through the friction between base material and rotating tool pin. The tool pin design governs the traverse speeds and deformation. In this section different types of pin design and their merit and demerit are discussed in open literature.

1.10.2.1 Round-bottom cylindrical pin

This is used to transfer the material from shoulder to pin bottom. The root diameter of the tool pin should be 70-85% of the pin diameter. It means the pin diameter root decreases up to the pin diameter as shown in Fig. 1.7. The weld quality was observed by the various past researchers [35] 2. The flexibility of the design is that the pin's diameter and length may be willingly changed to suit the user's requirements. The tool life may increase by removing stress concentration with the help of machining a root radius.

Figure 1.7: Design of round bottom cylindrical pin [36]

1.10.2.2 Flat-bottom cylindrical pin

This is one of the most popular friction stir welding tool pins. The benefit of flat-bottom pin over round-bottom pin is that the velocity of rotating cylinder increases to a higher value to the cylinder edge. The velocity of flat bottom cylindrical pin has 28 times the

round bottom pin, because of enhanced surface velocity, the throwing power of the flat pin also increases. The other advantage of flat over round is that the machining to flat pin is easier than the round pin and welding defect can be improved by the flat pin instead of round pin.

Figure 1.8: Design of flat bottom cylindrical pin [37]

1.10.2.3 Truncated cone pin

Past researchers were found that the cylindrical pin is sufficient for aluminum and magnesium alloy welding up to 13 mm thick plate, but they want faster travel speed of thick plates, so this reason truncated cone pin was introduced to increase the travel speed as well as decrease the welding time. The truncated cone pin has lower transverse load as compare to cylindrical pin. The truncated cone pin is designed for high temperature material as depicted in Fig. 1.9.

Figure 1.9: Design of truncated cone pin [38]

1.10.2.4 Thread less pin

Thread less pins are used in some specific friction stir welding application where thread pin feature could not survive without fracture {Fig. 1.10). The threaded tool pin cannot retain at high temperature or high abrasive composite alloys without excessive pin wear.

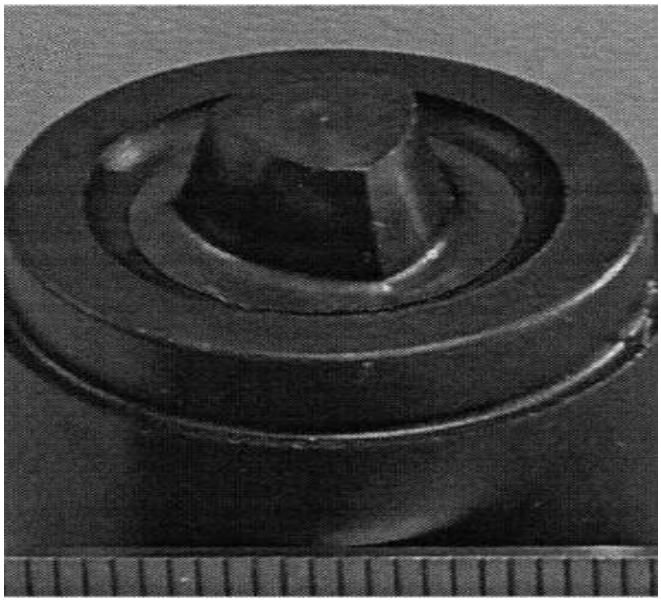

Figure 1.10: Design of thread less pin [39]

1.11 MICROSTRUCTURE CLASSIFICATION

The welding zone is divided into four discrete sections for the microstructure analysis. Fig. 1.11 depicts the microstructure zone of AA 6082.

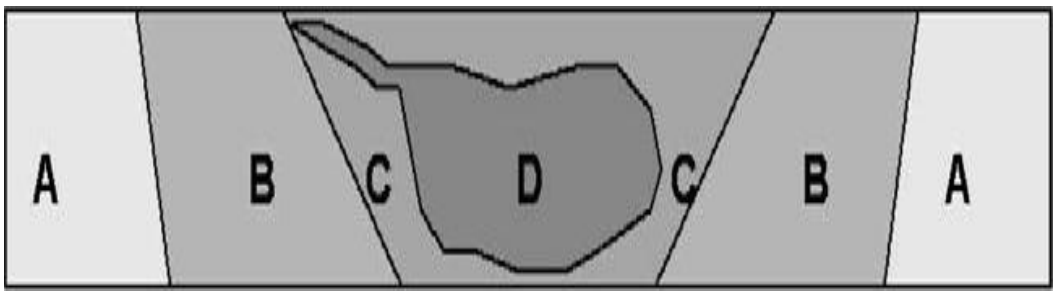

Figure 1.11: Cross-section of an FSW joint of AA 6082 [40]

The system categorizes the weld zone into the following regions:

A	Parent material
B	Heat-affected zone
C	Thermo-mechanical-affected zone
D	Nugget zone (Stir zone)

1.11.1 Unaffected material (parent material) (A)

This is material that has not been deformed and has not been impacted by the weld heat in terms of mechanical or microstructure qualities.

1.11.2 Heat affected zone (B)

Obviously, this zone is closer to the welding center. This region has experienced a heat cycle that has changed the material's microstructural evolution and/or mechanical characteristics. However, no plastic deformation takes place here.

1.11.3 Thermo-mechanically-affected zone (C)

In this zone, the material has been deformed plastically by the tool, and the heat produced by the process will change the material's characteristics and microstructure. In the case of aluminum, considerable plastic strain may be achieved without recrystallization in this region, and the deformed zones and the recrystallized zone of this zone are usually well separated. The characteristic recrystallized portion (the nugget) is missing in other materials, and the entire TMAZ seems to be recrystallized.

1.11.4 Weld nugget (D)

Weld nugget refers to the recrystallized region of the TMAZ. Because the grain structure is frequently distinct here, the region directly below the shoulder (that is obviously part of the TMAZ) should be given its own classification. This area should be classified as a separate TMAZ sub-zone, according to the experts.

1.12 JOINT GEOMETRICS

FSW is not affected by gravity. As a result, it may be employed to weld in any orientation, including annular vertical, and horizontal. As a consequence, FSW has been utilized to produce circumferential welds of fuel tanks in spacecraft. Regular corner and fillet welds as well as double V-butt joints, and other applications are also possible with FSW.

1.13 MATERIAL SUITABILITY

Within given parametric tolerances, the following aluminum alloys might be successfully welded to produce consistent high integrity welds:

2XXX aluminum series	(Al-Cu)
3XXX aluminum series	(Al-Mn)
4XXX aluminum series	(Al-Si)
5XXX aluminum series	(Al-Mg)
6XXX aluminum series	(Al-Mg-Si)
7XXX aluminum series	(Al-Zn)
8XXX aluminum series	(Al-Li)

1.13.1 Aluminum alloys

The various aluminum alloys are utilized in automobile and aerospace engineering industries. The major alloying elements which are used in different Al-alloys are Copper, manganese, Magnesium, Silicon, Magnesium, Zinc, and tin. The most important aluminum alloy is silicon base alloy (Al-Si), where high percentage 3.5 to 12% silicon is used. Silicon base aluminum alloy have excellent casting characteristics. These alloys are widely utilized in automobile sector, aerospace engineering such as metal skinned aircraft etc. The second widely used alloy is magnesium base aluminum alloy. These alloys are lighter than the all-aluminum alloys. Aluminum alloy have an attractive appearance in its natural finish, which may be shiny, lustrous and soft. Aluminum alloy can re recycle from the scrap value and providing environmental benefits and economics. It has easily fabrication and joining ability. The physical, chemical and mechanical characteristics of Al-alloys depend on composition of alloying elements (i.e. Cu, Si, Mg, Mn, Zn, Sn, and Fe), grain size and microstructure. The total amount of alloying elements should be less than or equal to 10% and the impurity elements should be less than 0.15%. There are wide range of mechanical and physical properties of aluminum alloy over a steel which are as given below.

- The density of aluminum alloy is only $1/3^{rd}$ that of steel.
- Aluminum alloys may have high ductility, high toughness and have high strength to weight ratio.
- Aluminum alloy have a high resistance to corrosion under critical service conditions and it's also used for cryogenic application

- Aluminum alloys are highly reflective material and it is an excellent conductor of heat and electricity.
- Aluminum alloys are nontoxic and non-ferromagnetic material and it can have used for food and beverages containers.

1.13.2 Types of Aluminum alloys

On the basis of alloying elements, the aluminum alloy may be classified into different categories which are as given below.

1XXX series

In wrought aluminum having 1XXX series have present various elements as inherent impurities in the smelter grade. AA 1100 and 1135 are the 1XXX series alloys. These alloys have specified minimum and maximum copper contents. Corrosion resistance, thermal conductivity and electrical conductivity of 1XXX series alloys is very high and may also obtained high tensile strength via strain hardening. The silicon, copper and iron are the alloying elements present in the highest percentage in 1XXX series.

2XXX series

Magnesium is the secondary alloying element in the 2XXX series, with copper (Cu) being the primary alloying element. For obtaining optimum mechanical and physical properties, these alloys required heat treatment. After heat treatment the mechanical properties of 2XXX series are very similar or sometimes exceed the low carbon steel. The corrosion protection properties of these alloys are not good as compare to other aluminum alloys or sometimes it shows intergranular corrosion. These alloys are commonly used to make suspension parts, structural part and aircraft wheel etc., and it also have high strength to weight ratio.

3XXX series

The main alloying element in the 3XXX series is manganese (Mn), the strength of 3XXX series alloys have 20% more than 1XXX series alloys. They are not heat-treated alloys, but having good corrosion properties. The alloying element Mn is limited (up to 1.5%) present in the aluminum solid solution and form precipitates Al_{12} $(Mn, Fe)_3Si$ or $Al_6(Mn, Fe)$ phase. These alloys are frequently utilized in cooking equipment, architectural product, chemical equipment's and resistance to corrosion.

4XXX series

In 4XXX series, the silicon is the major alloying element and it may be added upto 11% to the lowering the melting point without increasing of brittleness. The Al-Si alloys are mostly used as a welding filler wire with different grade for joining similar or dissimilar aluminum alloys. Mostly these alloys are not heat treatable. ER4043 is widely used as a filler wire. Due to containing of silicon they are demanded in architectural application, production of forged engine piston etc.

5XXX series

In this series, magnesium (Mg) is the main alloying element. When it is used with manganese (Mn), high strength alloy would get. Mg is more effective than Mn as harder. 0.8% magnesium is equal to 1.25 manganese for hardened the alloys. The 5XXX series shows good corrosion resistance in marine atmosphere and also has excellent welding characteristics. Magnesium base aluminum alloy like ER5356 used as a filler wire to join the different aluminum alloys with TIG or MIG welding processes.

6XXX series

The principal alloying elements in 6XXX series are Mg and Si, typically less than 1% each, and minor amount of chromium, copper, zinc and manganese. The magnesium silicate Mg_2Si was found in 6XXX series which is the hardening constituent. This alloy series are heat treatable, excellent corrosion resistance, versatile, highly formable, high strength, and excellent weldability, the weld metal cracking may be prevented by the use of different filler metal such as ER4043, and ER5356.

These alloys shouldn't be welded by an arc without filler since they are inherently susceptible to solidification cracks. Depending on the service and application requirements, 4xxx and 5xxx series filler material may be used for welding. These alloys are commonly used for automotive components and architectural extrusions.

7XXX series

Zinc (Zn) is the principal alloying element of this series, and it may be added from 2 to 10%. Due to its excellent mechanical characteristics, these alloys are used in high

performance application i.e. competitive sporting equipment, aerospace and aircraft engineering, automobile industries etc.

The inclusion of magnesium further complicates the issue by forming additional ternary eutectics and complicated intermetallic, which provide dispersion hardening and $MgZn_2$ precipitates. The copper zinc system produces $CuAl_2$ and an intermetallic, which together add to the precipitation's hardness. When welding, the zinc instantly turned into an oxide, lowering the weld pool's surface tension and increasing the chance of fusion defects, which is a problem specific to the 7XXX series. This necessitates the employment of welding processes that use a welding current that is 10–15 percent greater than that of a 5XXX alloy. It's also been discovered that using a shorter arc than usual improves material transfer to virtually globular levels.

8XXX series

This series is frequently utilized to designate alloys, such as 8001 (Aluminum-Ni-Fe) and 8020 (Aluminum-Ni-Fe) (Aluminum-Sn), that don’t easily fit into any of the prior groups. The Al-Li alloys, however, are a relatively recent class of high-strength alloys that offer a higher Young's modulus and significant weight reductions of about 15% compared to some other alloys of high-strength. Each 1% increase in lithium resulted in a weight loss of about 3%. These benefits indicate that lighter, weldable Al-Li alloys can replace high strength alloys, as of 2XXX family, in the design of aircraft structures, leading to considerable weight savings.in the design of aircraft structures, resulting in significant weight reductions.

After being given a name, the family of alloys known as "scandium-containing alloys" may also fit under this category. These are brand-new alloys that are still in the early stages of development. Scandium has been discovered to be quite successful in enhancing strength through grain refinement and age hardening, the latter of which is especially advantageous in welding of materials. Scandium maybe combined with additional alloying materials like zinc, magnesium, zirconium or lithium to produce tensile strengths of above 600 N/mm2 in laboratory tests.

1.13.3 Other materials

FSW/FSP method has also been employed to other materials, on which research is now being conducted. The following are a few of them:

- Magnesium and its alloys
- Lead
- Titanium and its alloy
- Mild steel
- Copper and its alloys
- Zinc

1.13.4 History of parent material

Aluminum alloy AA6061

The mechanical and physical properties of pure aluminum are fixed, when two or more metallic elements added in the pure aluminum alloy then new alloy blends the mechanical and physical properties to give better results, more flexible and more durable metal. Most of the aluminum alloy nearly as strong as steel. The heat treatable aluminum alloy AA6061 was initially produced in 1935 and is one of the most widely used alloys for commercial application. This alloy is Mg and Si base alloy and it also include Fe, Cr, Cu, Zn, Mn and Ti. The majority of aluminum alloys are challenging to weld due to their low conductivity, and chemical composition whereas AA6061 is heat treated alloys.

The most common uses of AA6061 are manufacture of automotive components, bicycle frames, yachts, camera lenses, couplings and valves, electrical fitting etc.

Aluminum alloy AA7075

The aluminum alloys are largely used in aerospace engineering. In 19^{th} century Count Ferinand Zeppelin used AA7075 to fabricate the frames of his iconic airships. The AA7075 was selected because it has excellent fatigue resistance, excellent mechanical characteristics, and high corrosion resistance and has similar strength like steel due to its high levels of zinc.

The writer Jules Verne was the first person to understand the potential of Al-alloy in the aerospace engineering. In World War I, the light weight Al-alloys became essential

in aircraft design and development and in Second World War the production of aluminum alloys was increased

The aluminum alloy can be machined easily and hence it was high preferred for fighter planes in world II, including the Mitsubish A6M0 fighter used by Japanese imperial Navy on their carriers between 1940 and 1945. Now these days, the AA7075 is still used in military aircraft.

CHAPTER-2

LITERATURE REVIEW

2.1 INTRODUCTION

This chapter includes a review of the literature on FSW joints (similar or dissimilar metal alloys), and composite fabrication using friction stir processing. To acquire a thorough picture of the work done in the field of processing utilizing reinforcement particles, a literature study is carefully examined from published articles. The research gap and the research objective are determined using the literature review.

2.2 REVIEW OF LITERATURE

Patrick B. Berbon et al. [41] investigated the microstructure of hot isostatic pressing (HIP) and friction stir processing. There are three distinct sections visible: the black parts are practically pure aluminum, while the lighter regions contain Al3Ti intermetallic (either fine or coarse). The microstructure formed owing to aluminum's quick diffusion rate, as opposed to the Al3Ti intermetallic problematic diffusion via titanium and aluminum diffusion. The aluminum-rich region is seen as extended black threads here. The material's tensile qualities were investigated at various temperatures, and highest tensile strength was observed at low temperatures.

Z.Y. Ma, R.S Mishra et al. [42] revealed the fine-grain microstructure of Al-alloy 7075 remained stable at high temperatures of 490°-530° C for one hour. Strain rates ranged from 1x10-3 to 1x10-1 at these temperatures. Elongation of 1250 percent was found at 480° C with strain rates ranging from $3x10^{-3}$ to $3x10^{-2}$, whereas maximum ductility (1042 percent) was observed at 500°C with strain rate $3x10^{-3}s^{-1}$ and grain size reduces from 7.6 to 3.7 m, resulting in significantly improved superplastic ductility, decreased flow stress, lower optimal temperature and higher optimum strain rates. The surface of distorted specimens displayed clear evidence of widespread grain boundary sliding when examined under a scanning electron microscope.

Indrajeet Charitet al. [43] created the multi-sheet structure by FSW and studied using diffusion bonding. Superplastic 7475 Al-alloy was employed in this experiment. For a 2.5 mm thick lap junction, they employed a single pass and six passes joint welding process. Six passes produced a finer grain size than a single pass. The base material’s

grain size was 10 µm whereas, the grain size of after one and six-pass welded joints was 3.2 and 2.2 µm, respectively. The microstructure of the six-pass welded joint remained stable, and the superplastic characteristics were maintained. The tensile strength of base material, welded joints after single-pass and six-passes was observed as 511, 402 and 451 MPa, respectively.

Y.S. Sato et al. [44] investigated FSW to AA1100 with high hardness and ultrafine-grained microstructure. Due to dynamic recrystallization, friction stir welding inhibited a significant drop in hardness in the accumulative roll-bonded material, while the NZ and TMAZ had modest reductions. In an accumulative roll-bonded AA 1100 with strain of 4.8 in the as-accumulated roll-bonded condition, friction stir welding may successfully avoid softening.

Moataz M. Attallah, et al. [45] investigated the abnormal grain growth (AGG) in the nugget zone of FSW of AA2095 in the post-welding heat treatment. The AGG is mostly determined by the welded joint's process parameters. The grain refining of the welded joint was done with a lower heat input, i.e. a lower rotating speed and a high feed rate. Following post-weld heat treatment, aberrant grain development becomes excessive, causing the welded joint's strength to decrease.

Su et al. [46] studied the microstructure commercial AA7075 after friction stir processing. Transmission-Electron-Microscopy (TEM) was utilized to examine the grain structure of the FSW treated region. The FSW area's microstructure did not have a homogeneous grain size distribution. The average grain size falls somewhat from top to bottom. Diffraction rings were also found, which confirms the massive misorientations between the individual grains, according to them. Even with equal grain sizes, the dislocation density was not homogeneous inside the stir zone; this result showed that non-uniform plastic deformation was imparted in the recrystallized grains. Any chosen plate size may be treated to an ultra-fined-grain microstructure by executing many overlapping passes. Multiple simultaneous passes demonstrated in the investigations has been used as an efficient approach to develop large bulk ultrafine grain material with uniformly distributed microstructure.

Z.Y Ma, S.R Sharma, R.S Mishra. [47] investigated multi-pass FSP on silicon-aluminum base A356, and found that as the distance from the fifth FSP pass, increases

the strength of the TMAZ and NZ diminishes. The strength and ductility after the fifth-pass are essentially identical to those of after the single-pass. Furthermore, in the current 5-pass FSP A356, the yield and tensile strength of various micro-structure regions produced by mining tensile specimens is higher than that of big specimens. The distribution of Si-particles, aspect ratio, and grain size of the welded plate were not affected by multi-pass FSP. During the multiple-pass procedure, the silicon particles were evenly dispersed.

G. Buffa et al. [48] suggested a 3D-thermo mechanical-coupled numerical method for FSW that employs a visco-plastic material description for the seam of weld. This model can forecast the influence of input factors on the process thermodynamics, like material flow, strain rate, temperature strain, and forces. With a drop in advancing speed, an extension of the HAZ was discovered, as well as an increase in the nugget's maximum temperature and maximum strain. The asymmetrically distributed flow in the weld zone (WZ) is found because the flow of material is largely influenced by rotating and advancing speeds.

A. Barcellona et al. [49] studied the metallurgical characteristics of different aluminum alloys AA7075 and AA2024 and discovered that the proportion of insoluble particles reduces owing to tool pin action. Both the base metal (AA7075 and AA2024) and the welded area were studied for grain size and dimensions. Due to precipitate density drops, the weldment's lowest hardness value was discovered at the thermo-mechanically impacted zone.

S. R. Ren et al. [50] observed the impact of input parameters on fracture behavior and tensile properties of FSWed joints of Mg, Si base aluminum alloy of Al-Mg-Si, and it was found that the higher tensile strength revealed at RS 1200 rpm, TS 400 mm/min of with 45° shear fracture, while lower tensile strength was found at RS 600 rpm, TS 100 mm/min. The higher hardness profile was noticed at RS 1200 rpm with a TS 400 mm/min.

H.W. Zhang et al. [51] analyzed the material flow under various FSW processing parameters using FEM. The modification of the axial load can impact the equivalent plastic strain dispersion in NZ, however HAZ and TMAZ were not affected. The corresponding plastic strain in the NZ can be raised as the axial load increases. The

flow behind the pin on RS is lower, whereas the flow of material in front of tool pin is faster. The plastic-strain distribution was not symmetric but the plastic strain on advancing side is maximum.

R. Nandan et al. [52] investigated theoretically and experimentally 3-D heat transfer and plastic flow of mild steel and Non-Newtonian viscosity was calculated. The calculated result revealed considerable visco-plastic flow near the tool surface, with convection being the dominant heat transfer mechanism in this area. During FSW of mild steel, the highest strain rate was 40 s^{-1} was observed.

Zhang et al. [53] used FEM based on solid mechanics to simulate 3D material flows and mechanical characteristics with variable processing settings. The impact of process parameters on the joining qualities of welds is also investigated using experimental data. According to simulation studies, the tangent flow accounts for the majority of the material flow which can be accelerated by the shoulder on the upper side of the friction stir weld.

Y. Wang and Shi et al. [54] analyzed the tensile characteristics of the as-extruded welded joints with various FSW process parameters. The ductility was increased by 11.7 percent with a small decrement in tensile strength. From 634 MPa to 565 MPa, there was a drop in yield strength. Dynamic recrystallization during FSW produced fine-grained microstructures.

A. Pirondi et al. [55] examined the fractural toughness of the FSWed joint and revealed that the fracture toughness of joints was nearly 25% less than the base material for W6A20A, whereas, it is 10–20% higher for W7A10A. FSW joining has the opposite effect on fatigue crack growth strength, especially at near the threshold growth rates of crack, as it does on fractural toughness, i.e. crack spread level is dropping in W6A20A than in base material, whereas it is greater in W7A10A.

M. Maalekian et al. [56] explored the rate of heat generation in orbital FSW of steel utilizing several approaches, including continuous coulomb friction and sliding sticking friction. Specific heat, thermal conductivity, and yield-strength are all affected by temperature. By comparing estimated and observed temperature data, all strategies described the actual heat production rate. The inverse conduction of heat approach is

the most precise and best describe the actual heat-input during the FSW, according to the findings.

Z. Zhang et al. [57] developed the thermo-mechanical model to estimate the distribution of temperature and material deformation. According to this model, the maximum temperature in the FSW is increased as RS increases. The TS can lead to enhance the efficient power input for friction stir welding system. The increasing RS and decreasing TS may lead to enhanced stirring of the rotating tool, which can modify the weld quality. When the traverse speed increases than the increment in the rotational speed is necessary to avoid welding defect. When the TS and RS is increased, residual stress also increased.

Z.Y. Ma, R.S Mishra et al. [58] studied the impact of double passes on the mechanical behaviour of FSP of aluminum alloy 7075. Almost similar grain sizes range from 5.3 to 5.8 μm were found in both single and double FSP pass. The higher temperature was observed in a double pass on comparison with single pass. Double FSP pass found an enhancement in superplastic elongation as compared to single-pass Al-7075. The double FSP pass on Al-7075 had the highest superplastic elongation of 1220 percent at 480°C. The main superplastic distortion approach for both double and single-pass FSP is grain boundary sliding, according to superplastic analysis.

Jerry Wong et al. [59] welded the AA6061 plates of 1 mm thickness and studied the impact of a rotating tool; the revolving and advancing speeds were adjusted. To assess joint strength, the specimens were sectioned. Vickers microhardness indentations and metallographic investigations were performed. As a result of crystallization, higher value of feed rates and intermediate value of rotational tool speed provide a better weld joint in the stir zone. The tensile test also shows that higher value of feed rates and intermediate values of rotational speed produce a better weld joint. Due to the heat input, lower advance and feed rates result in the dissolving of hardening precipitates, Mg_2Si in this case, and increased precipitation.

L. Commin et al. [60] found that the temperature distribution is consistent over the weld length but asymmetric between the AS and RS because of the heat input created by the plastic deformation. Grain growth was detected with a rise in the processing parameters that endorse heat generation, and stress levels were greater on the RS. The

grain size evolution follows the models proposed, which take into consideration the strain rate and processing temperature.

Olivier Lorrain et al. [61] has been done FSW on Al alloy with two different tool pin profiles. The first pin was unthreaded with a flat surface, whereas the second pin was unthreaded without a flat surface. In order to investigate the materials, the longitudinal-section and cross-section of the weldment with or without the use of material marking were observed. The material flow via the classic thread tool has the same characteristics as the flow of material via the classical thread tool. The macro weld cross-section shows that when product of the thrust force and the rotational speed is increased, the area affected by the rotation of the shoulder in the thickness direction is thicker than the tapered pin with three flats.

According to **Mohamed Assidi et al. [62]** realistic 3D simulation software provides for a far more thorough inverse analytical approach by simulating the complete complexity of the friction stir welding process. With an unthreaded concave tool, a friction stir welding experiment is performed on an AL 6061 aluminium plate. For varying traverse speeds, the tool temperatures and force are carefully measured in a steady welding condition. The simulations are based on the forging F.E software's ALE (arbitrary Langrangian Eulerian) formulation. Welding forces and tool temperatures are extremely sensitive to minor fluctuations in friction, allowing for precise friction coefficient determination.

D. Jacquin et al. [63] created a simple thermo-mechanical model for FSW that predicts the temperature gradients in the weld region, the sliding ratio at the shoulder-to-workpiece interface and power dissipation. The contact conditions analysis yields valuable information regarding the development of the relative sliding between the material and the shoulder of the tool. The sliding ratio rises with the rotating speed and falls with the temperature in the tool's proximity. To measure the temperature field during welding, velocity-fields are included in a steady state thermal computation.

Jian Qing Su, T.W Nelson et al. [64] revealed FSP is an effective approach for grain refining in materials employing tiny tools and enforcing quick cooling. Nanocrystalline structures were successfully generated in copper in a single step. After FSP with continuous quenching to increase the cooling rate, the microstructural of the various

zones beyond the tool pin were investigated. The substructure was built around a pin tool made out of every minute crystallites measuring a few tens of nanometers in size.

G. Buffa et al. [65] used a rigid thermo-mechanically coupled model (visco-plastic and elastoplastic) to forecast the distribution of residual stress in FSW of two AA6060-T4 plates of appropriate dimension.

Wang Kuai-she et al. [66] investigated underwater FSW to weld an AA 2017 pressed by equal channel angular processing with a mean size of grains of approx. 0.4 μm. Underwater friction stir welding at the weld nugget zone revealed a fine and evenly distributed grain structure. By using external water cooling during FSW, the ultra-fine grains in the NZ was observed.

Nilesh Kumar, R.S Mishsra. [67] produced defect free, uniform, ultrafine and equiaxed grain structure by adjusting the FSP process parameters using severe-plastic deformation mechanism. The aluminum alloy Al-Mg-Sc was processed with three different tools rotational speed (325, 400, and 800 rpm). Depending on the process parameters, the grain size of the welded joint ranged from 0.39 to 0.89 μm. When the Zener-Hollman parameter is increased, the reduction of grain size was observed. It was discovered that dynamic recrystallization during FSP might not be achievable under the existing deformation and microstructural conditions.

Jianqing Su, Jiye Wang et al. [68] investigated the friction stir processing on a 2mm thick plate of Ti-6Al-4V by different feed rate (1-4 IPM) and RS (800 rpm- 1000 rpm). The nugget zone of the FSP specimens shows a fully β transformed micro-structure characterized by basket weave lamellar structure (α/β). The higher TS and lower RS resulted in α colony and fine β grains size which gives the higher tensile strength. The higher tensile and yield strength was observed 1156 MPa and 1067 MPa respectively without losses of ductility at RS 900 rpm and a TS of 4 IPM.

J.F. Guo, et al. [69] examined the effect of parameters (constant RS of 1200 rpm and TS range 2-5 mm/sec) of FSWed dissimilar materials between AA7075 and AA6061 and analyzed that the grain size of welded joints reduces with an increase of TS. The micro hardness was less than that base materials. The minimum value of hardness was found in HAZ towards AA6061 and all the joints were fractured in HAZ of AA6061 where the minimum hardness was situated.

Ravi Kumar et al. [70] studied the impact of processing parameters (RS 800-1000 rpm, and TS 90-110 mm/min) on microstructural and mechanical behaviour of FSWed joint of AA7075 and AA6061 by FSW. The maximum tensile stress i.e. 205.23 MPa was found at a RS of 900 rpm with the TS 100 mm/min. The benign mixing of both metals was observed at high rotational speed with a lower feed rate.

H.I. Dawood et al. [71] examined the impact of profile of tool pin on the mechanical properties of the FSWed joint of Al-6061. Three different profiles i.e. threaded tapered cylindrical, triangular, and square were utilized and it was found that the triangular pin revealed the sound microstructural and mechanical characteristics of the FSWed joints in comparison to other pin profile, whereas the minimum hardness and strength were observed with the square pin profile. The fractured surface shows that the square and threaded tapered cylindrical specimens break with brittle fractured due to excess heat generation during FSW, while ductile fractured was observed in the triangular pin profile.

M. Ilangovan et al. [72] the welding of non-heat-treatable and heat-treatable similar or dissimilar aluminum alloys face many problems during fusion welding, to remove these problem FSW was utilized to join AA6061 and AA5086. The microstructure of different zone was observed by optical and scanning-electron microscopy (SEM) machine, the fine grain structure was noticed in the NZ as compared to TMAZ and HAZ. The joint efficiency was improved by 56%, this was occurring owing to the development of grain size strengthening. The stir zone had a hardness of 115 HV, which was more than the base metal and other adjoining zones.

T. Srinivasa Rao et al. [73] investigated the FSWed thick plate (10mm and 16 mm) of AA7075-T651 and obtained full penetration and defect-free weld after wisely selection of process parameters. In the HAZ, the value of micro-hardness decreased; this decrease in hardness was mostly attributable to increased heat. The tensile capabilities of a welded junction made of 10 mm thick plate were higher than those of a welded joint made of 16 mm thick plate. Whereas, the joint efficiency of plate of thickness 10 mm was found to be 70%, whereas that of plate of 16 mm thickness was observed to be 53%, and past researchers reported that 80-90% joint efficiency for 3-6 mm thick plate for the same material. The fractured occurred in the HAZ region for the cases.

Omar S. Salih et al. [74] investigated the microstructural and mechanical behaviour of aluminum matrix-composite (AMC) fabricated by FSW which was dependent on both FSW processing parameters and composition of AMC, hence the mechanical behaviour of FSW welded joint evaluated consequently. Formation of new grains structure with the enhancement of reinforcement grains in the weldment by controlling the processing parameters with different amount of heat was observed in the microstructure of AMC. The FSW process parameters i.e. tilt angle, TS, and RS have a substantial impact on heat input and strength of welded joints.

Jamshidi Aval Hamed [75] investigated the effect of post-weld heating and welding heat input on mechanical characteristics of FSWed joint of AA5086, and analyzed the effect of process parameters (RS- 900 and 1100 rpm with TS-100 mm/min) of weldment on residual stress, XRD, transmission electron microscopy, tensile strength, and optical microscopy. The nugget zone on the AA5086 side had a coarser grain size than the AA7075 side in each parameter. In the weld joint, the minimum hardness improved from the AA5086 side but reduced from the AA7075 side. There were no changes in residual stress on the AA5086 side, while there was a drop in residual stress in the NZ and TMAZ of AA7075.

Krishna Komerla et al. [76] studied the mechanical characteristics of dissimilar FSWed joint of DC04 and A6061 and observed intermetallic compound free and defect-free joint. Because of thermal effect and plastic deformation, different micro-hardness value and grain size were found in the various zone of the FSWed joint. The dynamic recrystallization was stimulated in the aluminum alloy 6061 due to high temperature and the high strain rate. The cumulative probability distribution of grain size exhibited fine grain microstructure in the all-welded zones in AA6061 side.

Narayanan et al. [77] evaluated the influences of processing parameters (shielding gas, and welding current) on TIG-welded joints of AA5083 and observed that the tensile strength of the FSWed joint was lesser than the base material. The maximum tensile strength (280.8 MPa) and hardness (73.5 HVN) was found at welding current of 200A with flow rate of shielding gas 15 *l*/min, whereas minimum tensile (258 MPa) strength and hardness (71.9 HVN) was observed at welding current of 250A with flow rate 10 *l*/min. The grain size of the welded region at HAZ was coarser then the base metal hence the failure of welded samples was brittle.

Harish Suthar et al. [78] examined the failure behaviour of AA6061 and AA7075 FSWed joints and found that the dissimilar FSW of AA7075/AA6061 softened at HAZ in the advancing side, which had a softer material (AA6061-T6) and a lower hardness value recorded in the area. The fracto-graphy revealed a decreased density of tiny dimples, indicating a lower strain during rupture with facet caused by insufficient material fusing at the SZ-TMAZ interface.

Mahmoud Abbasi et al. [79] processed the TIG welded joints via FSP as well as a innovative technique called friction stir vibration processing (FSVP). The specimen is vibrated when FSP is performed in FSVP. Both processing procedures result in grain refinement and enhance the strength and the ductility of TIG-welded specimen, according to the findings. Ductility and ultimate tensile strength improve by around 22% and 10%, respectively, when FSP is used on TIG welded specimens. As friction stir vibration processing is used, they grow by around 33% and 17%, respectively. The results further demonstrate that the effect of FSVP on the morphology of the weld region and its mechanical properties rises with increasing vibration frequency.

Navneet Khanna et al. [80] emphasizes on the FSW of dissimilar weld joint of AA 6061 and AA 8011. The effect of base plate location and tool offset on different characteristics is investigated while maintaining other welding settings (RS-1070 rpm, TS- 50 mm/min, and tilt angle- 2°). When the 1 mm tool offset towards the advancing side (softer alloy), the tensile testing results reveal higher strength and elongation of 77.88 MPa and 21.96 percent elongation, respectively. The various parameters have no effect on the hardness readings. To determine the quality of the weld surface, a visual inspection is performed. In order to have a broader insight of subsurface defects and material mixing, a radiography test is also performed. Time–temperature graphs are shown to evaluate the heat distribution throughout the welded zone, and the asymmetric shape of the graph reveals higher temperature on the advancing side. Microstructure examination reveals consistently dispersed grains, implying improved tensile characteristics, as well as a material flow pattern. As a consequence of the characterization data, it was determined that for improved weld quality, the softer material should be positioned on the advancing side.

Sameer Mohammed and Anil Kumar Birru [81] investigated friction stir welded AA6082-T6 plates with a thickness of 2 mm, employing Al_2O_3 nanoparticles as

reinforcement materials between adjacent plates. The joining was accomplished using a tungsten carbide hexagonal pin profile tool at RS of 710 and 900 rpm. The welds were passed two and three times each, with a constant TS of 40 mm/min. An optical microscope and SEM were utilized to investigate the microstructure. The microstructural data reveal that the weld produced at 710 rpm, 40 mm/min TS, and 3 passes has an excellent distribution of Al_2O_3 particles, resulting in grain refinement. The average grain size of the reinforced welded sample in three passes was 16.02, and it also had the greatest yield strength of 154.9 MPa, tensile strength of 227.61 MPa, and %elongation of 10.5 %. The weld nugget zone of the reinforced welded sample had the maximum hardness value of 74 HV.

Naresh Parumandla and Kumar Adepu [82] produced Al/Al_2O_3 and Al/SiC surface nanocomposites. As reinforcement, nano-sized Al_2O_3 and SiC particles were employed, while the matrix material was 6061-T6 aluminum alloy. Experiments were carried out at constant process settings (1150 rpm and 15 mm/min) with different volume percentages of nano reinforcements (2, 4, and 6). The method compared the impacts of nano reinforcement on surface nanocomposites' mechanical, microhardness, microstructural, and wear characteristics. Microstructure analysis indicated that Al_2O_3 and SiC nano particles were mostly arranged in clusters in the processed region. Additionally, the defect generation rate increases as the volume % of nano reinforcement increases. The mechanical characteristics of the surface nanocomposites were investigated using Vickers microhardness and tensile tests. Along the stir zone, superior microhardness qualities were attained. Microhardness increases with adding of ceramic particles in the material matrix; however yielding strength drops while wear resistance increases. Al/SiC composites had a lower average coefficient of friction than Al/Al_2O_3 composites. With enhancing the volume percentage of nano particles in the matrix material, the effect of nano reinforcements on wear resistance was enhanced.

Saeed Ahmadifard et al. [83] investigated the impact of Ti_3AlC_2 MAX phase into AA7075 by FSP in addition of nano-sized Al_2O_3 particles. After three FSP passes with RS of 1000 rpm and TS of 28 mm/min, these composites were effectively manufactured. The produced surface hybrid nanocomposites were characterized tensile, microhardness, and wear testing along with using optical microcopy and SEM. Due to enhanced grain refinement and excellent dispersion of nanoparticles, the Al-100 percent

Al_2O_3 composite acquired the highest hardness and tensile strength. The Ti_3AlC_2 MAX phase improved tribological characterization due to its laminar structure, whilst Al_2O_3 nanoparticles improved mechanical characteristics. For AA7075, the wear mechanism is adhesive; for nanocomposite specimens, it is adhesive-abrasive, according to scanning electron microscope examinations.

A. Abdollahzadeh1 et al. [84] placed silicon carbide (SiC) nano-powders into the adjacent side of AZ31 magnesium plates. FSP using a pin-less tool was used to ensure a proper dispersion of these nanoparticles. Second, utilizing a frustum pin tool, the best conditions for FSW of AA6061 and AZ31 alloy to were obtained by combining TSs and RSs. When compared to the FSPed joint without nanoparticles, the FSPed joint manufactured at 35 mm/min and 650 rpm showed a 28 % higher tensile strength and increased in elongation of threefold. SiC nanoparticles improved the microstructure of the banded zone and helped refine the grains in the stirred zone. The reinforced samples exhibit higher hardness in comparison to that of the nonreinforced samples owing to reduced grain size and the SiC articles with a high hardness. The non-reinforced sample fractured totally brittle, but the reinforced samples fractured in a ductile manner.

Mohsen Bahrami et al. [85] investigated the impact of SiC nano-sized particles on the mechanical behavior of FSWed AA7075. FSW at 1250rpm and 40mm/min was used to achieve this. Experiments were conducted with and without the nano-sized SiC particles along the joint line. Optical microscopy and SEM were employed to examine the cross-sectional microstructures of the joints (SEM). The presence of SiC particles was confirmed by X-ray diffraction (XRD) results. Furthermore, the volume proportion of the reinforcing particles was revealed to be 20%. SEM images revealed a good dispersion of SiC reinforcements, along with excellent bonding. The results of atomic force microscopy (AFM) were likewise quite similar to those of a recent SEM microstructure. Tensile strength, % elongation, fatigue life, and joint toughness all increased dramatically as a result of the presence of SiC nanoparticles. The morphologies of the fractures were in good accord with the ductility values.

Yahya Bozkurt et al. [86] demonstrated the viability of friction stir welding to weld identical AA2124 plates with SiC/25p. The weld zone features and performance were evaluated using microstructure parameters, microhardness, and tensile testing. XRD was employed to analyze the phase structure of a comparable composite weld. The weld

zone temperature was measured by employing thermo-couples to show that the composite joint may be shown without melting. The finding showed that FSW may be utilized to weld AA2124/SiC that are comparable. The SiO_2 phase was observed according to XRD measurements. Peak temperatures that were measured 15 mm out from the weld region varied from 201 to 270 ºC. It was also found that the tensile strength of the composite joints made by the AA2124/SiC was around 20% less than that of the basic composite. The novelty of this research stems from one of FSW's preliminary experiments on the mechanical features of the composite joint.

F. Cioffi et al. [87] studied the mechanical characteristics and microstructure evolution of composite joint (AA2124/ SiCp -25%vol) developed by FSW at different RSs with a high-volume fraction of SiCp, The initial particle-free zones vanish during the stirring process, resulting in a uniform particle distribution. Sometimes large particles are shattered. At low RS, tunnel flaws appear, while at high RS, they disappear. The TMAZ, expands in size as RS increases. In compression testing, the welds acquire a ductility of 10–15 percent, however in tension tests, the welds exhibit a brittle behaviour. Between compression and tensile tests, a strength differential, SD, effect is achieved. This explains why the FSW method has such a minor negative impact on the matrix–reinforcement interaction. The existence of a microscopic residual stress is thought to be the cause of the SD effect.

D. A. Dragatogiannis et al. [88] developed dissimilar FSw of thick plates of aluminum alloys incorporated with nano-sized TiC particles. In compared to an unreinforced weld, defect-free welds have better material mixing between the materials, as well as better particles dispersion and grain refinement. The generated metal matrix composites' local mechanical behaviour was investigated and compared to that of their bulk equivalents and source materials. Microstructure and the fillers are linked with observed mechanical parameters at the micro- and nanoscale (particularly hardness and elastic modulus). The inclusion of TiC nanoparticles increases the ultimate tensile strength, hardness, yield values, elastic modulus and %elongation.

S. Gopalakrishnan and N. Murugan [89] fabricated titanium carbide (TiC) based aluminum matrix composite (Al/TiCp) by indigenously designed stir-casting method. Weld joints are made using the friction stir welding procedure (FSW). For the analysis, welding factors such as TS, RS, % TiC, axial force, and tool pin profile were taken into

account. The tensile strength of FSWed joints is predicted by employing a mathematical modeling. A different set of characteristics investigated in FSWed specimens without any post-weld heating revealed a good joint efficiency (ranging from 90 to 98 percent) in comparison to the tensile strength of AA6061. The welding speed and pin shape shows a greater impact on the tensile strength, according to the model's analysis.

K. Kalaiselvan et al. [90] developed the AMC of AA6061/B_4C via stir-casting route with using K_2TiF_6 as flux. Castings were made into plates with a thickness of 6 mm, and friction stir welding was used to successfully butt weld them (FSW). A RS of 1000 rpm, axial force of 10 kN and a TS of 80 mm/min, were used in the FSW. A square pin profile tool was employed for FSW. Optical microscopy and SEM were employed to examine the microstructure of the welded junction. Four zones were visible in the welded junction, which are typical of FSW aluminum alloys. Fine granules and homogeneously distributed B_4C particles were visible in the weld zone. Under the experimental conditions, a joint efficiency of 93.4 percent was achieved. FSW, on the other hand, lowered the composite's ductility.

Atul Kumara et al. [91] studied the processes of simultaneous enhancement of tensile characteristics, corrosion resistance and wear behavior, of stir cast Al7075 with micro and nano SiC/2%wt composites using FSP. The microstructural development was studied using OM, SEM, and transmission electron microscopy (TEM). After the FSP, the nanoparticles reinforced composite outperformed the microparticles reinforced composite in terms of mechanical characteristics. With the simultaneous improvement in ductility, wear resistance (10 times) and tensile strength (>3 times) were shown to rise considerably. Reduced grain size, uniformly distributed SiC nano-sized particles inside the matrix, increased the matrix-particle interface properties, and removal the flaws of casting like porosity following the FSP are all credited with the improvement. Following the FSP, the as-cast composites' corrosion potentials altered in a noble direction. Following the FSP, corrosion resistance is said to have improved due to the reduction in surface irregularity and uniformly distributed particles. Because of the increased matrix/particle interface properties and dispersion strengthening, the nano-composite was shown to be superior to all of these positive impacts.

Seung-Joon Lee et al. [92] developed composites with the aid of multi-walled-carbon nanotubes (MWCNT) in aluminum metal matrix by employing FSW and studied the

mechanical properties and microstructural behaviour by controlling volume of MWCNT by 1 and 3%, and the plunging load of 400 and 600 kg. After the FSW, MWCNT exhibited some grain coarsening, uneven shear texturing, and accumulating dislocations; however, the differences produced by varying MWCNT and plunging load were insignificant. The FSWed composite produced with 600 kg plunging load and 3% MWCNT shows a two-fold better balance between ductility and strength than those of the base metal.

R. Ashok kumar and M.R. Thansekhar et al. [93] employed cumulative impact of FSW and FSP on dissimilar AA1350 and AA6101-T6. Alumina particles are utilized to strengthen the interface region of the AA6101-T6 and AA1350. For different diameters of grooves, FSW and FSP are done at the same time. Mechanical and wear tests are used to evaluate the welding quality and surface changes. The smallest groove, with a width of 0.5mm and a depth of 1mm, has the highest bending and tensile strengths, while the largest groove of width and depth 2mm and 3mm, respectively shows the highest wear resistance as and hardness. The Taguchi approach reveals that width of groove is the most important factor.

2.3 RESEARCH GAP

After going through the literature, the following gaps have been identified:

- A few researchers have incorporated the reinforcement particles in the weld zone to improve the weld quality using friction stir processing.
- Little work has been done on the comparison of type, size and volume fraction of reinforcement particles.
- Incorporation of reinforcing particles in case of joining similar and dissimilar materials is very challenging task for the researchers
- A few researchers have investigated the effects of hybrid metal matrix composite via friction stir processing.
- Very few researchers have been carried out the optimization of process parameters of friction stir processing.
- Friction stir processing of stainless steel, nickel and titanium alloys is also a challenging task for researchers.

2.4 RESEARCH OBJECTIVES

From the literature survey the research gaps were identified. Accordingly, the following objectives are formulated:

- To fabricate composite joints of dissimilar aluminum alloys using different sized Al_2O_3 particles.
- To study the effects of various process parameters (i.e. tool rotation speed, traverse speed, volume fraction of reinforcement particles) on weld quality of dissimilar FSPed composite joints.
- To determine the optimal parameters for processing of dissimilar aluminum alloy joints using friction stir processing via Response Surface Methodology (RSM).
- To characterize the composite joints by metallographic study such as scanning electron microscopy (SEM) and Optical Microscopy (OM).
- To study of tribological and mechanical characteristics of composite joints such as tensile strength, % elongation, micro-hardness and wear behavior.

CHAPTER-3

RESPONSE SURFACE METHODOLOGY

3.1 INTRODUCTION

The Response Surface Methodology (RSM) technique, which is an important subject in statistical experiment design, is a set of statistical and mathematical approach that can be employed for the analysis and modeling of the problems in which a desired response is impacted by multiple variables and the goal is to optimize the response [94]. The other techniques that can be used for modeling and optimizing the results are Taguchi's approach, particles Swarm optimization, grey relational analysis, teaching learning based outcomes (TLBO), Artificial Bee Colony (ABC) etc.

3.2 HISTORICAL BACKGROUND

G. E. P. Box and K. B. Wilson established the RSM technique in 1951.George Edward Pelham (G.E.P.) Box (October 18, 1919) is a statistician who has made significant contributions to the fields of quality control, experimental design, time series analysis, and Bayesian inference. He worked for the British Army on biochemical tests on the effect of deadly gases on tiny animals during World War-II. He required statistical assistance to interpret the findings of his experiments but couldn't find a statistician who could help him, so he taught himself statistics using books he had on hand. After the war, he earned a graduation degree in mathematics and statistics from University College London. In 1953, he obtained his PhD degree from the London University. From 1948 through 1956, Box was employed at Imperial Chemical Industries as a statistician. He took a year off from Imperial Chemical Industries to work as a guest lecturer at the now North Carolina State University in Raleigh. Later, at Princeton University, he attained to the position of Director of the Statistical Research Group. Box established the Department of Statistics at the University of Wisconsin–Madison in 1960. In 1980, he was named Vilas Research Professor of Statistics at the University of Wisconsin–Madison, the highest distinction bestowed on any academic member at the university. In 1984, Box and Bill Hunter cofounded the University of Wisconsin–Center Madison's for Quality and Productivity Improvement. Box became an Emeritus Professor in 1992, when he formally resigned.

3.3 RESPONSE SURFACE METHODOLOGY

The RSM approach is a set of mathematical and statistical strategies for the analysis and modelling of the problems in which a respondent is impacted by multiple variables and the purpose is optimizing that response [95]. It is a significant topic in statistical experiment design. Independent components can be represented quantitatively in various experimental circumstances (equation 3.1).

$$y = f(x_1, x_2) + e \tag{3.1}$$

This describes the relationship between $x_1, x_2 \ldots, x_k$ of k quantitative factors and response y. The response function or response surface is denoted by function f. The experimental errors are measured by the residual 'e'. A characteristic surface is generated for a given collection of independent variables. A polynomial can be used to accurately predict f's mathematical form when it is unknown within the experimental domain. The relationship increases with increasing polynomial degree, while experimental costs increase.

Multiple regression equations were developed using RSM to represent the quality attributes of FSPed joints produced by the FSP in this study. The dependent parameter is regarded as a surface on which a mathematical model is fitted when using the response surface approach. The second order response surface has been considered for the formulation of regression equations:

$$y = \beta_0 + \sum_{j=1}^{q} \beta_j x_j + \sum_{i=1}^{q} \beta_{jj} x_j^2 \sum\sum_{i<j} \beta_{ij} x_i x_j + \varepsilon \tag{3.2}$$

Where $x_i = (x_1, x_{2i}, \ldots\ldots, x_{iq})$, $\beta = (\beta_1, \beta_2, \ldots\ldots, \beta_q)$

This assumes that variable xj's linear, cross and squared product terms are present on surface y.

The regression coefficient can be estimated using a variety of methods.

3.3.1 Central Composite Design

The findings of any experiment may be used to estimate the standard error (SE) "e," of Y on the fitted surface at any point. The SE is a function of the point's xj's coordinates.

The SE is the similar for all points that are equidistant from the region's centre because of the rotatability criterion and meet the equation:

$$x_1^2 + x_2^2 + \ldots\ldots x_k^2 = \delta^2 = constant \quad (3.3)$$

However, in RSM a polynomial response surface has many benefits and certain drawbacks. One drawback is that when extended outside of the experimental zone, the polynomials are unreliable. Another significant drawback of utilizing second order polynomials is that with more than three X variables or levels, the size of trials increases too large and analysis becomes too difficult. A well-designed experimental strategy, on the other hand, can significantly minimize the overall number of trials. One of these methods is central composite designs (CCD). Continuing on, it has been shown that the second-order central composite designs are the most effective technique for establishing the mathematical relationship of the response surface with minimum feasible tests without sacrificing accuracy [96].

CCD is sectioned into three parts as following:

- 2k design points, where 2 indicates number of levels used to maintain the parameters during testing. and k denotes the number of parameters.
- Extra points known as star points, which are positioned on the co-ordinate axes to construct a core composite design with a size star arm.
- A few additional points were added to the center to offer the response Y with a radius of one substantially identical accuracy.

The factor α denotes sphere or circle's radius on which the star points are located. By adopting half replication of a 2k factorial design, the experimental size is lowered with k 5.

Table 3. 1: Components of second order Central Composite Design [97]

Variables (k)	Factorial Points(2^k)	Star Points (2k)	Centre Points(n)	Total (N)	Value of α
3**	8	6	6	20	1.68179
4	8	8	5	21	1.00000
5	16	10	6	32	2.00000
6	32	12	10	54	2.37841
****This is used in Present Work.**					

Becomes 2(k-1)/4 with half replication. Furthermore, no replication is required to get the error mean square, as this may be determined simply reproducing the center points. Table 3.1 demonstrates the components of a second order central composite rotatable design for various numbers of parameters.

3.3.2 Estimation of the Coefficients

As previously indicated, the regression equation for the response surface of second order was expected to be (Eq. 3.4):

$$Y = \beta_0 + \sum_{j=1}^{q} \beta_j x_j + \sum_{i=1}^{q} \beta_{jj} x_j^2 + \sum\sum_{i<j} \beta_{ij} x_i x_j + \varepsilon \quad (3.4)$$

Where, the estimated response is Y, the coefficients are β's, and the independent variables are xj's. To calculate the regression coefficients, the least squares approach can be employed.

3.3.3 Significance Test of the Coefficients

To evaluate the significance of specific coefficients, a null hypothesis must be established, and the estimated coefficients must be tested for difference from their mean by utilizing student's t-test [98]. When the design is totally randomised, the analysis of variance can be used to compare two treatments instead of the t-test. This is because a one-tailed F-test with 1 and n DOF (degrees of freedom) equals a two-tailed t-test with n DOF (t2 = F for 1 DOF). As a result, the F test with 1 and n0 DOF was employed to examine the significance of individual coefficients, where n0 is the total observations of the centre-point response surface.

3.4 ANALYSIS OF VARIANCE: BASIC NEED

The goal of product or process development is to enhance the product's or process' performance qualities in relation to consumer wants and expectations. The goal of experimentation should be to limit and regulate variances in a product or process, and then judgments on which parameters impact a product's or process' performance must be made. ANOVA is a statistical tool for interpreting and making judgments based on experimental data. Sir Ronald Fisher created the approach in the 1930s as a tool to analyses the findings of agricultural research. ANOVA is connected with a lot of mathematical elegance. It is a decision-making technique based on statistics for identifying any differences in the average performance among the groups of items under consideration.

3.5 RESPONSE SURFACE METHODOLOGY AND ROBUST DESIGN

RSM is a crucial component of experimental design. RSM is an important tool for creating new processes and improving their performance. RSM may frequently be used directly to achieve quality improvement goals such as reduced variability and improved process and product performance.

Variation in key performance criteria is widely established to lead to poor process and product quality. During the 1980s, process quality received a lot of attention, and a methodology for applying experimental design was established, especially for the following:

- To develop or design products and procedures that are resistant to component variation.
- To minimize variability in a product's or process's output response around a target value.
- For the purpose of creating goods and processes that are resistant to environmental conditions.

By robust, we mean that the product or process meets its objectives consistently and is generally unaffected by difficult-to-control circumstances. RSM implies that these noise components are uncontrolled in the field, but that they can be controlled during the creation of a process for the sake of a controlled experiment.

Table 3. 2: **ANOVA for Second Order Central-Composite Design [99]**

S. No.	Sources	Sum of Squares	DOF
1	First order terms	$\sum_{q=1}^{k} b_i \left(\sum_{q=1}^{N} x_{iq} Y_q \right)$	K
2	Second order terms	$b_o \left(\sum_{q=1}^{N} y_q \right)$	$\frac{k\,(k\,-1)}{2}$

		$+\sum_{i<j}^{k} b_{ij}\left(\sum_{q=1}^{N} x_{iq}\, x_{jq}\, y_q\right) - \frac{\left(\sum_{q=1}^{N} y_q\right)^2}{N}$	
3	Experimental error	$\sum_{s=1}^{n_o} (y_s - \bar{y}_o)^2$	n_o -1
4	Lack of fit	Found by subtraction	$N - n_o - \frac{k(k+3)}{2}$
5	Total	$\left(\sum_{q=1}^{N} y_q\right)^2 - \left[\frac{\left(\sum_{q=1}^{N} y_q\right)^2}{N}\right]$	N - 1

The F-ratio is specified as:

$$F(1, n_0) = \frac{b_i^2 / c_{ii}}{{S_e}^2} \tag{3.5}$$

Where c_{ii} = Element of error matrix (X' X) $^{-1}$

b_i =Regression Coefficient

S_e = Standard deviation of experimental error measured from the replicating observation at zero level:

$${S_e}^2 = \frac{1}{n_o - 1} \sum_{s=1}^{n_o} (y_s - \bar{y}_o)^2 \tag{3.6}$$

$$\text{Where,} \quad y_0 = \frac{1}{n_0} \sum_{s=1}^{n_0} y_s$$

Y_s = s^{th} response value at center

This estimated F value may be compared to the theoretical F value at 95% confidence level. If the calculated F value for a coefficient is more than theoretical value, the impact of that term is substantial. The irrelevant second-order elements in the equations can be removed, and the remaining coefficients recalculated.

3.5.1 Adequacy of the Model

The predicted regression equation is checked for adequacy of fit:

Evaluate the residual sum of square using:

$$S_1 = \sum_{q=1}^{K} \left(Y_q - \overline{Y_q}\right)^2 \quad (3.7)$$

Where the observations at experimental locations are denoted by Yq, and the mean of all observations is denoted by $\overline{Y_q}$. Where, k denotes the total variables, and N denotes the total observations. The DOF for residual sum of sum of squares will be computed as follows:

$$f_1 = N - \frac{(k+2)(k+3)}{2}$$

1. The error sum of squares may be calculated using repeated observations at the centre point as follows:

$$S_2 = \sum_{S=1}^{n_0} (Y_s - Y_0)^2 \quad (3.8)$$

Where, y_s denotes the s^{th} response value at centre.

2. Determine the total of squares fit inadequacy.

$$S_3 = S_1 - S_2 \quad (3.9)$$

For which the DOF is

$$f_3 = f_1 - f_2 = N - \frac{(k+1)(k+2)}{2} - n_0 - 1 \quad (3.10)$$

3. Apply F- test to test the adequacy of fit as:

$$F = \frac{S_3/f_3}{S_2/f_2} \quad (3.11)$$

If FF 0.05 (f3, f2) at confidence level of 95% or F F0.99 (f3, f2) at confidence level of 99%, the generated regression equation fits the data sufficiently.

CHAPTER-4

RESEARCH METHODOLOGY

4.1 INTRODUCTION

The aim was to fabricate the defect-free composite joints of AA7075/AA6061 for examining the influence of the dispersion pattern of different volume fractions of reinforcing particles (Al_2O_3 micro and nano-sized particles) along with different combinations of rotational speed and traverse speed on microstructural, wear and mechanical behavior. To the best of the researcher's knowledge, the FSPed composite joints of AA7075 and AA6061 with different volume fraction of reinforcing particles has not been explored. The following sequence of experimental activity was intended to achieve the key objectives: The flowchart below depicts the current investigation's experimental strategy (Fig. 4.1).

1. Evaluation of chemical composition and mechanical characteristics of parent materials i.e. AA 7075 ad AA 6061.
2. Evaluation of chemical composition of Al_2O_3 micro and nano-particles.
3. Cutting of AA 7075 and AA 6061 plates in the dimensions of 150*40*6 mm for the proper clamping in the fixture of FSW machine.
4. Fabrication of slots on the adjoining surfaces of AA7075 and AA6061 for incorporating reinforcement particles.
5. Design of experimentation (DOE) was obtained by Response surface methodology using full-factorial central composite design (CCD) to observed optimized input and output responses.
6. Fabrication of friction stir processed composite joint of AA7075 and AA6061 using DOE of different processing parameters such as tool rotational speed and traverse speed and volume fraction of reinforcement particles
7. Evaluation of tensile characteristics of the composite joints and fracture surface was examined via scanning electron microscope.
8. Microhardness of various zones was performed using Vickers hardness tester.
9. Evaluation of wear behaviour of FSPed joints using pin-disk tribometer.
10. To determine the optimal parameters for dissimilar FSPed composite joints of AA6061 and AA 7075 via Response Surface Methodology (RSM).

11. Characterization of FSPed composite joints using scanning-electron microscopy (SEM), optical microscope (OM), and Energy-dispersive X-rays spectroscopy (EDS) to reveal the material flow behavior, grain size, grain orientation and joint quality.
12. To perform the comparative analysis between the composite joints incorporated with Al_2O_3 micro and nano particles.

4.2 FLOW CHART

The flow chart is a condensed version of the detailed work. Fig. 4.1 depicts the flow chart for the present work, which shows the step-by-step approach or methodology used during the work.

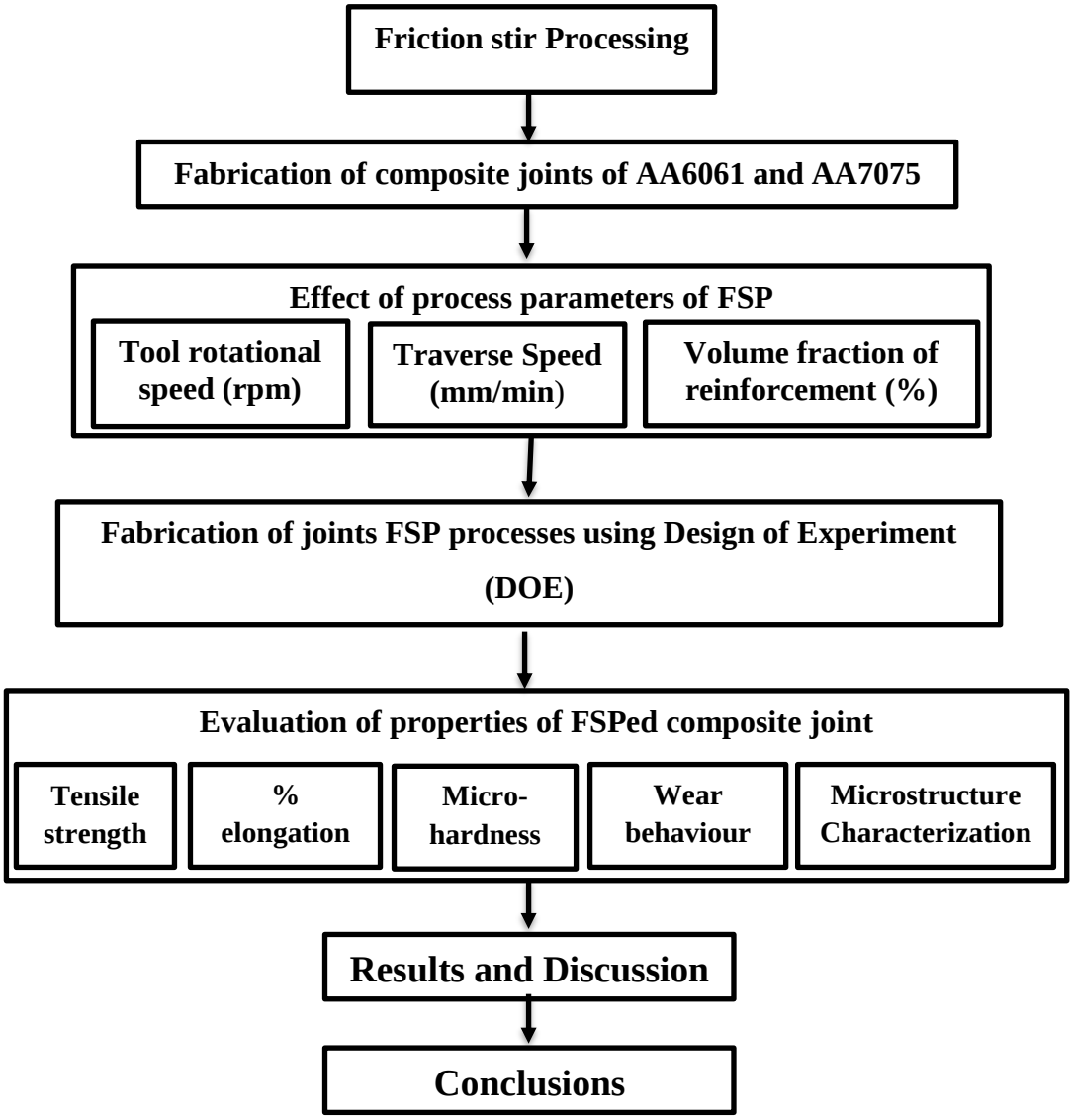

Figure 4.1: Work Plan

4.3 BASE MATERIALS

Modern progress in the automotive and military industries has shifted away from traditional materials toward the lighter materials such as aluminum alloys. Al-alloys are most widely utilized for making different elements such as, rockets, and rocket launchers, bumpers, axle shafts, and car bodies due to its excellent tribological and mechanical characteristics such as, high corrosion resistance, low density, high strength to weight ratio and high thermal conductivity [100]. FSW/FSP is utilized to make automotive and shipbuilding components, as well as aerospace structural components. Both AA6061 and AA7075 have a broad range of applications, especially for structural components in the aerospace, shipbuilding, and automotive industries. In aerospace applications, riveting of AA6061 and AA7075 results in stress concentration and increased structural weight [101]. These alloys' dissimilar welding and higher weld quality would increase the flexibility of structural designs and expand their applications. It was observed that researchers are focusing their efforts on developing lightweight materials for automotive applications. As a result, improving the friction and wear properties of these aluminum alloys is a major priority [102]. Aluminum-based composites have been used as advanced material for a variety of automotive components, including piston rings, pistons, cylinders, connecting rods, and more [103].

Figure 4.2: Base plates of AA 6061 and AA 7075

The main alloying components in AA6061 are silicon (Si) and magnesium (Mg) whereas AA7075 containing magnesium (Mg) and zinc (Zn) have major alloying

elements. AA6061 has low strength and high ductility and the properties near to the convectional weld zone results in loss strength around 75%. During the welding of aluminum alloy, the oxide layer should be removed for enhancing the properties of the weld joint. The raw plates of base materials (AA6061 and AA7075) is depicted in Fig. 4.2. Table 4.1 displays the chemical compositions of base materials obtained by chemical spectroscopy. Microstructure of base materials obtained by optical microcopy and scanning electron microscopy is depicted in Fig. 4.3 which reveals the grain boundaries/structure (elongated grains). Mechanical and wear characteristics of base materials are tested as per ASTM standard and tabulated in Table 4.2.

Table 4.1: Chemical composition of parent materials

Parent Materials	Si	Fe	Cu	Mg	Zn	Mn	Ti	Cr	Al
AA6061-T6	0.65	0.7	0.2	0.8	0.25	0.1	0.15	0.2	Bal.
AA7075-T6	0.57	0.35	1.3	2.1	5.3	0.13	0.05	0.2	Bal.

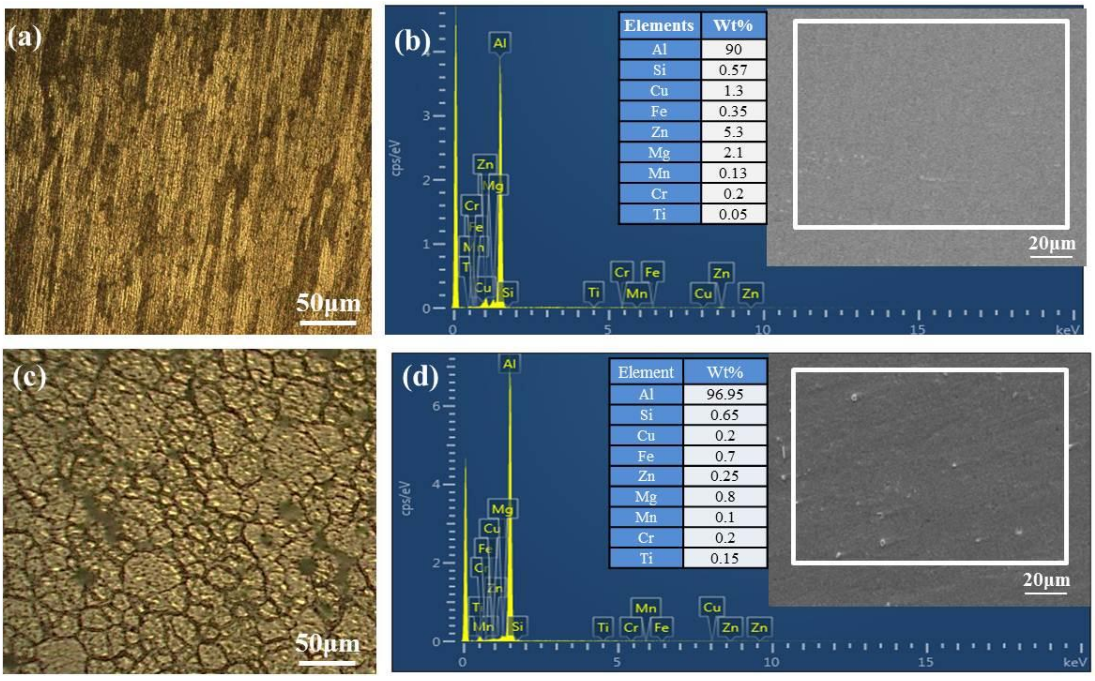

Figure 4.3: Optical micrographs, SEM micrographs and EDS analysis of base metal (a, b) AA7075, (c, d) AA6061

Table 4.2: Mechanical and Wear properties of base material

Base materials	Tensile strength (MPa)	%Elongation (%)	Microhardness (HV)	Wear (weight loss) in mg
AA7075-T6	495	21.6	170	12.2
AA6061-T6	288	18.4	96	14.3

4.4 REINFORCING PARTICLES

Al_2O_3 is an important reinforcing material in the development of MMCs. It exhibits high density (about 4.08 g/cm^3) and low melting temperature (around 2,050 ºC). Its popularity is growing because of good wettability, low melting temperature, and inexpensive cost. Several researchers used Al_2O_3 particles in surface matrix composites through FSP. Zarghani et al. [32] developed surface composites using Al6082/Al_2O_3. The employment of nano Al_2O_3 particles resulted in two to threefold increase in wear resistance and a 168 percent increase in microhardness. With increasing FSP pass counts, consistency in particles dispersion, wear resistance and microhardness improved. Raaft et al. [33] developed the mono base metal matrix composites of A356 using graphite and Al_2O_3 particles. It was found that that A356/Al_2O_3 composites (MMC) outperform A356/graphite composites in terms of wear and mechanical characteristics. In Al_2O_3-based composites, a maximum increase in microhardness of 82 percent was also observed. Therefore, in the present research, micro and nano sized particles of Al_2O_3 ware utilized as reinforcing candidates. The image of as received micro and nano particles are depicted in Fig 4.4 and 4.5 respectively. The SEM micrograph and EDS analysis of micro and nano sized Al_2O_3 particles are also depicted in Fig. 4.4 and 4.5, respectively.

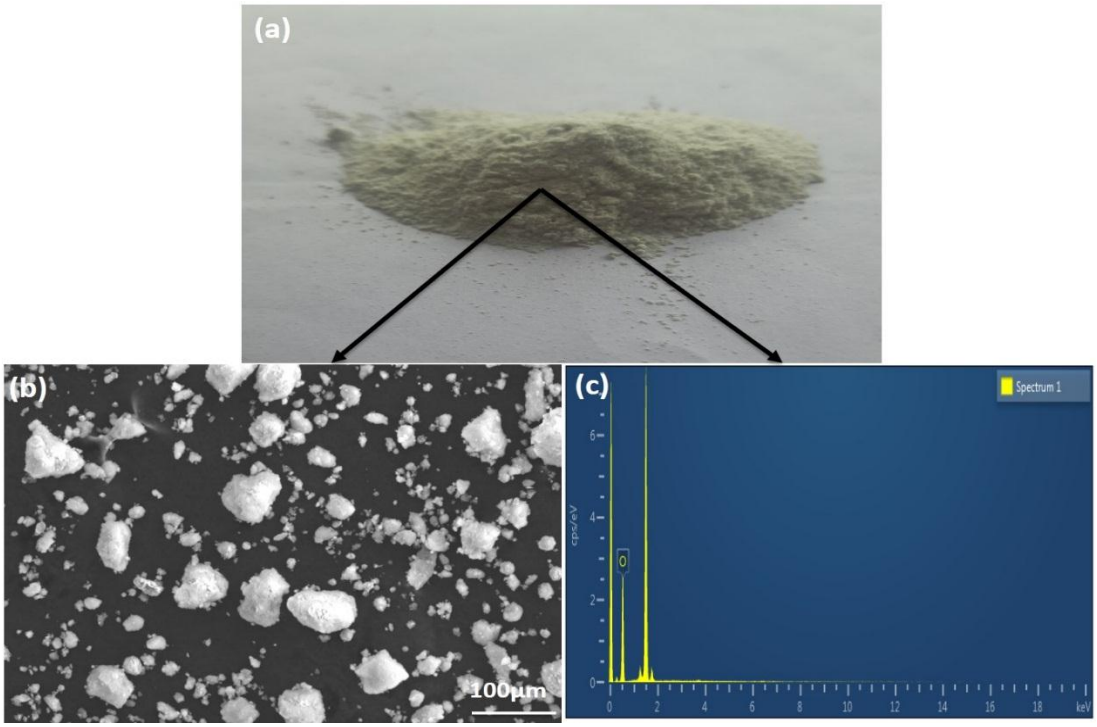

Figure 4.4: Al_2O_3 micro particles (a) as received particles (b) SEM micrograph (c) EDS analysis

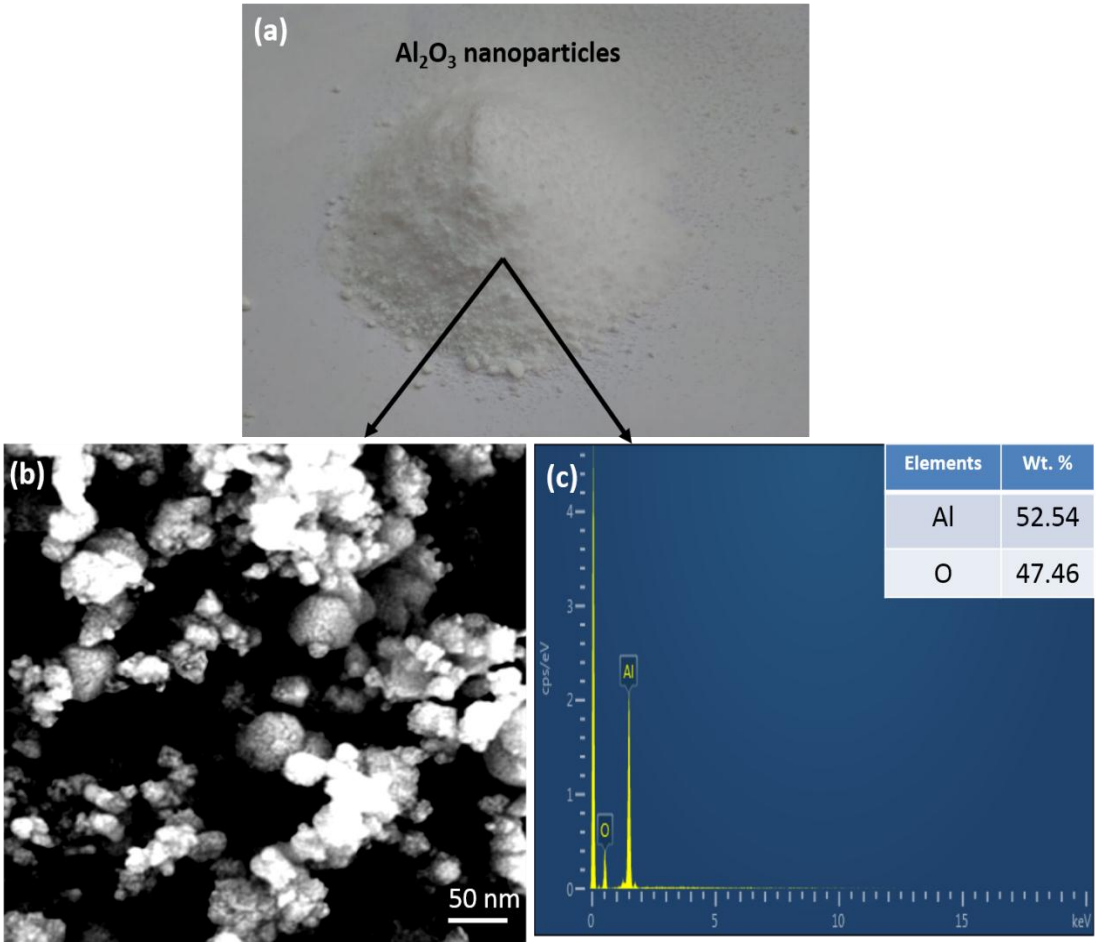

Figure 4.5: Al_2O_3 nanoparticles (a) as received particles (b) SEM micrograph (c) EDS analysis

4.5 EXPERIMENTAL PROCEDURE

Experimentation work was carried by using friction stir welding machine (R.V. machine tools, FSW4T-HYD) (15 hp; 3000 rpm; 25 kN) as depicted in Fig. 4.6. The tool is held by a vertical spindle, and the work piece is held by a fixture with four hydraulically driven clamps and a backing plate with groove of size 200×80 mm. The backing plate groove is designed to securely support the work component. The spindle's maximum operating speed is 3000 rpm. On this machine, the traverse speed and rotational speed can be varied easily. The composite joints of AA6061 and AA7075 plates of thickness 6 mm was fabricated using reinforcing particles. The friction stir processing was employed on Al_2O_3 particles incorporated plates of AA6061 and AA7075 with different processing parameters. The following steps of experimentation are as given below.

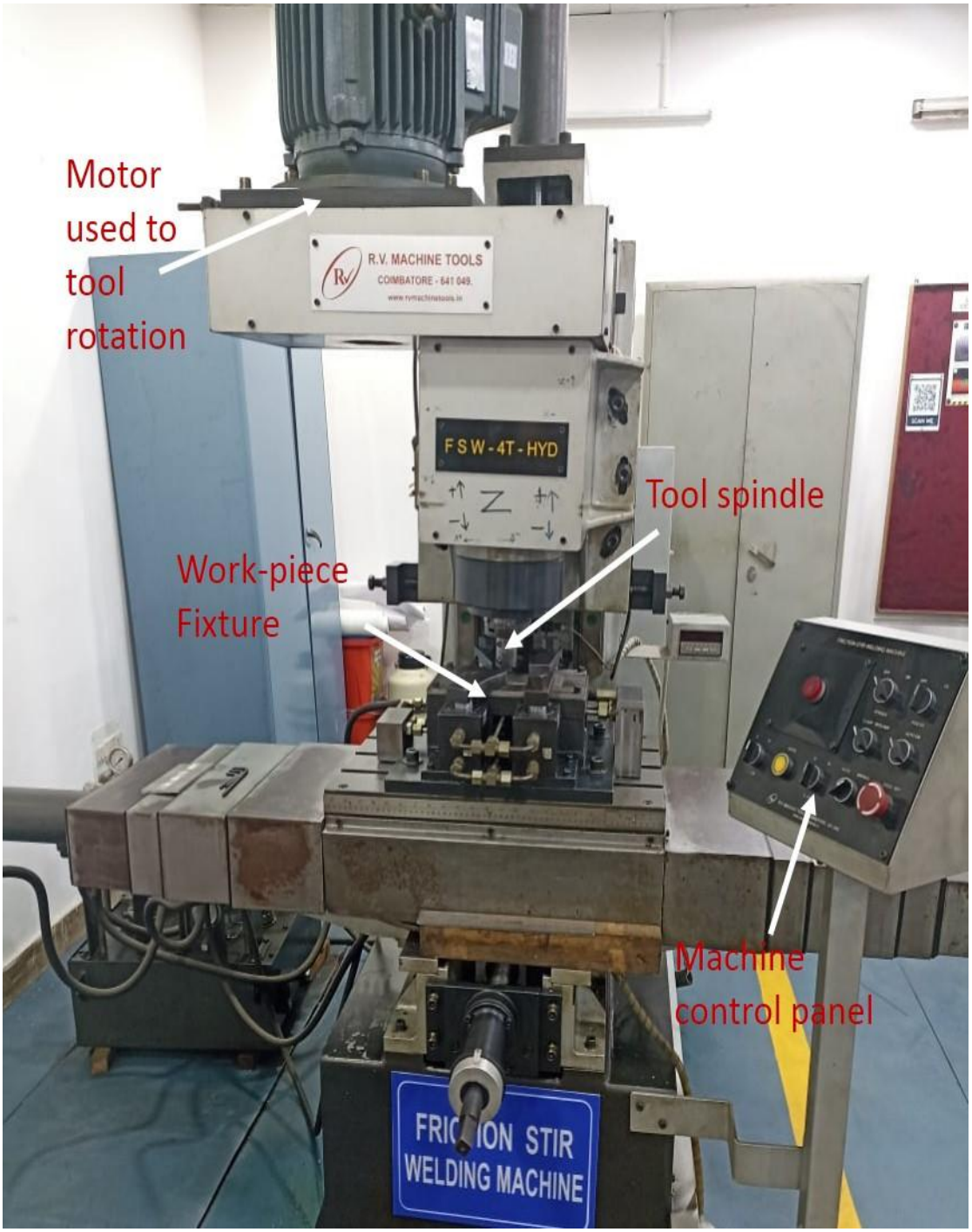

Figure 4.6: Friction stir processing/welding machine used for experimentation

4.5.1 Preparation of samples

Plates of AA6061 and AA7075 of thickness 6 mm were utilized as base materials for the present work. Aluminum plates a dimension of 150 x 40 mm were cut with the help of milling cutter and grinding done at the edge to smooth the surface to be joined as depicted in Fig. 4.7.

Figure 4.7: Sample preparation for FSPed composite joints using milling machine

4.5.2 Groove preparation

To incorporate the reinforcing particles into the processed zone, grooves of depth 3 mm were plowed by using milling machine along the adjoining faces of base plates below 0.3 mm from the top, to avoid the use of the pin-less tool, as depicted in Fig. 4.8 and 4.9. The surface grinder was employed for better surface finish and dimensional accuracy. The grooves of different widths (0.24, 0.42 and 0.60 mm) were plowed to vary the volume fraction of reinforcing particles in the processed zone.

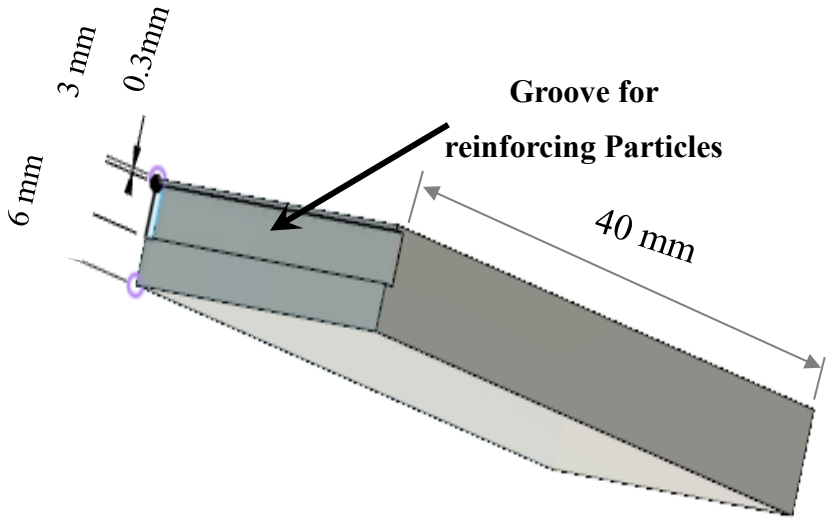

Figure 4.8: Systematic diagram of groove milled on adjoining face of base plate

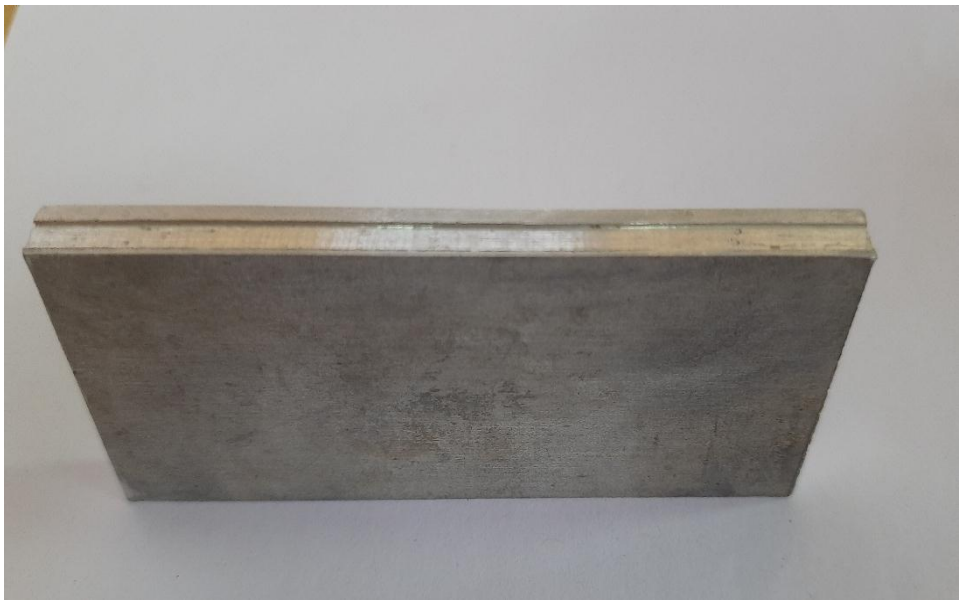

Figure 4.9: Groove for filling reinforcing particles

4.5.3 Incorporation of reinforcing particles in the grooves

To incorporate the reinforcement particles into the stir zone, a thick slurry of reinforcement particles and 99% pure ethanol was prepared for the proper filling of reinforcement particles into the grooves as depicted in Fig. 4.10. Before filling, the grooves were properly cleaned with acetone to avoid contamination. Thereafter, reinforcement particles were filled into the grooves and left to dry for about an hour at room temperature.

Figure 4.10: Ethanol used for making Al_2O_3 slurry

4.6 FABRICATION OF FSPED COMPOSITE JOINT

4.6.1 Making of FSP tool

In this work, the threaded cylindrical pin profiled tool was utilized to fabricate the FSP composite joint because of the threaded pin profile yield defect-free joints and it is preferred over the other pin profile [104] and the material was used for the

manufacturing the tool is H13 tool steel due to its high wear and shock resistance among different tool steel grades. The process of manufacturing of tool pin profile as depicted in Fig. 4.11-4.14.

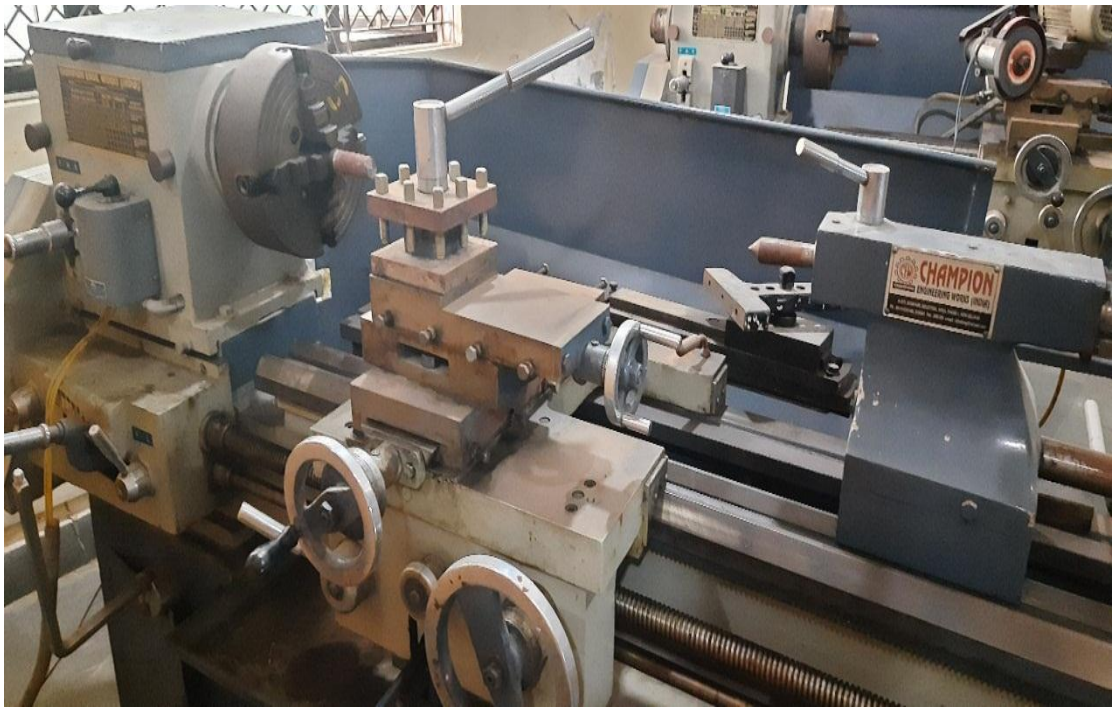

Figure 4.11: Lathe machine used for making FSP tool

Figure 4.12: Tool making using 4-Jaw chuck

Figure 4.13: Picture of final FSP Tool

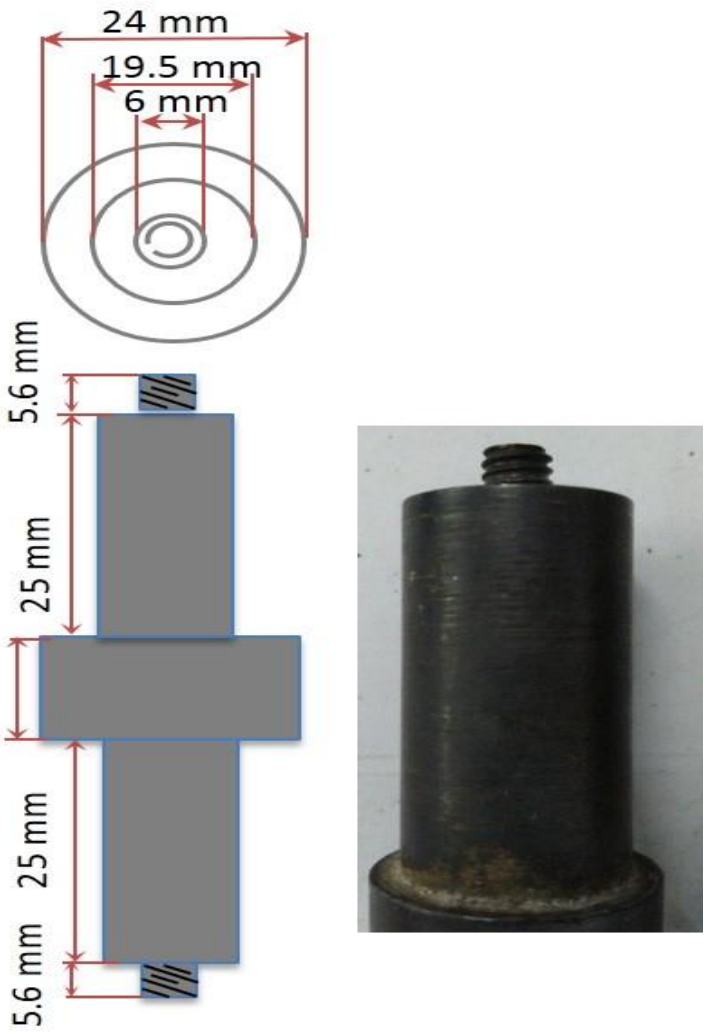

Figure 4.14: dimensional features of FSP tool

4.7 FRICTION STIR PROCESSING

In the present study, an indigenously developed NC-FSW machine was employed to produce the composite joints. The non-consumable tool manufactured of tool steel H13 was used for experimentations. The dimensional features of tool are depicted in Fig. 4.14. The slurry of reinforcing particles and ethanol was filled into the grooves made at the adjoining faces of the base plates as depicted in Fig. 4.15. Thereafter, AA7075 and AA6061 plates were securely secured to prevent the plates from abutting during processing as depicted in Fig. 4.16.

For FSP, the rotating tool was plunged slowly into the parting line of base plates of AA6061 and AA7075 until the tool pin is completely inserted into the base plates. The tool was maintained at this position for a dwell period of around 60 sec in order to preheat the material. Thereafter, the tool was allowed to move along the parting line of the base plates at a particular traverse speed as depicted in Fig. 4.17.

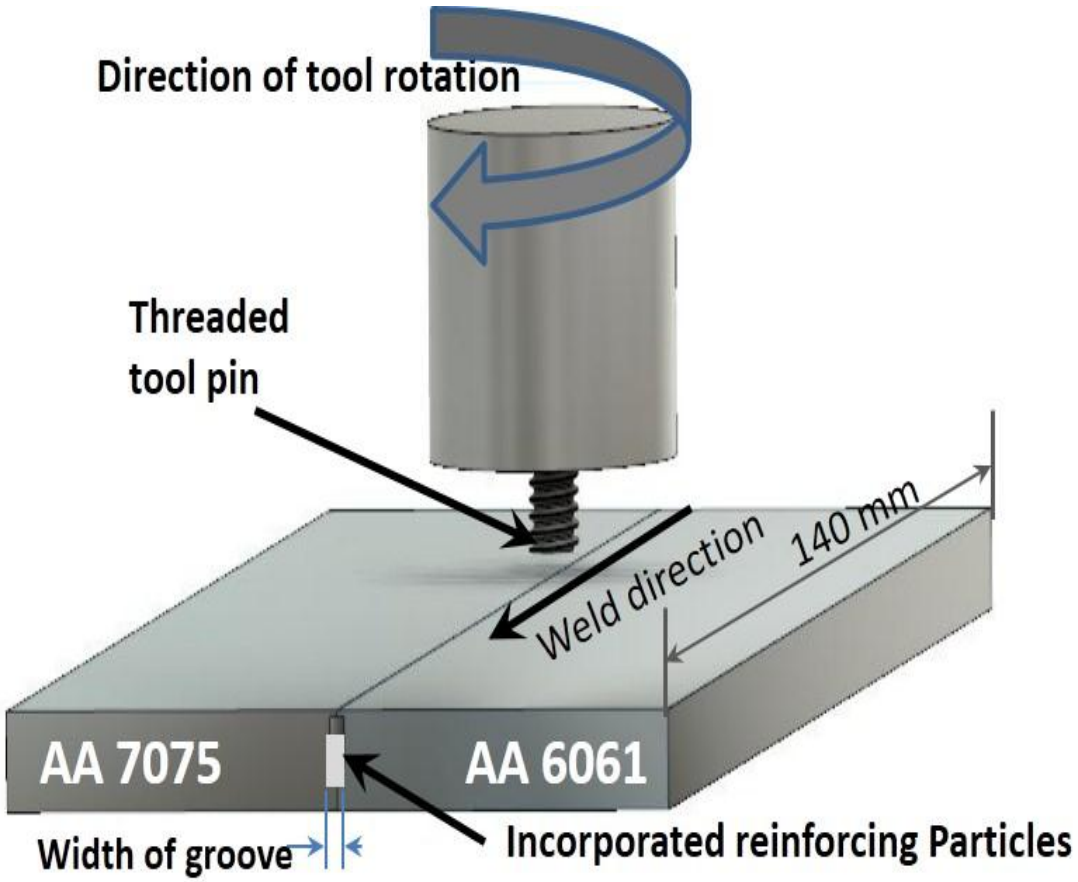

Figure 4.15: Representation of Friction stir processing setup

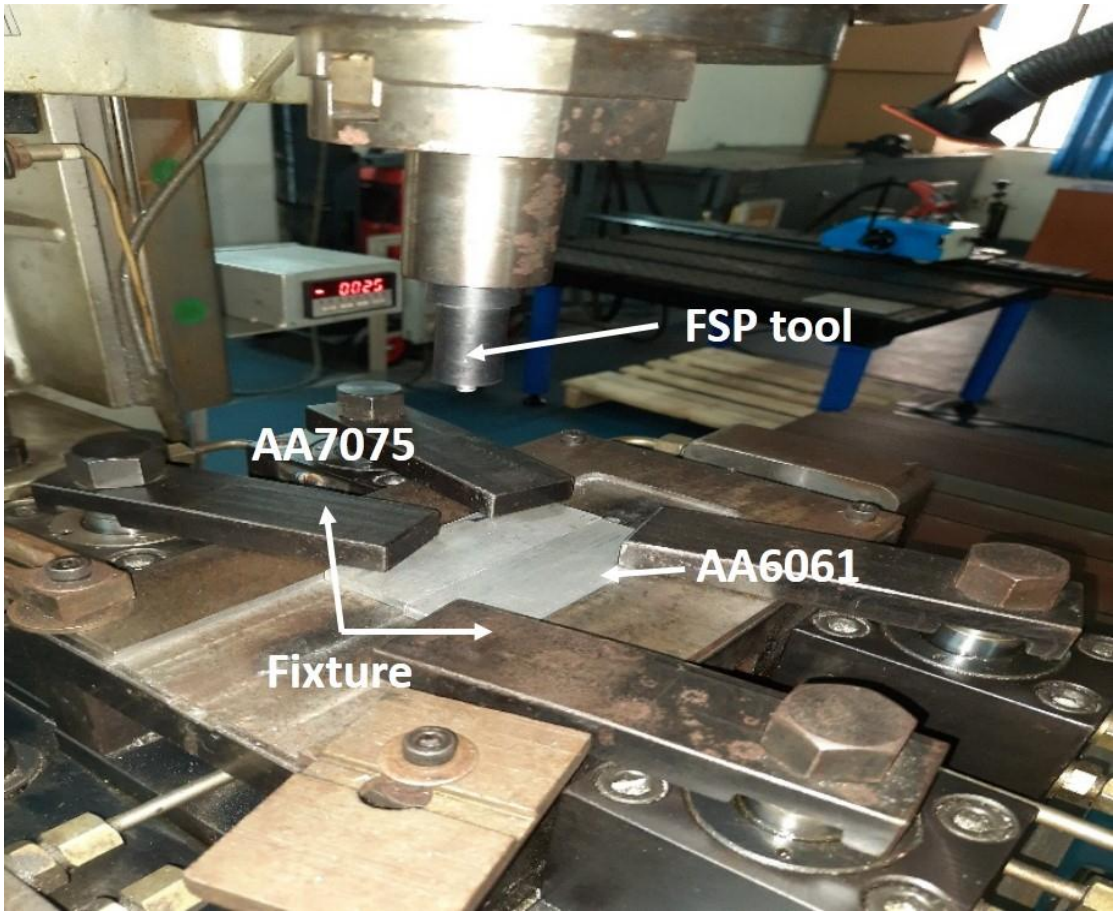

Figure 4.16: Clamping of base plates on the Fixture of FSW machine

Figure 4.17: FSP processing

Figure 4.18: Composite joint after FSP

The temperature distribution, material flow pattern, and subsequent microstructural evolution of the processed zone are all mainly influenced by the tool rotational speed and traverse speed in friction stir processing/welding. The process parameters such as tool rotation speed of 700-1100 rpm, tool traverse speeds of 40-60 mm/min and volume fraction of reinforcing particles of 4-10 % were utilized to fabricate the FSPed composite joints shown in Fig.4.18. The range of process parameters was selected on the basis of preliminary trails and working range of FSW machine. The process parameters along with their levels used in this study are illustrated in Tables 4.3.

Table 4.3: Processing parameter and its level used for FSP

Process Parameters	Units	Notation	Range	Levels		
				-1	0	1
Tool rotational Speed	rpm	A	700-1100	700	900	1100
Traverse Speed	mm/min	B	40-60	40	50	60
Volume fraction of reinforcing particles	%	C	4-10	4	7	10

A threaded pin profile tool was utilized for fabrication of the composite joints. The dimensional features of threaded pin tool and the images of the tool during manufactured are depicted in Fig. 4.11-4.14. There are total twenty number of experiments were performed obtained as per design of experiment of central composite full factorial design using response surface methodology (RSM) and illustrated in Table.4.4. The FSP composites joints after experimentation are depicted in Fig. 4.19.

Table 4. 4: Design of Experiments

Std	Run	A: Tools Rotations Speeds (rpm)	B: Traverses Speeds (mm/min)	C: volume fraction of reinforcing particles (%)
19	1	900	50	7
5	2	700	40	10
17	3	900	50	7
10	4	1100	50	7
11	5	900	40	7
7	6	700	60	10
18	7	900	50	7
20	8	900	50	7
14	9	900	50	10
2	10	1100	40	4
8	11	1100	60	10
16	12	900	50	7
12	13	900	60	7
15	14	900	50	7
6	15	1100	40	10
13	16	900	50	4
4	17	1100	60	4
3	18	700	60	4
1	19	700	40	4
9	20	700	50	7

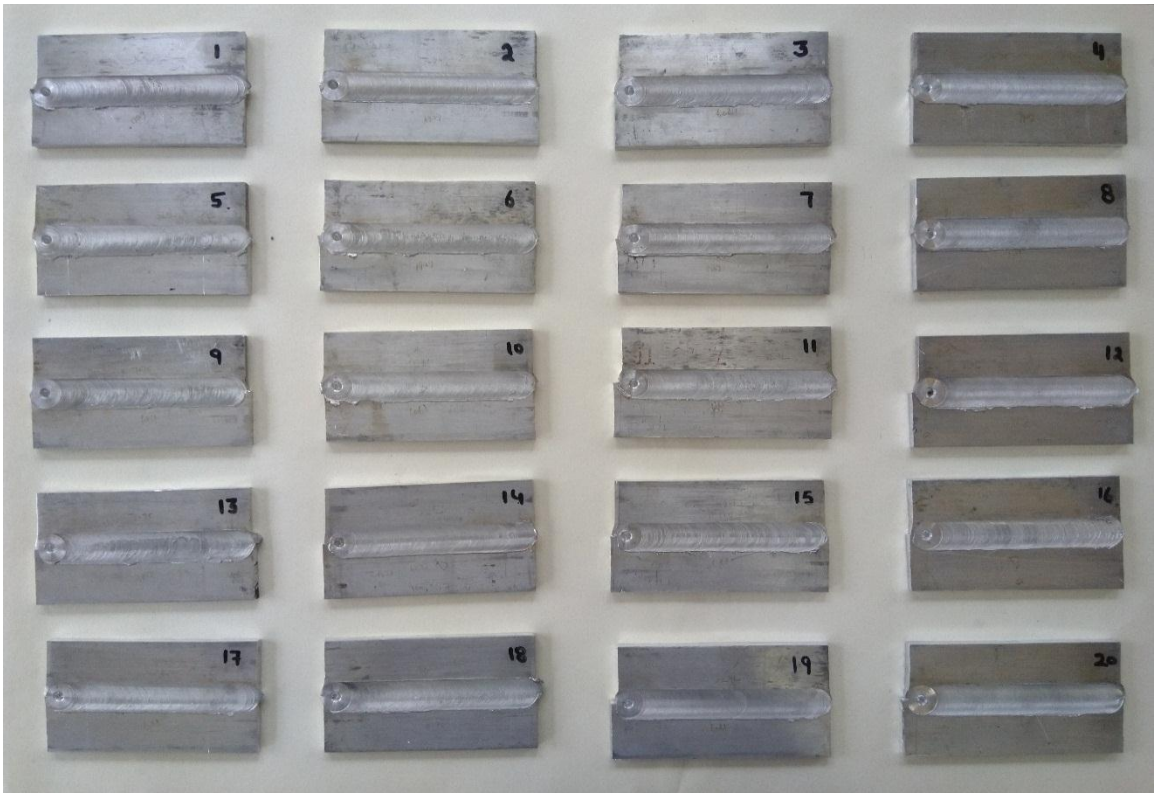

Figure 4.19: Various friction stir processed joint

4.8 TEST SAMPLES PREPARATION

The samples required for tensile test, micro-hardness test, wear test and microstructural characterization were extracted from the friction stir processed composite joints by employing wire-cut CNC machine for better dimensional accuracy, as shown in Fig. 4.20.

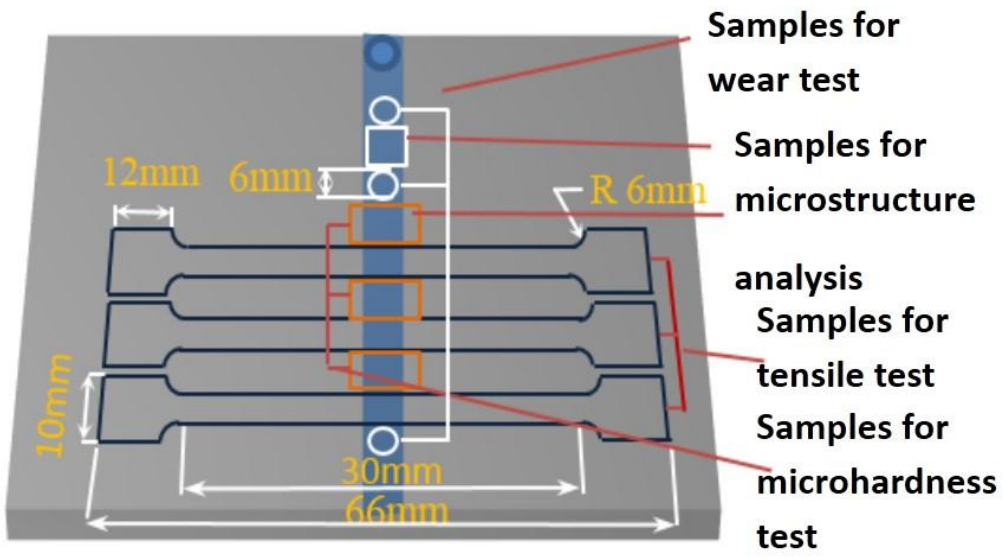

Figure 4.20: Dimensional features of various test samples

4.8.1 Tensile test

The strength of the material undergoing a basic lengthening operation is determined by tensile testing. The main functions of the testing apparatus are to produce the curve of load vs displacement and the curve of stress vs strain. Tensile test results can be applied for engineering applications in the selection of materials. Tensile properties are commonly involved in material specifications to assure quality. Tensile samples were extracted (Fig. 4.21) using CNC wire cut-EDM (Electrical Discharge Machining) as per the ASTM E8 standard as presented in Fig. 4.22. In this work, a single sheet size is 150 x 40 mm which is to be butt joint with the same size of the sheet. After the processing, the total fabricated sample is 150 x 80 mm in size with 80 mm for cross-sectional side. Due to this, a sub-size tensile samples (66 mm length of tensile sample) is preferred.

Figure 4.21: Tensile test specimen extracted from FSP composite joint

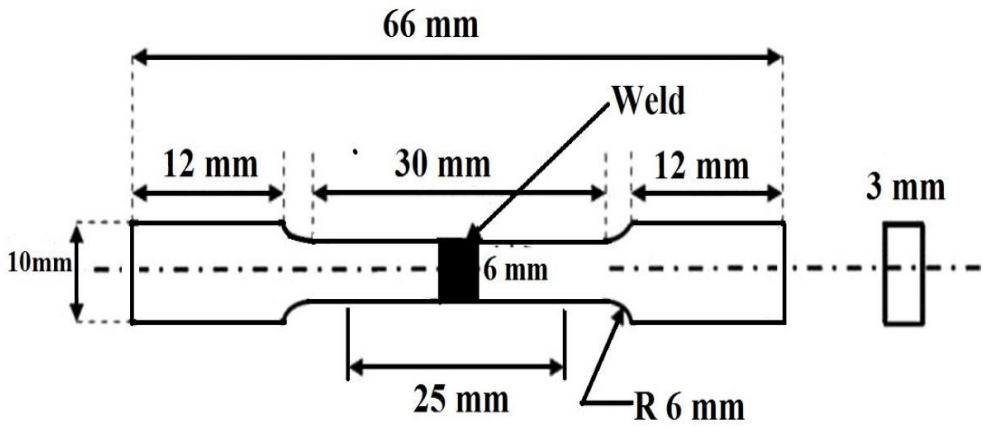

Figure 4.22: Dimensional features of tensile test sample as per ASTM E-8 standard [105]

Tensile testing of composite joint samples was carried out by Universal Testing Machine (Model: Biss UT-02-0100) as shown in Fig. 4.23. Three samples were extracted for each FSPed specimen and the tensile test was performed at room temperature and the average of three results were reported. Make sure samples free from crack or notches or other defects that would disparagingly affect the test results.

Figure 4.23: Universal testing machine (UTM)

4.8.2 Micro-hardness test

The micro-hardness variation of the FSPed composite joints of AA7075 and AA6061 processed under different combinations of processing parameters were evaluated using

Vickers hardness tester. The ASTM (E 384-99) standards were followed for sample preparation and testing methods for micro-hardness measurements. Prior to indentation, the samples were polished properly using emery papers from 600-1500 grade. The double disc polishing machine utilized for polishing is depicted in Fig. 4.24.

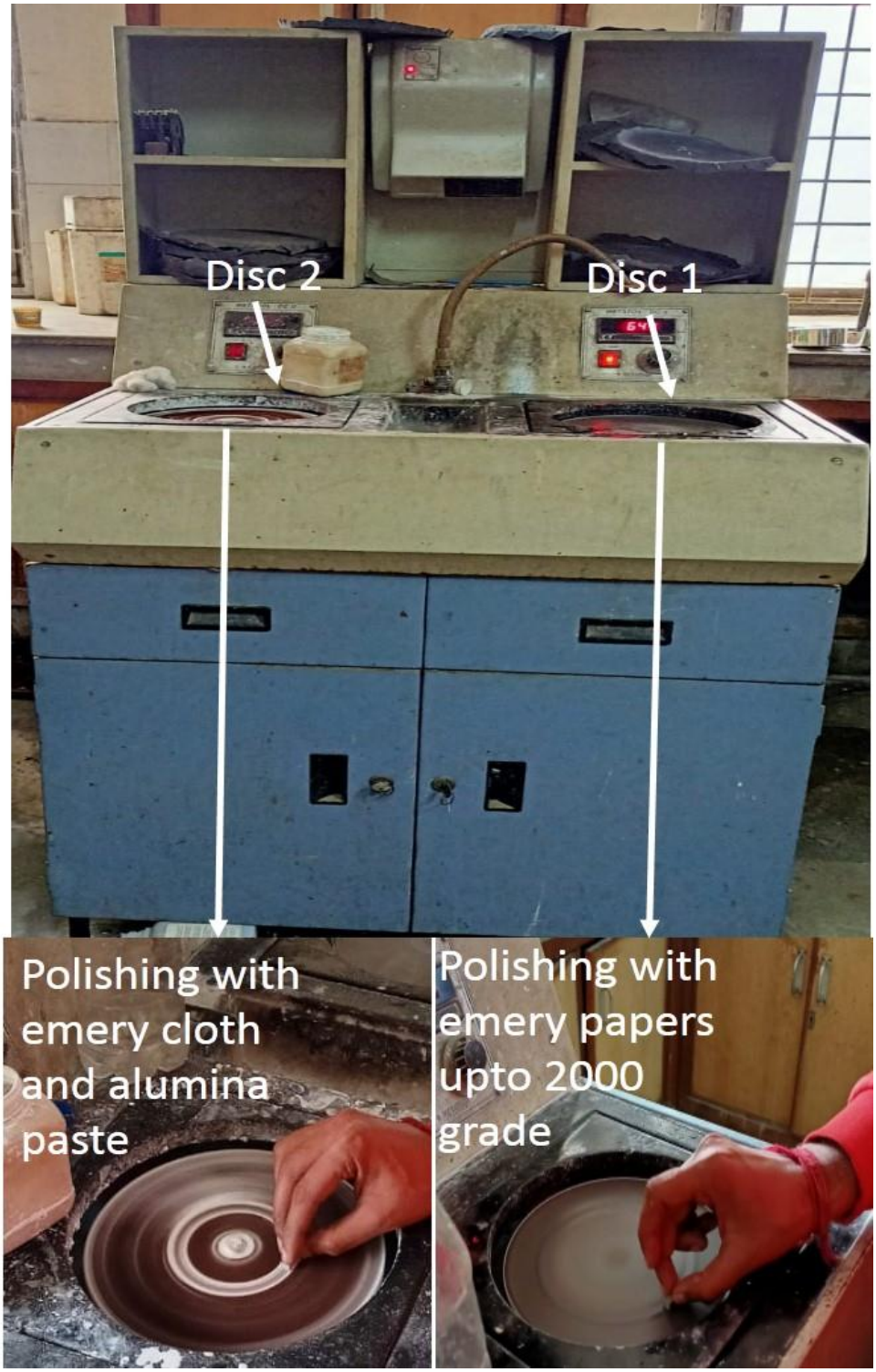

Figure 4.24: Double disc polishing machine

The indentations were carried-out on the lateral surface at 2 mm below the top surface. Vickers microhardness tester (Fig 4.25) was employed to evaluate the hardness profile at 100 gm load for 15 s dwell time by taking 1 mm gap between the indentations.

Figure 4.25: Vickers micro hardness testing process

4.8.3 Wear measurement

To evaluate the wear behavior, a Pin on disk tribometer (Model: DUCOM TR-20) was employed as depicted in Fig. 4.26. The wear samples (pin) of diameter 6 mm were extruded from the center of the processed zone. The samples were polished using different emery paper up to 1500 grade, prior to the wear test. The disk used for the wear test was made of EN-31 steel, having a hardness of 65 HRC. The weight of samples was measured before and after the wear test and the difference was calculated as weight loss. The wear tests were carried out by applying sliding speed of 2 m/s and a normal load of 20 N for the time period of 17 min. After the wear test, the worn

surfaces of samples were cleaned with acetone. Thereafter, the worn surface of samples was characterized using SEM to analyses the wear mechanism.

Figure 4.26: Tribometer setup

4.8.4 Microstructural Characteristics Evaluation

In this analysis, some characterization procedures went through to analyze the microstructure of the FSPed composite joints.

- The specimens having the dimensions (10 mm x 5mm x 6mm) were extracted from the FSPed composite joints.
- The examining surface of the samples was polished with emery papers from grit size from 100 to 2000 grade to get fine polish. The polishing machine used is depicted in Fig. 4.24.
- Final polishing was done using alumina powder with emery cloth using disc polishing machine. Thereafter, the polished surface of samples was etched with Keller reagent (HNO_3, HF, and HCL) as per ASTM E407 standard.
- The chemical etchants were mopped and washed in running water after that the samples were placed in the optical microscope machine (as depicted in Fig. 4.27) to analyze the microstructure of the FSPed composite joints

Figure 4.27: Optical microscope used to grain structure evolution of FSPed composite joints

- Thereafter, the samples were analyzed using SEM machine to evaluate the particles dispersion pattern in the stir zone. SEM machine used for microstructure evaluation is depicted in Fig. 4.28 and 4.29.
- To analyze the fracture surface of the samples extracted from the tensile test, the fractured surfaces were analyzed using SEM. The fractured surface was examined to better understand the mode of failure of the composite joints under tensile loading.
- The chemical composition of the base material and FSPed composite joints were analyzed using EDX/EDS analysis.

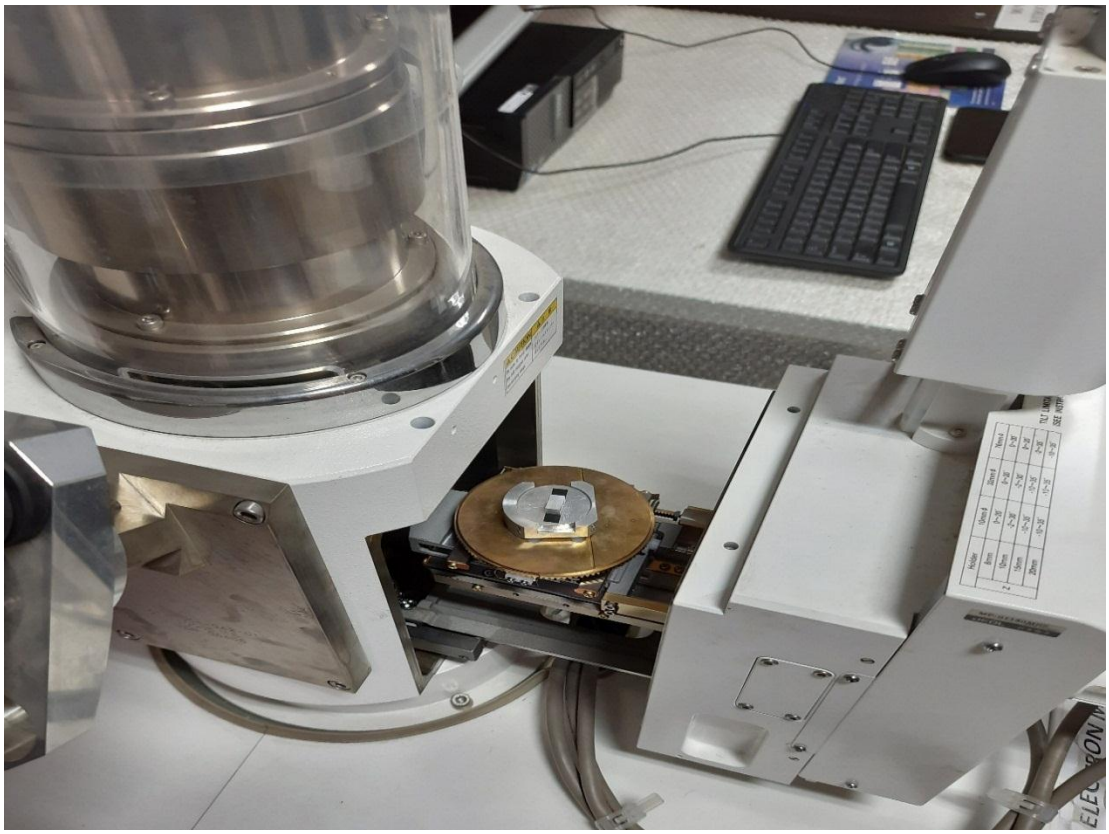

Figure 4.28: Microstructure test sample placed in scanning electron microscopy

Figure 4.29: SEM and EDX machine used during Microstructure evolution

CHAPTER-5

RESULT AND DISCUSSION

5.1 RESULT AND DISCUSSION

The experimental and optimization results are presented and analyzed in this chapter. The major research objectives of the current thesis have been discussed thoroughly with the supporting literature.

5.2 OPTIMIZATION OF PROCESSING PARAMETERS OF FSPED COMPOSITE JOINTS INCORPORATED WITH AL_2O_3 MICROPARTICLES

The friction stir processing was employed for the successful fabrication of dissimilar composite joints of AA6061 and AA7075 with the incorporation of Al_2O_3 microparticles (Al_2O_3mp) in order to enhance the mechanical and wear characteristics of the FSPed composite joints is depicted in Fig. 5.1. A non-consumable with threaded profiled pin manufactured of tool steel (H13) was utilized for experimentation. The input processing parameters for FSP approach have been taken as tool rotational speed (700 – 1100 rpm), traverse speed (40 - 60 mm/min) and volume fraction of Al_2O_3mp (4-10%).

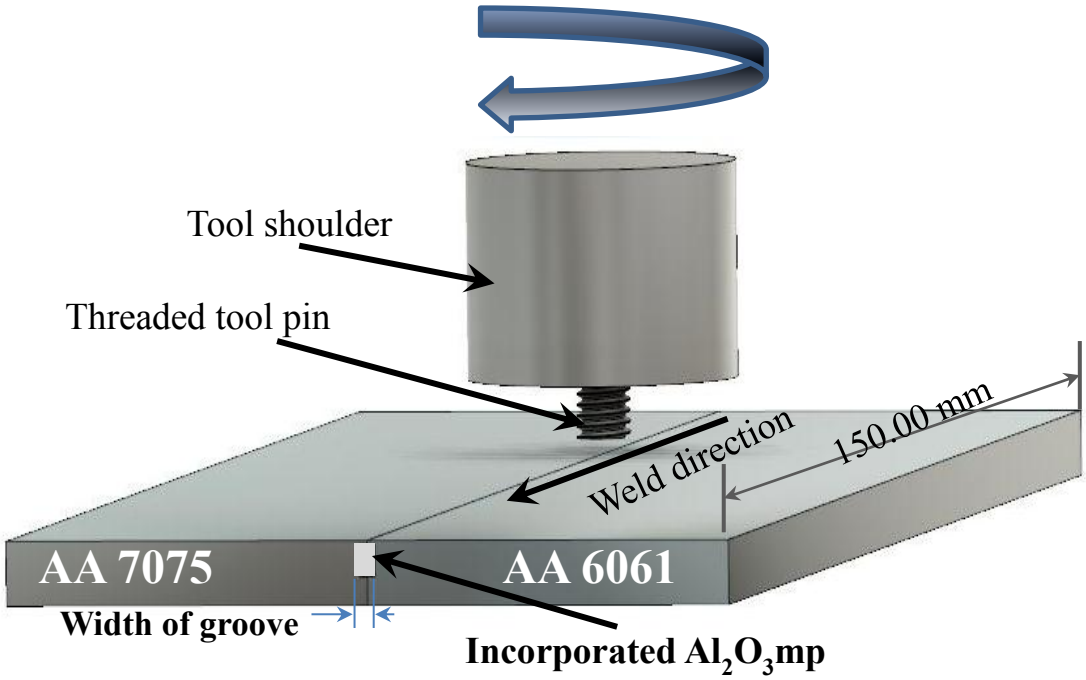

Figure 5.1: Systematic diagram of FSP welding approach

Single FSP pass was employed to fabricate FSPed composite joints as depicted in Fig. 5.1. The samples for various testing were extracted from the composite joint plates with the help of CNC wire cut EDM. The dimensions of samples for tensile testing were taken according to ASTM E8-standard as mentioned in the Fig. 5.2. The tensile test was analyzed using the computer-controlled UTM machine. Three tensile samples were tested from each composite joint and average result was reported. As per design expert software recommendation, there are 20 FSPed composite joints were fabricated under different processing conditions as depicted in the Fig. 4.19.

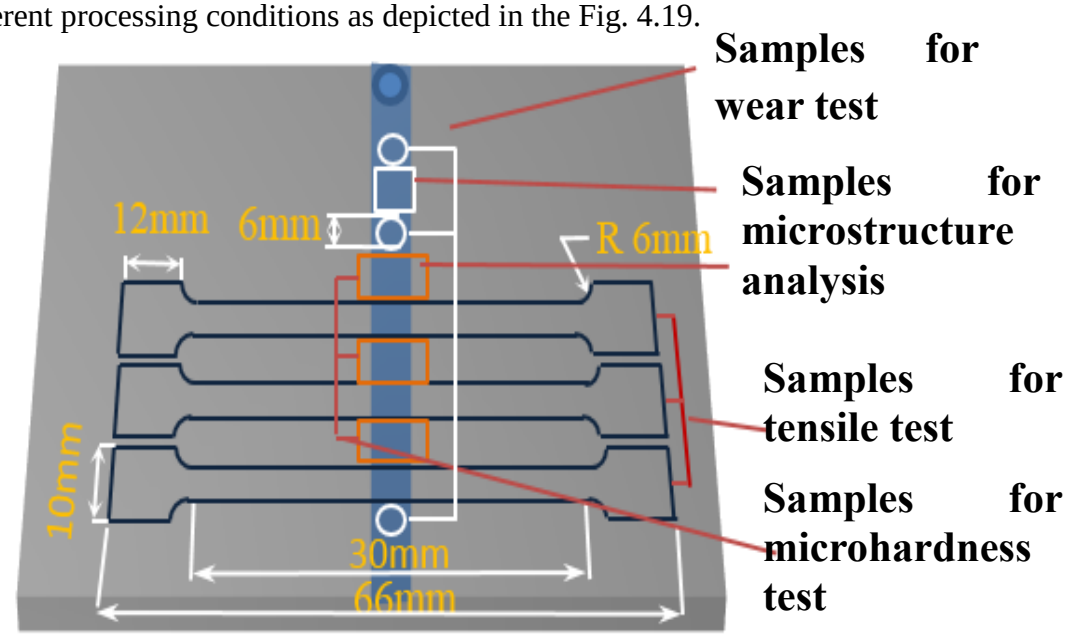

Figure 5.2: Dimension of welded tensile test samples

Various researchers have utilized a variety of experimental design strategies for the development of regression equations but central-composite design (CCD) is one of the best and most accurate design approaches [106-108]. To obtained the design of experiments (DOE) based on full factorial CCD, the process parameters and their levels were assigned, where the samples upper and lower values were coded as +1 and -1 respectively.

Table 5.1: Processing parameter of FSP-Al_2O_3mp with their levels

Parameters	Symbols	Units	Range	Levels		
				-1	0	1
Rotational Speed (RS)	A	rpm	700-1100	700	900	1100
Traverse speed (TS)	B	mm/min	40-60	40	50	60
Volume fraction of Al_2O_3mp	C	Percentage (%)	4-10	4	7	10

The face centered central composite design contains twenty experimental combinations with three independent input parameters namely tool rotational speed (RS), traverse speed (TS) and volume fraction of Al_2O_3 microparticles (VF-Al_2O_3mp) with their three levels. The Processing parameter of FSPed composite and their levels are illustrated in Table 5.1.

5.2.1 Tensile strength

In order to investigate the impact of FSP parameters along with varying volume fraction of Al_2O_3 micro-particles on the weld quality of dissimilar composite joint of AA7075 and AA6061, a universal testing machine (UTM) was utilized to apply the tensile load on FSPed composite joints at room temperature and observed the tensile strength of different FSPed composite joints. The samples for tensile testing were extruded transversely to composite joint. The average tensile strength and % elongation of FSPed composite joints under various processing conditions were tabulated in Table 5.2 and 5.3, respectively.

The tensile properties for base materials AA6061 and AA7075 were observed as 288 and 495 MPa, respectively, whereas % elongation was observed as 18.4% and 21.6%, respectively. Fig. 5.3-5.5 depicts the stress-strain diagram of the various composite joints produced at rotational speed of 700, 900 and 1100 rpm with different traverse speed and volume fraction of Al_2O_3mp. The tensile strength of the FSPed composite joints processed under different processing conditions were varied from 169.56 MPa to 241.35 MPa as depicted in Fig. 5.6. In accordance with the tensile strength, the composite joints processed at lower rotational speed of 700 and 900 rpm exhibited tunnel and small hole-like defects, respectively. These defects were occurred due to inadequate material mixing, which resulting in agglomeration of Al_2O_3mp. During tensile loading, some samples were fractured from the welded region due to defects whereas some samples fractured were observed on base material AA6061 side at heat affacted zone (HAZ) region where the strength and hardness were minimal [109]. Due to the materials' movement around the tool, strain is difficult to measure. One method is to measure the strain distributions in the SZ using FSW model. The three-dimensional viscoplastic flow and heat transfer model utilized to compute strain [110, 111]. The velocity and temperature fields are computed using the numerical model.

When calculating the velocity and temperature field, strain hardening was neglected. The strain rate is calculated using local velocity gradients as follows:

$$\dot{\varepsilon}_{ij} = \frac{\partial u_i}{\partial x_j} + \frac{\partial u_j}{\partial x_i} \tag{5.1}$$

Integrating the strain rate tensor with time along a streamline yields the strain [112]:

$$\varepsilon_{ij} = \int_0^t \dot{\varepsilon}_{ij}\, dt \tag{5.2}$$

Considerable material mixing and homogenous dispersion of Al_2O_3mp was observed due to enough strain produced as higher rotational speed of 1100 rpm. The best material mixing with onion rings was observed in the specimen processed at 1100 rpm, 40 mm/min and 10% volume fraction of Al_2O_3mp. The tensile strength of composite joints is mainly influenced by grain refinement, pinning effect produced by Al_2O_3mp and bonding between Al_2O_3mp and metal-matrix. As a result of the higher grain refinement due to pinning effect of the uniform distributed Al_2O_3mp, specimen produced at 1100 rpm, 40 mm/min and 10% volume fraction of Al_2O_3mp exhibits the finer grains.

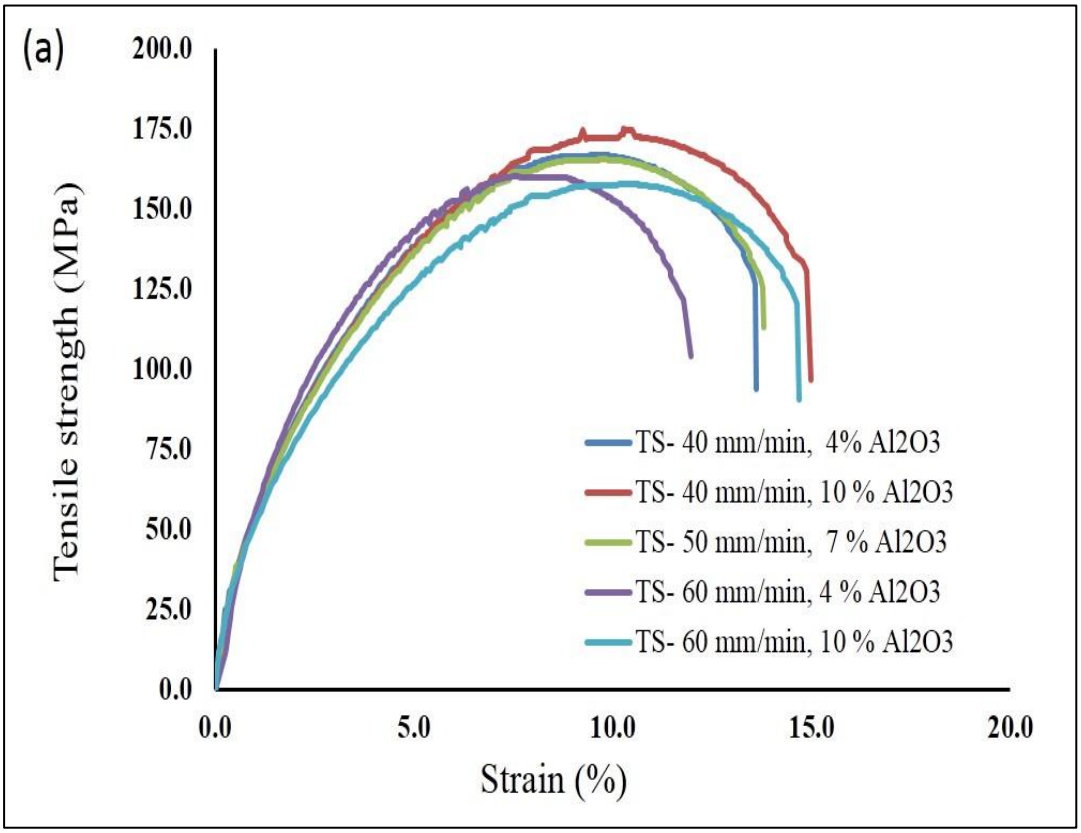

Figure 5.3: Stress strain diagram of various composite joints produced at 700 rpm with various traverse speed and volume fraction of Al_2O_3 microparticles

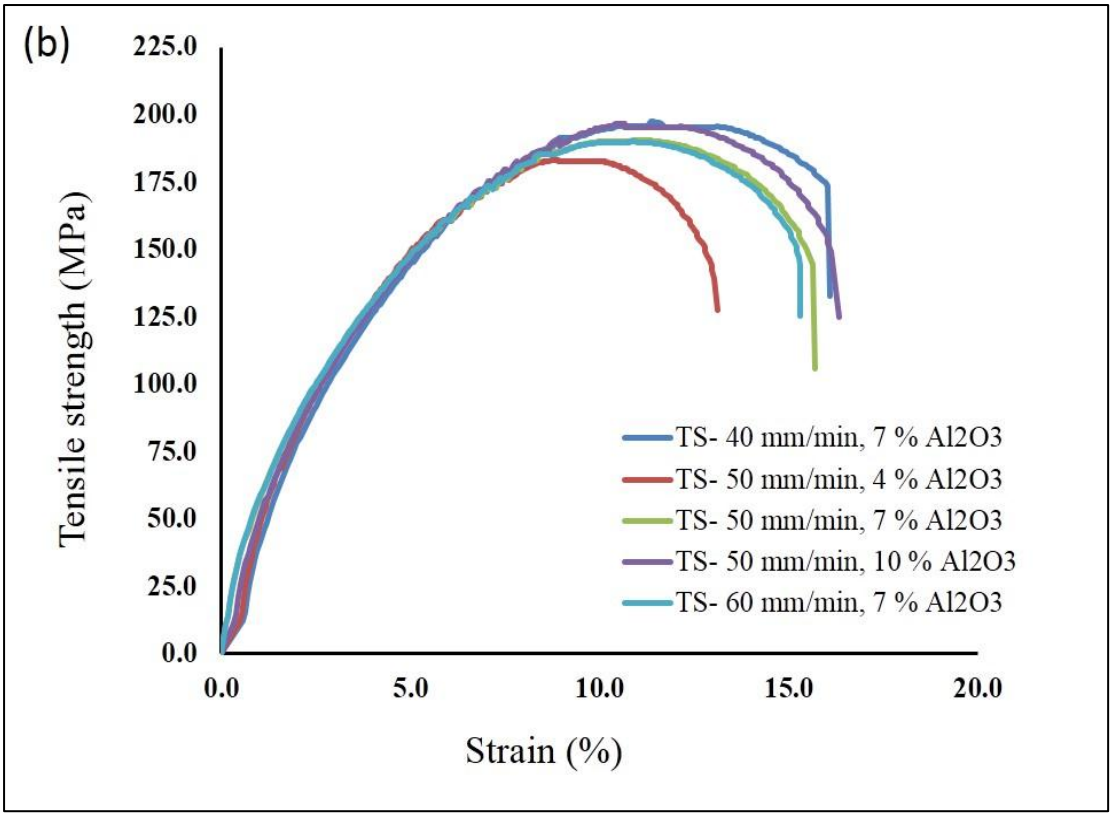

Figure 5.4: Stress strain diagram of various composite joints produced at 900 rpm

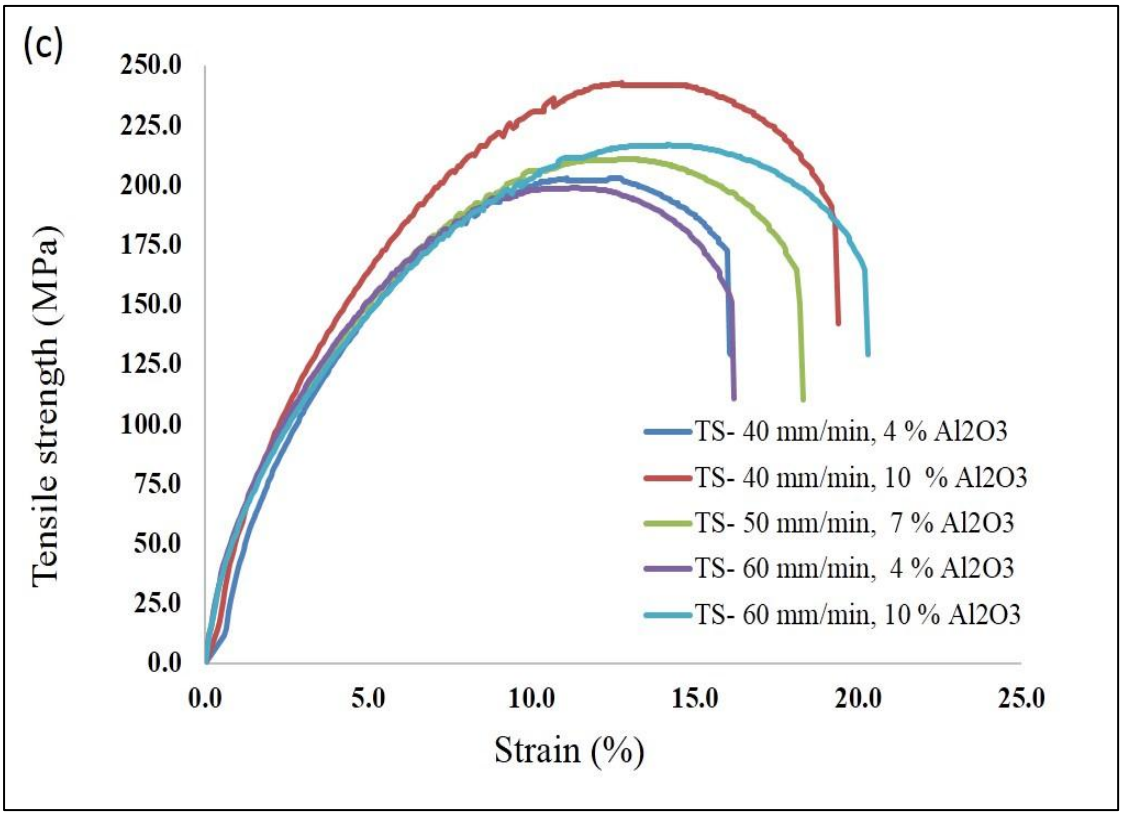

Figure 5.5: Stress strain diagram of various composite joints produced at 1100 rpm

Tensile strength is inversely proportional to grain's size, as defined by Hall-patch relationship $\sigma_1 = \sigma_i + kd^{(-1/2)}$ [113]. The grain size in FSPed composite joint was very small as compare to base materials. Because of presence of Al_2O_3mp presented in the stir zone which reduced the grain size as per Zener pinning effect [114]. Consequently, composite joint produced at 1100 rpm, 40 mm/min and 10% volume fraction of Al_2O_3mp exhibited the highest tensile strength of 241.35 MPa with joint efficiency of 83.80%. The joint efficiency of the FSPed composite joint was calculated on the basis on the tensile strength of as received AA6061 base material. Joint efficiency was calculated as: tensile strength of FSPed composite joint×100/tensile strength of AA6061. The minimum value of tensile strength (169.5 MPa) was observed in the composite joint processed at rotational speed 700 rpm, traverse speed 60 mm/min with the incorporation of 10% VF-Al_2O_3mp, which is about 58.88 % of the tensile strength of as received AA6061 as tabulated in Table 5.2.

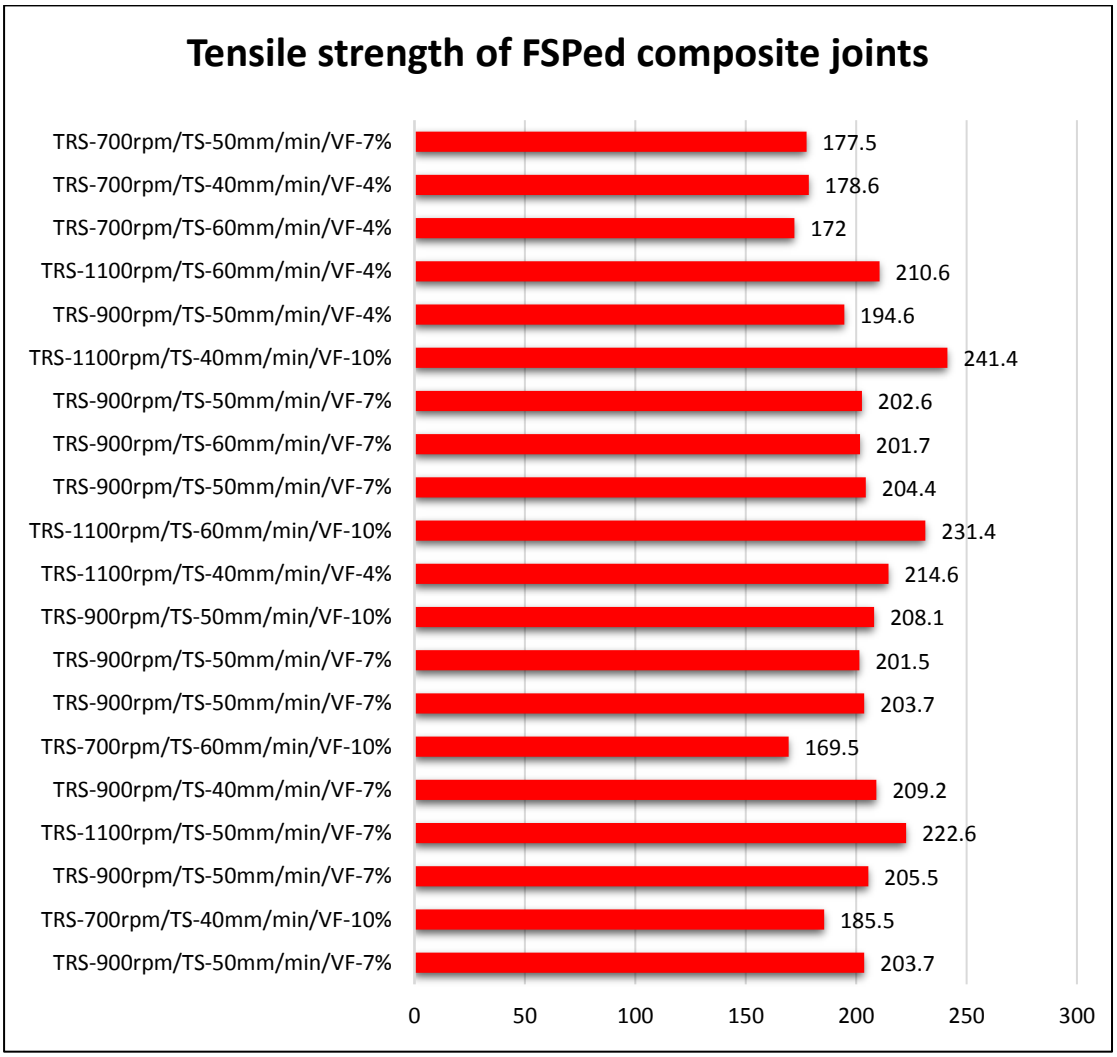

Figure 5.6: UTS of various FSPed composite joints

The %elongation (%El) of FSPed composite joints was observed higher than that of as received base materials, the higher percentage improvement of %elongation of 20.3 was observed at 1100 rpm rotational speed, 60 mm/min traverse speed, with the incorporation of 10% VF-Al_2O_3mp which was about 10.3 % higher than that of as received AA 6061 (base material).

In this experimental investigation, three statistical variables such as standard error (SE), standard deviation (SD), and confidence interval of 95% were analyzed for FSPed composite joints incorporated with Al_2O_3mp as presented in Tables 5.2-5.5. The standard deviation was measured as [SD= $\Sigma (X_i - M)^2 / (N - 1)]^{½}$, which gives the deviation of experimental values from the mean. The standard error is measured as, SE=SD/$N^{1/2}$ and used to find the closeness between the prediction values and the experimental values. Where M= mean, and N= the number of observations. The 95% confidence interval reveals that on increasing the value of tool rotational speed, the tensile strength, %elongation, and micro-hardness increases while the wear (weight loss) decrease.

5.2.2 Micro-hardness

Vickers hardness testing was employed to analyses the distribution of micro-hardness in the processed zone of FSPed composite joints of AA6061 and AA7075 processed under various processing conditions as shown in Fig. 5.7 (a-c). Vickers micro-hardness tester was employed to evaluate the hardness profile at 100 gm load for 15 s dwell time by taking 1 mm gap between the indentations. The asymmetrical distributions of micro-hardness in the processed zone due to the unsteady plastic flow in the retreating and advancing side in the processed region [115]. Fig. 5.7 depicts the micro-hardness variation towards both sides from the weld-center of all the composite joint incorporated with Al_2O_3mp. The mean micro-hardness of base materials AA6061 and AA7075 were observed as 96 and 170 HV, respectively. The value of mean micro-hardness at the center of weld line of all the composite joints was tabulated in Table 5.4. From the micro-harness results, it was observed that unreinforced FSPed composite joint exhibits the minimum hardness in comparison with composite joints. Among all the composite joint specimens, the specimen no-15 processed at rotational speed of 1100 rpm, traverse speed 40 mm/min with 10% VF-Al_2O_3mp exhibits the maximum micro-hardness of 157.5 HV as depicted in Fig. 5.8.

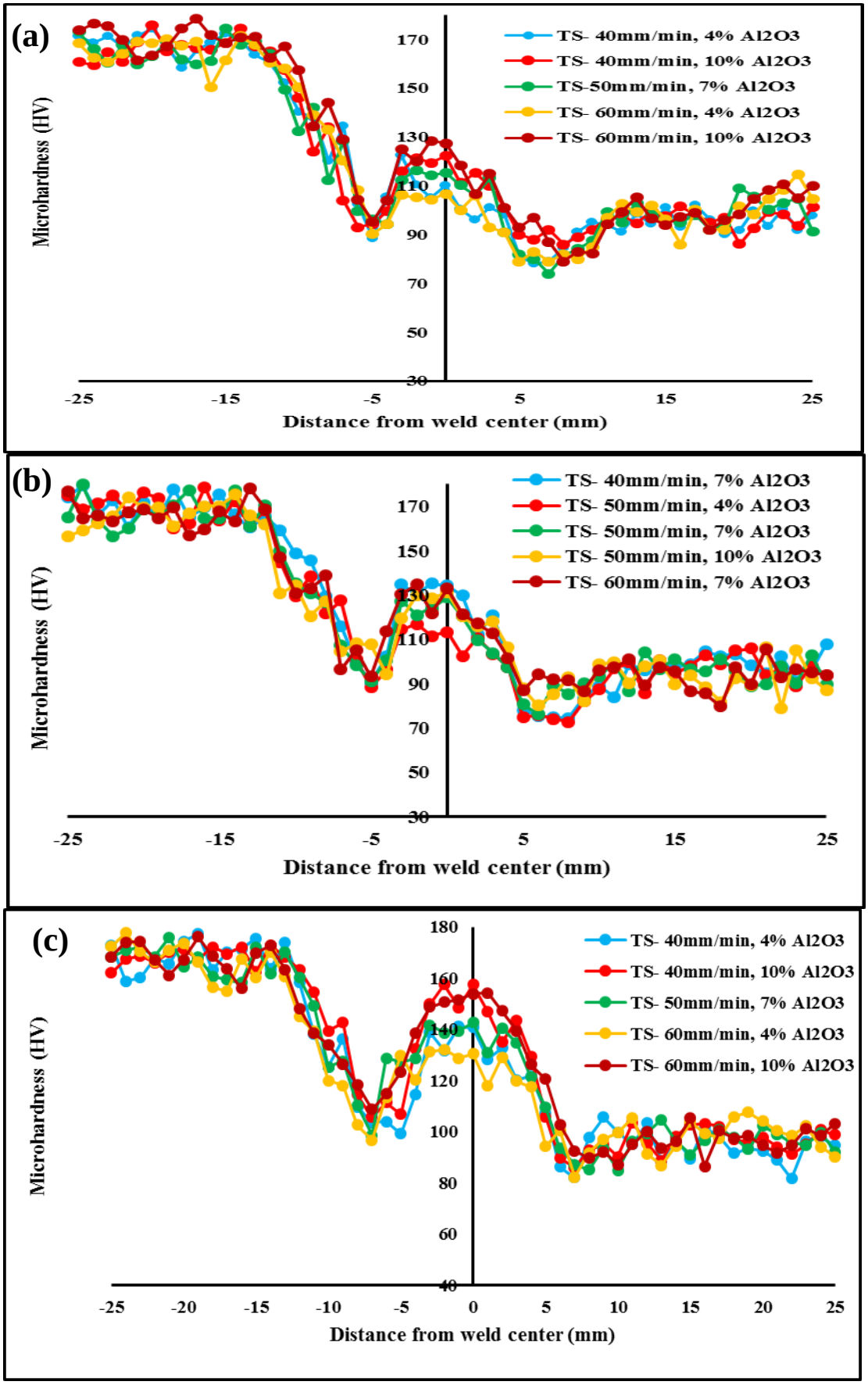

Figure 5.7: Micro-hardness distribution of composite joints produced at rotational speed 1100 rpm

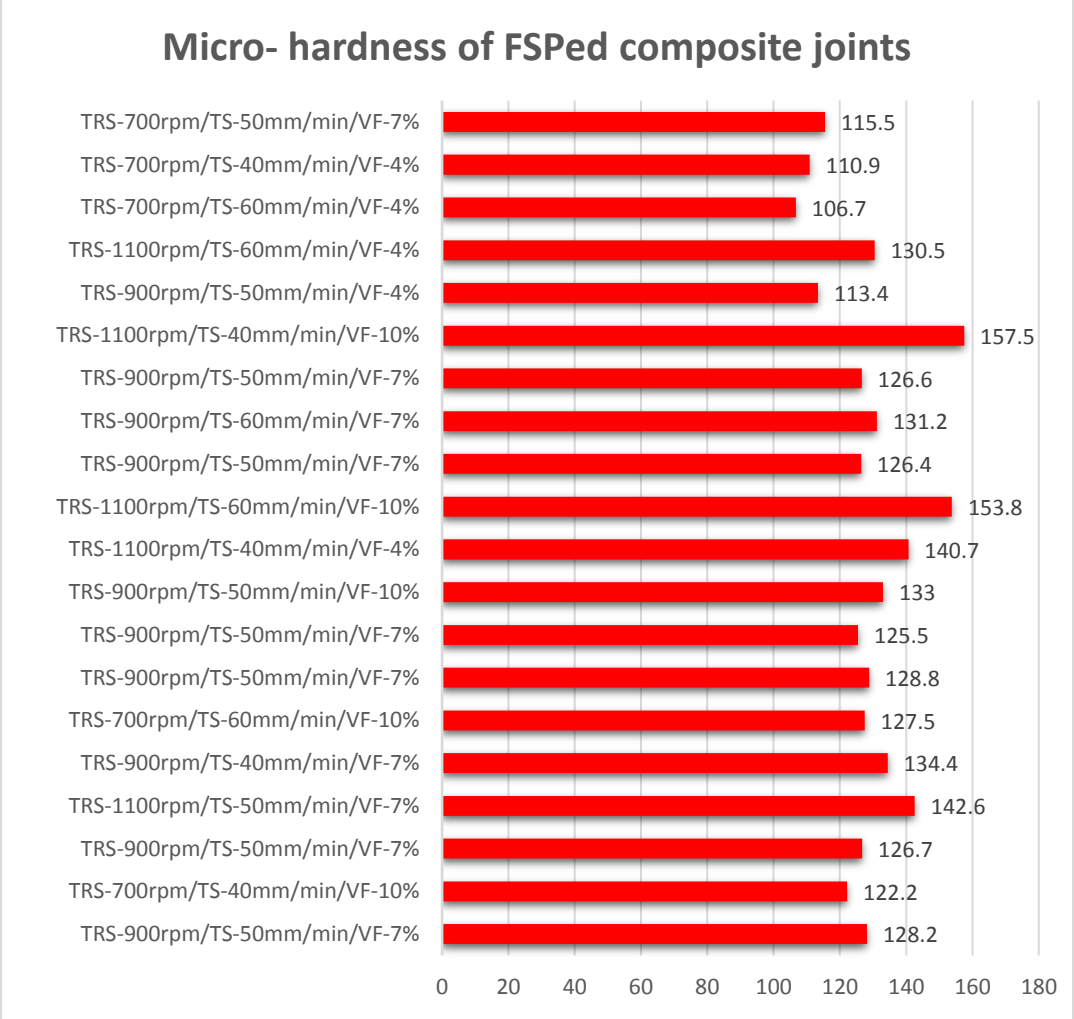

Figure 5.8: Micro-hardness variation to the processing parameters

The highest micro-hardness was observed in the stir zone in comparison with the other adjacent zones due to fine and equiaxed grain structure due to dynamic recrystallization and pinning effect of Al_2O_3mp, whereas TMAZ and HAZ exhibit low micro-hardness due to coarsening of grain, elevated temperatures, over aging during the FSP [116]. Smaller grain size exhibits higher hardness as per hall-patch relationship [117-119]. The micro-hardness of the composite joints embedded with reinforcement particles also enhanced due to the presence of hard Al_2O_3 particles. Therefore, the strengthening impact of Al_2O_3mp in specimen no- 15 was observed higher in comparison with other specimens, due to the increased volume fraction of hard Al_2O_3mp, higher grain refinement and enhanced material mixing rule.

5.2.3 Wear behaviour

To assess the wear behaviour of several specimens, Pin on disk tribometer was employed. The factors controlling the wear resistance of the various specimens

subjected to FSP were identified as, surface contact between the wear samples (pin) and the disk, homogeneity in the distribution of reinforcing particles and, the bond between the metal matrix and the reinforcing particles [120]. SEM was employed to examine the worn surfaces following the wear testing to assess the involved wear mechanism. The mean weight loss of as received base materials AA 6061 and AA7075 was observed as 14.35 and 12.23 mg. The mean weight loss of the composite joints was found less than that of the base material AA6061 and AA7075. This ascribed to the hard Al_2O_3mp, which enhances the wear resistance and reduced surface contact between the pin and the disk.

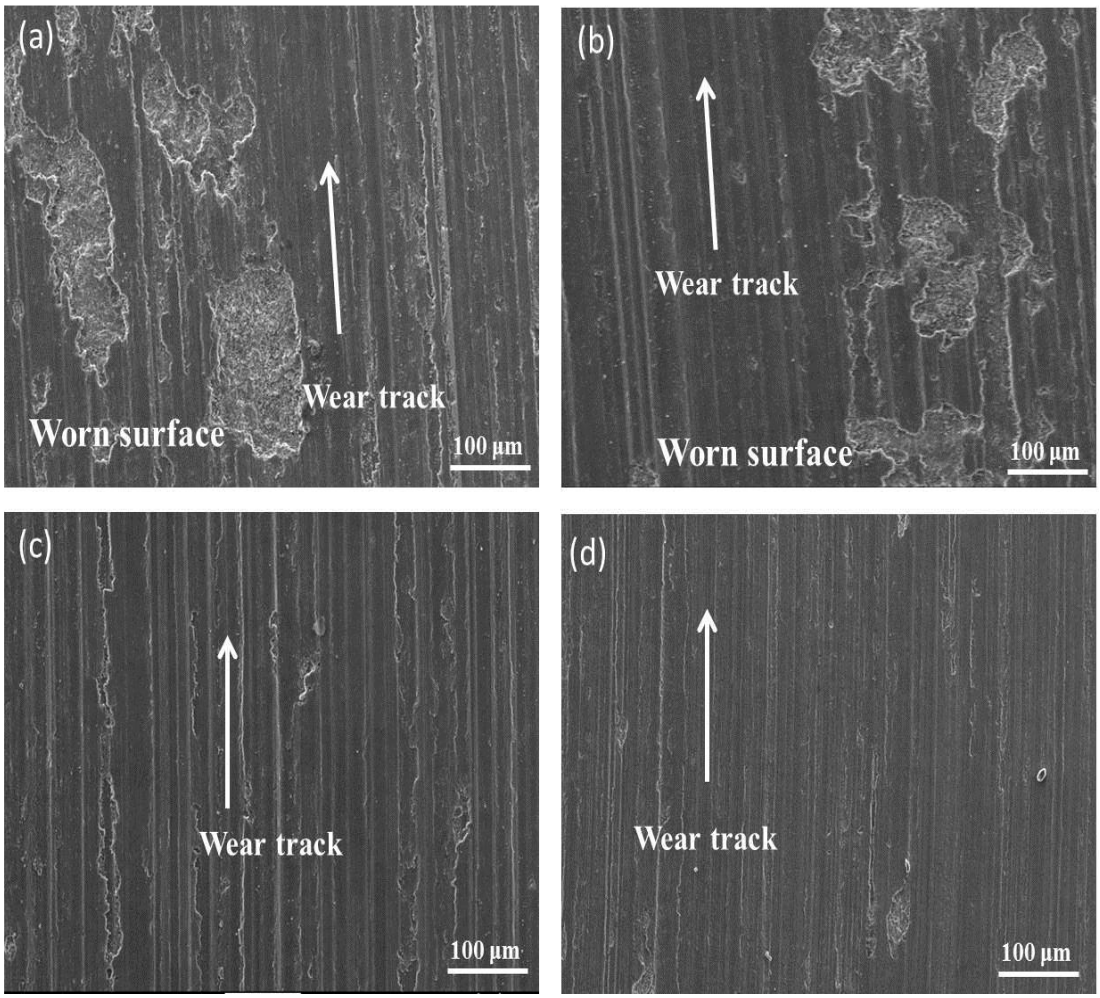

Figure 5.9: **SEM photomicrograph of different composite joints, (a) specimen no-6, (b) specimen no- 9, (c) specimen no- 10, (d) specimen no- 15.**

A higher weight loss was observed at low rotational speed value compared with that of high rotational speed, due to poor bonding of Al_2O_3mp with metal matrix at low rotational speed due to particles agglomeration, as revealed in SEM photomicrograph Fig. 5.9 d. Consequently, irregular pit along the sliding direction were observed in

specimens processed at 700 rpm and 900 rpm (Fig. 5.9 a, b), which evident the poor particle-metal matrix bonding. A smooth wear track was observed at 1100 rpm, with small plastic deformation (Fig. 5.9 c, d). The homogenous distribution of hard Al_2O_3mp after FSP at higher rotational speed offers enough hard larger surface area to prevent immediate deformation and loss of material during wear testing. Consequently, the avg. weight loss was found to be lower for specimen no. 10 processed at 1100 rpm, 40mm/min with 10% VF-Al_2O_3mp in comparison with specimen no-15 processed at 1100 rpm, 40mm/min with 4% VF-Al_2O_3mp. This ascribed to the presence of homogeneous dispersion of Al_2O_3mp with higher volume fraction in the SZ of specimen no-15, which reduces the surface contact between the pin and the disk [121]. Hence, the specimen processed at 1100 rpm, 40mm/min with 10 % VF-Al_2O_3mp had the best wear resistance among all selected specimens. Craters were found absent on the worn surface owing to the homogeneous distribution of the Al_2O_3mp and indicated the modified wear mode from adhesive to abrasive type. Table 5.5 illustrated the avg. weight loss of various FSPed composite joints. Hence, grain refinement, reduced surface contact between the pin and the disc due to hard Al_2O_3mp, homogenous distribution of Al_2O_3mp, and stronger bond between the Al_2O_3mp and the metal-matrix are all factors that contribute to the wear resistance of different composite joints.

5.3 DEVELOPING THE MATHEMATICAL MODEL

ANOVA techniques was utilized the empirical correlation for the response variable was developed by which are presented in equations. 5.3-5.6. the actual experimental condition of FSP process parameters and their level as tabulated in Table 5.1. Fisher's F test was used to evaluate the developed models with a 95% confidence level. The F-value is the proportion of variance within a factor to variation between factors. P-value of less than 0.05 is required, P stands for probability. The percentage of the independent factors' impact on the responses is known as contribution and implies the factor’s sensitivity. The output of the response will be significantly changed by changing the value of the factor with the largest percentage contribution. The standard F-value must exceed the estimated F-value in order for the model to be considered adequate. The models are significant when the lack of fit is not significant. Tables 5.6–5.9 provide the results of the ANOVAs for the response variables such as, tensile strength, micro-hardness, %elongation, and wear at the stir zone for FSPed composite joints.

Table 5.2: Tensile strength of FSPed composite joint incorporated with Al_2O_3mp

Specimen no.	Processing Parameter			Tensile Strength (MPa)			Mean tensile strength MPa	Standard Deviation	Standard error	95% confidence Interval	
	A: RS (rpm)	B: TS (mm/min)	C: VF-Al_2O_3mp (%)	Sample-1	Sample-2	Sample-3				Minimum	Maximum
1	900	50	7	199.9	208.7	202.4	203.7	4.53	2.62	198.5	208.8
2	700	40	10	189.8	182.6	184.2	185.5	3.78	2.18	181.3	189.8
3	900	50	7	203.6	207.3	205.7	205.5	1.86	1.07	203.4	207.6
4	1100	50	7	222.2	226.2	219.50	222.6	3.37	1.95	218.8	226.4
5	900	40	7	207.4	206.6	213.5	209.2	3.77	2.18	204.9	213.4
6	700	60	10	166.2	169.8	172.5	169.5	3.16	1.82	165.9	173.1
7	900	50	7	207.8	200.7	202.6	203.7	3.68	2.12	199.5	207.9
8	900	50	7	199.5	198.7	206.2	201.5	4.12	2.38	196.8	206.1
9	900	50	10	212.6	205.3	206.5	208.1	3.91	2.26	203.7	212.6
10	1100	40	4	217.4	215.2	211.3	214.6	3.09	1.78	211.1	218.1
11	1100	60	10	227.2	232.5	234.4	231.4	3.73	2.15	227.1	235.6
12	900	50	7	207.3	202.5	203.3	204.4	2.57	1.48	201.5	207.3
13	900	60	7	204.1	198.6	202.3	201.7	2.80	1.62	198.5	204.8
14	900	50	7	200.9	203.7	203.2	202.6	1.49	0.86	200.9	204.3
15	1100	40	10	241.7	244.5	237.9	241.4	3.31	1.91	237.6	245.1
16	900	50	4	197.3	196.1	190.4	194.6	3.69	2.13	190.4	198.8
17	1100	60	4	207.8	213.6	210.4	210.6	2.91	1.68	207.3	213.9
18	700	60	4	170.6	173.8	171.5	172.0	1.65	0.95	170.1	173.8
19	700	40	4	183.8	177.7	174.2	178.6	4.86	2.80	173.1	184.1
20	700	50	7	178.4	180.3	173.9	177.5	3.29	1.90	173.8	181.3

Table 5.3: % elongation of FSPed composite joint incorporated with Al_2O_3mp

Specimen no.	Processing Parameter			%Elongation (%)			Mean %Elongation (%)	Standard Deviation	Standard error	95% confidence Interval	
	A: RS (rpm)	B: TS (mm/min)	C: VF-Al_2O_3mp (%)	Sample 1	Sample 2	Sample 3				Minimum	Maximum
1	900	50	7	15.7	14.8	16.5	15.7	0.85	0.49	14.7	16.6
2	700	40	10	15.2	15.8	13.6	14.9	1.14	0.66	13.6	16.2
3	900	50	7	14.8	15.9	14.5	15.1	0.74	0.43	14.2	15.9
4	1100	50	7	17.3	18.9	18.6	18.3	0.85	0.49	17.3	19.2
5	900	40	7	15.9	16.7	15.6	16.1	0.57	0.33	15.4	16.7
6	700	60	10	14.6	14.2	15.2	14.7	0.50	0.29	14.1	15.2
7	900	50	7	16.9	15.1	15.3	15.8	0.99	0.57	14.7	16.9
8	900	50	7	15.4	16.6	15.1	15.7	0.79	0.46	14.8	16.6
9	900	50	10	17.1	16.1	15.6	16.3	0.76	0.44	15.4	17.1
10	1100	40	4	17.0	16.2	16.8	16.7	0.42	0.24	16.2	17.1
11	1100	60	10	20.8	20.1	19.9	20.3	0.47	0.27	19.7	20.8
12	900	50	7	15.5	14.8	15.1	15.1	0.35	0.20	14.7	15.5
13	900	60	7	15.9	14.9	15.2	15.3	0.51	0.30	14.8	15.9
14	900	50	7	14.6	15.3	15.4	15.1	0.44	0.25	14.6	15.6
15	1100	40	10	19.6	19.8	18.7	19.4	0.59	0.34	18.7	20.0
16	900	50	4	13.8	12.7	12.8	13.1	0.61	0.35	12.4	13.8
17	1100	60	4	16.3	16.5	15.8	16.2	0.36	0.21	15.8	16.6
18	700	60	4	11.4	11.9	12.3	11.9	0.45	0.26	11.4	12.4
19	700	40	4	14.4	13.3	13.2	13.6	0.67	0.38	12.9	14.4
20	700	50	7	13.8	13.3	14.2	13.8	0.45	0.26	13.3	14.3

Table 5.4: Micro-hardness of FSPed composite joint incorporated with Al_2O_3mp

Specimen no.	Processing Parameter			Micro-hardness (HV)			Mean Micro-hardness (HV)	Standard Deviation	Standard error	95% confidence Interval	
	A:RS (rpm)	B: TS (mm/min)	C: VF-Al_2O_3mp (%)	Sample 1	Sample 2	Sample 3				Minimum	Maximum
1	900	50	7	131.1	128.2	125.3	128.2	2.90	1.67	124.9	131.5
2	700	40	10	125.0	121.4	120.2	122.2	2.50	1.44	119.4	125.0
3	900	50	7	123.6	126.7	129.8	126.7	3.10	1.79	123.2	130.2
4	1100	50	7	146.6	138.5	142.7	142.6	4.05	2.34	138.0	147.2
5	900	40	7	134.6	131.5	137.1	134.4	2.81	1.62	131.2	137.6
6	700	60	10	127.0	124.2	131.3	127.5	3.58	2.06	123.5	131.5
7	900	50	7	124.2	130.1	132.1	128.8	4.11	2.37	124.2	133.4
8	900	50	7	129.2	121.7	125.6	125.5	3.75	2.17	121.3	129.7
9	900	50	10	138.2	131.4	129.4	133.0	4.61	2.66	127.8	138.2
10	1100	40	4	138.8	139.7	143.6	140.7	2.55	1.47	137.8	143.6
11	1100	60	10	152.9	156.7	151.8	153.8	2.57	1.48	150.9	156.7
12	900	50	7	125.8	123.8	129.6	126.4	2.95	1.70	123.1	129.7
13	900	60	7	133.0	134.4	126.2	131.2	4.39	2.53	126.2	136.2
14	900	50	7	128.6	122.8	128.4	126.6	3.29	1.90	122.9	130.3
15	1100	40	10	157.5	160.8	154.2	157.5	3.30	1.91	153.8	161.2
16	900	50	4	112.5	117.4	110.3	113.4	3.63	2.10	109.3	117.5
17	1100	60	4	129.7	126.8	135.0	130.5	4.16	2.40	125.8	135.2
18	700	60	4	102.9	111.8	105.4	106.7	4.59	2.65	101.5	111.9
19	700	40	4	111.2	115.4	106.0	110.9	4.71	2.72	105.5	116.2
20	700	50	7	118.0	115.3	113.2	115.5	2.41	1.39	112.8	118.2

Table 5.5: Wear behavior (Weight loss) of FSP composite joint incorporated with Al_2O_3mp

Specimen no	Processing Parameter			Weight loss (mg)			Mean weight loss (mg)	Standard Deviation	Standard error	95% confidence Interval	
	A: RS (rpm)	B: TS (mm/min)	C: VF-Al_2O_3mp (%)	Sample 1	Sample 2	Sample 3				Minimum	Maximum
1	900	50	7	11.52	10.84	11.96	11.44	0.56	0.33	10.8	12.1
2	700	40	10	11.22	11.86	11.14	11.41	0.39	0.23	11.0	11.9
3	900	50	7	11.81	10.90	11.55	11.42	0.47	0.27	10.9	12.0
4	1100	50	7	9.96	11.15	10.76	10.62	0.61	0.35	9.9	11.3
5	900	40	7	10.94	11.71	11.14	11.26	0.40	0.23	10.8	11.7
6	700	60	10	11.48	12.24	11.28	11.67	0.51	0.29	11.1	12.2
7	900	50	7	10.94	11.31	11.82	11.36	0.44	0.26	10.9	11.9
8	900	50	7	11.24	11.83	11.18	11.42	0.36	0.21	11.0	11.8
9	900	50	10	10.98	11.18	11.97	11.38	0.52	0.30	10.8	12.0
10	1100	40	4	11.44	10.65	11.21	11.10	0.41	0.23	10.6	11.6
11	1100	60	10	10.78	10.35	10.06	10.40	0.36	0.21	10.0	10.8
12	900	50	7	11.61	11.41	11.12	11.38	0.25	0.14	11.1	11.7
13	900	60	7	11.34	11.17	11.72	11.41	0.28	0.16	11.1	11.7
14	900	50	7	10.94	11.53	11.62	11.36	0.37	0.21	10.9	11.8
15	1100	40	10	10.62	10.21	10.07	10.30	0.29	0.17	10.0	10.6
16	900	50	4	12.38	11.52	11.74	11.88	0.45	0.26	11.4	12.4
17	1100	60	4	10.58	10.64	11.48	10.90	0.50	0.29	10.3	11.5
18	700	60	4	11.70	12.38	12.23	12.10	0.36	0.21	11.7	12.5
19	700	40	4	12.64	11.47	11.83	11.98	0.60	0.35	11.3	12.7
20	700	50	7	11.62	12.35	11.27	11.75	0.55	0.32	11.1	12.4

The final mathematical model equations developed in terms of coded variables are given below.

$$\textbf{Tensile strength} = +203.48+23.75\times A-4.40\times B+6.55\times C+1.09\times AB+5.38\times AC-1.92\times BC -3.27\times A^2 +2.15\times B^2 -1.92\times C^2 \quad (5.3)$$

$$\textbf{\%elongation} = +15.37+2.20\times A-0.23\times B+1.41\times C+0.29\times AB+0.34\times AC+0.36\times BC +0.76\times A^2 +0.41\times B^2 \quad (5.4)$$

$$\textbf{Micro-hardness} = +127.01+14.30\times A-1.53\times B+9.25\times C-1.96\times AB+0.91\times AC+1.91\times BC +2.07\times A^2 +5.82\times B^2 -3.78\times C^2 \quad (5.5)$$

$$\textbf{Wear (wt. loss)} = +11.41-0.56\times A+0.043\times B-0.28\times C-0.060\times AB-0.037\times AC+0.055\times BC-0.26\times A^2 -0.11\times B^2 +0.19\times C^2 \quad (5.6)$$

The final mathematical model equations in terms of actual variables are represented in equations 5.7-5.10.

$$\textbf{Tensile strength} = + 203.48 + 23.75 \times \text{Rotational speed} - 4.40 \times \text{Traverse speed} + 6.55 \times \text{VF-}Al_2O_3\text{mp} + 1.09 \times \text{A Rotational speed} \times \text{Traverse speed} + 5.38 \times \text{Rotational speed} \times \text{VF-}Al_2O_3\text{mp} - 1.92 \times \text{Traverse speed} \times \text{VF-}Al_2O_3\text{mp} - 3.27 \times \text{Rotational speed}^2 + 2.15 \times \text{Traverse speed}^2 - 1.92 \times \text{VF-}Al_2O_3\text{mp}^2 \quad (5.7)$$

$$\textbf{\%elongation} = +15.37+2.20\times \text{Rotational speed} -0.23\times \text{Traverse speed} +1.41\times \text{VF-}Al_2O_3\text{mp} +0.29\times \text{Rotational speed B} +0.34\times \text{Rotational speed VF-}Al_2O_3\text{mp} +0.36\times \text{Traverse speed VF-}Al_2O_3\text{mp} +0.76\times \text{Rotational speed}^2 +0.41\times \text{Traverse speed}^2 \quad (5.8)$$

$$\textbf{Micro-hardness} = +127.01+14.30 \times \text{Rotational speed} - 1.53 \times \text{Traverse speed} + 9.25 \times \text{VF-}Al_2O_3\text{mp} - 1.96 \times \text{Rotational speed} \times \text{Traverse speed} + 0.91 \times \text{Rotational speed} \times \text{VF-}Al_2O_3\text{mp} + 1.91 \times \text{Traverse speed} \times \text{VF-}Al_2O_3\text{mp} + 2.07 \times \text{Rotational speed}^2 + 5.82 \times \text{Traverse speed}^2 -3.78 \times \text{VF-}Al_2O_3\text{mp}^2 \quad (5.9)$$

Wear (wt. loss) = +11.41- 0.56 × Rotational speed + 0.043 × Traverse speed - 0.28 × VF-Al_2O_3mp - 0.060 × Rotational speed × Traverse speed - 0.037 × Rotational speed × VF-Al_2O_3mp + 0.055 × Traverse speed × VF-Al_2O_3mp - 0.26 × Rotational speed^2 - 0.11 × Traverse speed^2 +0.19 × VF-Al_2O_3mp^2 (5.10)

The tool rotational speed coefficient (A) is positive, it implies that the on increasing value of rotational speed, increases the tensile strength, because at lower value of rotational speed produced insufficient heat input resulting in tunnel and small holes like defects in the stir zone. Whereas decreasing traverse speed reduces the adverse influence of the tool rotation speed. The volume fraction of Al_2O_3mp is also significantly affecting the tensile strength.

Table 5.6: ANOVA table of full quadratic model for tensile strength

Tensile Strength						
Sources	SS	DOF	MS	F-value	P-value	
Model	6600.63	9.00	733.40	456.32	< 0.0001	Significant
A-RS	5641.58	1.00	5641.58	3510.18	< 0.0001	
B-TS	193.25	1.00	193.25	120.24	< 0.0001	
C-VF-Al_2O_3mp	429.55	1.00	429.55	267.26	< 0.0001	
AB	9.42	1.00	9.42	5.86	0.04	
AC	231.56	1.00	231.56	144.07	< 0.0001	
BC	29.49	1.00	29.49	18.35	0.00	
A^2	29.42	1.00	29.42	18.31	0.00	
B^2	12.70	1.00	12.70	7.90	0.02	
C^2	10.15	1.00	10.15	6.31	0.03	
Residual	16.07	10.00	1.61			
Lack of Fit	6.28	5.00	1.26	0.64	0.68	not significant
Pure Error	9.80	5.00	1.96			
Cor Total	6616.70	19.00				
Std. Dev.	1.27	R^2		0.9976		
Mean	201.96	Adjusted R^2		0.9914		
C.V. %	0.63	Predicted R^2		0.9872		
		Adeq Precision		79.08		

Table 5.7: ANOVA table for %elongation

% elongation						
Sources	SS	df	MS	F-value	P-value	
Model	74.62	9	8.29	99.83	< 0.0001	Significant
A-RS	48.40	1	48.40	582.77	< 0.0001	
B-TS	0.53	1	0.53	6.37	0.0302	
C-VF-Al_2O_3mp	19.88	1	19.88	239.38	< 0.0001	
AB	0.66	1	0.66	7.96	0.0181	
AC	0.91	1	0.91	10.97	0.0078	
BC	1.05	1	1.05	12.66	0.0052	
A^2	1.58	1	1.58	19.08	0.0014	
B^2	0.46	1	0.46	5.54	0.0404	
C^2	0.96	1	0.96	11.56	0.0068	
Residual	0.83	10	0.08			
Lack of Fit	0.22	5	0.04	0.37	0.8534	not significant
Pure Error	0.61	5	0.12			
Cor Total	75.45	19				
Std. Dev.	0.288	R^2		0.9891		
Mean	15.65	Adjusted R^2		0.9791		
C.V. %	1.84	Predicted R^2		0.9690		
		Adeq Precision		41.80		

Table 5.8: ANOVA table for micro-hardness at stir zone

Micro-hardness						
Sources	SS	DOF	MS	F-value	P-value	
Model	3146.48	9	349.61	336.82	< 0.0001	Significant
A-RS	2044.90	1	2044.90	1970.09	< 0.0001	
B-TS	23.41	1	23.41	22.55	0.0008	
C-VF-Al_2O_3mp	855.63	1	855.63	824.33	< 0.0001	
AB	30.81	1	30.81	29.68	0.0003	
AC	6.66	1	6.66	6.42	0.0297	
BC	29.26	1	29.26	28.19	0.0003	
A^2	11.81	1	11.81	11.38	0.0071	

B^2	93.24	1	93.24	89.83	< 0.0001	
C^2	39.24	1	39.24	37.80	0.0001	
Residual	10.38	10	1.04			
Lack of Fit	2.85	5	0.57	0.38	0.8454	not significant
Pure Error	7.53	5	1.51			
Cor Total	3156.86	19				
Std. Dev.	1.02	R^2		0.9967		
Mean	129.07	Adjusted R^2		0.9938		
C.V. %	0.79	Predicted R^2		0.9867		
		Adeq Precision		69.63		

Table 5.9: ANOVA table for wear (weight loss) at stir zone

wear (weight loss)						
Sources	SS	DOF	MS	F-value	P-value	
Model	4.31	9	0.48	230.64	< 0.0001	Significant
A-RS	3.12	1	3.12	1505.14	< 0.0001	
B-TS	0.02	1	0.02	8.91	0.0137	
C-VF-Al_2O_3mp	0.78	1	0.78	377.63	< 0.0001	
AB	0.03	1	0.03	13.87	0.0039	
AC	0.01	1	0.01	5.42	0.0422	
BC	0.02	1	0.02	11.66	0.0066	
A^2	0.18	1	0.18	87.37	< 0.0001	
B^2	0.03	1	0.03	15.11	0.0030	
C^2	0.10	1	0.10	46.91	< 0.0001	
Residual	0.02	10	0.00			
Lack-of-Fit	0.01	5	0.00	2.50	0.1688	not significant
Pure Error	0.01	5	0.00			
Cor Total	4.33	19				
SD	0.046	R^2		0.9952		
Mean	11.33	Adjusted R^2		0.9909		
C.V. %	0.40	Predicted R^2		0.9657		
		Adeq Precision		54.75		

The composite joints incorporated with higher VF- Al_2O_3mp exhibits higher tensile strength, %elongation and micro-hardness. Uniform plastic flow and symmetric microstructure were noticed at higher rotational speed of 1100 rpm [122]. The heat input and rotational speed are directly related [123]. High heat input at higher rotational speed produces the sufficient strain resulting in proper material flow [124]. Whereas, the increase in traverse speed gives the adverse consequence on mechanical properties of composite joints.

Table 5.6-5.9 demonstrated that the fisher's F value for tensile strength, % elongation, micro-hardness at the stir zone and wear weight loss at the stir zone are 456.32, 99.83, 336.82, and 230.64 respectively and indicated that their models are significant. The P value in mathematical model for RS (A), TS (B) and VF-Al_2O_3mp (C) for FSPed composite joints is less than 0.05 indicating that they are significant. Lack of fit is found not significant in the ANOVA Tables 5.6-5.9, as the P-value is higher than 0.1. The R^2 value demonstrates how well the models are fit.

Predicted R^2 values for all response parameters are relatively close to adjusted R^2 values. The maximum number of points that can fall within the regression line depends on how closely projected R^2 and modified R^2 values coincide. The main distinction between predicted and adjusted R^2 is that predicted R^2 makes the assumption that each individual variable can account for all of the variation in dependent variable. Only the independent variables that have an actual impact on the dependent variable are revealed by the adjusted R^2. The R^2 value for the tensile strength is 0.99 reveals 99% of the complete variability which is evaluated by the model after taking into account the essential factors. The difference between value of R^2 (99.72%) and adjusted R^2 (99.14 %) is 0.62%, indicating that the model does not explain 0.62 % of the total variation and the model is not over fitted.

5.3.1 Processing parameters effect on the response parameters

The predicted values vs actual experimental values for response parameters including tensile strength, microhardness, %elongation and wear behavior of FSPed composite joint incorporated with Al_2O_3mp is depicted in Fig. 5.10. The scattered plots show that the response variables are lying very close to the straight lines indicating the uniform scattering of error throughout the model. The plot of the response values' experimental

and anticipated values demonstrates remarkable correlation. The aforementioned correlation reveals that the regression models are adequate.

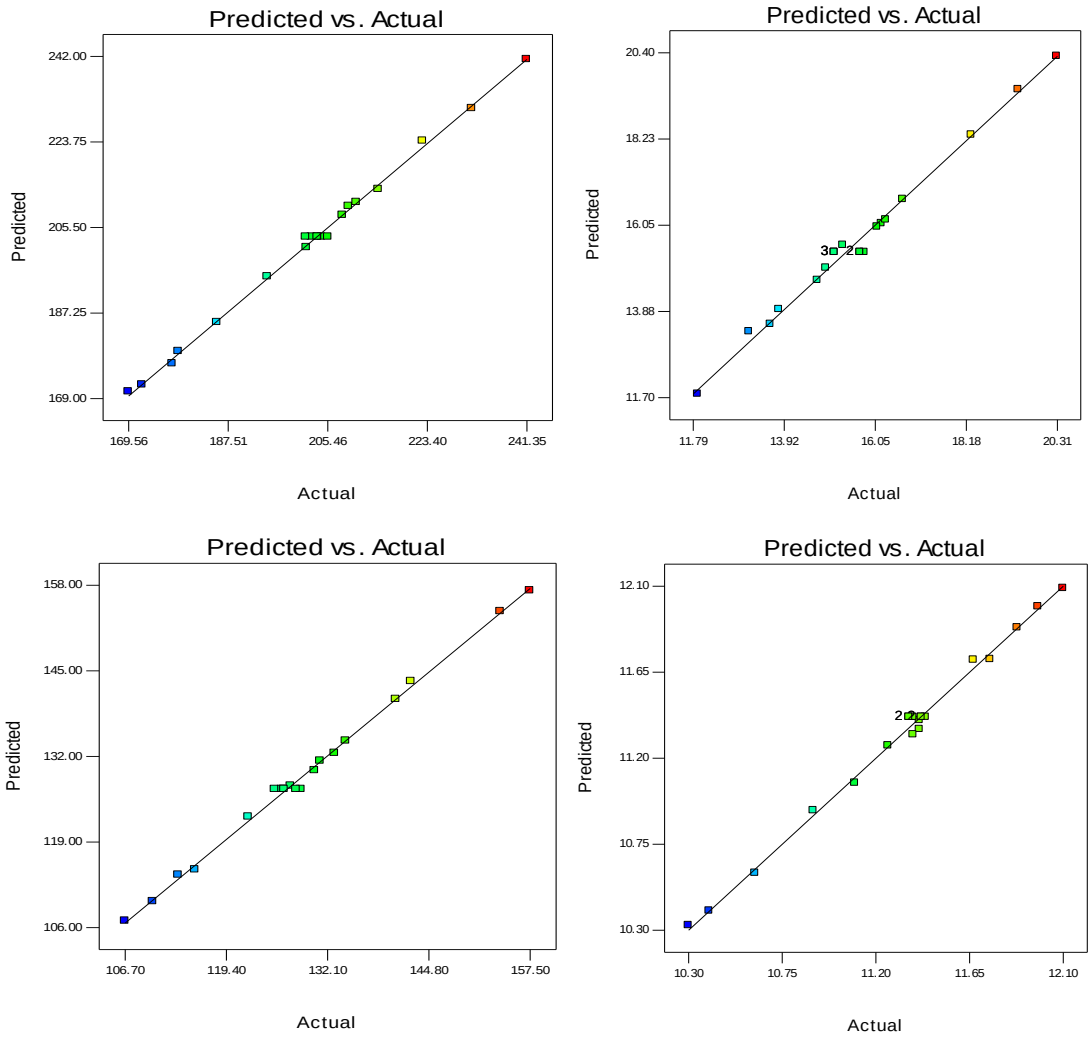

Figure 5.10: Plots between Predicted vs actual values, (a) Tensile strength, (b) %elongation, (c) Micro-hardness, (d) Wear behavior.

The 3D responses surfaces and contour plots of the regression model for tensile strength, micro-hardness, %elongation and weight loss at stir zone are shown in Figs. 5.11-5.14. The apex of the response surfaces represents the optimum output responses. By analyzing the 3D responses surfaces and contour plots, it is easy to examine the impact of different factors on the responses. The significance of grain refinement can be revealed by dynamic recrystallisation and pinning effect caused by Al_2O_3mp. It was observed that as the rotational speed increases, tensile strength, microhardness and %elongation increases, whereas wear weight loss decreases due to more uniform dispersion of speed Al_2O_3mp resulting in enhanced pinning effect and reduced the grain size.

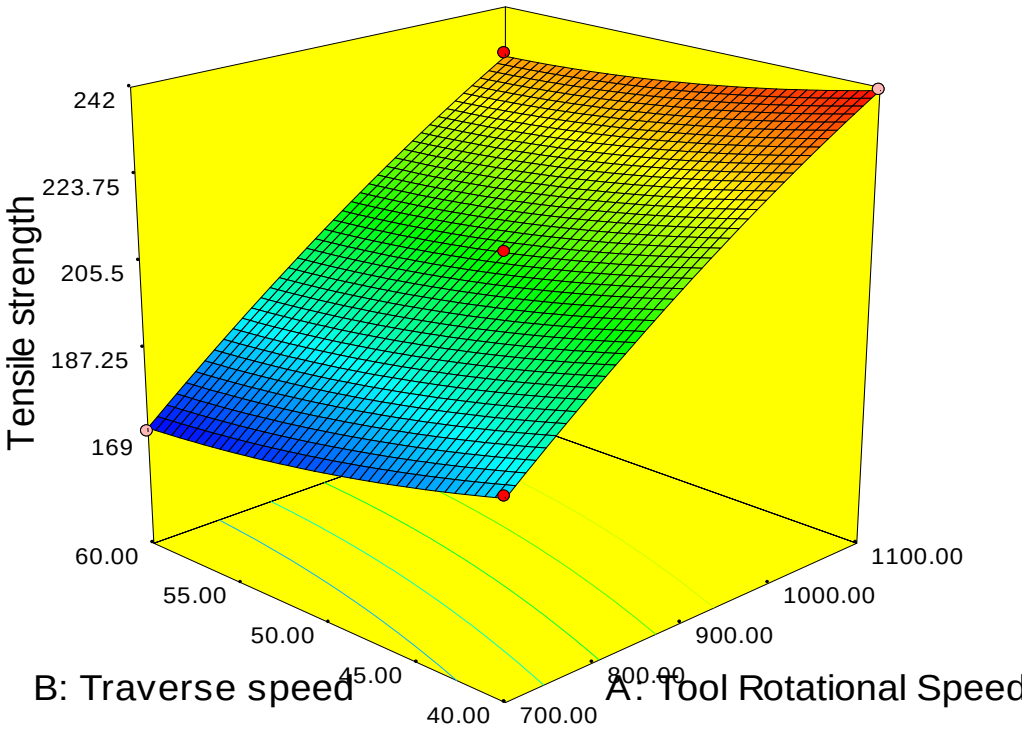
Tensile strength
242
223.75
205.5
187.25
169
60.00
55.00
50.00
45.00
40.00
B: Traverse speed
700.00
800.00
900.00
1000.00
1100.00
A: Tool Rotational Speed

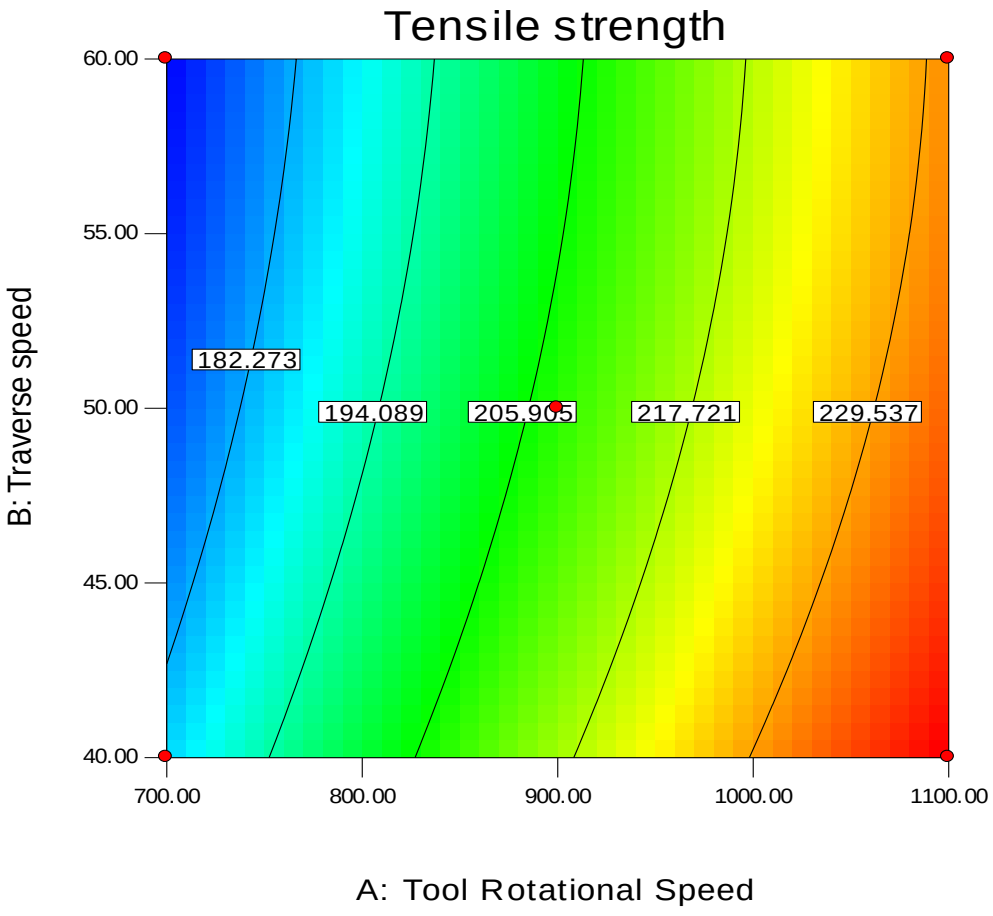
Tensile strength
60.00
55.00
50.00
45.00
40.00
B: Traverse speed
182.273
194.089
205.905
217.721
229.537
700.00
800.00
900.00
1000.00
1100.00
A: Tool Rotational Speed

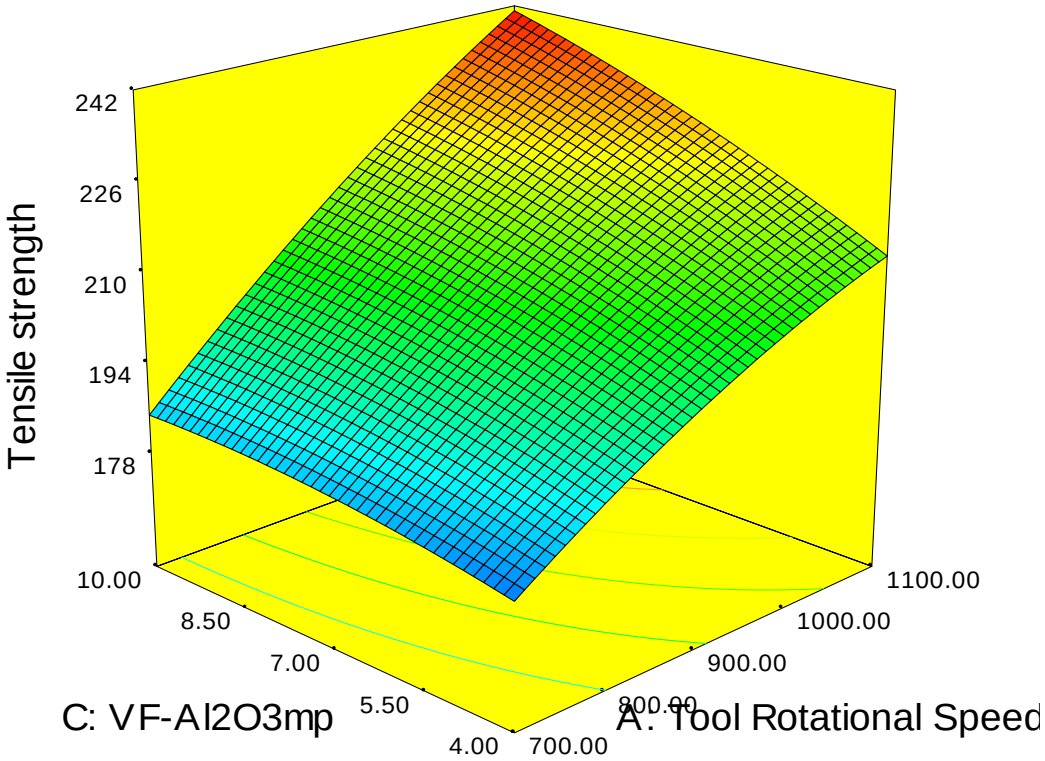
Tensile strength
242
226
210
194
178
10.00
8.50
7.00
5.50
4.00
C: VF-Al2O3mp
700.00
800.00
900.00
1000.00
1100.00
A: Tool Rotational Speed

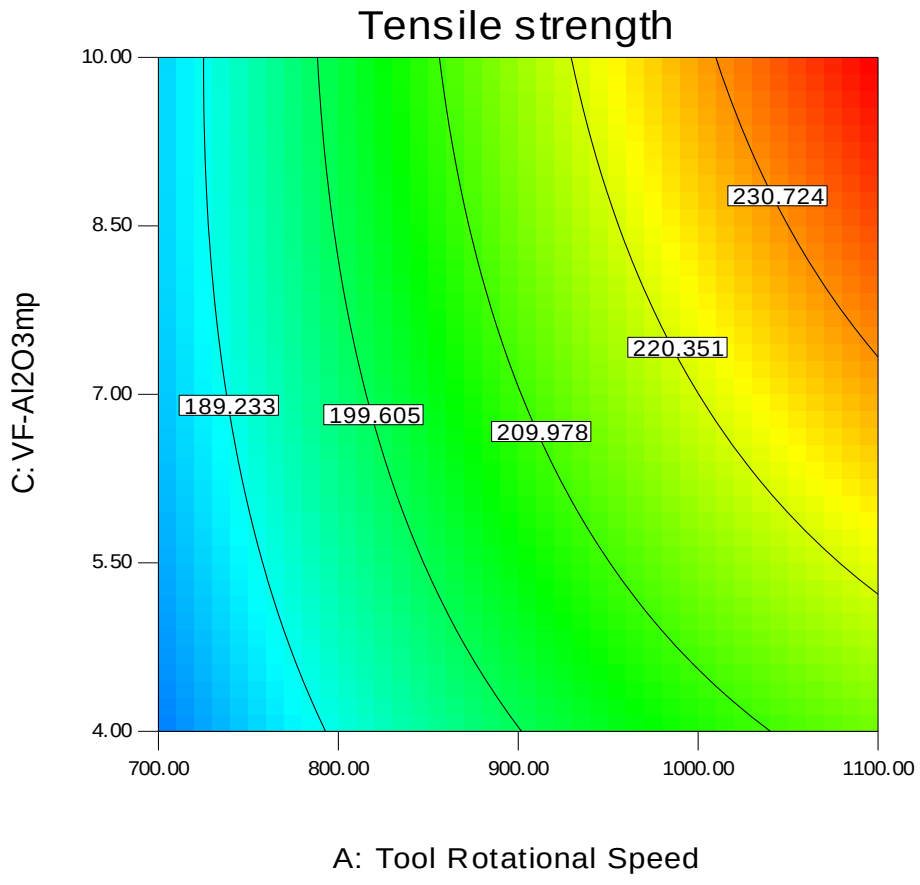
Tensile strength
10.00
8.50
7.00
5.50
4.00
C: VF-Al2O3mp
189.233
199.605
209.978
220.351
230.724
700.00
800.00
900.00
1000.00
1100.00
A: Tool Rotational Speed

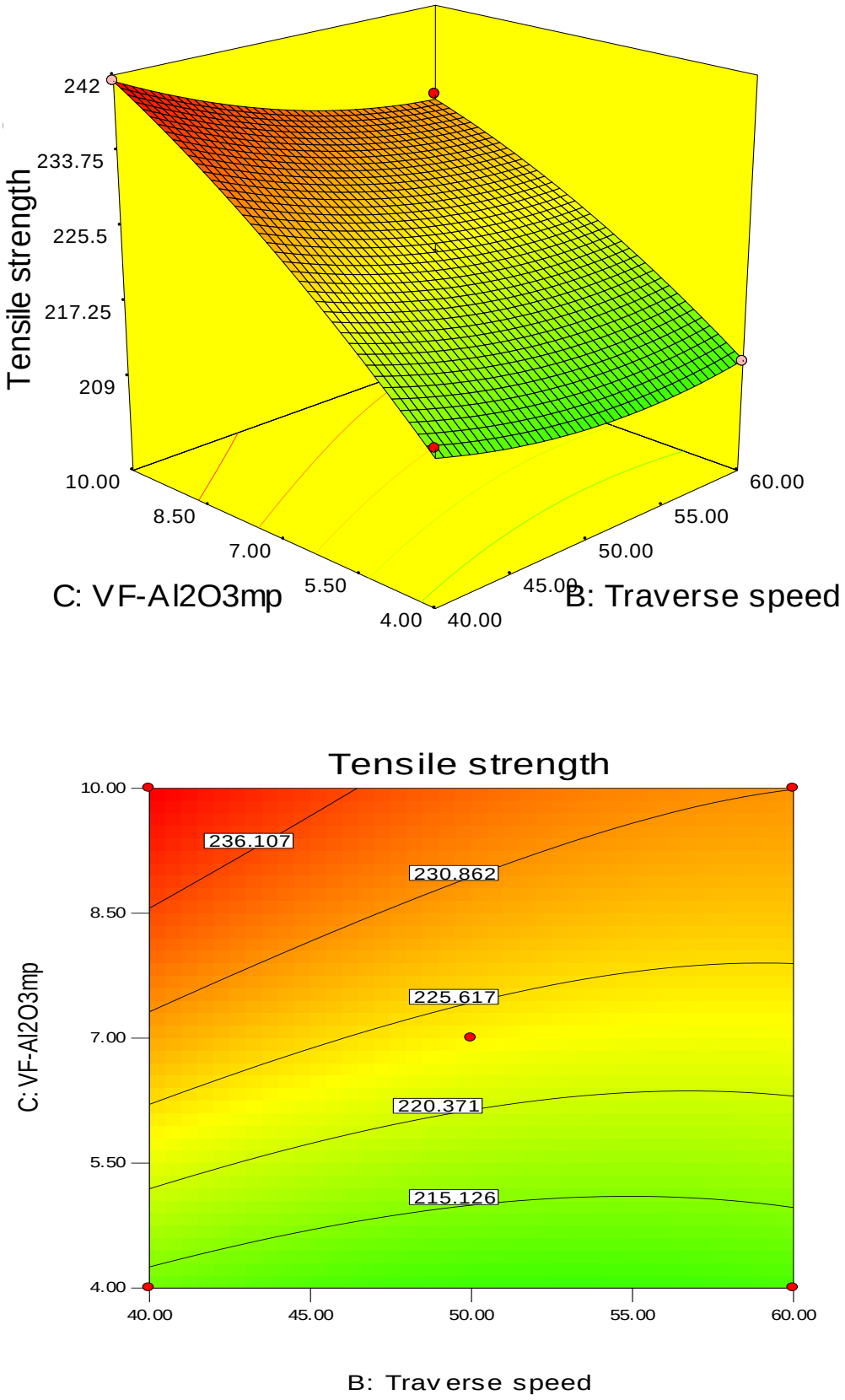

Figure 5.11: 3D response contour and surface plot of Tensile strength of FSPed composite joint incorporated with Al_2O_3mp

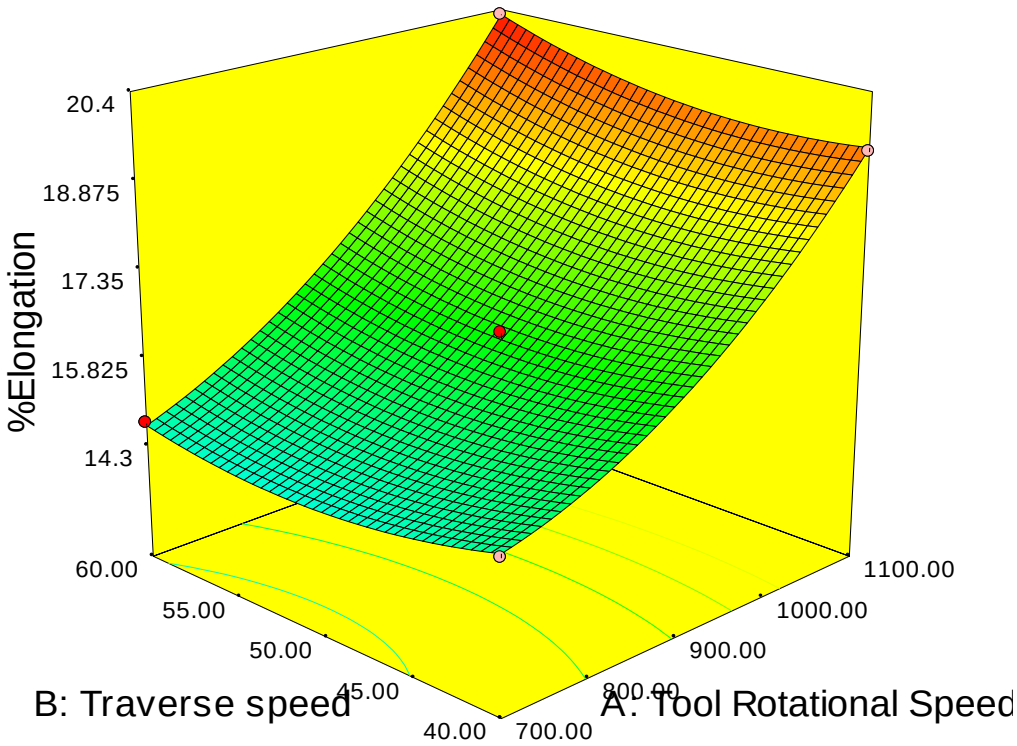
20.4
18.875
17.35
15.825
14.3
%Elongation
60.00
55.00
50.00
45.00
40.00
B: Traverse speed
700.00
800.00
900.00
1000.00
1100.00
A: Tool Rotational Speed

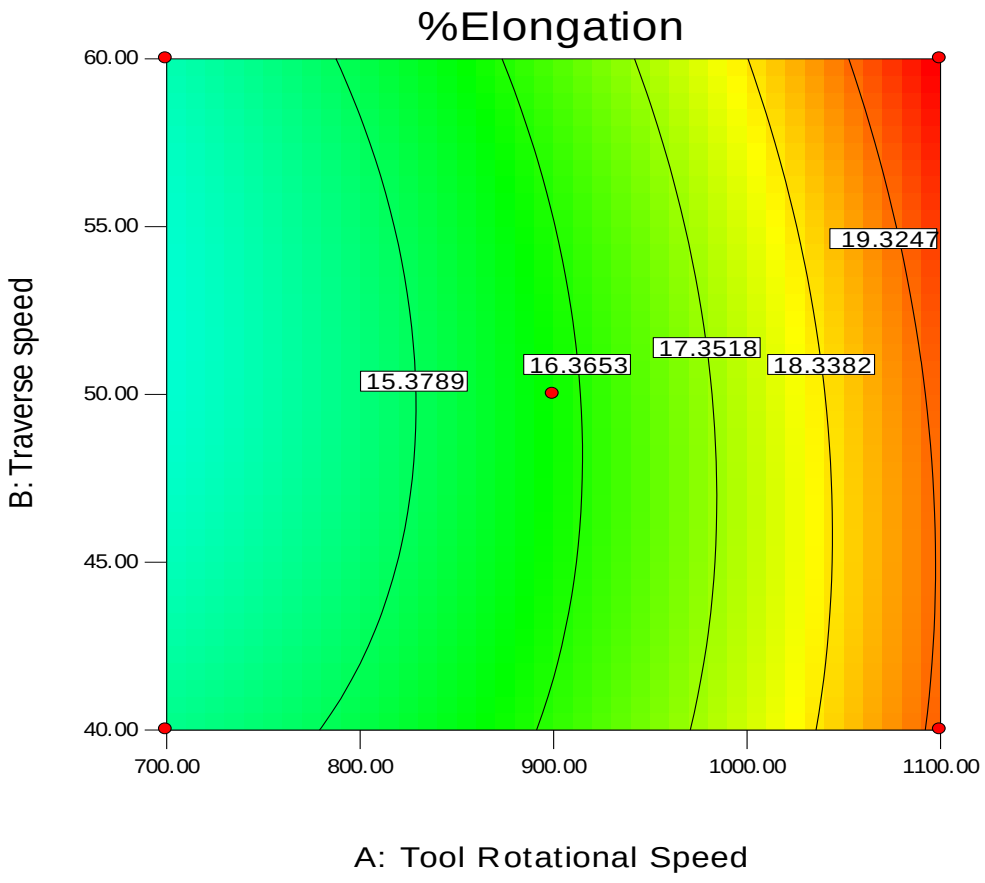
%Elongation
60.00
55.00
50.00
45.00
40.00
B: Traverse speed
15.3789
16.3653
17.3518
18.3382
19.3247
700.00
800.00
900.00
1000.00
1100.00
A: Tool Rotational Speed

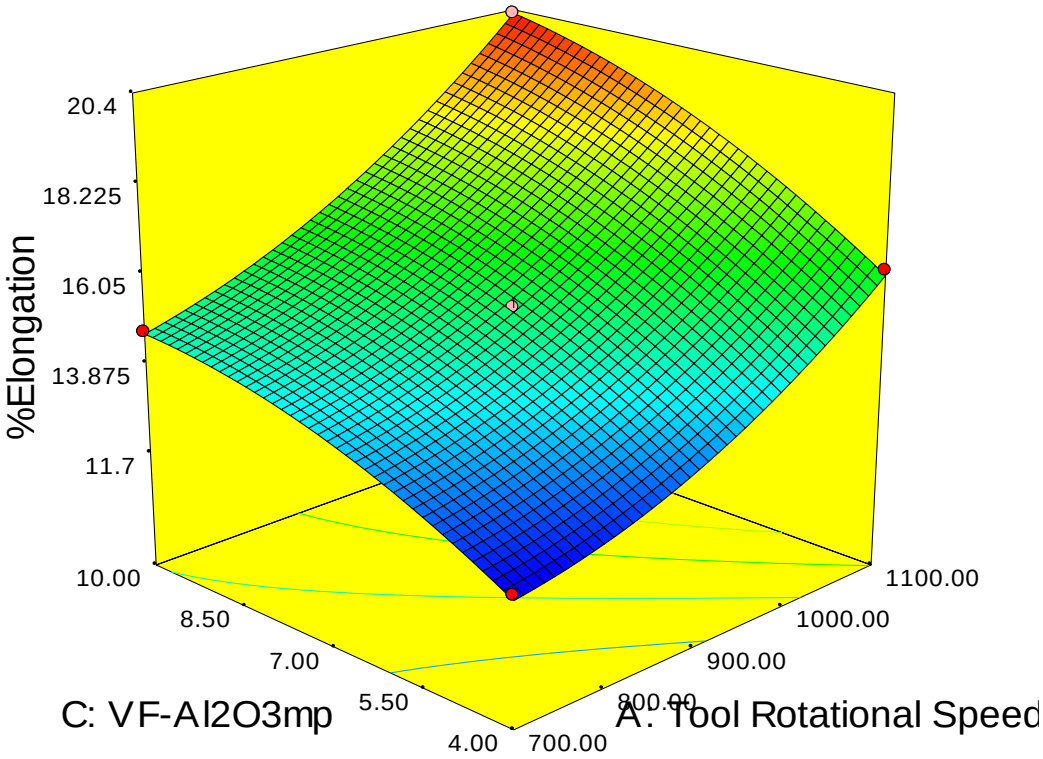
%Elongation
20.4
18.225
16.05
13.875
11.7
10.00
8.50
7.00
5.50
4.00
C: VF-Al2O3mp
700.00
800.00
900.00
1000.00
1100.00
A: Tool Rotational Speed

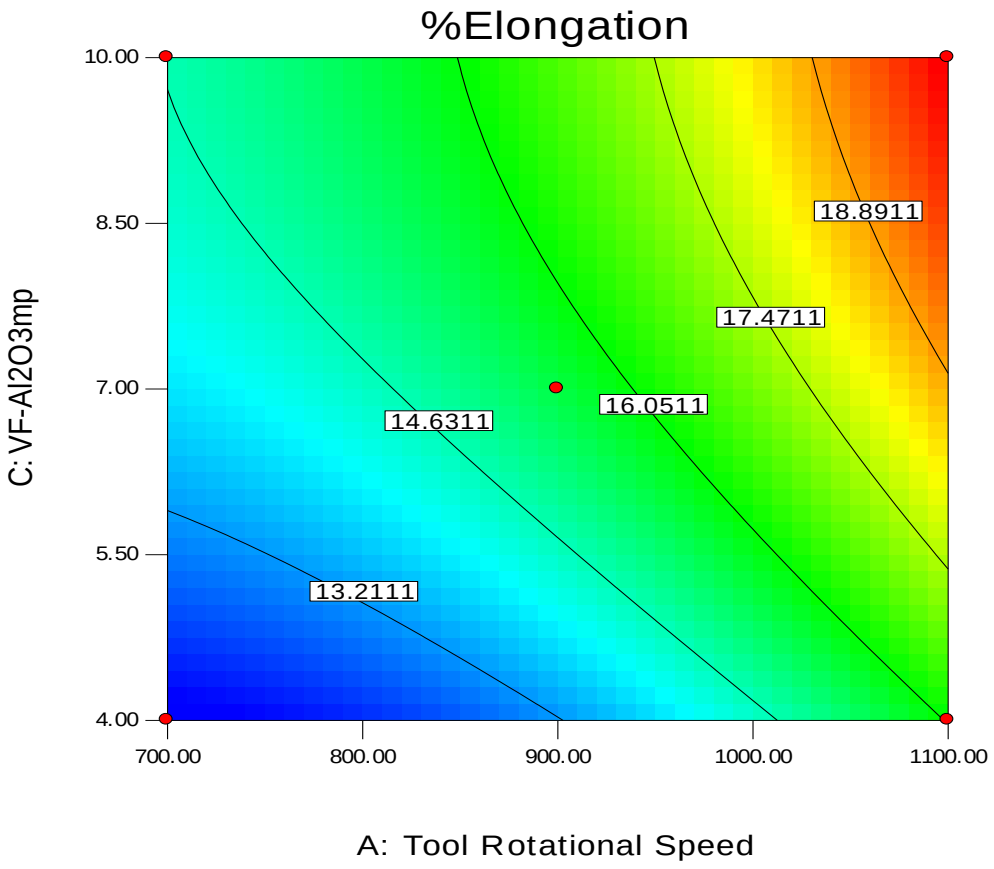
%Elongation
10.00
8.50
7.00
5.50
4.00
C: VF-Al2O3mp
18.8911
17.4711
16.0511
14.6311
13.2111
700.00
800.00
900.00
1000.00
1100.00
A: Tool Rotational Speed

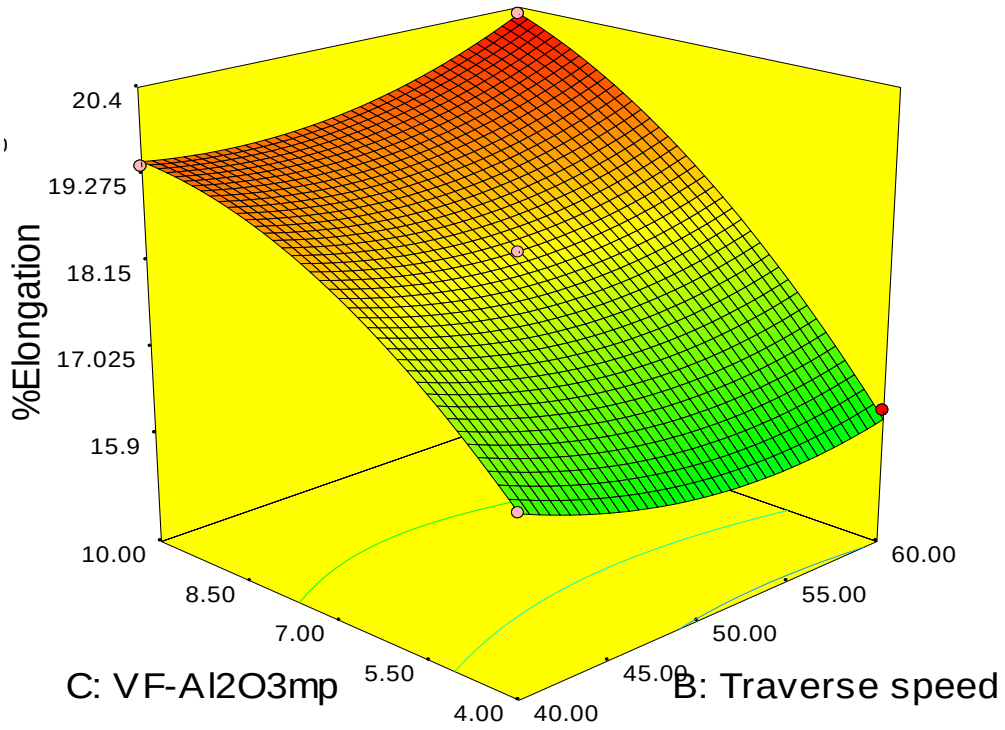

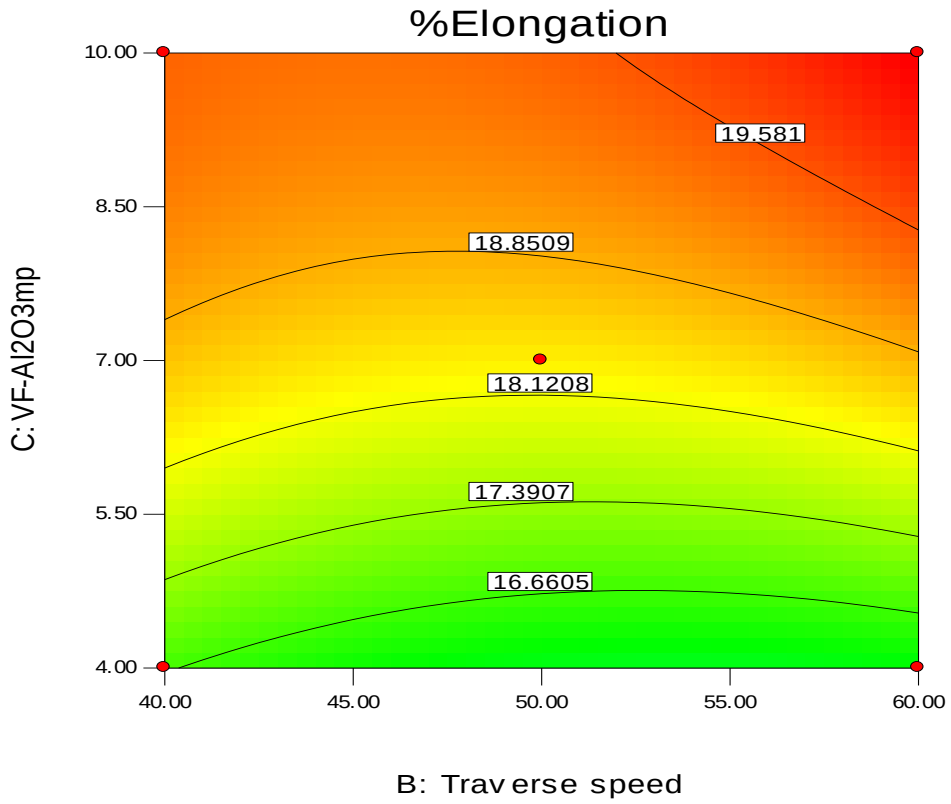

Figure 5.12: 3D response contour and surface plot of %elongation of FSP composite joint incorporated with Al_2O_3mp

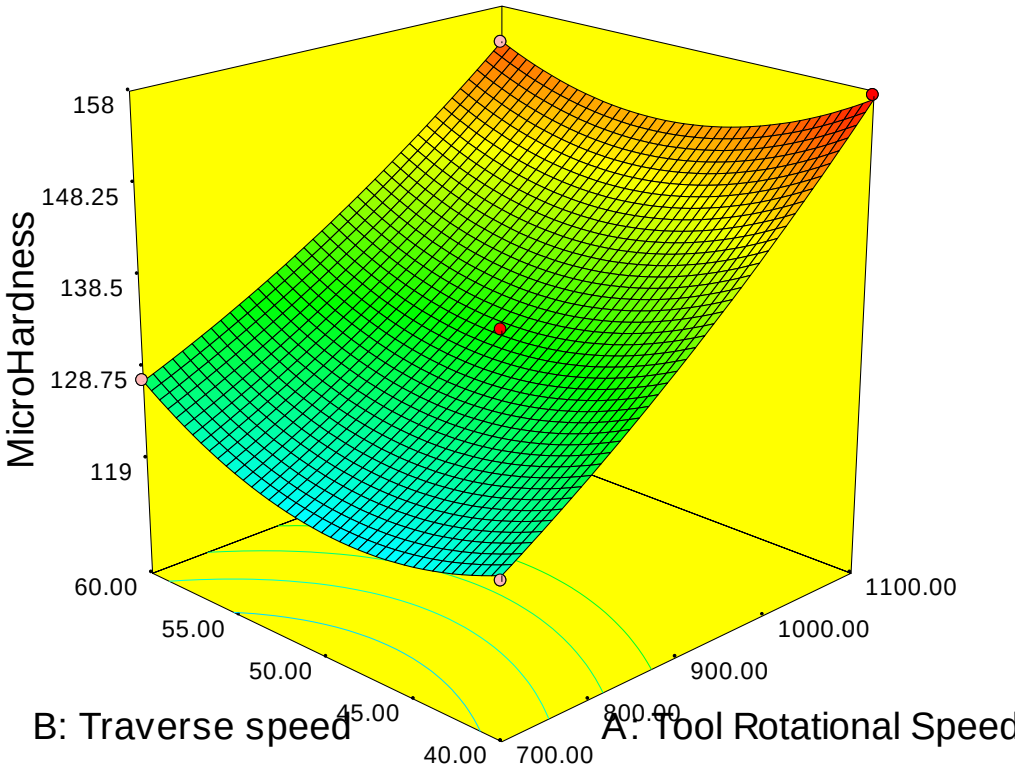
MicroHardness
158
148.25
138.5
128.75
119
60.00
55.00
50.00
45.00
40.00
B: Traverse speed
700.00
800.00
900.00
1000.00
1100.00
A: Tool Rotational Speed

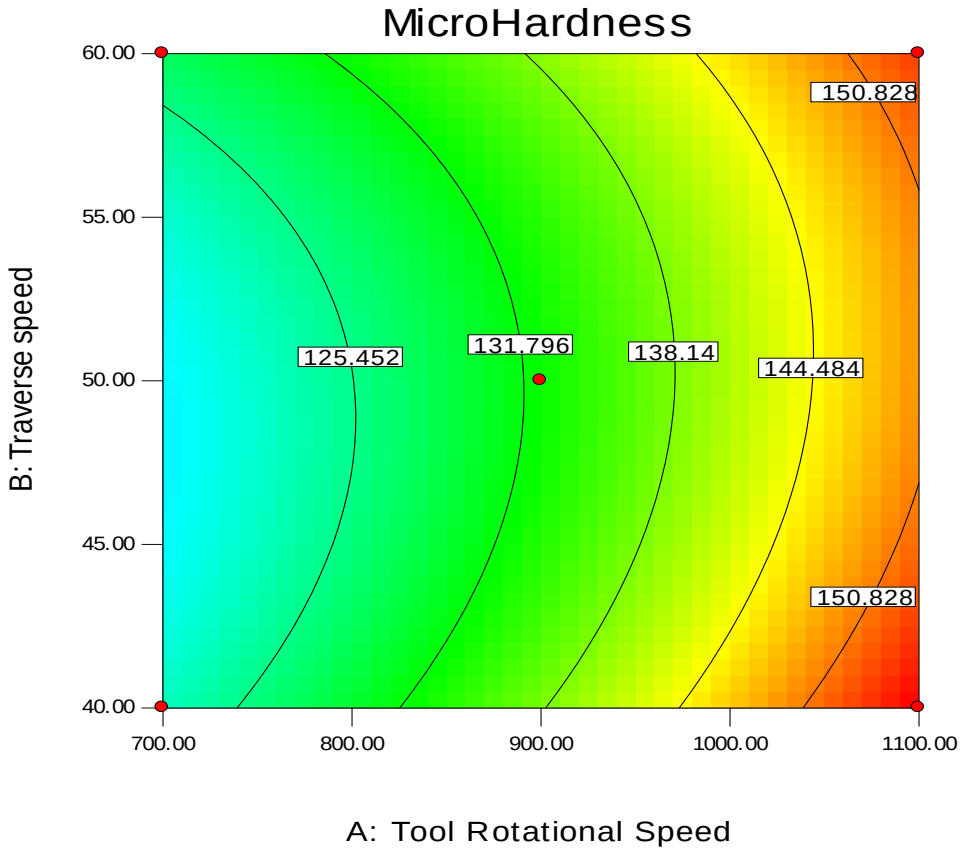
MicroHardness
60.00
55.00
50.00
45.00
40.00
B: Traverse speed
125.452
131.796
138.14
144.484
150.828
150.828
700.00
800.00
900.00
1000.00
1100.00
A: Tool Rotational Speed

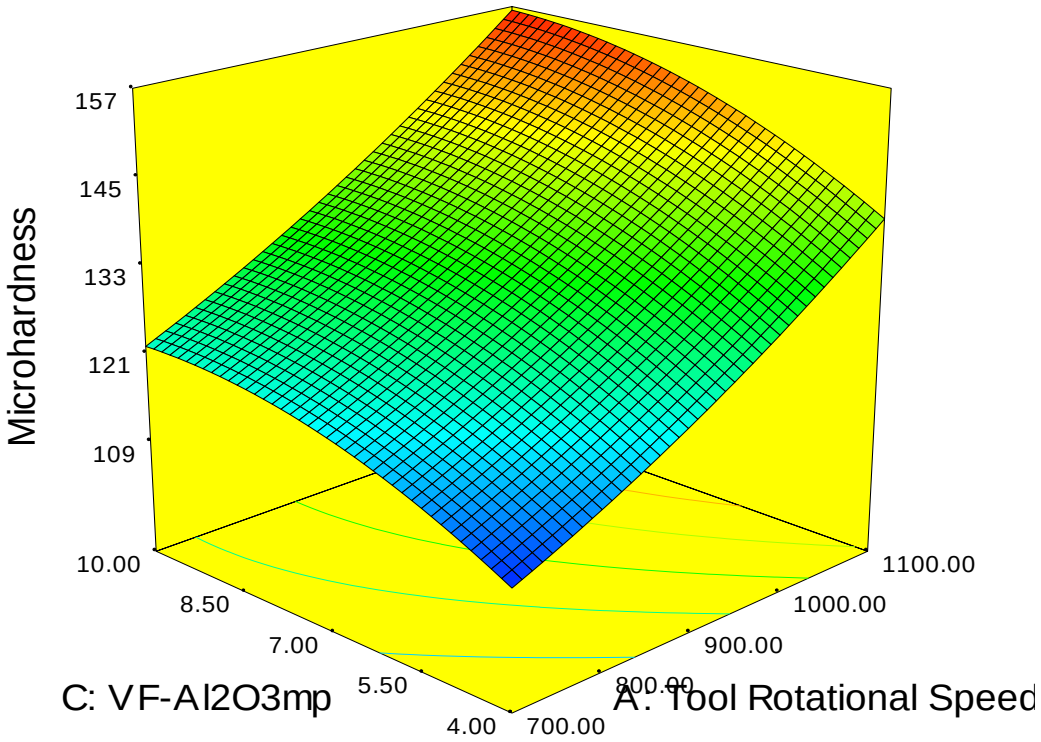
Microhardness
157
145
133
121
109
10.00
8.50
7.00
5.50
4.00
C: VF-Al2O3mp
700.00
800.00
900.00
1000.00
1100.00
A: Tool Rotational Speed

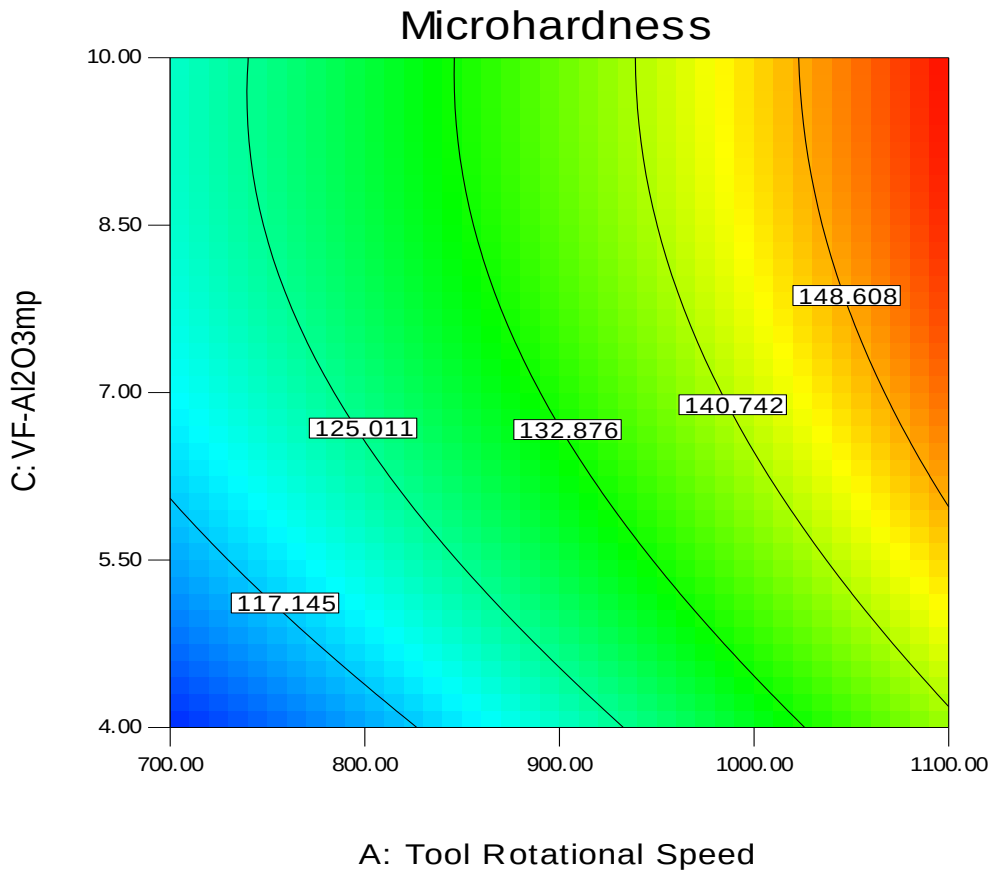
Microhardness
10.00
8.50
7.00
5.50
4.00
C: VF-Al2O3mp
148.608
140.742
132.876
125.011
117.145
700.00
800.00
900.00
1000.00
1100.00
A: Tool Rotational Speed

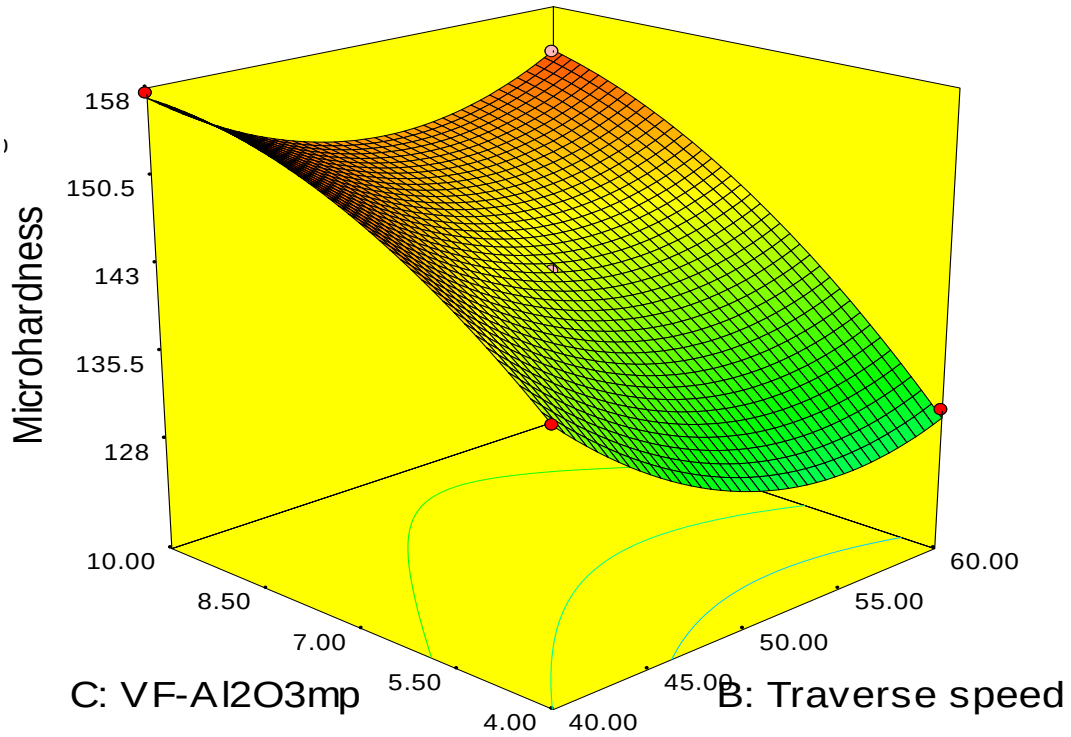

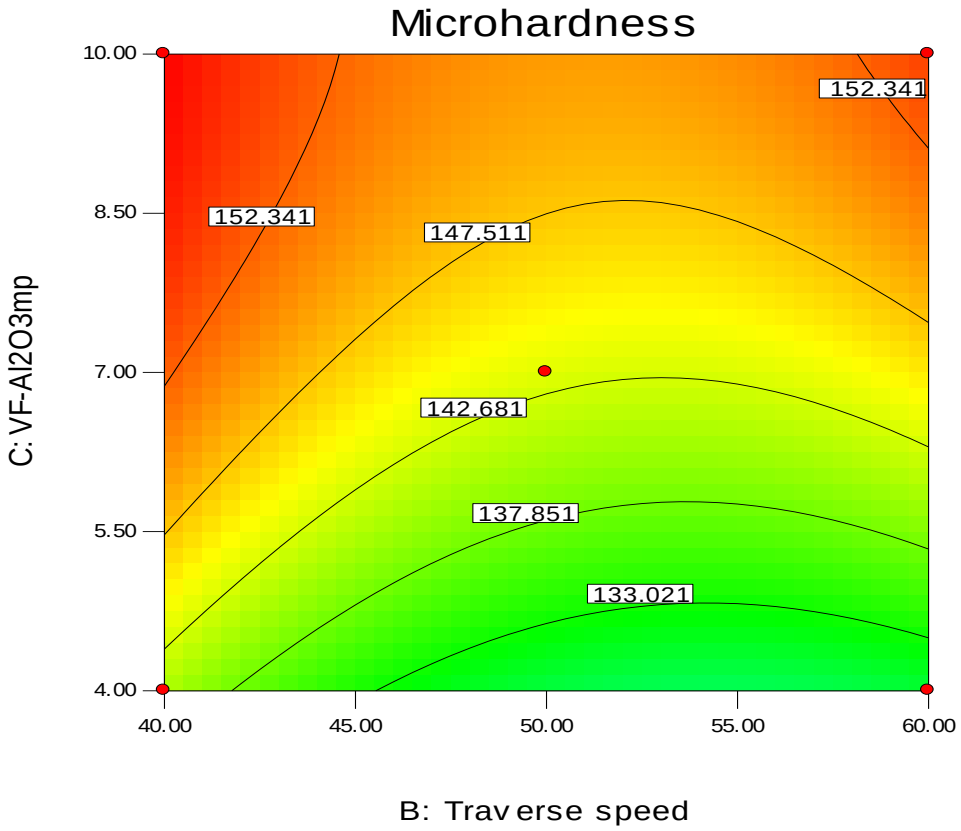

Figure 5.13: 3D response contour and surface plot of micro-hardness at SZ of FSP composite joints incorporated with Al_2O_3mp

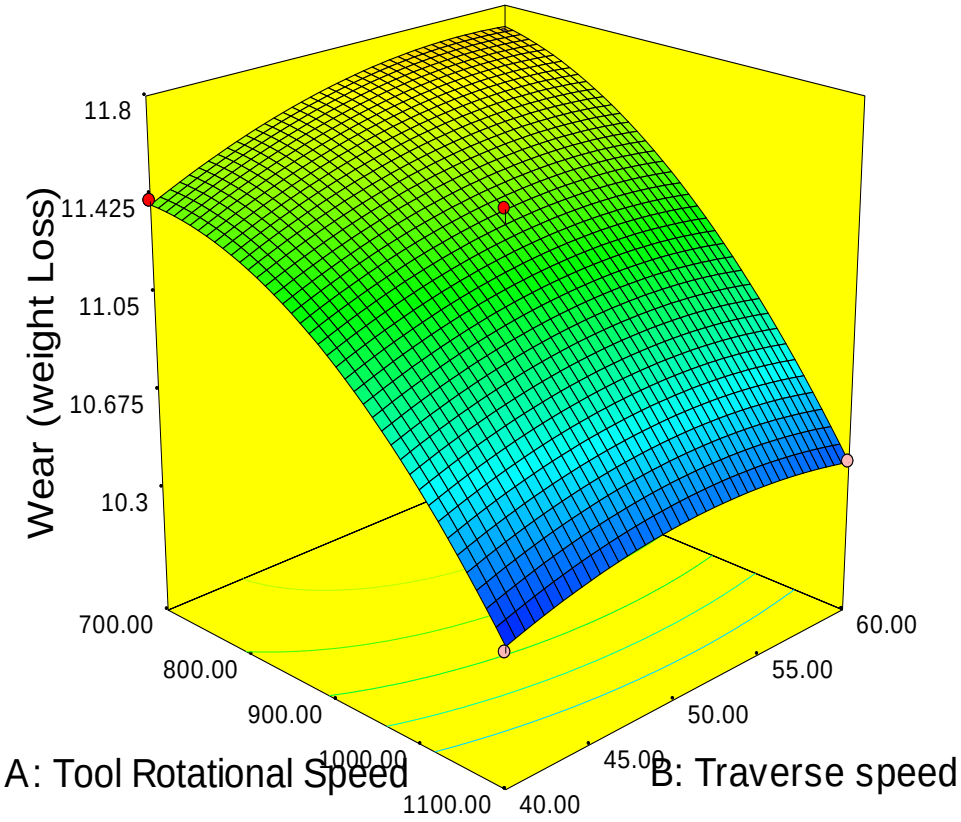
Wear (weight Loss)
11.8
11.425
11.05
10.675
10.3
700.00
800.00
900.00
1000.00
1100.00
A: Tool Rotational Speed
40.00
45.00
50.00
55.00
60.00
B: Traverse speed

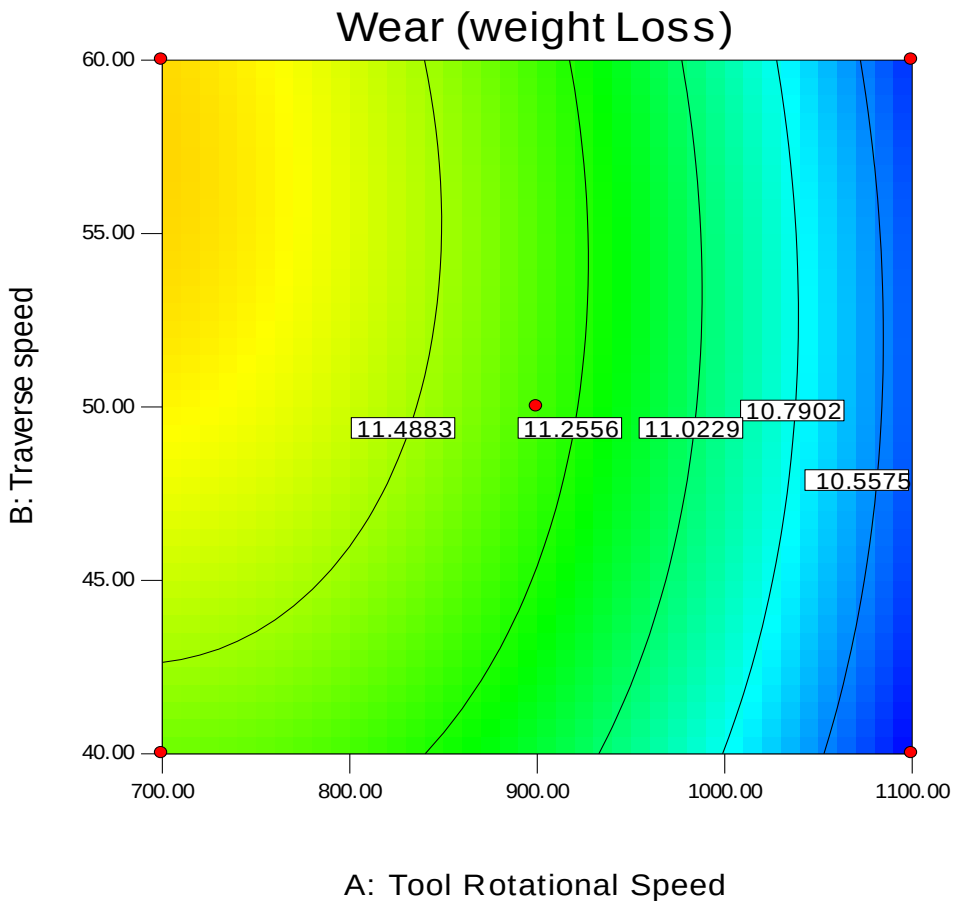
Wear (weight Loss)
60.00
55.00
50.00
45.00
40.00
B: Traverse speed
11.4883
11.2556
11.0229
10.7902
10.5575
700.00
800.00
900.00
1000.00
1100.00
A: Tool Rotational Speed

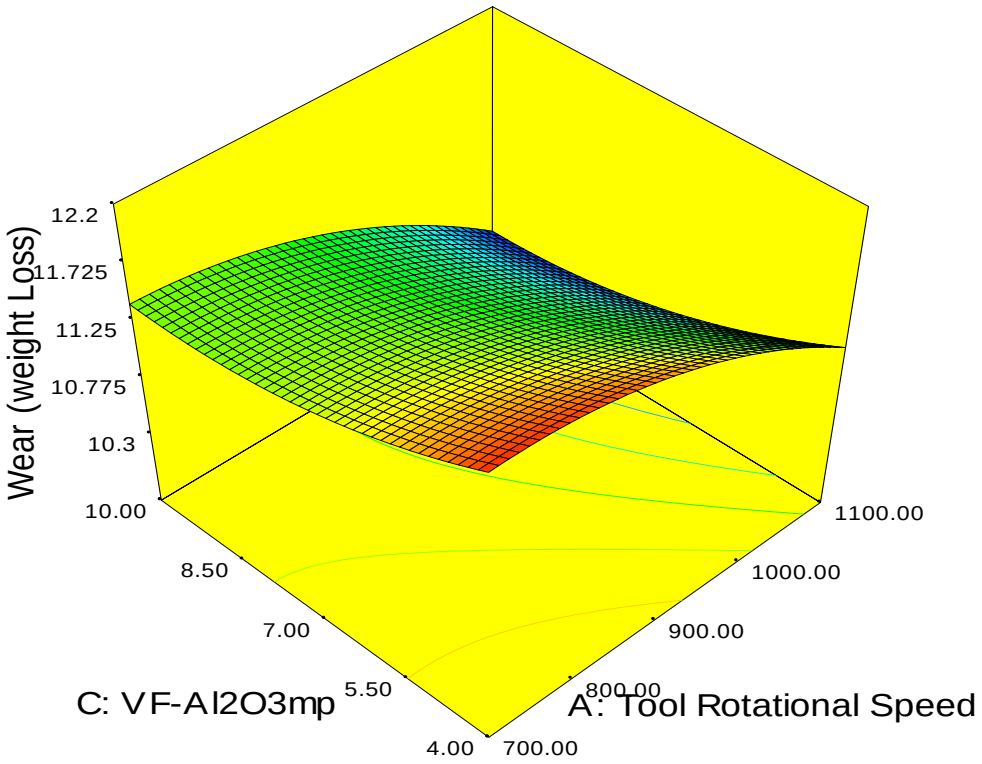
Wear (weight Loss)
12.2
11.725
11.25
10.775
10.3
10.00
C: VF-Al2O3mp
8.50
7.00
5.50
4.00
A: Tool Rotational Speed
700.00
800.00
900.00
1000.00
1100.00

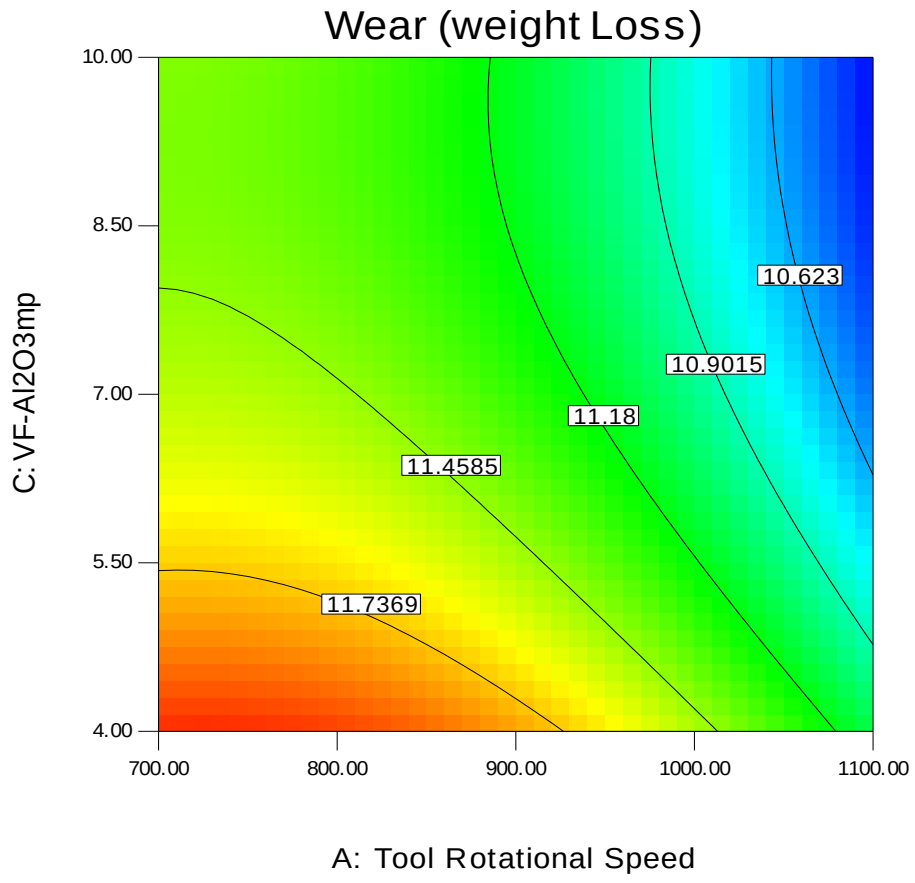
Wear (weight Loss)
10.00
8.50
7.00
5.50
4.00
C: VF-Al2O3mp
10.623
10.9015
11.18
11.4585
11.7369
700.00
800.00
900.00
1000.00
1100.00
A: Tool Rotational Speed

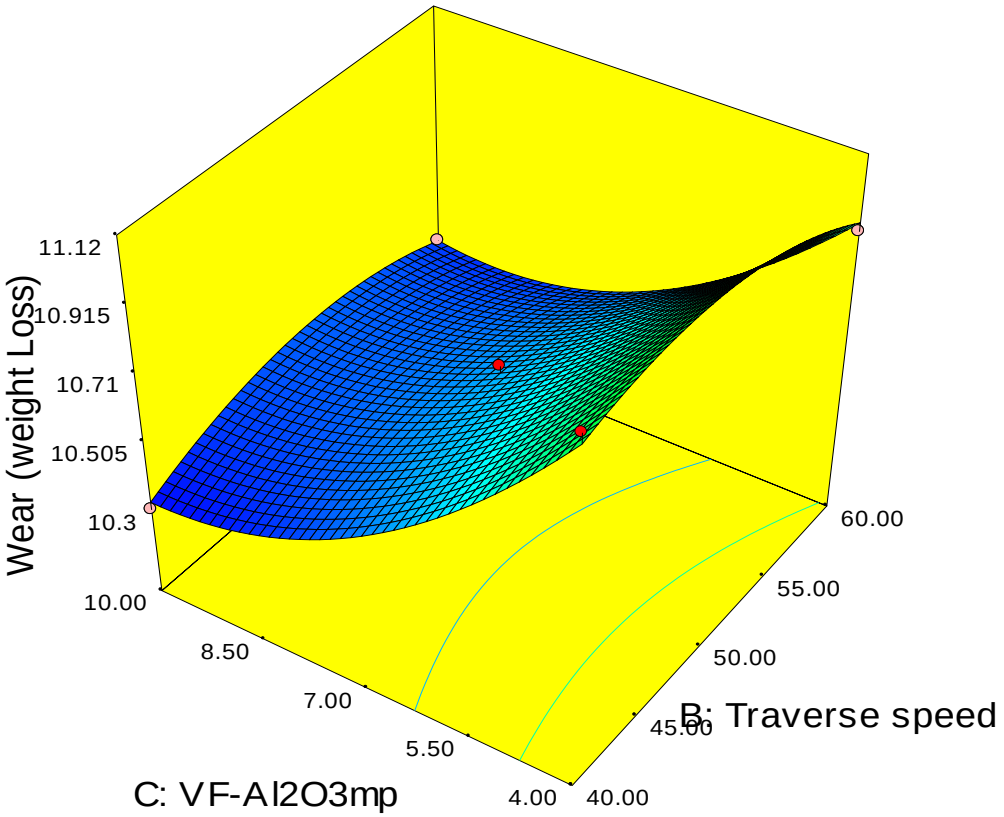

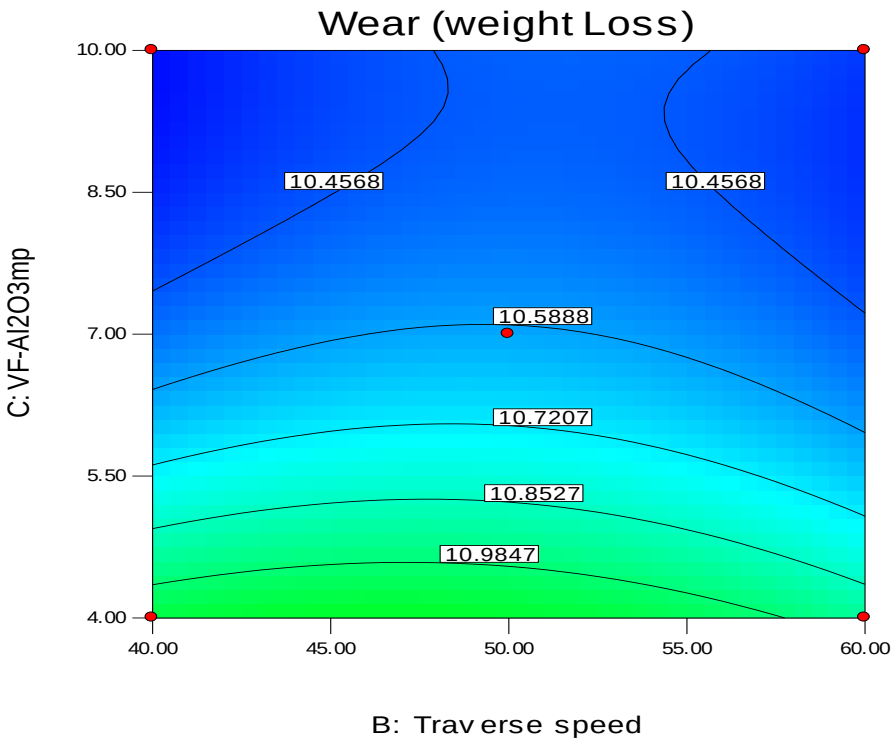

Figure 5.14: 3D response contour and surface plot of wear behavior at the SZ of FSPed composite joints incorporated with Al_2O_3mp

It was also observed that decreasing value of traverse speed, increase the tensile strength of composite joints. The minimum value of tensile strength (169.5 MPa) was observed at lower RS (700 rpm), higher TS (60 mm/min) with 10% VF-Al_2O_3mp, whereas as minimum microhardness of 106.7 HV and maximum wear weight loss of 12.10 mg, was found at lower RS (700 rpm), higher TS (60 mm/min) with 4% VF-Al_2O_3mp due to inadequate material mixing resulting in agglomeration of Al_2O_3mp in the SZ. The maximum value of tensile strength (241.35 MPa), microhardness (157.5 HV) and minimum value of weight loss (10.3 mg) was observed at 1100 rpm, 40 mm/min and 10 % volume fraction of Al_2O_3mp. On increasing the traverses speed, the tensile strength and microhardness decreases, whereas, wear weight loss increases. The higher volume fraction of Al_2O_3mp also enhanced the tensile strength, hardness of composite joints and reduced the wear weight loss as shown in Fig. 5.11-5.14.

5.4 MULTI RESPONSE OPTIMIZATION: DESIRABILITY

Desirability is a multiple response technique that was explained by Derringer and Suich [97]. This method is used for the optimization of various quality characteristic problems which is relevant to industry. The method uses an objective function, D(X), referred to as the desirability function (utility transfer function), to transform a predicted response into a scale-free value (di) which is denoted as desirability. The geometric mean of weightage of each response's individual desirability is known as the composite desirability. The ideal parameter circumstances are regarded to be the factor settings that have the highest overall desirability. The optimization is carried through using:

(i) Determining each response's specific desirability (d);

(ii) Obtained the composite desirability (D) by combining each response's specific desirability;

(iii) Finding the optimal settings by maximizing the obtained composite desirability.

In the present investigation, desirability function is employed to obtained the optimal parameters for FSPed composite joints to optimize tensile strength, % elongation, microhardness and wear behavior. In order to identify the best combination of variables and their levels for friction stir processing of AA6061 and AA7075, a second order CCD with three variables (rotational speed, traverse speed, and volume % of Al_2O_3mp)

with three levels was utilized. The desirability function was used to achieve the multi-response optimization.

5.4.1 Multi-response optimization

Multi-response optimization was performed utilizing the desirability function via RSM in order to resolve the problems associated with single-response optimization of contradicting responses. To effectively assess the effect of each response on overall desirability, limits and goals for each response were specified. Weights are applied in order to highlight a goal value, the upper or lower boundaries, or both. According to the particular industry, importance is allocated. Importance varies 1 to 3, 1 is allocated for the least important and 3 to the most important.

The goals and importance of processing parameters such as rotational speed, traverse speed and VF-Al_2O_3mp, and the response parameters like tensile strength, micro-hardness, % elongation and wear behaviour are tabulated in Table 5.10. Tensile strength, micro-hardness, %elongation, and wear behavior all have been assigned with an importance of 3, lower and upper weight for UTS, %elongation, micro-hardness and wear behaviour is to be assigned 1. Finding an optimal setting of parameters that will meet all the goals is the major objective of optimization process.

Table 5.10: Range and importance of Input and Response Parameters for Desirability

Name	Goal	Lower-Limit	Upper-Limit	Lower-Weight	Upper-Weight	Importance
Tool Rotational Speed	in range	700	1100	1	1	3
Traverse speed	in range	40	60	1	1	3
VF-Al_2O_3mp	in range	4	10	1	1	3
Tensile strength	in range	169.56	241.35	1	1	3
%Elongation	in range	11.9	20.3	1	1	3
Micro-hardness	in range	106.7	157.5	1	1	3
Wear behaviour (weight Loss)	in range	10.3	12.1	1	1	3

The value of desirability does not mandatory to be 1 as if the any one response is increases then the other decreases. In other words, the value depends solely on how nearly the lower and upper limits are selected in relation to the actual optimum. For the given design space constraints, seven optimal solutions are derived as tabulated in Table 5.11. The set of optimal parameters having higher desirability required for get the desired response parameters within the constraints is tabulated in Table 5.11.

The ramp function graph (Fig. 5.15) derived from Design Expert (7) software, demonstrates the desirability for tensile strength, %elongation, microhardness and wear. Each ramp's dot indicates the response characteristic's factor setting or response prediction. The height of the dot indicates how desired it is. Since the weight for each parameter was set to 1, a linear ramp function was established between the low value and the goal or the high value and the goal. The range of desirability, ranging 0 to 1, depends on how closely the response comes to achieving the target.

Table 5.11: Set of Optimal Solutions

Number	Tool Rotational Speed	Traverse speed	VF-Al_2O_3mp	Tensile strength	% Elongation	Micro-hardness	Wear (weight Loss)	Desirability	
1	**1096.76**	**55.59**	**8.64**	**227.80**	**19.31**	**147.97**	**10.474**	**1**	**Selected**
2	1080.44	44.63	5.65	218.73	17.27	140.23	10.868	1	
3	1058.20	41.01	5.37	217.77	17.01	141.50	10.980	1	
4	1048.68	48.59	5.89	215.60	16.75	135.23	10.998	1	
5	834.84	53.42	7.97	195.16	15.07	125.66	11.518	1	
6	951.60	53.25	9.98	213.65	16.99	137.10	11.167	1	
7	770.32	42.64	4.80	187.31	13.79	114.63	11.869	1	

Desirability 3D-plots were first drawn keeping input parameters in range tensile strength, % elongation and micro-hardness at maximum whereas, wear at minimum. Employing this methodology, several objective functions may be optimized. The desirable value for the optimized input and responses parameters is 1. The multi-optimized value of response parameters such as tensile strength, %elongation, micro-

hardness at the SZ and wear behavior (weight loss) at the SZ are 227.80 MPa, 19.31, 147.97 HV and 10.474 mg respectively, whereas the optimum value of process parameters such as tool rotational speed, traverse speed and VF-Al_2O_3mp are 1096.76 rpm, 55.59 mm/min and 8.64 % respectively as depicted in Fig. 5.15. Fig. 5.16 shows the desirability plots of desired responses for composite joints of AA 6061 and AA7075, according to rotational speed, traverse speed and VF-Al_2O_3mp. It can be shown that overall desirability is increasing with increasing the rotational speed, desirability value is 1 for the high rotational speed level 3 (1100 RPM). As the traverse speed decreases, the desirability increases as shown in Fig. 5.16.

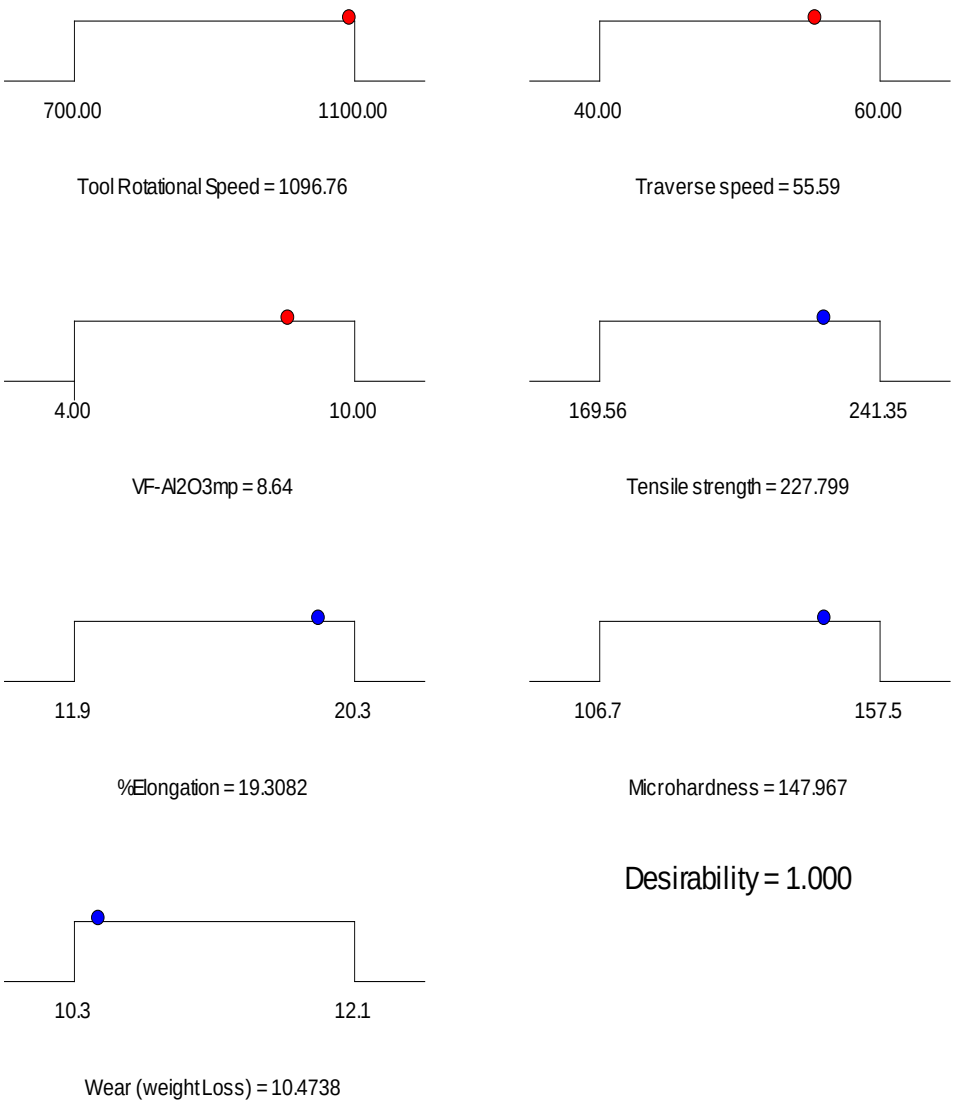

Figure 5.15: Ramp fraction plots of multi response optimization

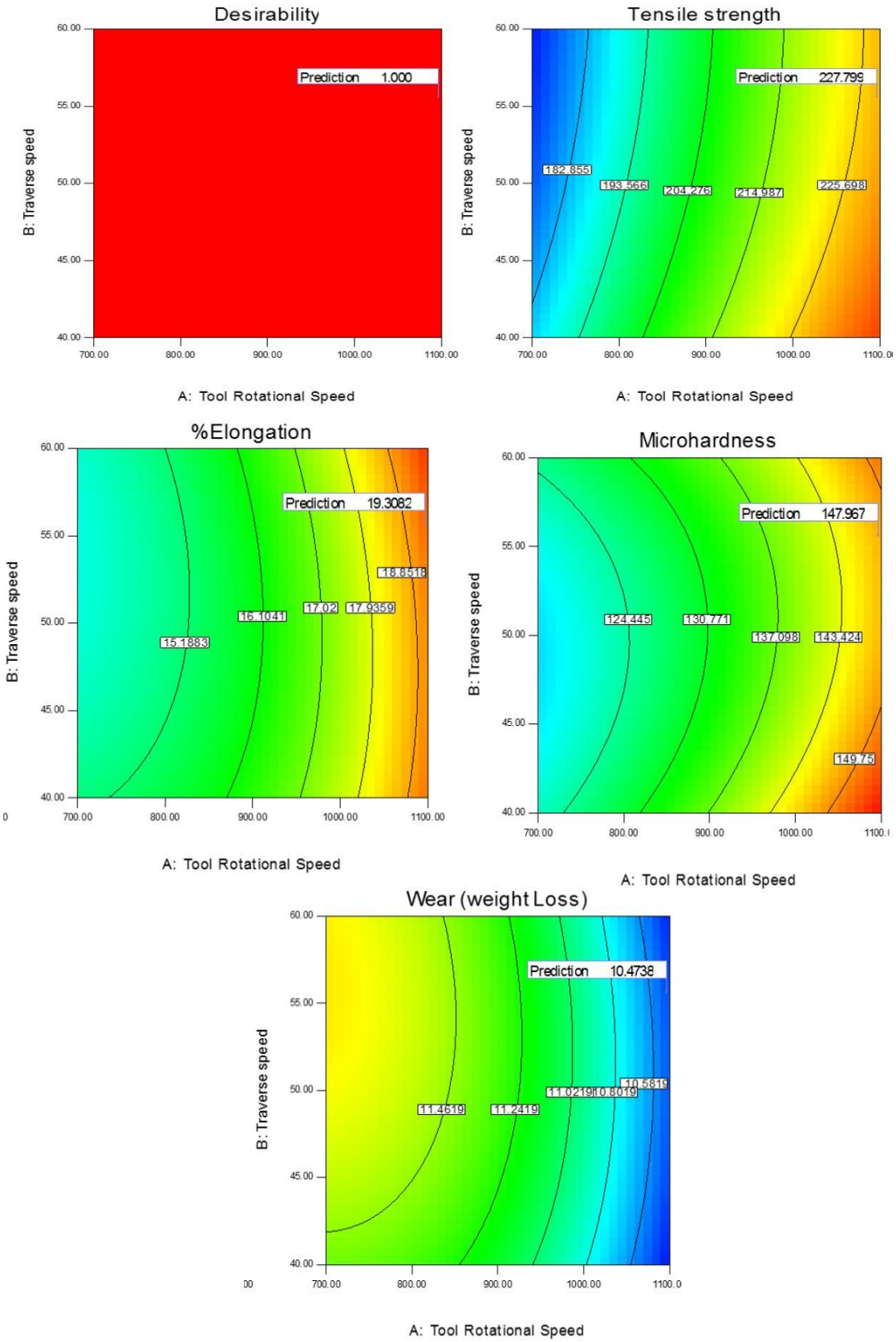

Figure 5.16: Optimized out responses of FSPed composite joints incorporated with Al_2O_3mp

5.4.2 Results of confirmation test

The confirmation experiment was performed to confirm the adequacy of the developed mathematical models for each response at optimal levels of the processing parameters. The average values of the characteristics were obtained and compared with the predicted values. The results of the test are presented in Table 5.12 which clearly shows that the developed models are adequate to predict the responses.

Table 5.12: Confirmation test

Performance Measures/ Response parameters	Optimal set of parameters	Predicted optimal value	Experimental Value	% Error
Tensile strength (MPa)	RS=1097 rpm; TS= 55.59 mm/min; VF-Al_2O_3mp = 8.64 %	227.80	236.38	3.77
% elongation (%)		19.31	20.12	4.20
Micro-hardness (HV)		147.97	143.56	-2.98
Wear weight loss (mg)		10.47	10.22	-2.38

5.5 MICROSTRUCTURAL ANALYSIS OF FSPED COMPOSITE JOINTS INCORPORATED WITH AL_2O_3 MICROPARTICLES

To investigate the influence of Al_2O_3mp on microstructural refinement, the study associated with grain structure and particle distribution in the weld zone at various processing conditions was carried out. The microstructural characterization of base materials AA7075 and AA6061 was depicted in Fig. 4.3 (a, c).

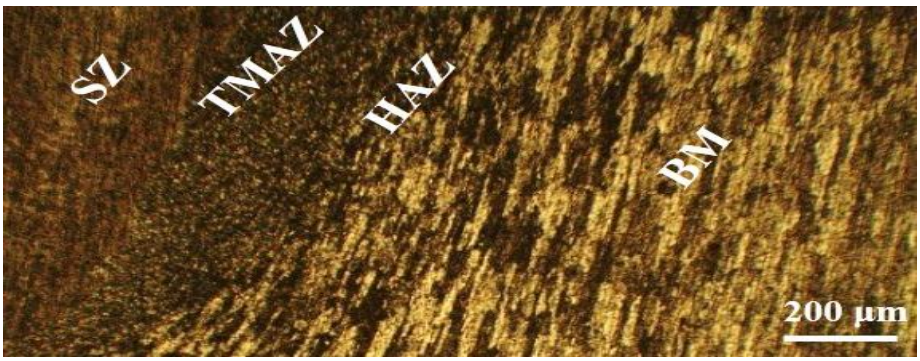

Figure 5.17: Optical graph of various zones of FSPed composite joint of AA6061 and AA7075

The coarse grain structure of AA7075 and AA6061 was observed with a mean grain size of 47 and 36 µm, respectively. The grain size was analysed by ImageJ software. The grain structure of base materials was considerably refined in the processed region during FSW owing to severe plastic deformation caused by the stirring action of the tool, resulting in dynamic recrystallization (DRX) [125].

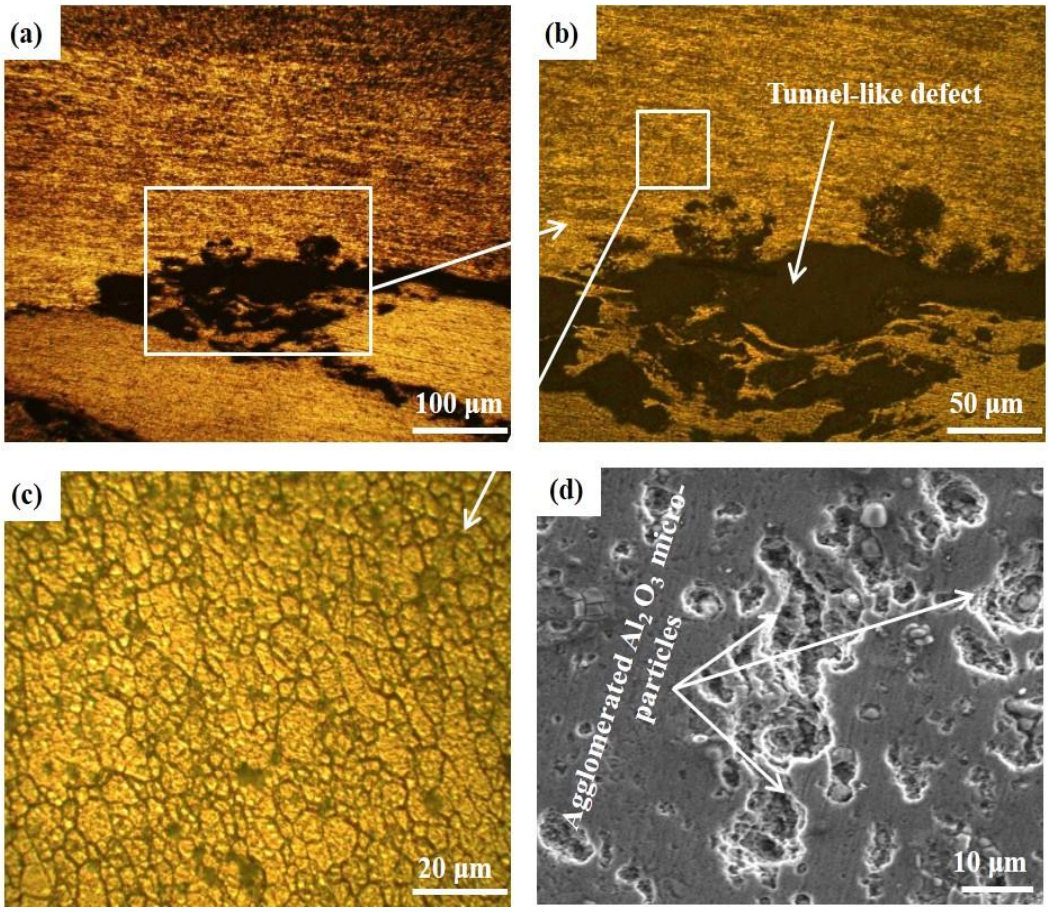

Figure 5.18: Optical micrograph and SEM image of the SZ of specimen no.-6(a, b) Optical micrograph depicts the tunnel-like defect, (c) Grain structure, (d) SEM photomicrograph of agglomerated Al_2O_3mp.

The processed region distinctly showed heat-affected zone (HAZ), thermo mechanical affected zone/partially recrystallization zone (TMAZ/PRZ) and shear zone/recrystallization zone (SZ/RZ). Such zones in the processed region were demonstrated in Fig 5.17. The grain structure refinement was noticed to be higher in the SZ than in the TMAZ and HAZ [126, 127]. Fig 5.18 (a-c) depicts the micrograph of the SZ of specimen no- 6 processed at rotational speed of 700 rpm and traverse speed of 60 mm/min with 10% VF-Al_2O_3mp. A tunnel-like defect (Fig. 5.18 a) was observed

due to inadequate material mixing resulting from inadequate heat input [128]. The tunnel defect is obvious in the highlighted region depicts in Fig. 5.18 b. The grain structure with mean grain size of 18.4 µm was observed in Fig. 5.18 c. Due to unusual material mixing, agglomeration of Al_2O_3mp along with poor bonding with surrounded metal matrix occurs that is obvious in SEM photomicrograph depicted in Fig. 5.18 d.

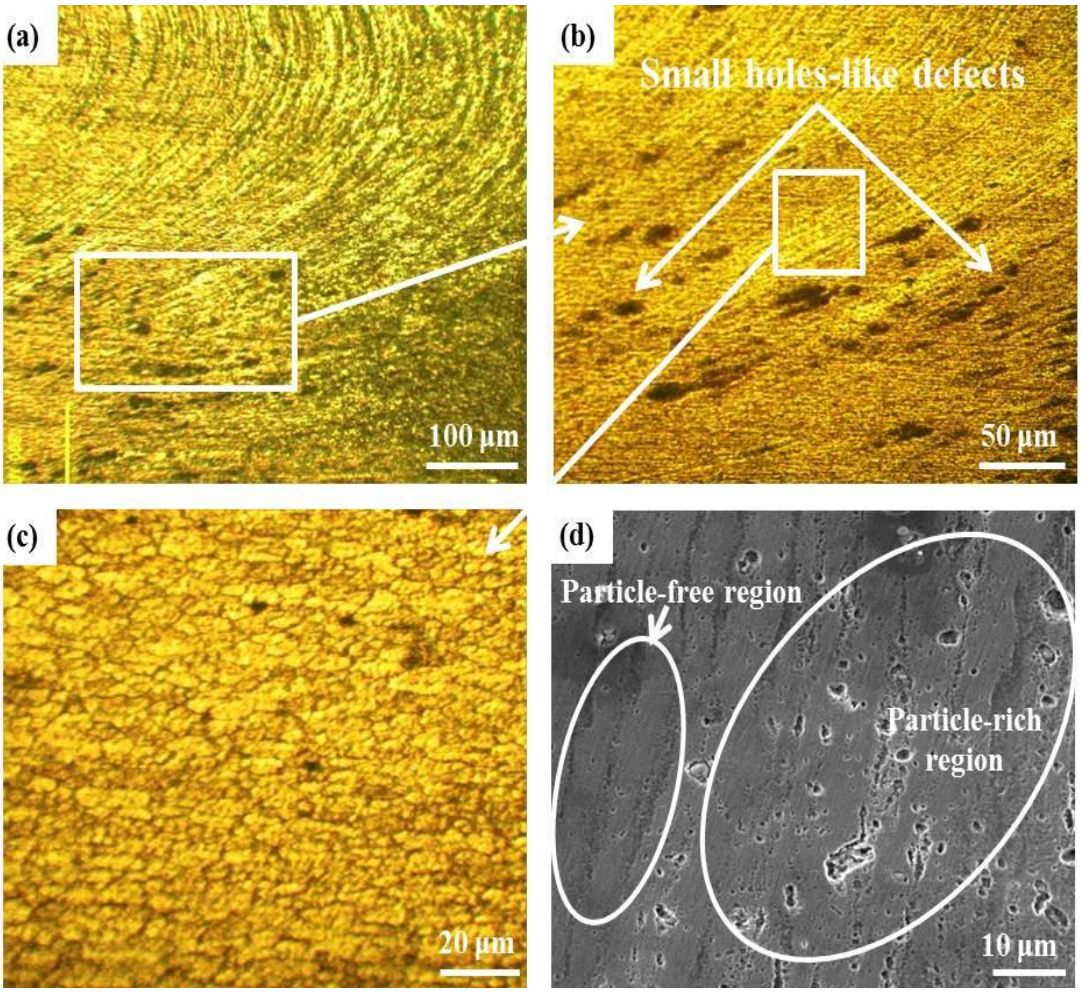

Figure 5.19: Optical micrograph and SEM image of the SZ of specimen no-9 (a, b) Optical micrograph depicts small holes-like defects, (c) Grain structure, (d) SEM photomicrograph of distribution of Al_2O_3mp.

Whereas, very small hole-like defects were observed (Fig. 5.19 a) in specimen no-9 processed at rotational speed of 900 rpm and traverse speed of 50 mm/min with 10% VF-Al_2O_3mp.At higher magnification, these holes-like defects can be observed distinctly in Fig. 5.19 b. The clustering of Al_2O_3mp reduces and moderate dispersion of Al_2O_3mp, including particles-free region and particles-rich region was observed, as depicted in Fig. 5.19 d. This reveals that at lower rotational speed, sufficient strain was

not produced to overcome particles' agglomeration [129]. Fig. 5.19 c illustrated the grain structure with a mean grain size of 15 µm. Defect-free composite joints with onion rings structure were obtained at rotational speed of 1100 rpm, as depicted in Fig. 5.20 a and 5.21 a. These onion rings evident the improved and significant material mixing due to enough strain produced by the tool's increased stirring action.

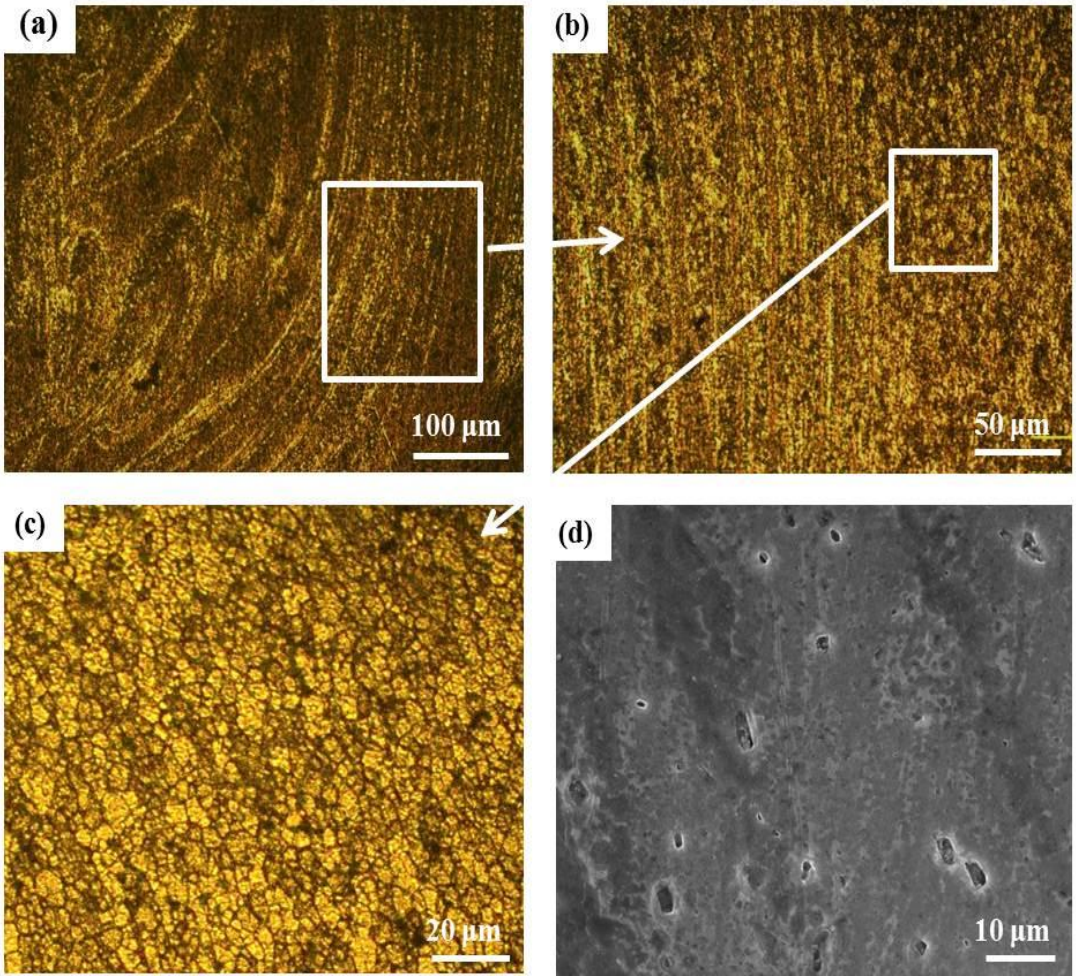

Figure 5.20: Optical micrograph and SEM image of the SZ of specimen no- 10 (a, b) Optical micrograph depicts sound composite joint, (c) Grain structure of mentioned region, (d) SEM micrograph depicts the homogeneous distribution of Al_2O_3mp.

High rotational speed enhances the mobility of particles in the SZ and breaks the bigger particles through the abrasive action of the rotating tool [130-131]. Consequently, the homogeneous distribution with significant fragmentation of particles was observed, as depicted in Fig. 5.20 d and 5.21 d. No particles' agglomeration indicating the sound bonding between the particles and surrounded aluminum matrix. The size of

fragmented particles was observed smaller at the higher rotational speed than the lower rotational speed [114]. Referring the Fig. 5.21 c and 5.20 c, the mean grain size of specimen no-15 (7.2 µm) was found smaller than that of specimen no-10 (10.7 µm). This can only be ascribed to the presence of the higher volume fraction of uniform distributed and fragmented Al_2O_3mp via pinning effect. The presence of higher volume of uniform distributed Al_2O_3mp increases the pinning effect resulting in higher grain refinement. The small sized Al_2O_3 particles provide hindrance to the mobility of grain boundaries and restriction to the grain growth via pinning effect [114].

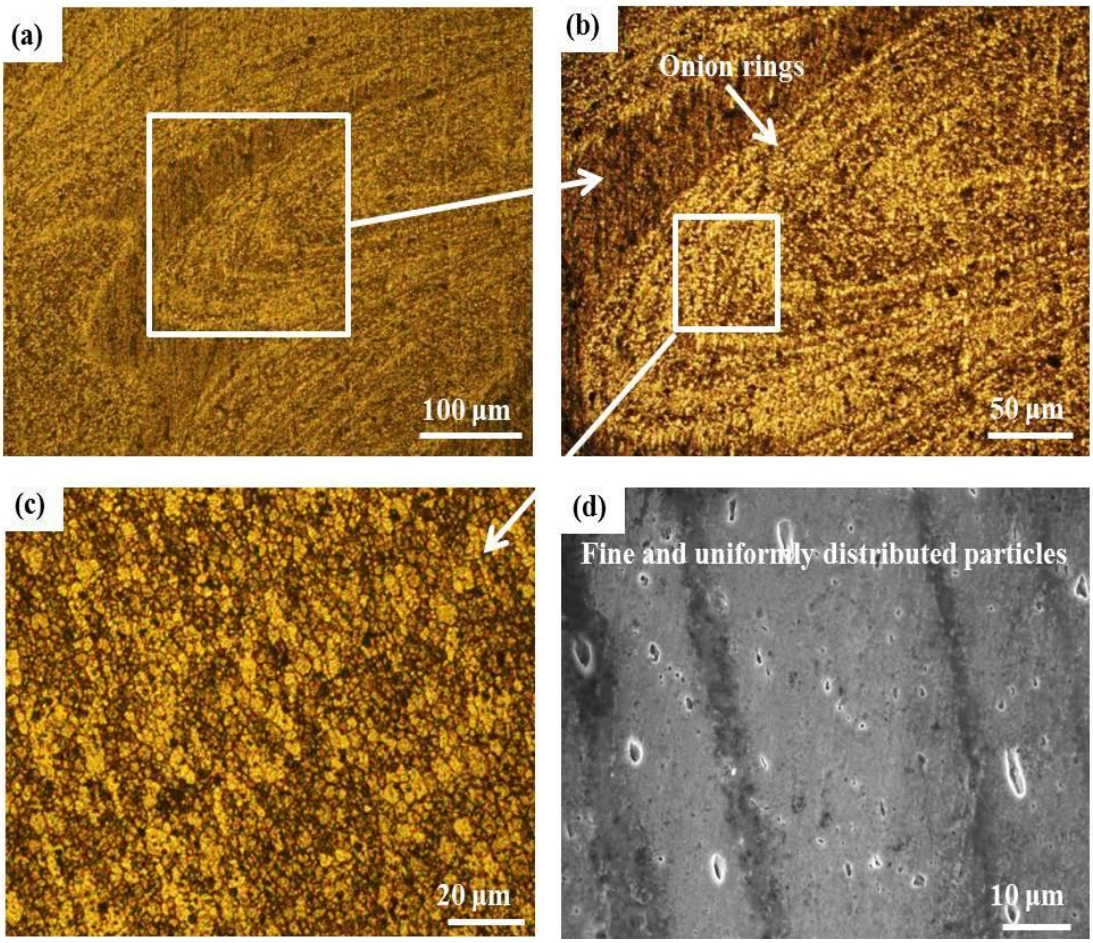

Figure 5.21: Optical micrograph and SEM image of the SZ of specimen no- 15 (a, b) Optical micrograph depicts sound composite joint with onion rings, (c) Grain structure, (d) SEM photomicrograph

These results confirmed the consequence of Al_2O_3mp on microstructural refinement. The grain size of the SZ was related with Zener - Holloman variable [132]. The mean grain size was determined by applying the following equation: $R_c = \frac{4r}{3v_f}$, where R_c is

critical radius. On comparing specimen no- 10 and 15, it was found that incorporation of higher volume fraction of Al_2O_3mp enhanced the grain refinement. The growth rate of grains due to 2nd phase micro-particles is given by eq. 5.11 [133].

$$\frac{dR_g}{dt} = (P_d - P_{zp})M_b = \left(\frac{g_c \gamma_{be}}{R_g} - \frac{3V_f\gamma_{be}}{2r_p}\right) M_b \qquad (5.11)$$

Where M_b denotes the mobility of grain boundaries, R_g denotes the grain's radius, V_f denotes volume fraction, P_d denotes driving pressure generated by grains boundary's curvature, P_{zp} represents Zener-pinning pressure, γ_{be} is the energy linked with grain boundary, g_c is geometrical constant, and r_p is the radius of 2nd phase particles. The growth of grains will end at $P_{zp}=P_d$.

$$\frac{g_c \gamma_{be}}{R_g} = \frac{3V_f\gamma_{be}}{2r_p} \qquad (5.12)$$

The Zener's limiting size of grains may be observed (g_c=1), if the radius of curvature (Rg) equals the mean granularly radius (D), then $D_{zl} = \frac{4r_p}{3V_f}$.

Consequently, the specimen produced with higher rotational speed, lower traverse speed and higher volume fraction of Al_2O_3mp exhibits homogeneous dispersion of particles and reduced grain size in the SZ. These results revealed that the microstructural modification could be achieved by the incorporation of Al_2O_3mp in the SZ.

Fig. 5.22 (a, b) illustrated the results obtained by EDS analysis of specimens no- 10 and 15, which were processed with 4 and 10% volume fraction of Al_2O_3mp, respectively whereas, the other processing parameters are same. The presence of oxygen peaks in the EDS analysis (Fig. 5.22 a, b) reveals the incorporation of Al_2O_3mp in the SZ of the specimens no- 10 and 15. The elemental identification obtained by EDS analysis indicated the different percentage of oxygen as 1.58 and 4.67% at the SZ of specimens no-10 and 15, respectively. The higher percentage of oxygen in the elemental characterization of EDS analysis reveals the higher concentration of Al_2O_3mp in the SZ of specimen no-15 in comparison with specimen no-10. The percentages of other main elements were Zn-3.75%, Fe-1.28%, and Mg-1.29% observed in the SZ of specimen no-10 whereas Zn-3.32%, Fe-1.20%, and Mg-1.63%

were observed in specimen no- 15. As a consequence, the EDS data show that Al_2O_3mp with different volume fractions were incorporated in the SZ.

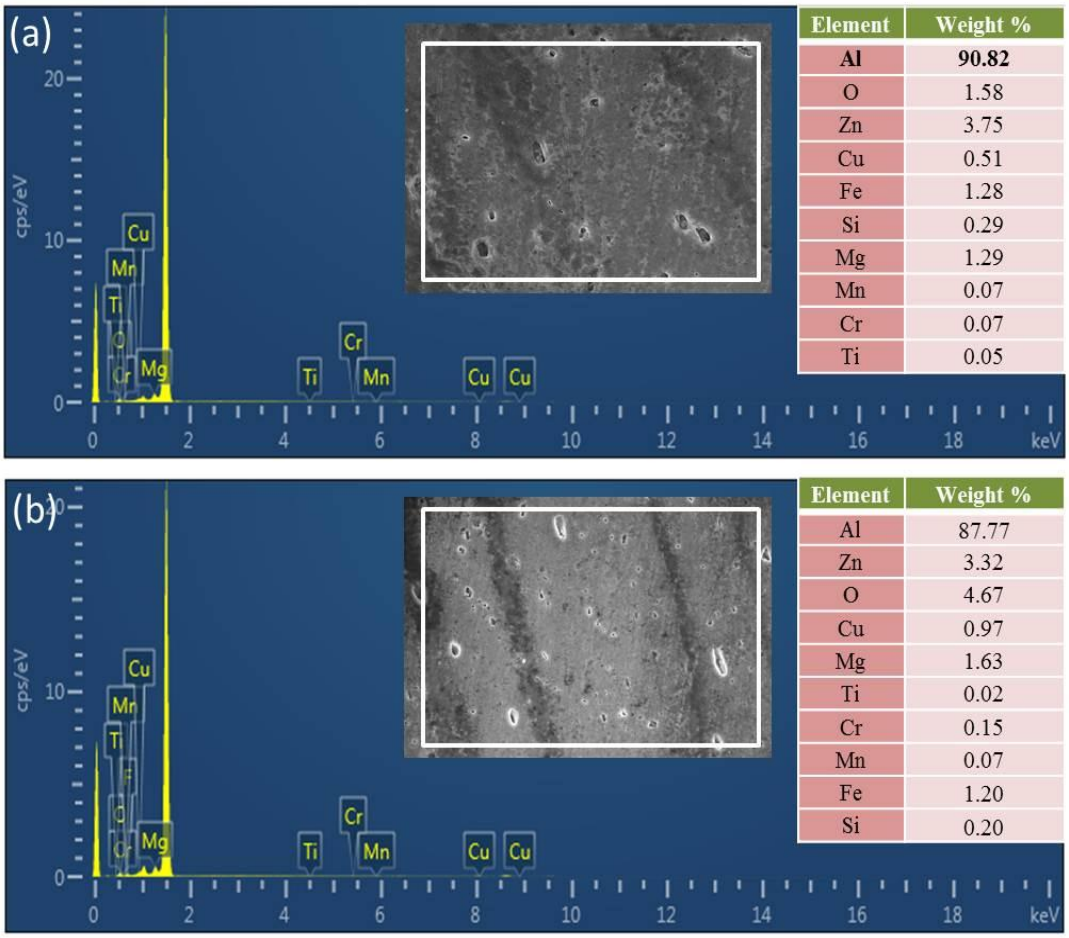

Figure 5.22: EDS peaks of composite joint produced at 1100 rpm, 40 mm/min with 4 and 10% Al_2O_3mp, (a) Specimen no-10, (b) Specimen no- 15.

5.5.1 Fracture Surface analysis

The morphology of fractured surfaces of tensile samples of various composite joints was depicted in Fig. 5.23-5.26. The microstructure of fractured surfaces was examined by employing SEM to understand the mode of failure during tensile testing. After tensile testing, the fractured surfaces of all the samples showed the dimple fracture, indicating the failure of ductile mode. The probability of strengthening in any composite matrix depends upon the transferring stress from base material to the reinforcement particles. Due to poor interfacial contact, the interface could fail before transmitting stress to micro-particles, resulting in no strengthening [134]. During the tensile loading, the cup-cone shaped shear plane was produced along the periphery of the test samples.

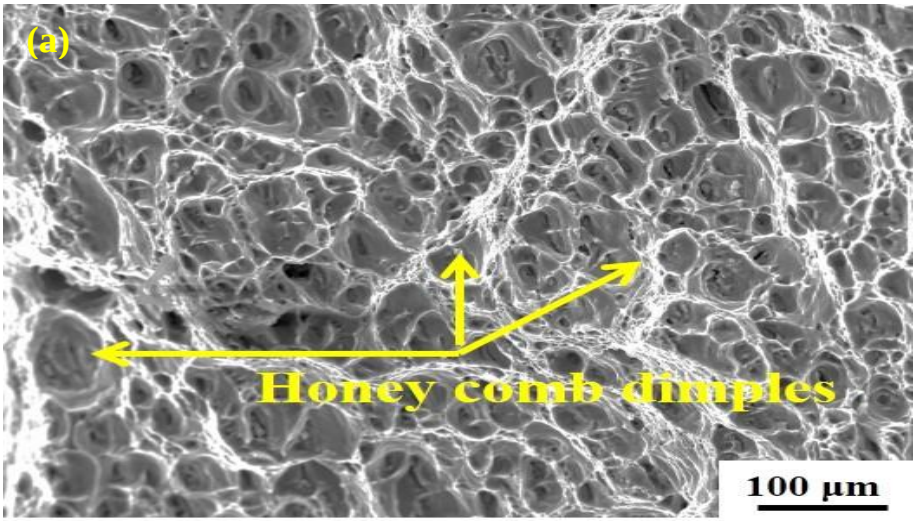

Figure 5.23: SEM images of various tensile fractured specimen no-6

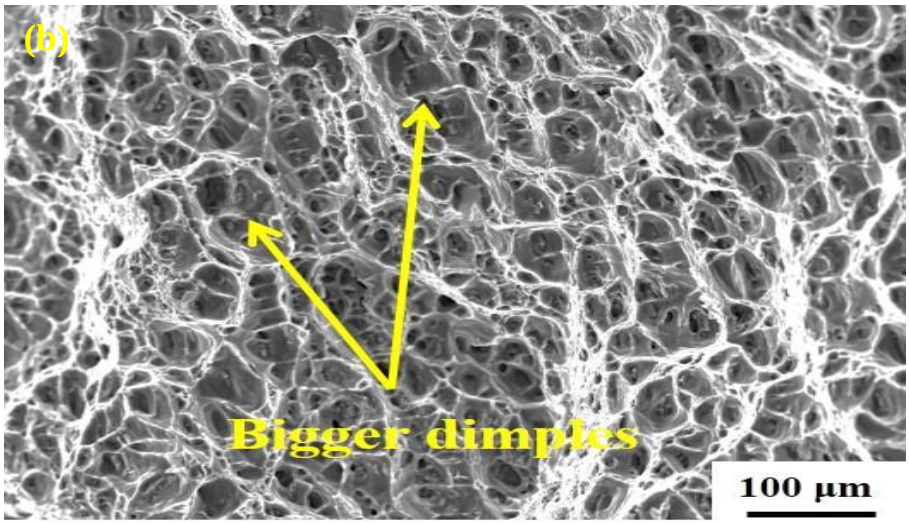

Figure 5.24: SEM images of various tensile fractured of specimen no-9

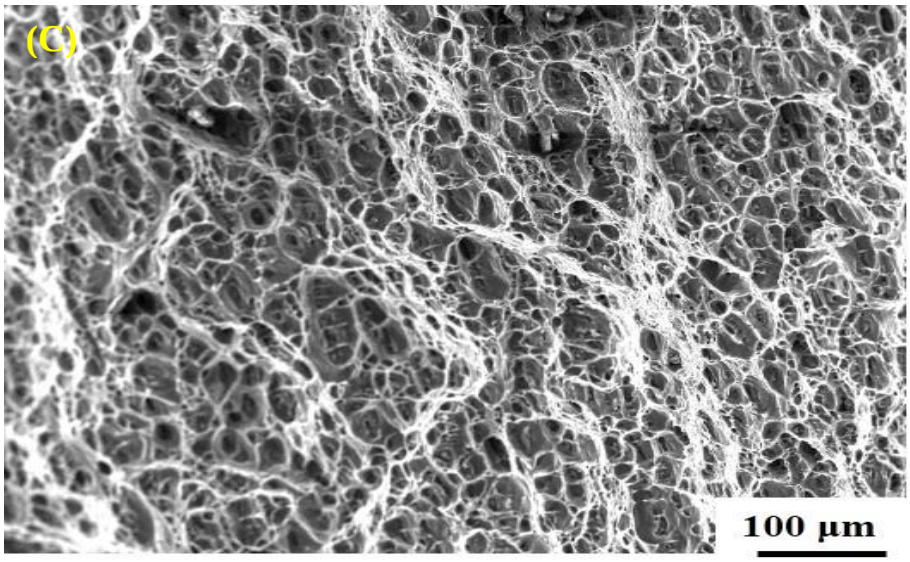

Figure 5.25: SEM images of various tensile fractured of specimen no-11

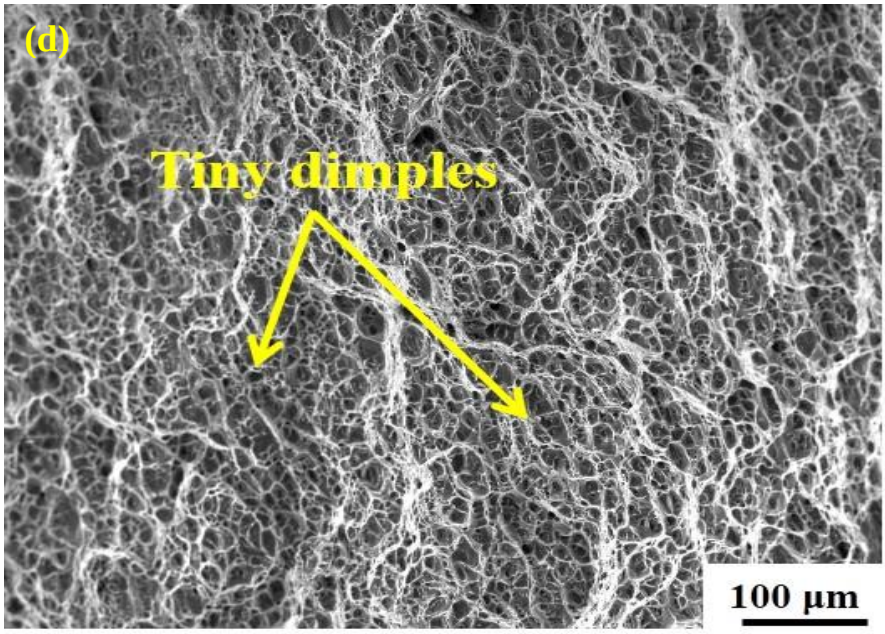

Figure 5.26: SEM images of various tensile fractured of specimen no-15.

In specimen no- 6 (Fig. 5.23), ductile fracture with honeycomb dimples was found, illustrating the regularly separated characteristics of cleavage and plastic deformation [135, 136]. The homogeneous dispersion of Al_2O_3mp and reduced grain size was observed at higher rotational speed due to effectual material mixing. In comparison to specimens no- 6, 9 and 10 (Fig. 5.23-5.25), the morphology of the fractured surface of specimen no- 15 (Fig. 5.26) indicated tiny and equiaxed dimples. The ductile fracture of composite joints is caused by the development of cavities or voids, which then increase and consolidate. If the cavity nucleation could be inhibited, the ductility may be improved [137]. Micro voids' coalescence at the fractured surface resulted in fine and equiaxed dimples [138]. Leading to enhanced ductility, the fractured metal-matrix found at HAZ was validated by variation of micro-hardness. Thus, the incorporation of Al_2O_3mp increased the tensile strength of composite joints, according to the analysis of fractured surface of the tensile samples.

5.6 OPTIMIZATION OF PROCESS PARAMETERS OF FSP COMPOSITE JOINTS OF AL_2O_3 NANOPARTICLES

The FSP was performed to fabricate dissimilar composite joints of AA7075 and AA6061 with the incorporation of Al_2O_3 nano-particles (Al_2O_3np) to enhance the tribological and mechanical characteristics of the FSPed composite joints is depicted in Fig. 5.27.

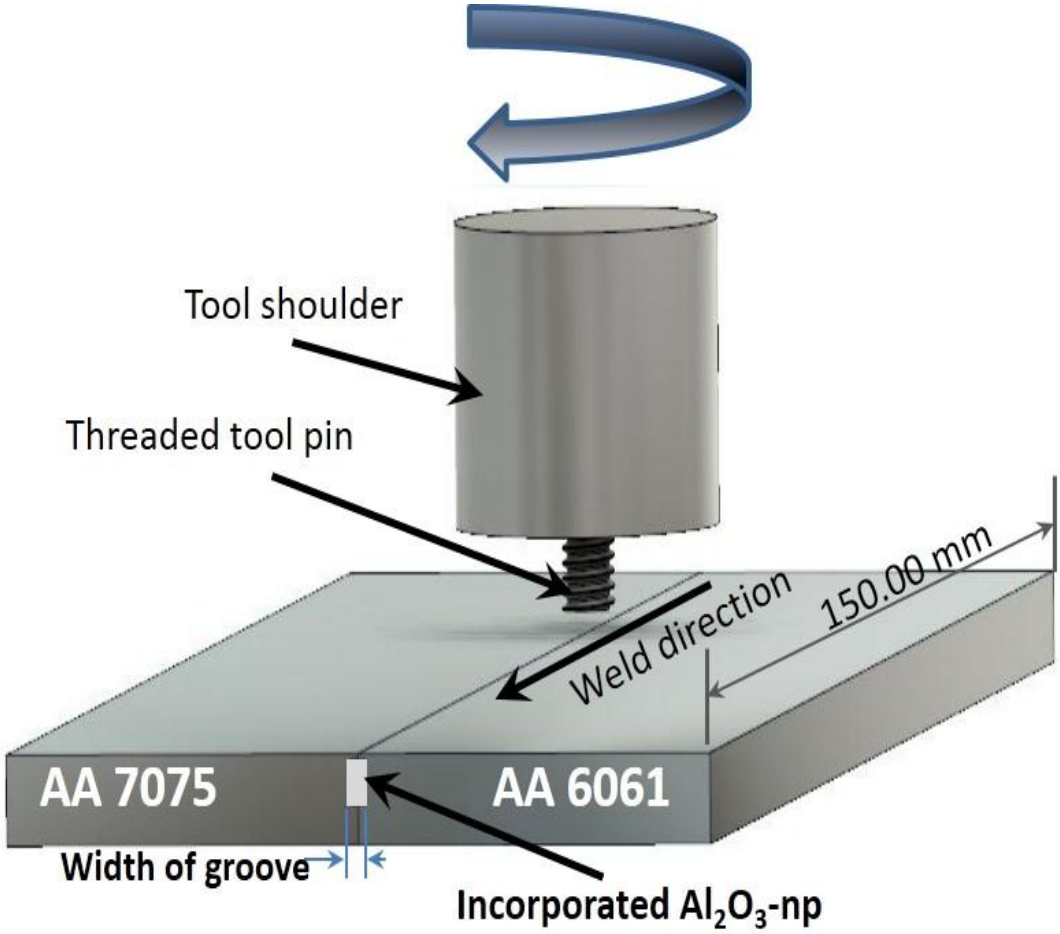

Figure 5.27: FSPed composite joint incorporated with Al_2O_3 nanoparticles

A non-consumable tool with threaded profiled pin manufactured of tool steel (H13) was utilized for experimentation. The processing parameters for FSP approach have been taken as rotational speed (700 – 100 rpm), traverse speed (40 - 60 mm/min) and volume fraction of Al_2O_3np (4-10%).

The dimensional features of tensile test sample were taken according to ASTM E8-standard as mentioned in the Fig. 5.28. The tensile samples were extruded from the welded plates using wire cut CNC EDM. Single pass FSP is employed to fabricate FSPed composite joints as shown in Fig. 5.27. The computer controlled UTM machine was employed to analyzed the tensile test. Three tensile samples were tested from each composite joint and average result was reported. As per design expert software recommendation, there are 20 FSPed composite joints incorporated with Al_2O_3 nanoparticles were fabricated as per design of experiment.

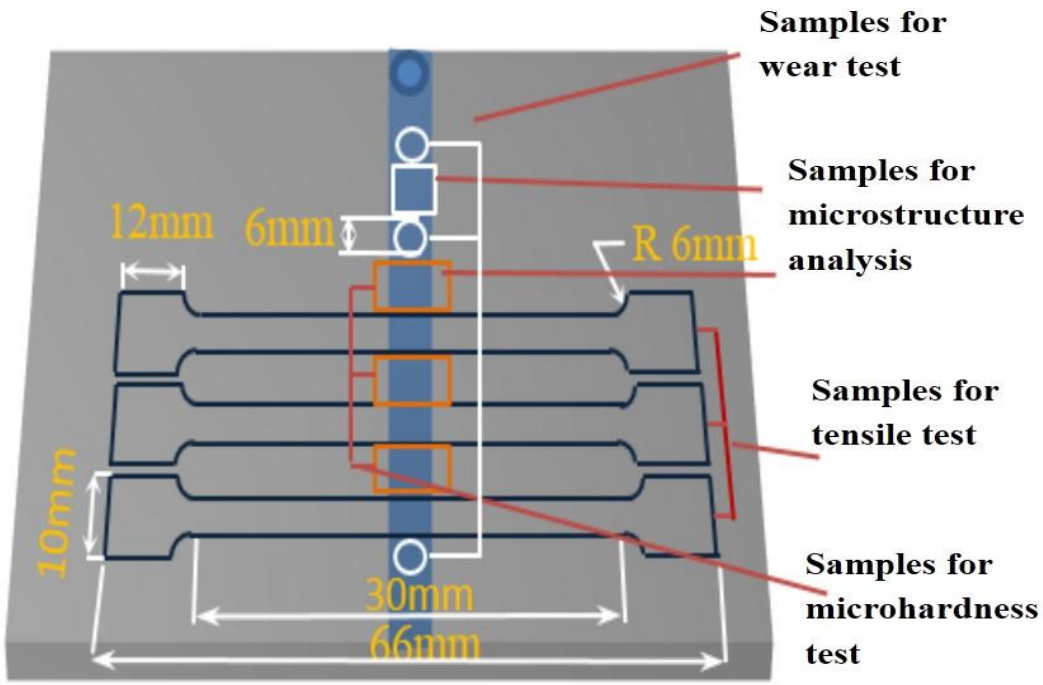

Figure 5.28: Dimension of FSP welded test samples

Various researchers have utilized a variety of experimental design strategies for the development of regression equations but central-composite design is one of the best and most accurate design approaches [106-108]. To obtained the design of experiments using full factorial central-composite design the process parameters and their levels were assigned, where the upper and lower values were coded as +1 and -1, respectively. The face-centered central composite design contains twenty experimental combinations with three independent input parameters namely tool rotational speed (RS), traverse speed (TS) and volume fraction of Al_2O_3 nanoparticles (VF-Al_2O_3np) with their three levels. The Processing parameter of FSPed composite and their levels are tabulated in Table 5.13.

Table 5. 13: Processing parameter of FSP-Al_2O_3np with their levels

Parameters	Symbols	Units	Range	Levels		
				-1	0	1
Rotational Speed (RS)	A	rpm	700-1100	700	900	1100
Traverse speed (TS)	B	mm/min	40-60	40	50	60
Volume fraction of Al_2O_3np	C	Percentage (%)	4-10	4	7	10

5.6.1 Tensile strength

In order to investigate the impact of FSP parameters along with varying volume fraction of Al_2O_3 nano-particles on the weld quality of dissimilar composite joint of AA7075 and AA6061, a UTM was utilized to apply the tensile load on FSPed composite joints at room temperature and observed the tensile strength of different FSPed composite joints. The samples for tensile testing were extruded transversely to composite joint. The average tensile strength and % elongation of FSPed composite joints under various processing conditions were tabulated in Table 5.14-5.17.

The tensile strength of base materials AA6061 and AA7075 was observed as 288 and 496 MPa, respectively, whereas % elongation was observed as 18.4% and 21.6%, respectively. The tensile strength of the FSPed composite joints are varied from 171.70 MPa to 254.90 MPa at different process parameters conditions. Fig. 5.29-5.31 shows the stress-strain diagram of FSPed composites joints incorporated with Al_2O_3np under tensile loading and it is found that the tensile strength of all composite joints is less than that of the as received base materials AA 6061 and AA7075. During tensile loading, some samples were fractured from the welded region whereas some samples were fractured in heat affacted zone (HAZ) region on the side base material AA6061 where the strength and hardness were minimal.

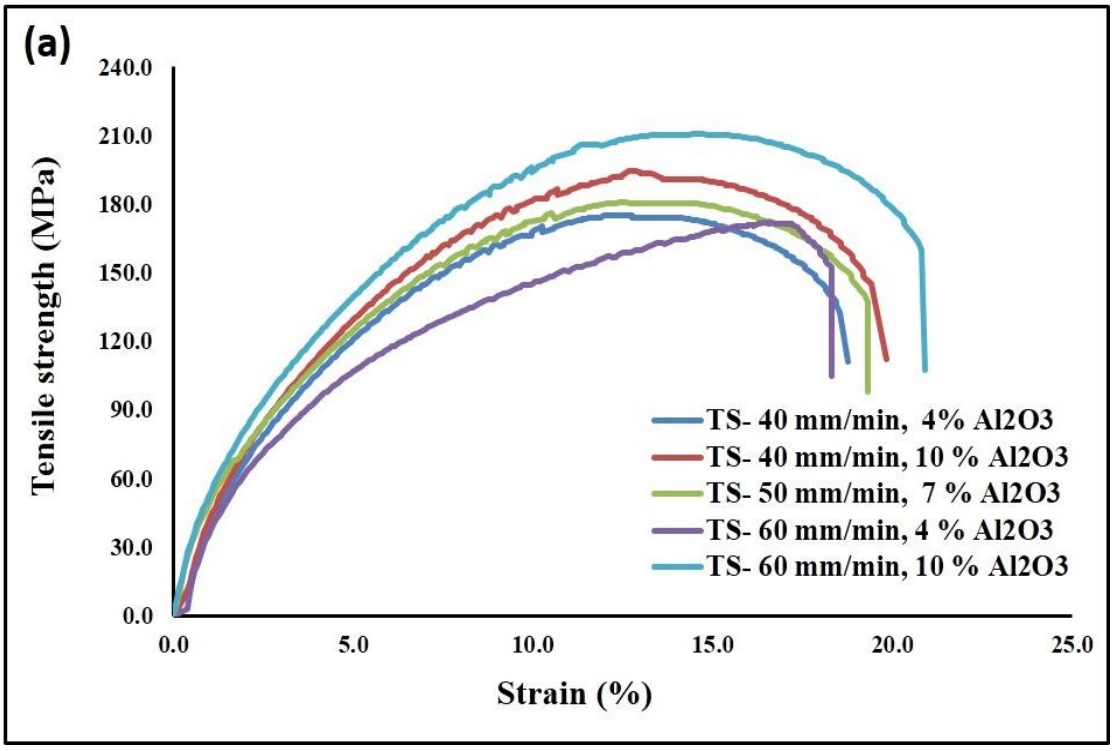

Figure 5.29: Stress strain diagram of composite joints at RS 700 rpm

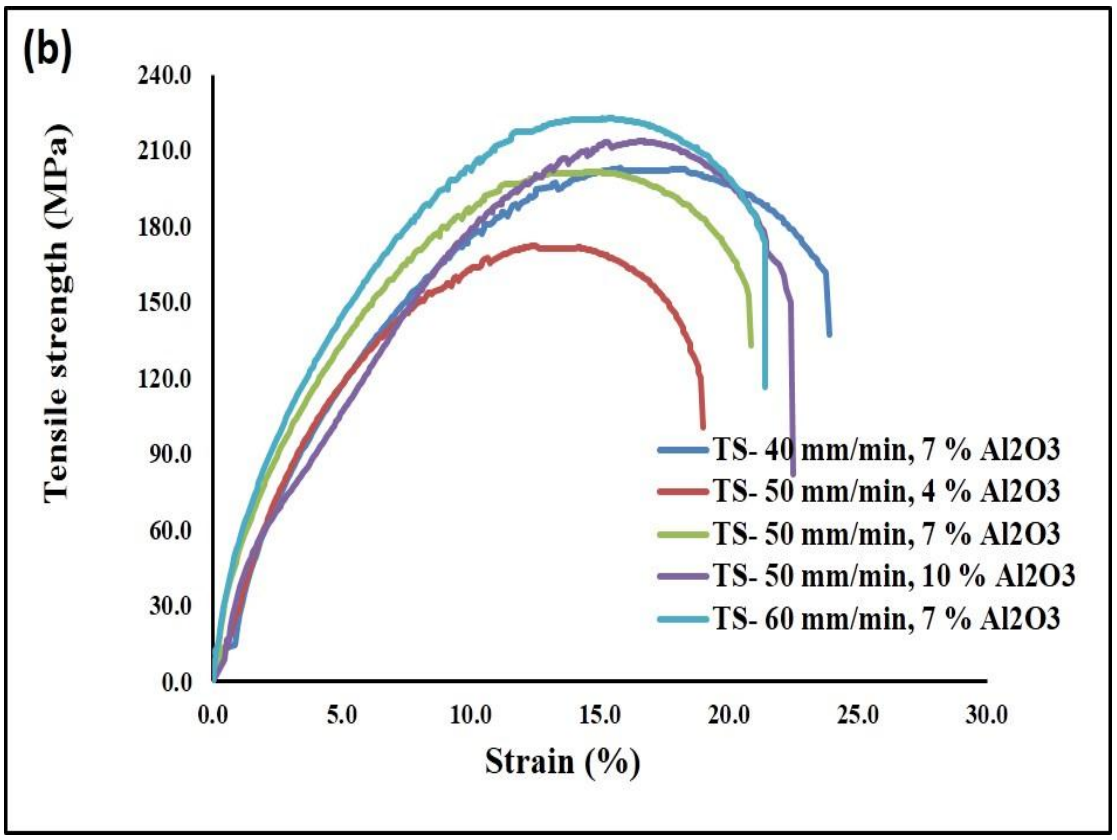

Figure 5.30: Stress strain diagram of composite joints at RS 900 rpm

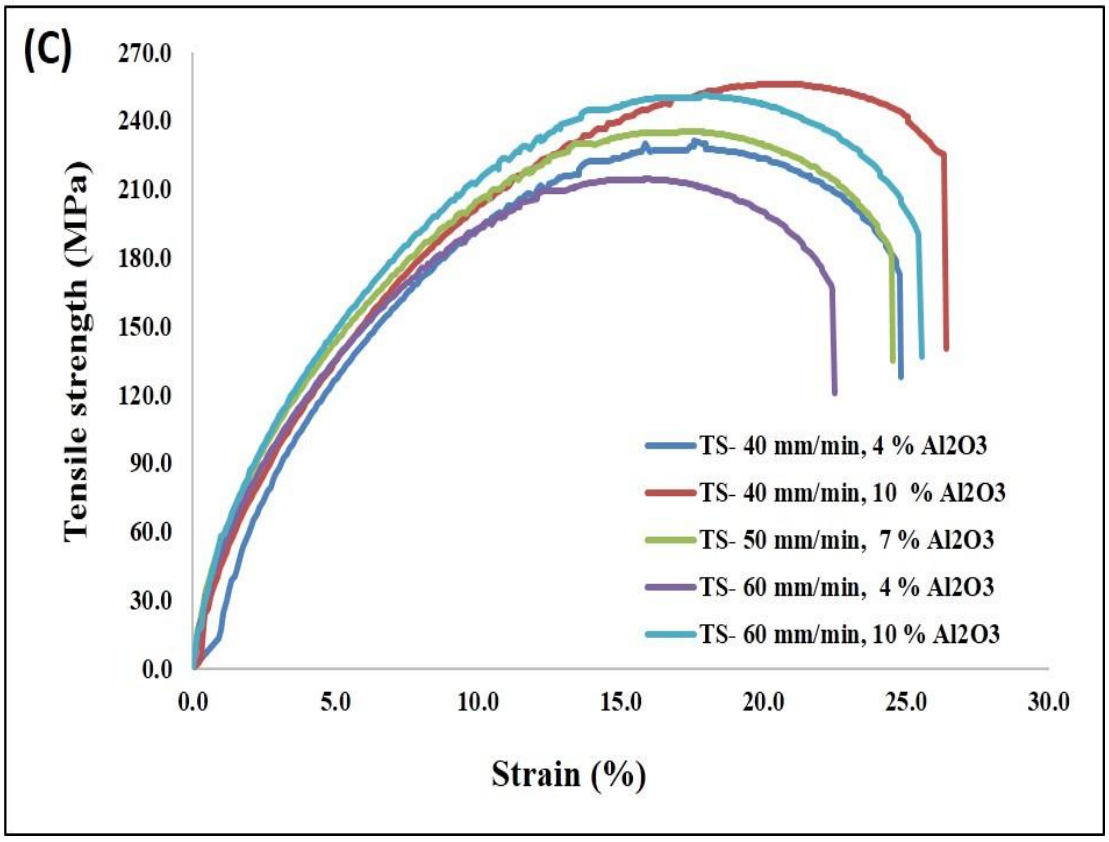

Figure 5.31: Stress strain diagram of composite joints at RS 1100 rpm

Previous studies were also revealed that the composite joints generally fractured at the HAZ towards weaker base material in case of FSWed dissimilar aluminum alloys [139-140]. This may result in the improved level of dispersion and fragmentation of Al_2O_3 particles and the tendency to fragment Al_2O_3 particles to resist dislocation movement during the axial loading. The tensile strength of AA6061 exhibited 288 MPa and % elongation of 18.4. After the implementation of FSP, the maximum value of the tensile strength 254.90 MPa could be obtained, which is approximately 88% of the tensile strength of parent metal AA6061 as depicted in Fig. 5.32. The maximum tensile strength was observed at the rotational speed of 1100 rpm and traverse speed of 40 mm/min with 10% VF-Al_2O_3np. The imparted Al_2O_3np in the weld zone yield increased the tensile strength as reported [141-143]. These Al_2O_3 particles may contribute to the strengthening mechanism by acting as nucleation locations to generate dislocation via strain divergence and plastic constraints [144]. According to Tables 5.14 and 5.15 the Al_2O_3np are positively ameliorating both tensile strength and % elongation, respectively.

Tensile strength is inversely proportional to grain's size, as defined by Hall-patch relationship $\sigma_1 = \sigma_i + kd^{(-1/2)}$ [113]. The grain size in FSPed composite joint was very small as compare to base materials. Because of presence of Al_2O_3-mp presented in the SZ which reduced the grain size as per Zener pinning effect [114]. The tensile strength of the composite joints increases on increasing rotational speed. The highest tensile strength (254.9 MPa) was observed in composite joint processed at RS of 1100 rpm, TS of 40 mm/min incorporated with 10% Al_2O_3np. In this experimental investigation, three statistical variables such as standard error (SE), standard deviation (SD), and confidence interval of 95% were analyzed for FSPed composite joints incorporated with Al_2O_3np as tabulated in Table 5.14-5.17. The standard deviation was measured as [SD= $\Sigma(Xi - M)2 / (N - 1)]$ ½, which gives the deviation of experimental values from the mean. The standard error is measured as, $SE=SD/N^{1/2}$ and used to find the closeness between the prediction values and the experimental values. where M denotes the mean and, N denotes the no. of observation. It is obvious from the 95 % confidence interval reveals that on increasing the value of tool rotational speed, the tensile strength, %elongation, and micro-hardness increases while the wear (weight loss) decrease.

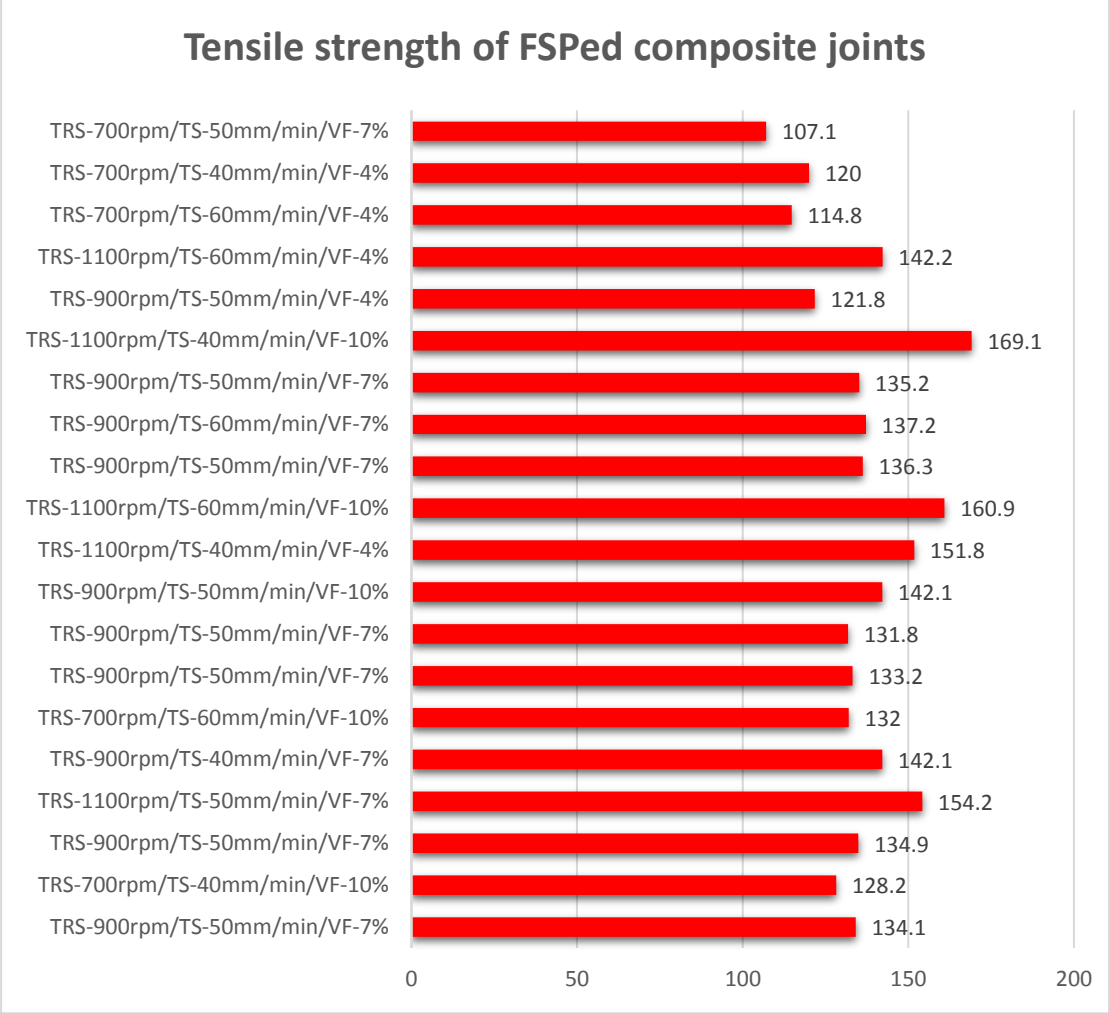

Figure 5.32: Tensile strength of various composite joints

5.6.2 Micro-hardness

Vickers hardness testing was employed to analyses the distribution of micro-hardness in the processed zone of FSPed composite joints of AA6061 and AA7075 processed under various processing conditions as shown in Fig.5.33 (a-c). Vickers micro-hardness tester was employed to evaluate the hardness profile at 100 gm load for 15 s dwell time by taking 1 mm gap between the indentations. As we know that the FSPed composite joint is a heterogeneous composite with varying mechanical characteristics at its interface [115]. Fig. 5.33, revealed the variation of Vickers hardness to the distance from the weld center of the composite joints incorporated with Al_2O_3np. The base metal AA6061 and AA7075 exhibited a means indentation hardness of 96 HV and 170 HV, respectively. The hardness of the SZ may be attributed to the grain refinement and dispersion of Al_2O_3np in the SZ. The refined grain size in the SZ was associated with the thermal input during FSP [117, 145].

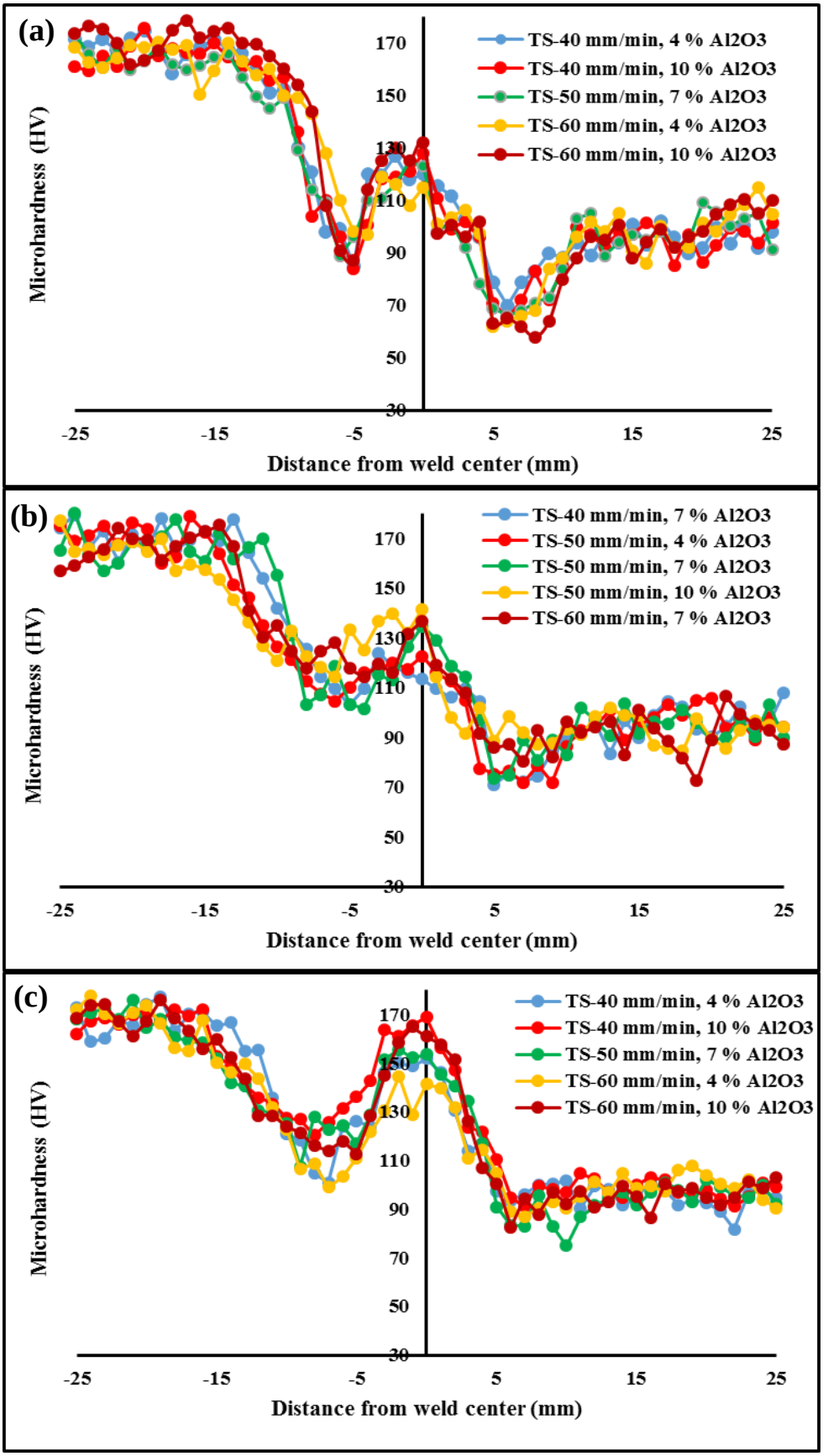

Figure 5.33: (a-c) Micro-hardness distribution of FSPed composite joints incorporated with Al_2O_3np (a) at 700 rpm, (b) at 900 rpm, (c) at 1100 rpm

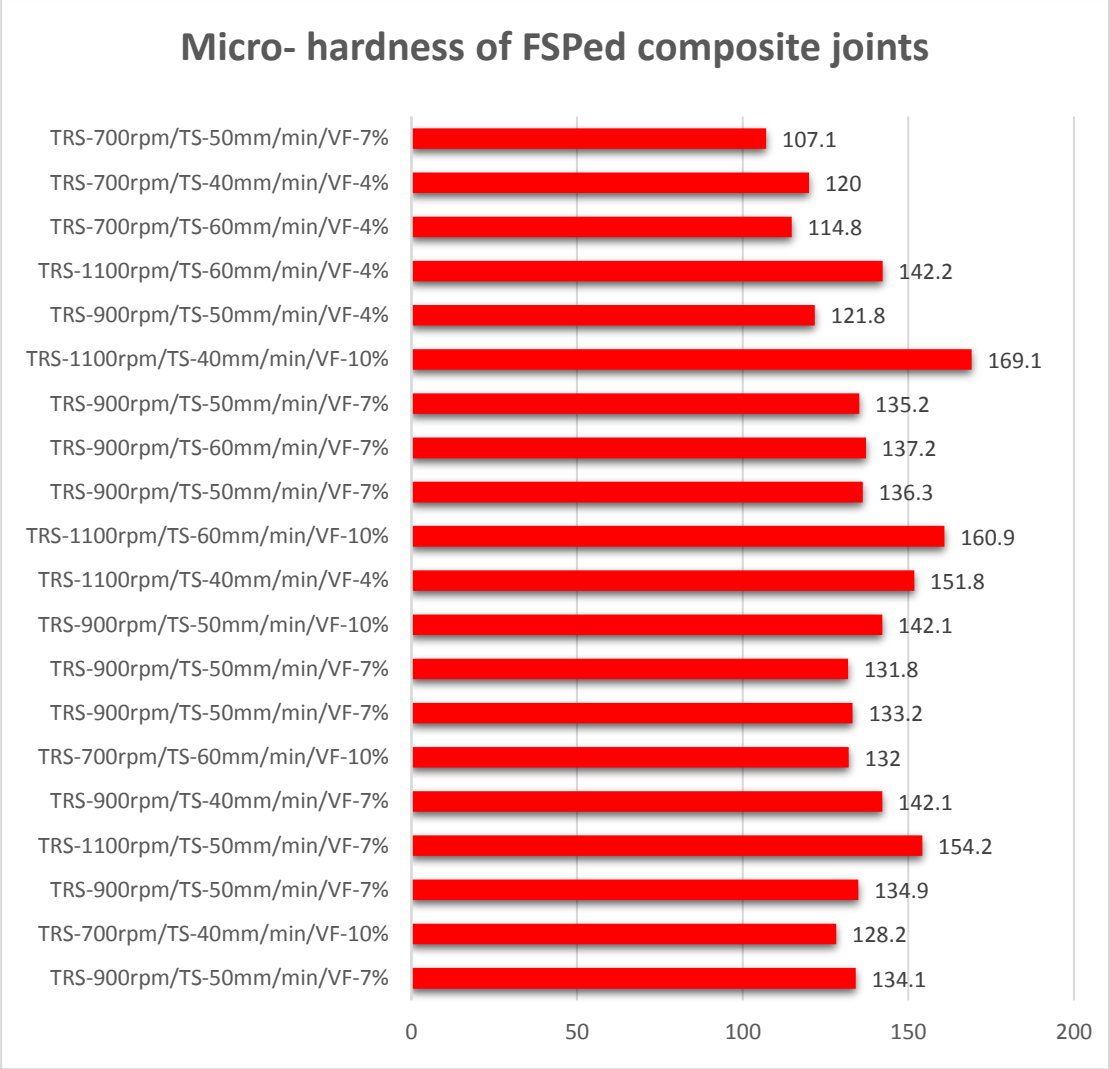

Figure 5.34: Micro-hardness of various composite joints

The maximum hardness value along the centerline (stir zone) was observed as 169.1 HV at specimen no-15 processed at the rotational speed of 1100 rpm, traverse speed of 40 mm/min with 10% of Al_2O_3np as depicted in Fig. 5.34. In comparison, the maximum micro-hardness of 169.1 HV was found in specimen no-15, which is approximately equal to the hardness of base metal AA7075. Low fluctuation in hardness in the TMAZ of all fabricated FSP/Al_2O_3np was observed due to dispersion and intermixing of base metal and Al_2O_3np. The strengthening effect of Al_2O_3 particles in specimen no-15 was more compared to other specimens due to the hard nature of the Al_2O_3 phase, refined grains, and material mixing rule.

So, the enhancement of micro-hardness of the FSPed composite joint may be attributed to the combined effect of grain refinement, high hardness of Al_2O_3 particles, and dispersion strengthening [146]. The precipitation hardening depends on the distribution

of strengthening precipitates, shape, size, and volume. It was observed that the micro-hardness of the SZ was found higher than that of the HAZ and TMAZ due to smaller grains in the SZ [147-149]. The micro-hardness was decreased in the TMAZ because of precipitates' dissolution. The micro-hardness decreased in the HAZ was because of coarsening of precipitates and the vanishing of the Guinier-Preston zone [150]. It is obvious that two HAZ, two TMAZ and one nugget zone have developed in the micro-hardness distribution region of the composite joints, therefore the composite joints' tensile strength is lower than that of the base material [118].

The stir zone exhibits the higher micro-hardness than that of adjacent zones due to grain refinement via dynamic recrystallization and pinning effect of Al_2O_3np, whereas TMAZ and HAZ exhibit the low micro-hardness due to coarsening of grain, elevated temperatures, over aging during the FSP. The micro-hardness of the composite joints embedded with reinforcement particles also enhanced due to the presence of hard Al_2O_3 particles. The highest value of micro-hardness (169.1 HV) at the SZ was observed at rotational speed 1100 rpm and traverse speed 40 mm/min with incorporation of 10% Al_2O_3np, while the boundary between the HAZ and TMAZ on advancing side exhibited the minimum value of hardness as compare to the SZ as depicted in the Fig. 5.33.

5.6.3 Wear behaviour of FSPed composite joints incorporated with Al_2O_3np

To assess the wear behaviour of all the FSPed composite specimens, Pin on disk tribometer was employed. The factors controlling the wear resistance of FSPed specimens subjected to friction stir processing incorporated with Al_2O_3np were identified as, surface contact between the wear samples (pin) and the disk, homogeneity in the distribution of reinforcing particles and, the bond between the metal matrix and the reinforcing particles [120]. SEM was employed to examine the worn surfaces following the wear testing to assess the involved wear mechanism. The mean weight loss of as received base materials AA 6061 and AA7075 was observed as 14.35 and 12.23 mg. The mean weight loss of the composite joints was found less than that of the base material AA6061 and AA7075. This ascribed to the hard Al_2O_3np, which enhances the wear resistance and reduced surface contact between the pin and the disk. A higher weight loss was observed at low rotational speed compared with that of high rotational speed, due to poor bonding of Al_2O_3np with metal matrix at low rotational speed due to particles agglomeration, as revealed in SEM photomicrograph Fig. 5.35 d.

Table 5.14: Tensile strength of FSPed composite joints incorporated with Al_2O_3np

Specimen no.	Processing Parameter			Tensile Strength (MPa)			Mean Tensile Strength (MPa)	Standard Deviation	Standard error	95% confidence Interval	
	A: RS (rpm)	B:TS (mm/min)	C: VF-Al_2O_3np (%)	Sample 1	Sample 2	Sample 3				Minimum	Maximum
1	900	50	7	194.9	200.7	203.8	199.8	4.52	2.61	194.7	204.9
2	700	40	10	194.4	186.2	187.6	189.4	4.39	2.53	184.4	194.4
3	900	50	7	200.6	202	206.7	203.1	3.20	1.84	199.5	206.7
4	1100	50	7	232.7	238.2	234.6	235.2	2.79	1.61	232.0	238.3
5	900	40	7	214.4	216.6	209.5	213.5	3.63	2.10	209.4	217.6
6	700	60	10	193.2	197.8	201.5	197.5	4.16	2.40	192.8	202.2
7	900	50	7	195.6	199.2	203.3	199.4	3.85	2.22	195.0	203.7
8	900	50	7	201.5	198.7	194.1	198.1	3.74	2.16	193.9	202.3
9	900	50	10	211.9	213.6	219.5	215.0	3.99	2.30	210.5	219.5
10	1100	40	4	231	226.6	236.3	231.3	4.86	2.80	225.8	236.8
11	1100	60	10	251.2	247.5	245.3	248.0	2.98	1.72	244.6	251.4
12	900	50	7	207.1	198.5	201.3	202.3	4.39	2.53	197.3	207.3
13	900	60	7	208.1	203.6	200.3	204.0	3.92	2.26	199.6	208.4
14	900	50	7	197.9	205.5	202	201.8	3.80	2.20	197.5	206.1
15	1100	40	10	251.9	256.9	255.9	254.9	2.65	1.53	251.9	257.9
16	900	50	4	177.3	183	180.6	180.3	2.86	1.65	177.1	183.5
17	1100	60	4	209.4	217.6	214.4	213.8	4.13	2.39	209.1	218.5
18	700	60	4	171.4	175.2	168.5	171.7	3.36	1.94	167.9	175.5
19	700	40	4	171.8	177.1	175.2	174.7	2.69	1.55	171.7	177.7
20	700	50	7	183.5	180.8	176.9	180.4	3.32	1.92	176.6	184.2

Table 5.15: %Elongation of FSPed composite joint incorporated with Al_2O_3np

Specimen no.	Processing Parameter			%elongation (%)			Mean %elongation (%)	Standard Deviation	Standard error	95% confidence Interval	
	A: RS (rpm)	B: TS (mm/min)	C: VF-Al_2O_3np (%)	Sample 1	Sample 2	Sample 3				Minimum	Maximum
1	900	50	7	20.1	20.6	22.6	21.1	1.32	0.76	19.6	22.6
2	700	40	10	20.9	19.2	20.2	20.1	0.85	0.49	19.1	21.1
3	900	50	7	20.7	21.5	23.2	21.8	1.28	0.74	20.4	23.2
4	1100	50	7	23.5	25.7	24.4	24.5	1.11	0.64	23.3	25.8
5	900	40	7	21.8	23.2	21.8	22.3	0.81	0.47	21.4	23.2
6	700	60	10	21.1	20.1	21.5	20.9	0.72	0.42	20.1	21.7
7	900	50	7	22.3	21.2	19.5	21.0	1.41	0.81	19.4	22.6
8	900	50	7	20.1	21.8	20.7	20.9	0.86	0.50	19.9	21.8
9	900	50	10	21.4	22.8	23.2	22.5	0.95	0.55	21.4	23.5
10	1100	40	4	24.8	23.2	23.7	23.9	0.82	0.47	23.0	24.8
11	1100	60	10	25.4	24.9	26.3	25.5	0.71	0.41	24.7	26.3
12	900	50	7	21.6	21.9	20.4	21.3	0.79	0.46	20.4	22.2
13	900	60	7	21.9	20.8	21.8	21.5	0.61	0.35	20.8	22.2
14	900	50	7	21.4	22.1	20.4	21.3	0.85	0.49	20.3	22.3
15	1100	40	10	25.9	27.4	26.4	26.6	0.76	0.44	25.7	27.4
16	900	50	4	18.6	19.9	19.3	19.3	0.65	0.38	18.5	20.0
17	1100	60	4	23.2	21.5	22.4	22.4	0.85	0.49	21.4	23.3
18	700	60	4	18.8	17.8	17.6	18.1	0.64	0.37	17.3	18.8
19	700	40	4	18.6	18.2	19.5	18.8	0.67	0.38	18.0	19.5
20	700	50	7	18.6	20.3	19.2	19.4	0.86	0.50	18.4	20.3

Table 5.16: Micro-hardness of FSPed composite joint incorporated with Al_2O_3np

Specimen no.	Processing Parameter			Micro-hardness (HV)			Mean Micro-hardness (HV)	Standard Deviation	Standard error	95% confidence Interval	
	A: RS (rpm)	B: TS (mm/min)	C: VF-Al_2O_3np (%)	Sample 1	Sample 2	Sample 3				Minimum	Maximum
1	900	50	7	137.4	134.7	130.2	134.1	3.64	2.10	130.0	138.2
2	700	40	10	123.8	127.5	133.2	128.2	4.74	2.73	122.8	133.5
3	900	50	7	135.6	138.7	130.3	134.9	4.25	2.45	130.1	139.7
4	1100	50	7	154.2	150.8	157.6	154.2	3.40	1.96	150.4	158.0
5	900	40	7	147.8	137.6	140.8	142.1	5.22	3.01	136.2	148.0
6	700	60	10	129.8	131.6	134.6	132.0	2.42	1.40	129.3	134.7
7	900	50	7	133.8	136.2	129.5	133.2	3.39	1.96	129.3	137.0
8	900	50	7	132.6	127.1	135.6	131.8	4.31	2.49	126.9	136.6
9	900	50	10	145.5	138.8	142.1	142.1	3.35	1.93	138.3	145.9
10	1100	40	4	157.4	151.4	146.7	151.8	5.36	3.10	145.8	157.9
11	1100	60	10	164.8	158.2	161.6	161.5	3.30	1.91	157.8	165.3
12	900	50	7	132.6	139.7	136.6	136.3	3.56	2.06	132.3	140.3
13	900	60	7	141.7	137.5	132.5	137.2	4.61	2.66	132.0	142.4
14	900	50	7	130.6	140.6	134.5	135.2	5.04	2.91	129.5	140.9
15	1100	40	10	164.8	167.4	175.1	169.1	5.36	3.09	163.0	175.2
16	900	50	4	122.2	125.4	117.8	121.8	3.82	2.20	117.5	126.1
17	1100	60	4	143.3	136.3	145.2	141.6	4.69	2.71	136.3	146.9
18	700	60	4	116.2	110.3	117.8	114.8	3.95	2.28	110.3	119.2
19	700	40	4	124.0	119.4	116.7	120.0	3.69	2.13	115.9	124.2
20	700	50	7	119.7	124.1	125.6	123.1	3.07	1.77	119.7	126.6

Table 5.17: Wear behavior (weight loss) of FSPed composite joint incorporated with Al_2O_3np

Specimen no.	Processing Parameter			Weight loss (mg)			Mean weight loss (mg)	Standard Deviation	Standard error	95% confidence Interval	
	A: RS (rpm)	B: TS (mm/min)	C: VF-Al_2O_3np (%)	Sample 1	Sample 2	Sample 3				Minimum	Maximum
1	900	50	7	10.54	9.72	10.33	10.20	0.43	0.25	9.7	10.7
2	700	40	10	10.81	10.37	10.26	10.48	0.29	0.17	10.2	10.8
3	900	50	7	9.98	10.12	10.44	10.18	0.24	0.14	9.9	10.4
4	1100	50	7	9.22	9.63	9.42	9.42	0.21	0.12	9.2	9.7
5	900	40	7	9.88	9.94	10.25	10.02	0.20	0.11	9.8	10.2
6	700	60	10	10.98	11.16	10.96	11.03	0.11	0.06	10.9	11.2
7	900	50	7	10.15	10.22	9.98	10.12	0.12	0.07	10.0	10.3
8	900	50	7	10.06	10.26	10.21	10.18	0.10	0.06	10.1	10.3
9	900	50	10	10.29	10.11	10.03	10.14	0.13	0.08	10.0	10.3
10	1100	40	4	9.88	9.96	9.70	9.85	0.13	0.08	9.7	10.0
11	1100	60	10	9.08	8.90	8.94	8.97	0.09	0.05	8.9	9.1
12	900	50	7	10.23	10.19	9.99	10.14	0.13	0.07	10.0	10.3
13	900	60	7	10.07	10.25	10.19	10.17	0.09	0.05	10.1	10.3
14	900	50	7	10.16	10.09	10.20	10.15	0.06	0.03	10.1	10.2
15	1100	40	10	9.21	9.28	8.98	9.16	0.16	0.09	9.0	9.3
16	900	50	4	10.40	10.51	10.54	10.48	0.07	0.04	10.4	10.6
17	1100	60	4	9.65	9.59	9.73	9.66	0.07	0.04	9.6	9.7
18	700	60	4	10.82	10.93	10.71	10.82	0.11	0.06	10.7	10.9
19	700	40	4	10.60	10.74	10.57	10.64	0.09	0.05	10.5	10.7
20	700	50	7	10.56	10.71	10.78	10.68	0.11	0.06	10.6	10.8

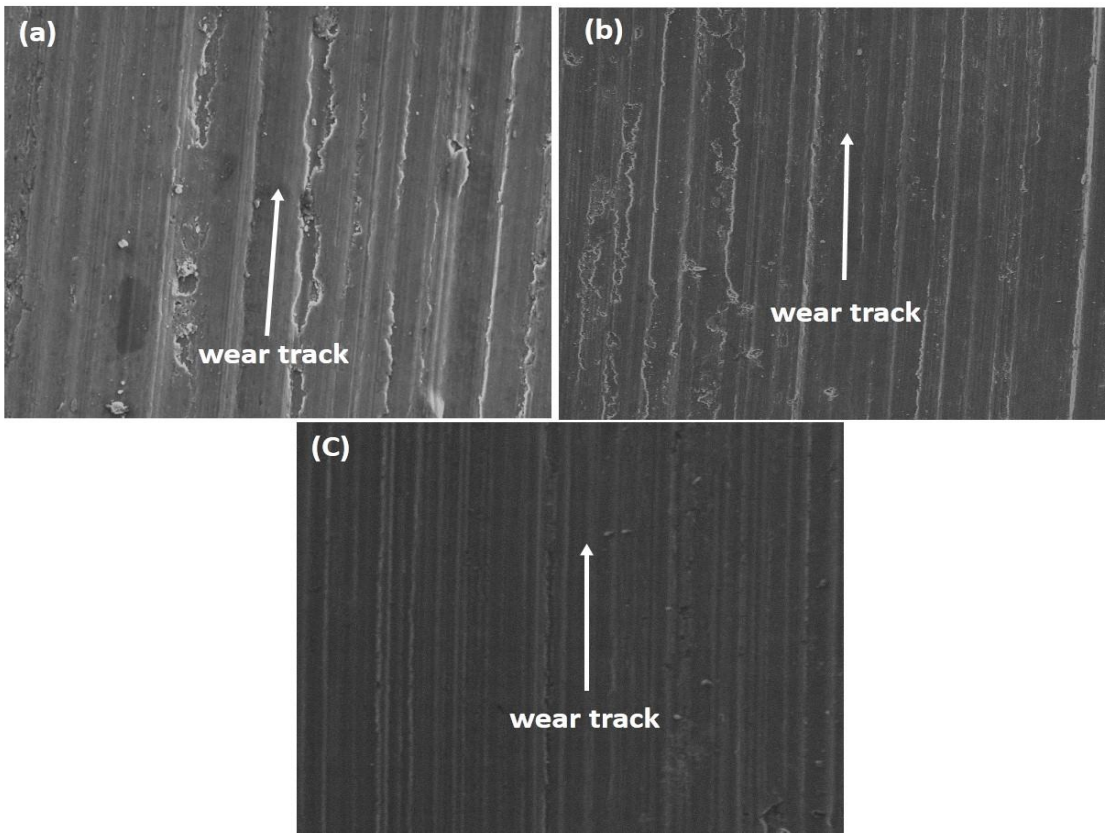

Figure 5.35: SEM photomicrograph of different composite joints, (a) specimen no- 6, (b) specimen no- 9, (c) specimen no- 11.

Consequently, small irregular pit along the sliding direction were observed in specimens processed at 700 rpm and 900 rpm (Fig. 5.35 a, b), which evident the poor particle-metal matrix bonding. A smooth wear track was observed at 1100 rpm, with small plastic deformation (Fig. 5.35 c). The homogenous distribution of hard Al_2O_3np after FSP at higher rotational speed offers enough hard larger surface area to prevent immediate deformation and loss of material during wear testing. Consequently, the avg. weight loss was found to be lower for specimen no- 11 processed at 1100 rpm, 60mm/min with 10% VF-Al_2O_3np in comparison other specimens. This ascribed to the presence of homogeneous dispersion of Al_2O_3np with higher volume fraction in the SZ of specimen no-11, which reduces the surface contact between the pin and the disk [121]. Hence, the specimen processed at 1100 rpm, 60mm/min with 10 % VF-Al_2O_3np had the best wear resistance among all selected welded specimens. Table 5.17 illustrated the avg. weight loss of all the FSPed composite joints. Hence, grain refinement, reduced surface contact between the pin and the disc due to hard Al_2O_3np, homogenous distribution of Al_2O_3np, and stronger bond between the Al_2O_3np and the

metal-matrix are all factors that contribute to the wear resistance of different composite joints.

5.6.4 Developing the mathematical model

Twenty experiments are utilized as input data to generate mathematical equation using response surface methodology using design expert software. The response functions are ultimate tensile strength, % elongation, micro-hardness and wear weight loss at stir zone whereas input parameters are rotational speed-A, traverse speed-B and volume fraction of Al_2O_3np-C. It may be expressed as

Tensile strength = *f (A, B, C)*

% Elongation = *f (A, B, C)*

Micro-hardness = *f (A, B, C)*

Wear behavior = *f (A, B, C)*

As a representation of the response surface, the second order polynomial regression equation is given by:

$Y=a_0+\sum a_i x_i+\sum a_{ii} x_i^2+\sum a_{ij} x_i x_j$

The selected polynomial can be represented as:

$Y=a_0 + a_1A+ a_2B+ a_3C+ a_{11}A^2+ a_{22}B^2+ a_{33}C^2+ a_{12}A\times B+ a_{13}A\times C+ a_{23}B\times C$

Where a_0 represents the mean response, a_1, a_2, and a_3 are linear terms, a_{11}, a_{22}, and a_{33} are quadratic terms, while a_{12}, a_{13}, and a_{23} are interaction terms. At a confidence level of 95%, the significance of each coefficient was assessed and tested. By employing the ANOVA technique and second order regression equations, the final mathematical model for the FSPed composite joint incorporating Al_2O_3np is presented below. In order for a model to be regarded acceptable with a 95% confidence level, the standard Fisher's F value must be higher than the estimated value of F. The models are significant when the lack of fit is not significant. Tables 5.18 to 5.21 provide the results of the ANOVAs for the responses for tensile strength, % elongation, micro-hardness at the stir zone, and wear (weight loss) at the stir zone for FSPed composite joints. The final mathematical empirical equation that was developed has been provided below in coded form.

$$\textbf{Tensile strength} = +201.12 +26.95\times A -2.88\times B +13.30\times C -3.69 \times AB +2.16\times AC +2.71\times BC +6.13\times A^2 +7.08\times B^2 -4.02\times C^2 \quad (5.13)$$

%Elongation = +21.23 +2.56×A -0.33×B +1.31×C -0.34×AB +0.21×AC +0.24×BC +0.64×A^2 +0.59×B^2 -0.41×C^2 (5.14)

Microhardness = 134.43 +16.00×A -2.40×B +8.10×C -2.12×AB +1.38×AC +1.38×BC +3.68×A^2 +4.68×B^2 -2.82 ×C^2 (5.15)

Wear (weight loss) = +10.17 -0.66× A +0.049× B -0.17× C -0.14×AB -0.18 ×AC +0.048× BC -0.13× A^2 -0.085×B^2 +0.13×C^2 (5.16)

The final mathematical model equations in terms of actual variables are represented in equations 5.17-5.20.

Tensile strength = +201.12 + 26.95 × Rotational speed - 2.88 × Traverse speed + 13.30 × VF-Al_2O_3np - 3.69 × Rotational speed × Traverse speed + 2.16 × Rotational speed × VF-Al_2O_3np + 2.71 × Traverse speed × VF-Al_2O_3np + 6.13 × Rotational $speed^2$ + 7.08 × Traverse $speed^2$ - 4.02 × VF-$Al_2O_3$$np^2$ (5.17)

%elongation = +21.23 + 2.56 × Rotational speed - 0.33 × Traverse speed + 1.31 × VF-Al_2O_3np - 0.34 × Rotational speed × Traverse speed + 0.21 × Rotational speed × VF-Al_2O_3np + 0.24 × Traverse speed × VF-Al_2O_3np + 0.64 × Rotational $speed^2$ + 0.59 × Traverse $speed^2$ - 0.41 × VF-$Al_2O_3$$np^2$ (5.18)

Micro-hardness = 134.43 +16.00 × Rotational speed -2.40 × Traverse speed + 8.10 × VF-Al_2O_3np - 2.12 × Rotational speed × Traverse speed + 1.38 × Rotational speed × VF-Al_2O_3np + 1.38 × Traverse speed × VF-Al_2O_3np + 3.68 × Rotational $speed^2$ + 4.68 × Traverse $speed^2$ - 2.82 × VF-$Al_2O_3$$np^2$ (5.19)

Wear (wt. loss) = +10.17 - 0.66 × Rotational speed + 0.049 × Traverse speed - 0.17 × VF-Al_2O_3np - 0.14 × Rotational speed × Traverse speed - 0.18 × Rotational speed × VF-Al_2O_3np + 0.048 × Traverse speed × VF-Al_2O_3np - 0.13 × Rotational $speed^2$ - 0.085 × Traverse $speed^2$ + 0.13 × VF-$Al_2O_3$$np^2$ (5.20)

The tool rotational speed coefficient (A) is positive, it implies that the tensile strength increases when the tool rotation speed increases, because at lower rotational speed produced insufficient heat input causes unusual material mixing resulting in agglomeration of Al_2O_3 particles. The uniform plastic flow and symmetric microstructure was observed in the stir zone (SZ) at increased rotational speed of 1100 rpm [122]. The VF of Al_2O_3np is also significantly affecting the tensile strength. Higher VF of Al_2O_3np shows the higher tensile strength, %elongation and micro-hardness and the lower wear weight loss.

Table 5.18: ANOVA for tensile strength (surface quadratic model)

Ultimate tensile Strength (UTS)						
Sources	SS	DOF	MS	F-value	P-value	
Model	9780.47	9	1086.72	151.20	< 0.0001	significant
A-RS	7263.02	1	7263.02	1010.57	< 0.0001	
B-TS	82.94	1	82.94	11.54	0.0068	
C-VF-Al_2O_3np	1768.90	1	1768.90	246.12	< 0.0001	
AB	108.78	1	108.78	15.14	0.0030	
AC	37.41	1	37.41	5.21	0.0457	
BC	58.86	1	58.86	8.19	0.0169	
A^2	103.24	1	103.24	14.37	0.0035	
B^2	137.74	1	137.74	19.17	0.0014	
C^2	44.50	1	44.50	6.19	0.0321	
Residual	71.87	10	7.19			
Lack of Fit	53.10	5	10.62	2.83	0.1392	not significant
Pure Error	18.77	5	3.75			
Cor Total	9852.34	19				
Std. Dev.	2.68	R^2		0.9927		
Mean	205.71	Adjusted R^2		0.9861		
C.V. %	1.30	Predicted R^2		0.9567		
PRESS	2.68	Adeq Precision		45.504		

Table 5.19: ANOVA for %elongation

% elongation						
Sources	SS	DOF	MS	F-value	P-value	
Model	89.39	9	9.93	147.26	< 0.0001	significant
A-RS	65.54	1	65.54	971.59	< 0.0001	
B-TS	1.09	1	1.09	16.14	0.0024	
C-VF-Al_2O_3np	17.16	1	17.16	254.42	< 0.0001	
AB	0.91	1	0.91	13.51	0.0043	
AC	0.36	1	0.36	5.36	0.0432	
BC	0.45	1	0.45	6.69	0.0271	
A^2	1.13	1	1.13	16.75	0.0022	
B^2	0.96	1	0.96	14.24	0.0036	
C^2	0.46	1	0.46	6.82	0.0259	
Residual	0.67	10	0.067			
Lack of Fit	0.43	5	0.085	1.72	0.2839	not significant
Pure Error	0.25	5	0.050			
Cor Total	90.07	19				
Std. Dev.	0.26	R^2		0.9925		
Mean	21.65	Adjusted R^2		0.9858		
C.V. %	1.20	Predicted R^2		0.9356		
		Adeq Precision		45.740		

Table 5.20: ANOVA for micro-hardness at stir zone

Micro-hardness						
Sources	SS	DOF	MS	F-value	P-value	
Model	3555.58	9	395.06	138.66	< 0.0001	significant
A-RS	2563.20	1	2563.20	899.65	< 0.0001	
B-TS	58.08	1	58.08	20.39	0.0011	
C-VF-Al_2O_3np	687.24	1	687.24	241.21	< 0.0001	
AB	33.62	1	33.62	11.80	0.0064	
AC	17.41	1	17.41	6.11	0.0330	
BC	16.82	1	16.82	5.90	0.0355	
A^2	38.02	1	38.02	13.34	0.0044	

B^2	61.22	1	61.22	21.49	0.0009	
C^2	24.45	1	24.45	8.58	0.0151	
Residual	28.49	10	2.85			
Lack of Fit	15.84	5	3.17	1.25	0.4058	not significant
Pure Error	12.66	5	2.53			
Cor Total	3584.07	19				
Std. Dev.	1.69	R^2		0.9921		
Mean	137.25	Adjusted R^2		0.9849		
C.V. %	1.23	Predicted R^2		0.9404		
		Adeq Precision		44.76		

Table 5.21: ANOVA for wear (weight loss) at stir zone

Wear (weight loss)						
Sources	SS	DOF	MS	F-value	P-value	
Model	5.17	9.00	0.57	208.36	< 0.0001	significant
A-RS	4.33	1.00	4.33	1569.28	< 0.0001	
B-TS	0.02	1.00	0.02	8.70	0.0145	
C-VF-Al_2O_3np	0.28	1.00	0.28	102.30	< 0.0001	
AB	0.16	1.00	0.16	56.83	< 0.0001	
AC	0.26	1.00	0.26	93.95	< 0.0001	
BC	0.02	1.00	0.02	6.54	0.0285	
A^2	0.05	1.00	0.05	16.84	0.0021	
B^2	0.02	1.00	0.02	7.20	0.0230	
C^2	0.05	1.00	0.05	16.84	0.0021	
Residual	0.03	10.00	0.002			
Lack of Fit	0.02	5.00	0.004	3.65	0.0908	not significant
Pure Error	0.01	5.00	0.001			
Cor Total	5.20	19.00				
Std. Dev.	0.053	R-Squared		0.9947		
Mean	10.12	Adj R-Squared		0.9809		
C.V. %	0.52	Pred R-Squared		0.9188		
		Adeq Precision		52.66		

5.6.5 Adequacy of developed model

Table 5.18 to 5.21 presents the statistical findings of the empirical correlation that was developed. when R^2 value is 1, the value of predicted empirical relationship perfectly matched the experimental value. The value of R^2 approaches 1 and lower value to standard error indicate that the empirical relationships are sufficient and can be utilized to predict the responses without a significant amount of error.

The higher adjusted R^2 value suggests more meaningful variables in the current model and increases variation. In this developed model, results give a higher R^2 value of 0.9927, 0.9925, 0.9921 and 0.9947 and adjusted R^2 value of 0.9861, 0.9858, 0.9849 and 0.9809 for ultimate tensile strength, % elongation, micro-hardness at SZ and wear (weight loss) at SZ respectively. When the rotational speed of tool is 700 rpm then the agglomeration of Al_2O_3np at rotational speed was observed due to insufficient of material maxing due to insufficient heat generation FSPed composite joints, whereas at higher RS of 1100 rpm uniform dispersion of Al_2O_3np was observed due to sufficient material mixing caused by sufficient plastic strain caused by enhanced tool's stirring action. ANOVA Table 5.18 for tensile strength of FSPed composite joints of AA6061 and AA7075 incorporated with Al_2O_3np shows the Fisher's F value of 151.20 for the tensile strength indicating that the model is significant. The ANOAVA Table 5.19 shows the elongation of FSPed composite joint, value of the fisher's F is 147.26, indicates that the model is significant. The R^2 value demonstrates how well the models are fit. Value of R^2 which is 0.9927 for tensile strength indicating 99.27% of the complete variability which is evaluated by the model after taking into account the essential factors. The difference between the value of R^2 (99.27%) and adjusted R^2 (98.61%) is 0.66%, indicating that the model does not explain 0.66 % of the total variation and the model is not over fitted. According to ANOVA surface quadratic model (Table 5.18-5.21) the fisher's F value for % elongation, micro-hardness at SZ, and wear (weight loss) at SZ is 147.26, 138.66, and 208.36, respectively. These results demonstrated the model's importance.

5.6.6 Process parameter effects on response parameters

The predicted values vs. actual experimental values for ultimate tensile strength, micro-hardness, % elongation and wear weight loss of FSPed composite joints incorporated with Al_2O_3np as presented in Fig. 5.36. The scattered plots are observed very closed to

45º line; it shows the response variables are lying on the straight lines indicating the uniform scattering of error throughout the model. The plot of the response values' experimental and anticipated values demonstrates remarkable correlation. The aforementioned correlation reveals that the regression models are adequate.

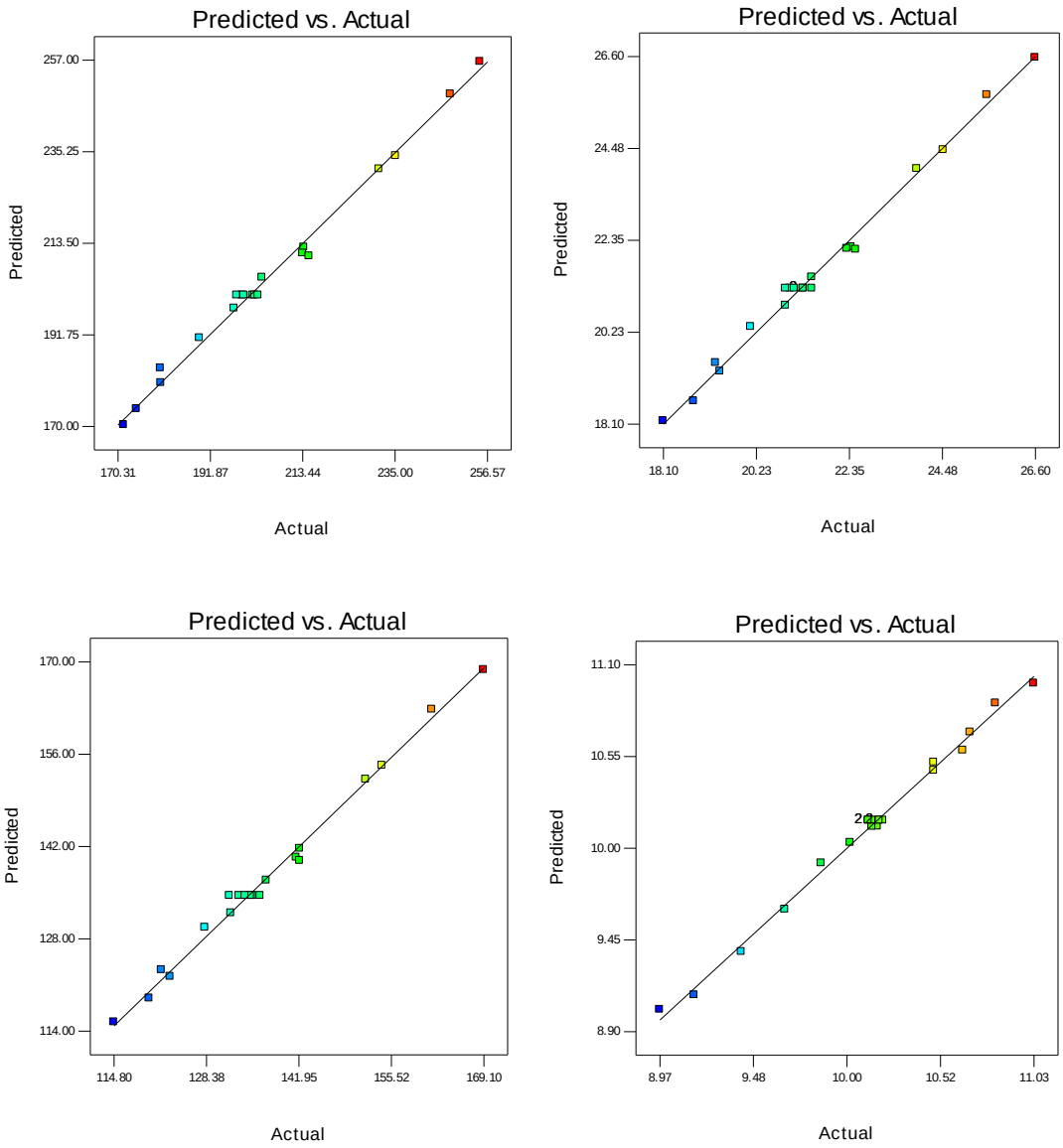

Figure 5.36: Predicted vs experimental, (a) Tensile strength, (b) %Elongation, (c) Micro-hardness, (d) Wear behaviour

Fig. 5.37-5.40, shows the 3D responses surfaces plot and contour of tensile strength, microhardness, %elongation and wear weight loss at stir zone from the regression model. The apex of the response surfaces displays the best output responses. By analyzing the 3D responses and contour plots, it is simpler to see how different factors interact to affect the response.

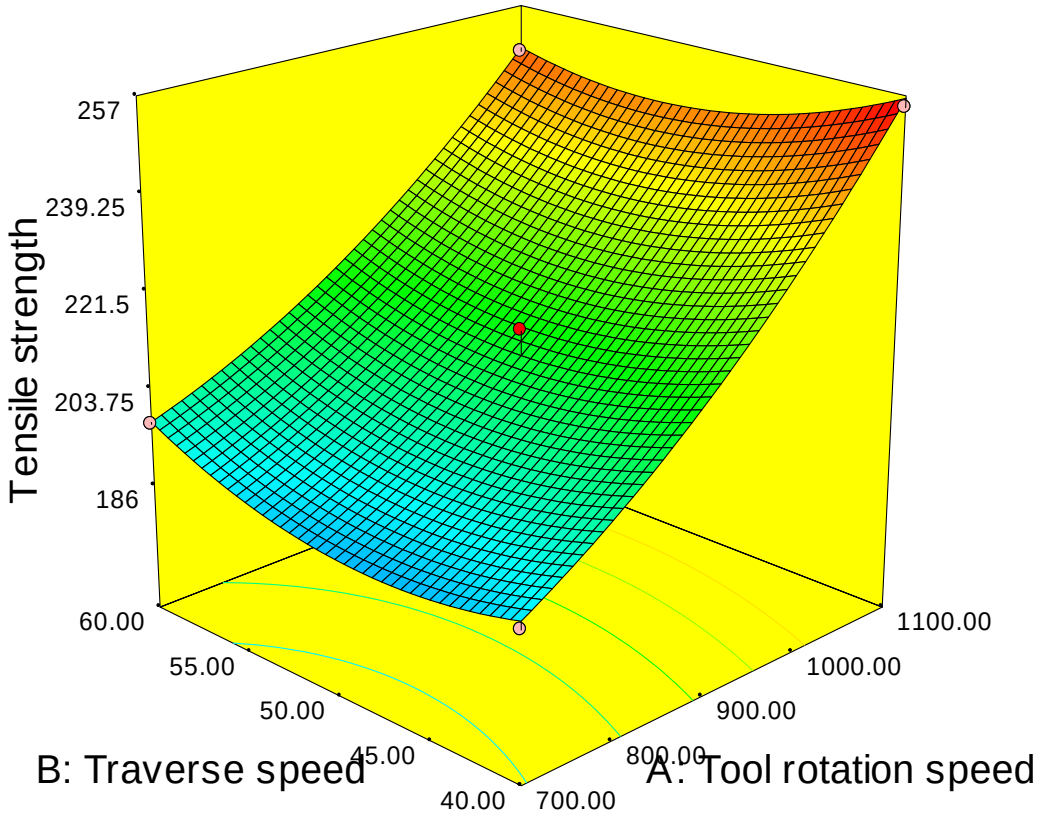
Tensile strength
257
239.25
221.5
203.75
186
60.00
55.00
50.00
45.00
40.00
B: Traverse speed
700.00
800.00
900.00
1000.00
1100.00
A: Tool rotation speed

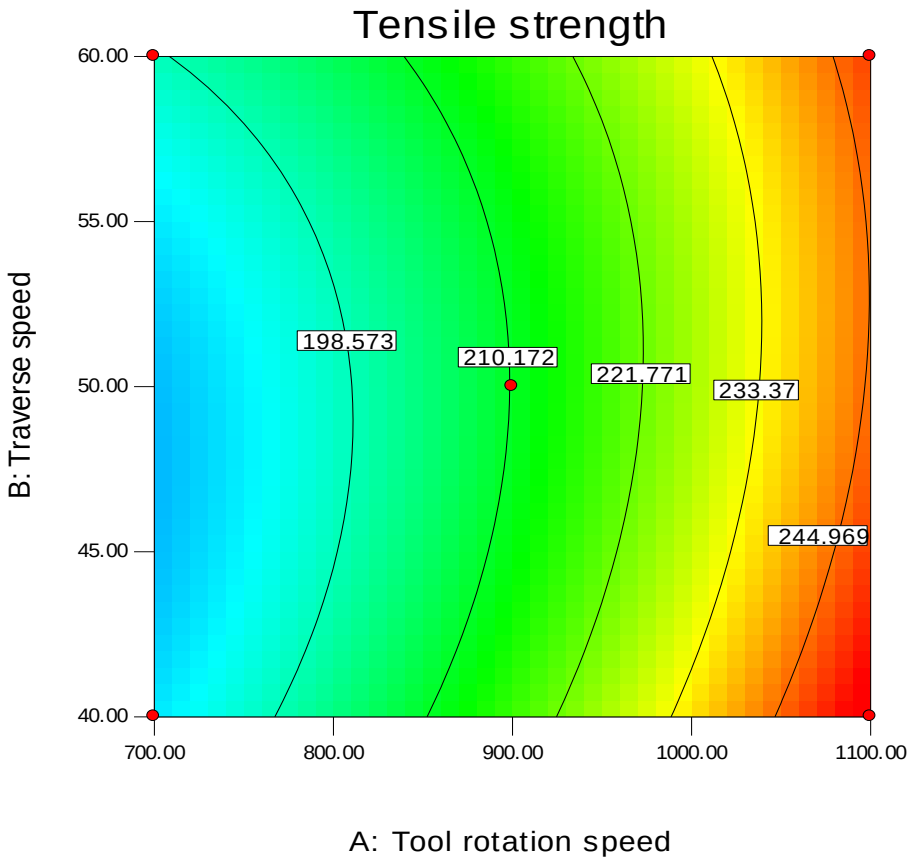
Tensile strength
60.00
55.00
50.00
45.00
40.00
B: Traverse speed
198.573
210.172
221.771
233.37
244.969
700.00
800.00
900.00
1000.00
1100.00
A: Tool rotation speed

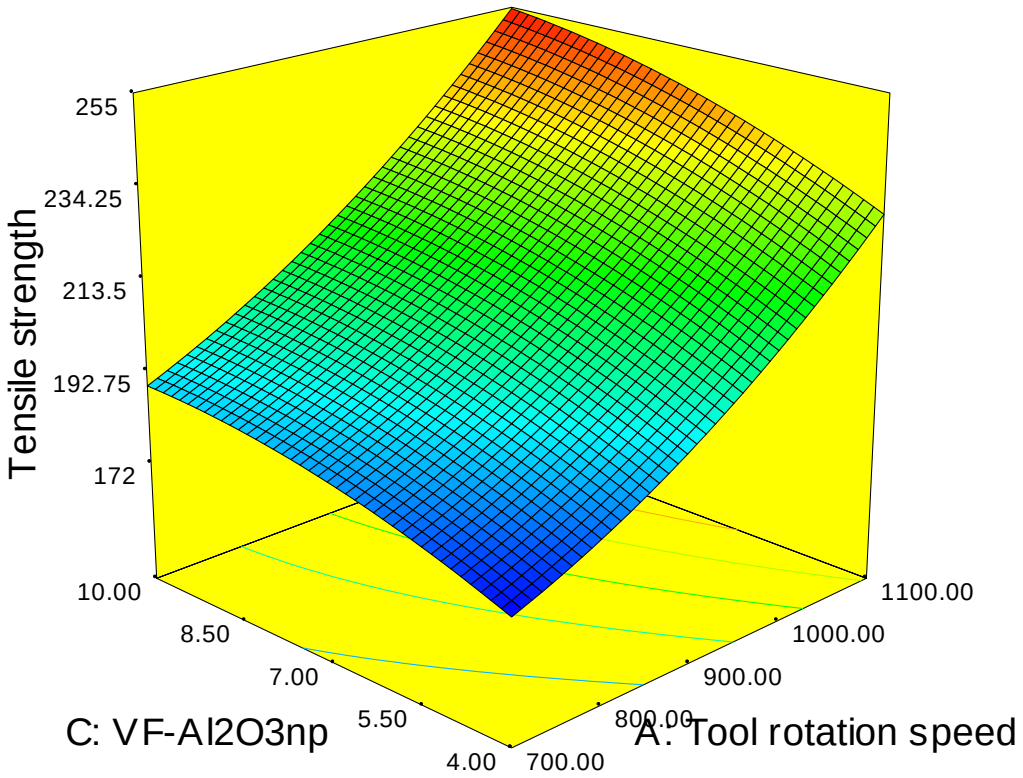
Tensile strength
255
234.25
213.5
192.75
172
10.00
8.50
7.00
5.50
4.00
C: VF-Al2O3np
700.00
800.00
900.00
1000.00
1100.00
A: Tool rotation speed

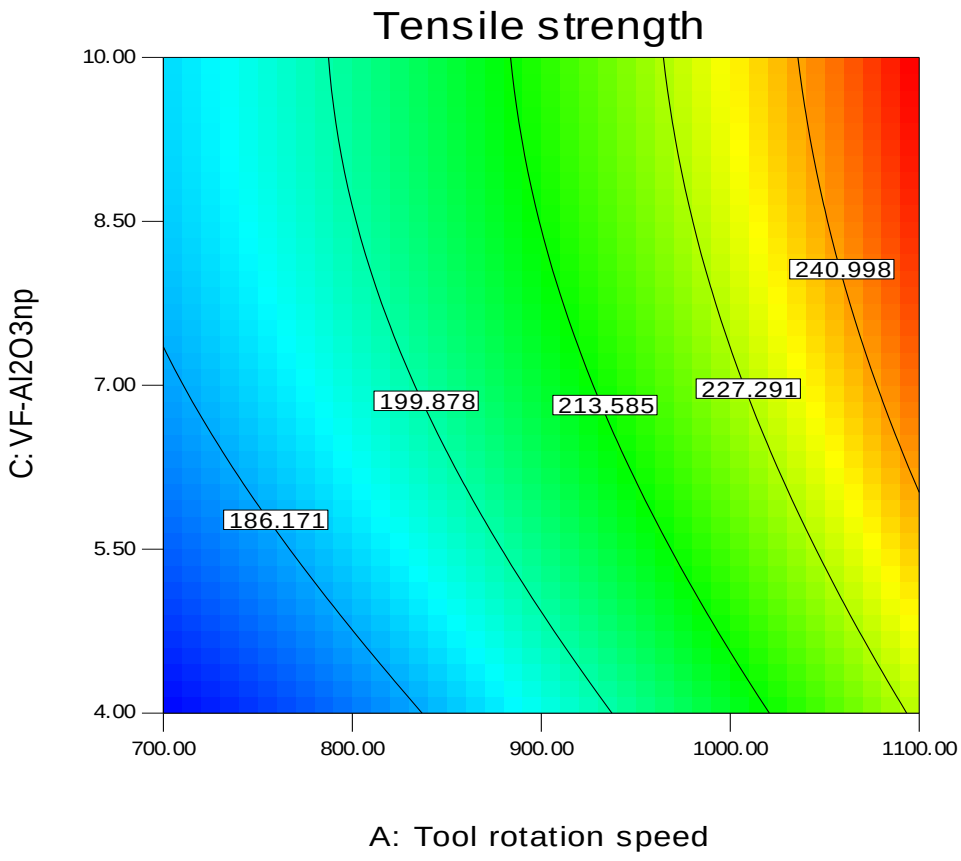
Tensile strength
10.00
8.50
7.00
5.50
4.00
C: VF-Al2O3np
186.171
199.878
213.585
227.291
240.998
700.00
800.00
900.00
1000.00
1100.00
A: Tool rotation speed

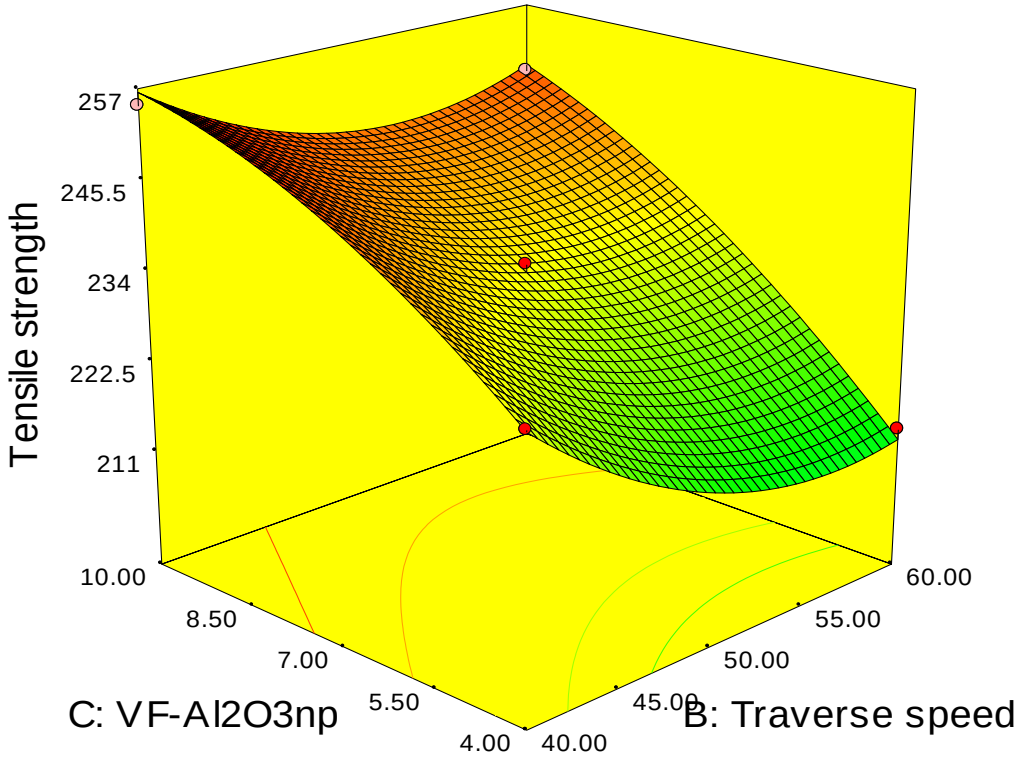

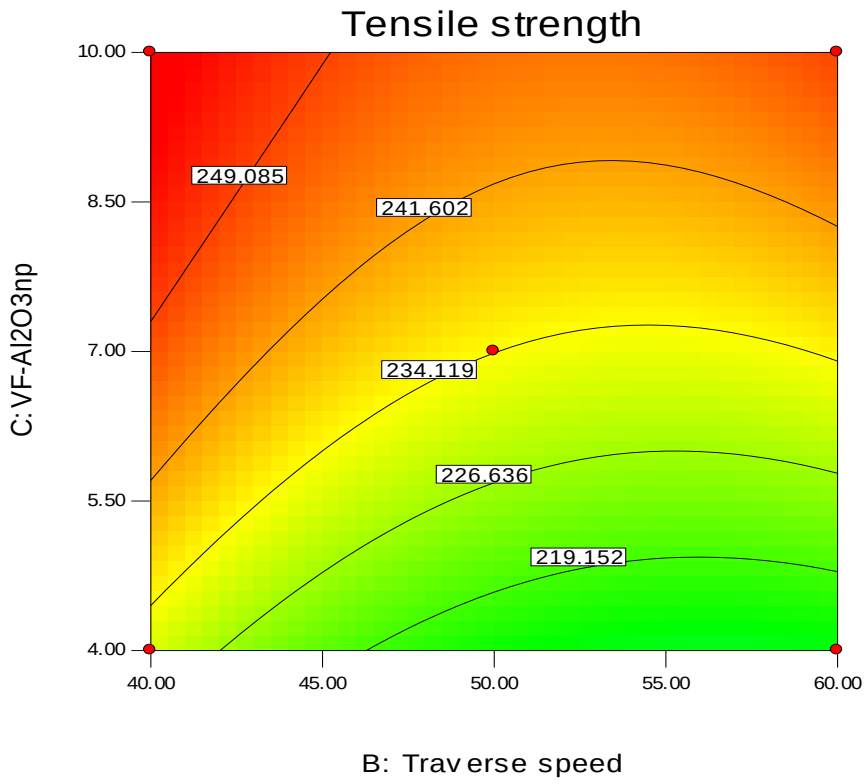

Figure 5.37: 3D response surface and contour plots of tensile strength of composite joints incorporated with Al_2O_3np

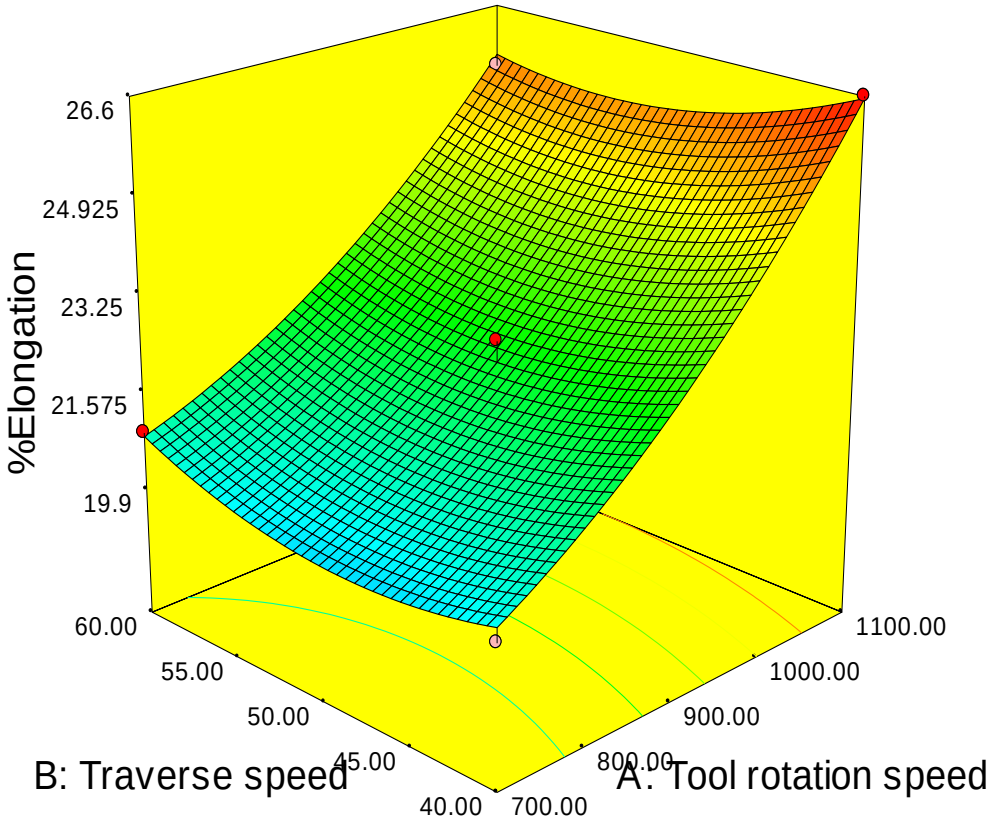
%Elongation
26.6
24.925
23.25
21.575
19.9
60.00
55.00
50.00
45.00
40.00
B: Traverse speed
700.00
800.00
900.00
1000.00
1100.00
A: Tool rotation speed

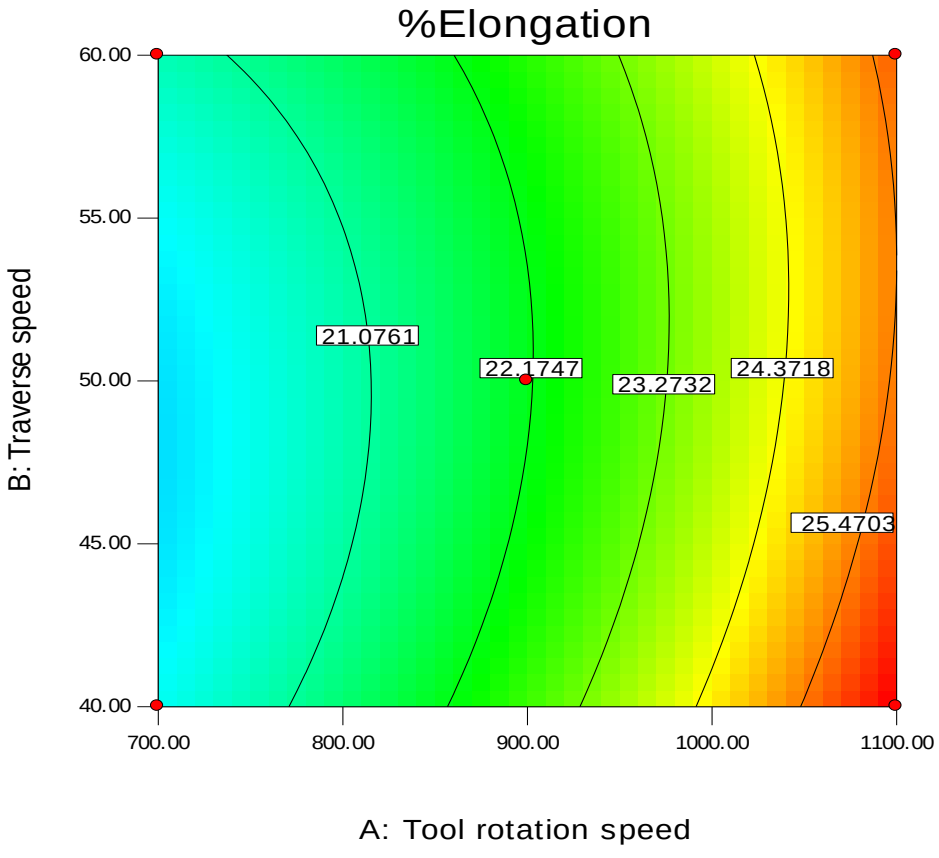
%Elongation
60.00
55.00
50.00
45.00
40.00
B: Traverse speed
21.0761
22.1747
23.2732
24.3718
25.4703
700.00
800.00
900.00
1000.00
1100.00
A: Tool rotation speed

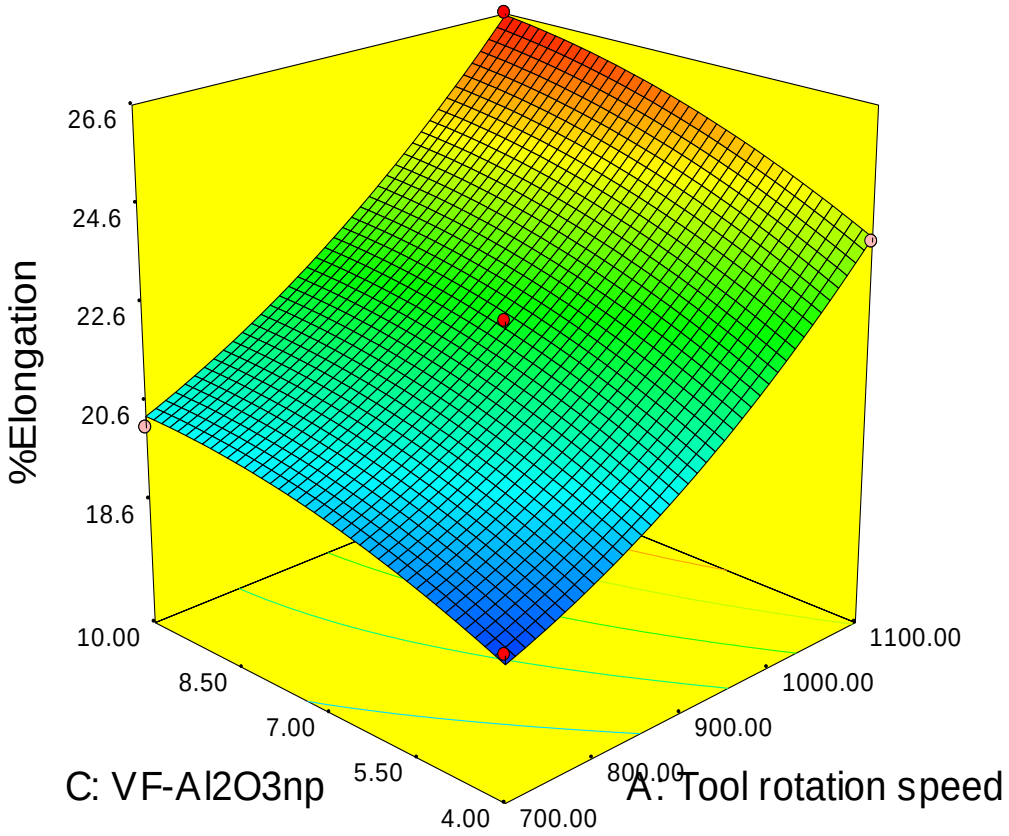
%Elongation
26.6
24.6
22.6
20.6
18.6
10.00
8.50
7.00
5.50
4.00
C: VF-Al2O3np
700.00
800.00
900.00
1000.00
1100.00
A: Tool rotation speed

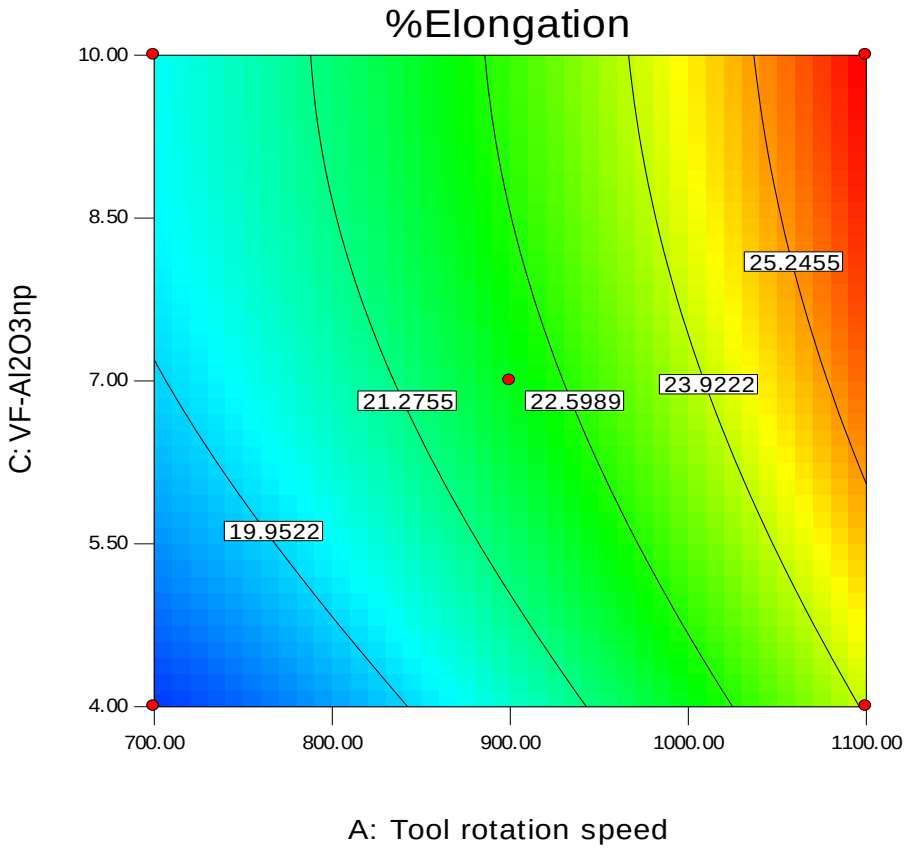
%Elongation
10.00
8.50
7.00
5.50
4.00
C: VF-Al2O3np
25.2455
23.9222
22.5989
21.2755
19.9522
700.00
800.00
900.00
1000.00
1100.00
A: Tool rotation speed

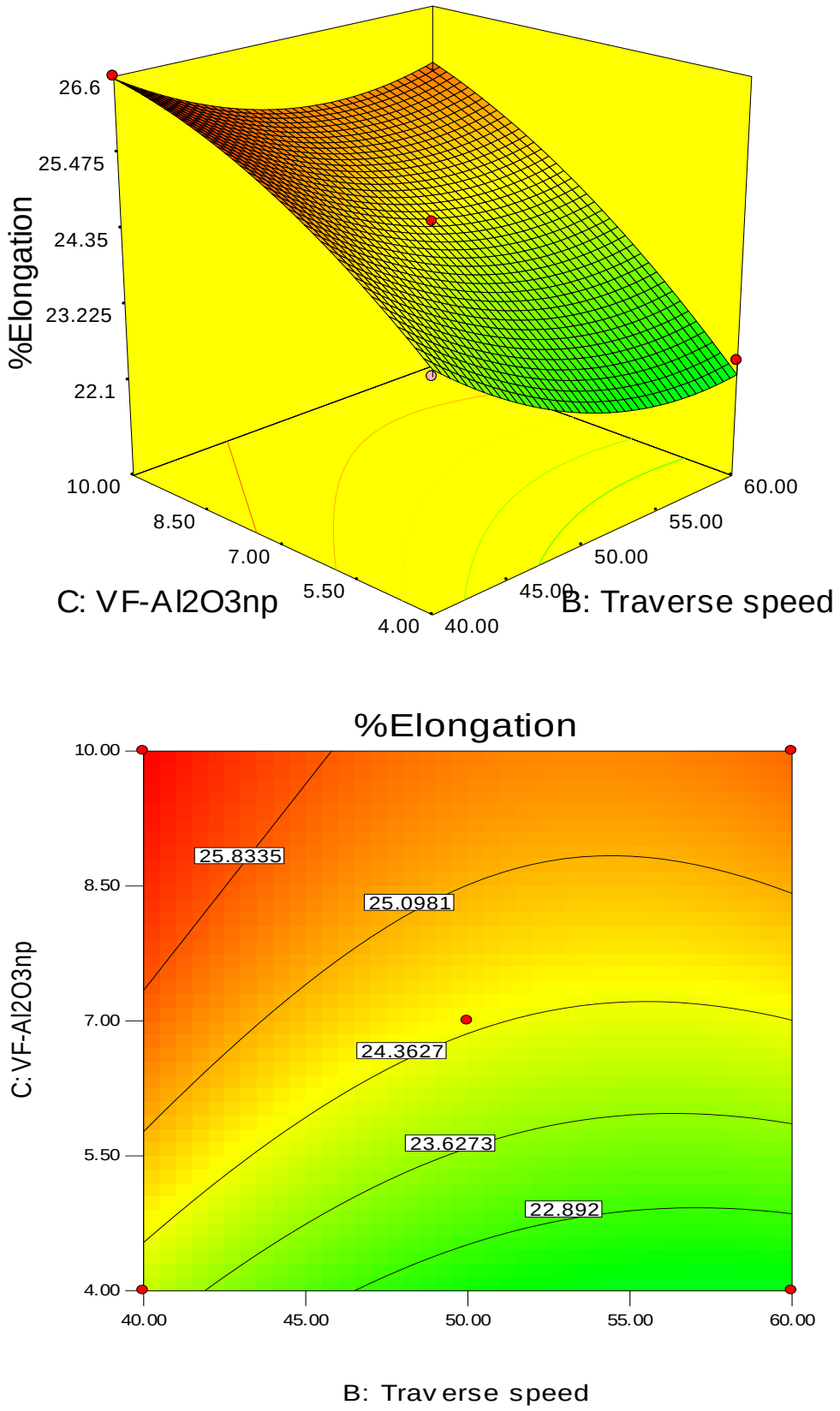

Figure 5.38: 3D response surface and contour plots of %elongation of composite joints incorporated with Al_2O_3np

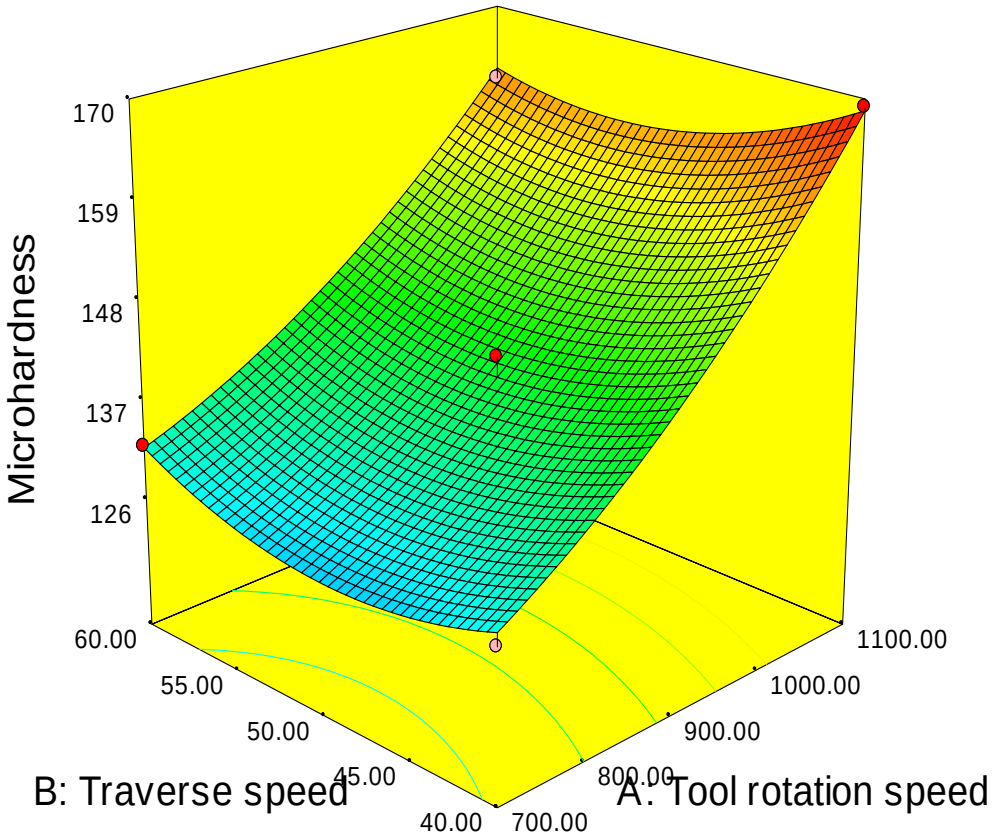
Microhardness
170
159
148
137
126
60.00
55.00
50.00
45.00
40.00
B: Traverse speed
700.00
800.00
900.00
1000.00
1100.00
A: Tool rotation speed

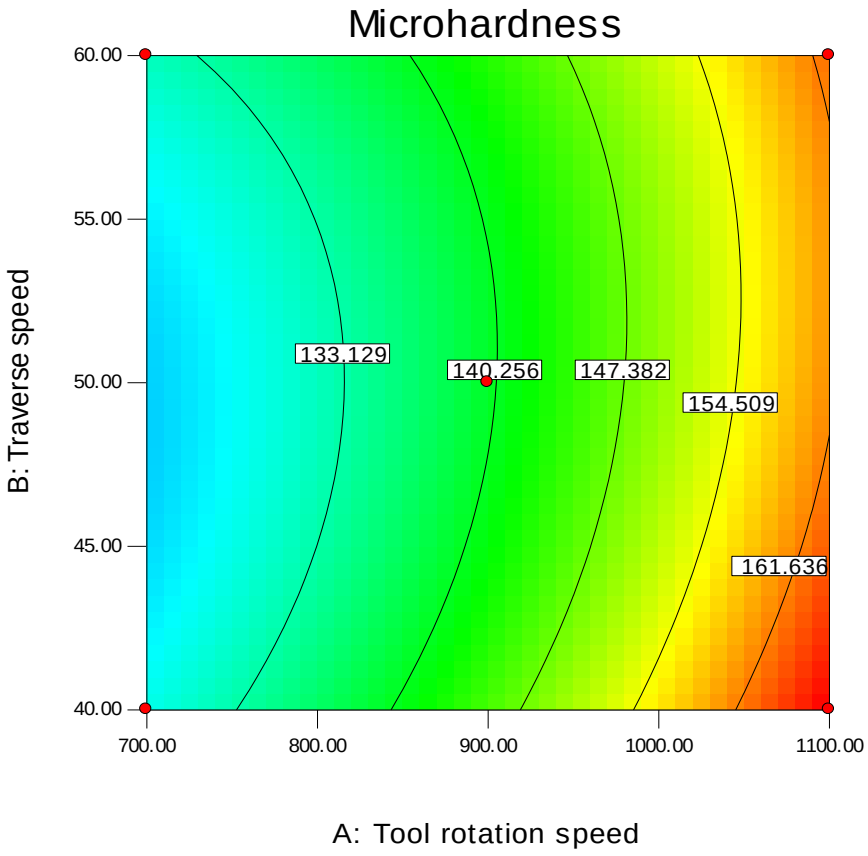
Microhardness
60.00
55.00
50.00
45.00
40.00
B: Traverse speed
133.129
140.256
147.382
154.509
161.636
700.00
800.00
900.00
1000.00
1100.00
A: Tool rotation speed

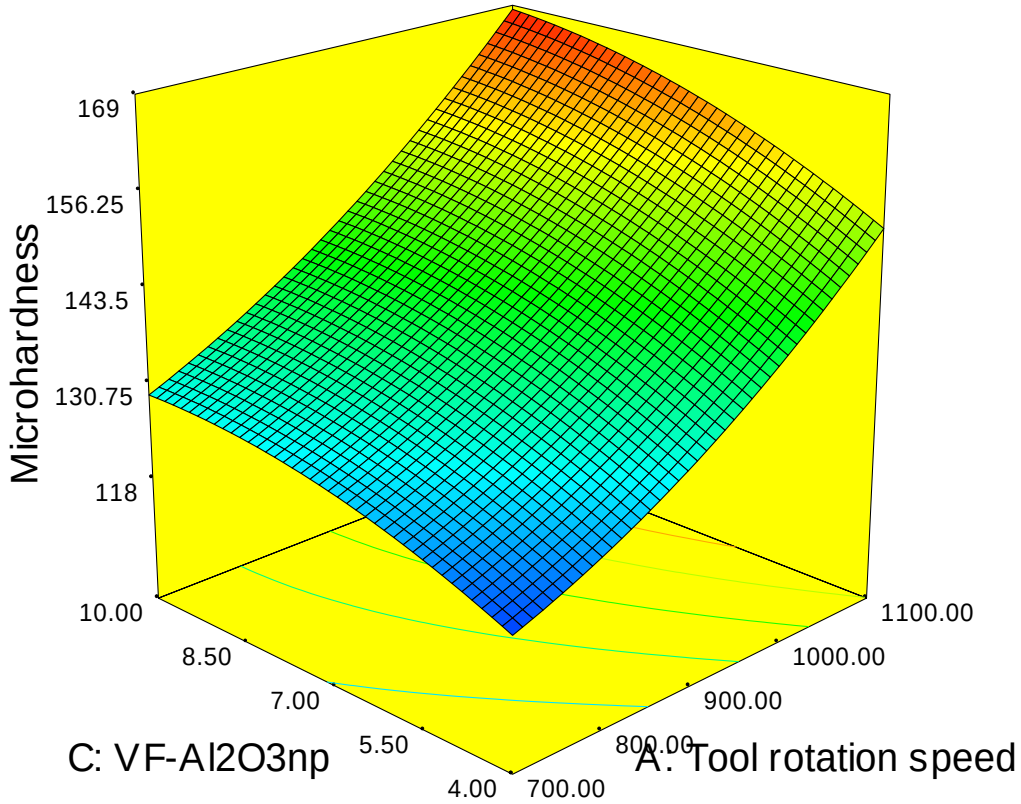
Microhardness
169
156.25
143.5
130.75
118
10.00
8.50
7.00
5.50
4.00
C: VF-Al2O3np
700.00
800.00
900.00
1000.00
1100.00
A: Tool rotation speed

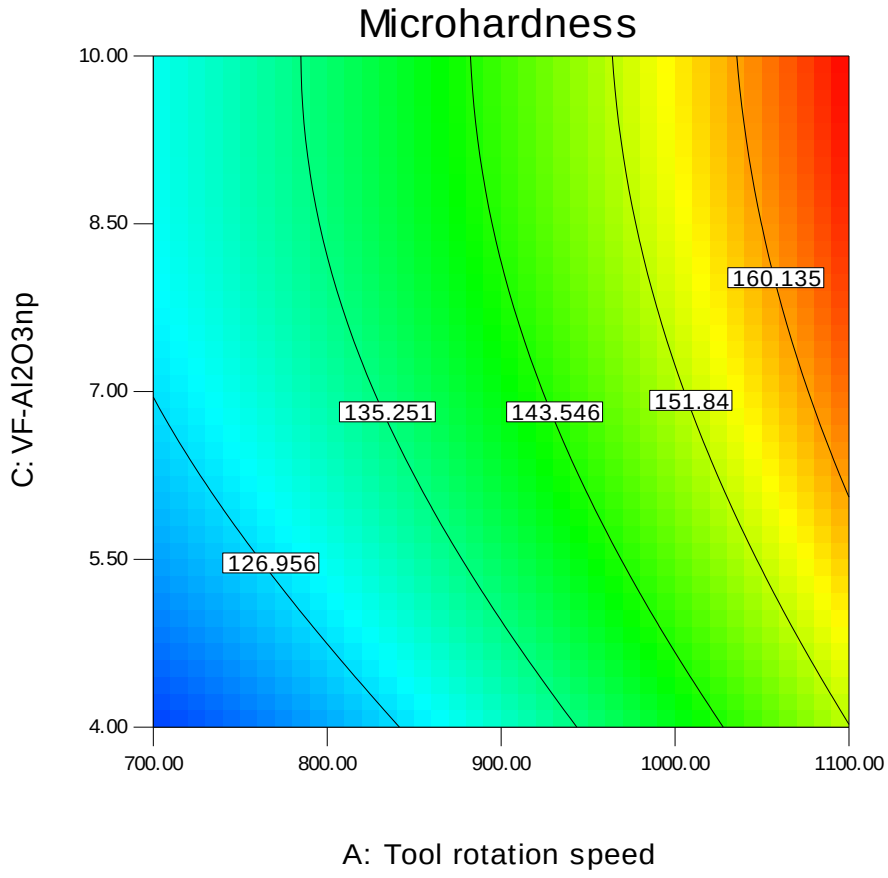
Microhardness
10.00
8.50
7.00
5.50
4.00
C: VF-Al2O3np
160.135
151.84
143.546
135.251
126.956
700.00
800.00
900.00
1000.00
1100.00
A: Tool rotation speed

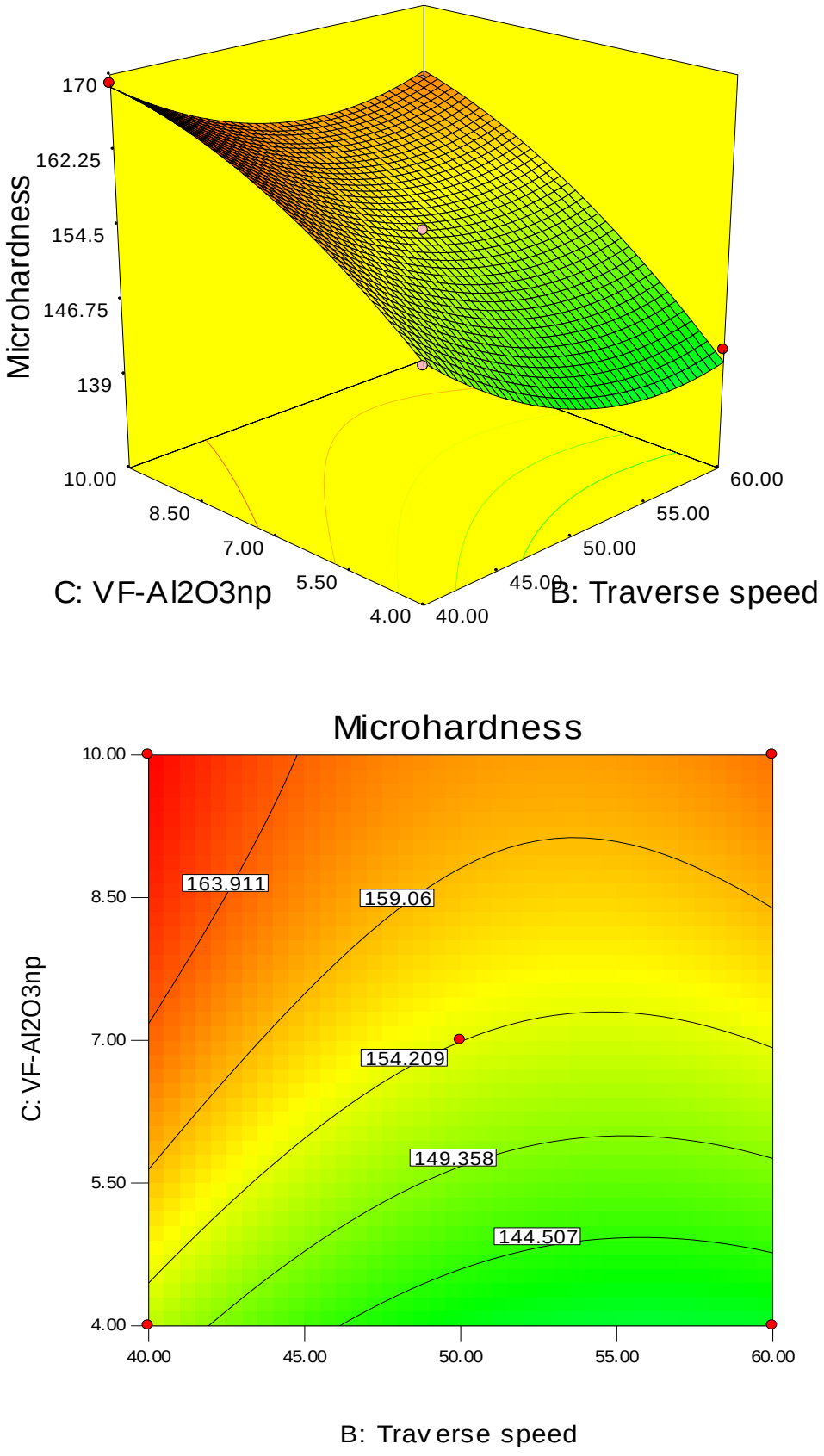

Figure 5.39: 3D response surface and contour plots of micro-hardness at stir zone of composite joints incorporated with Al_2O_3np

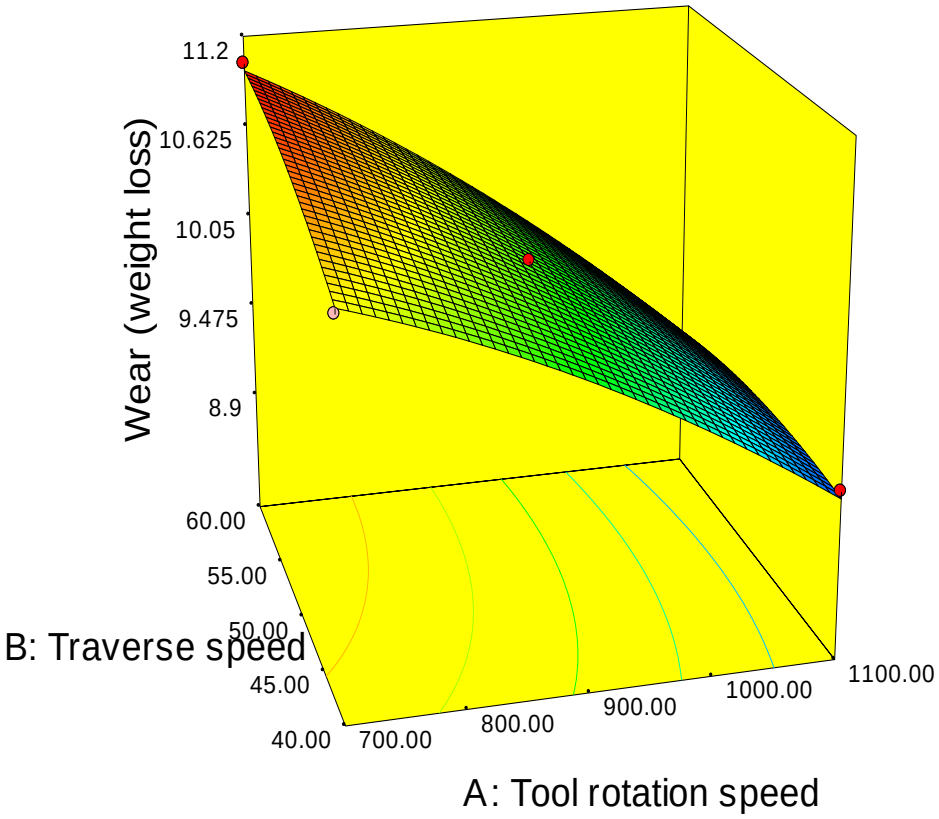
Wear (weight loss)
11.2
10.625
10.05
9.475
8.9
B: Traverse speed
60.00
55.00
50.00
45.00
40.00
700.00
800.00
900.00
1000.00
1100.00
A: Tool rotation speed

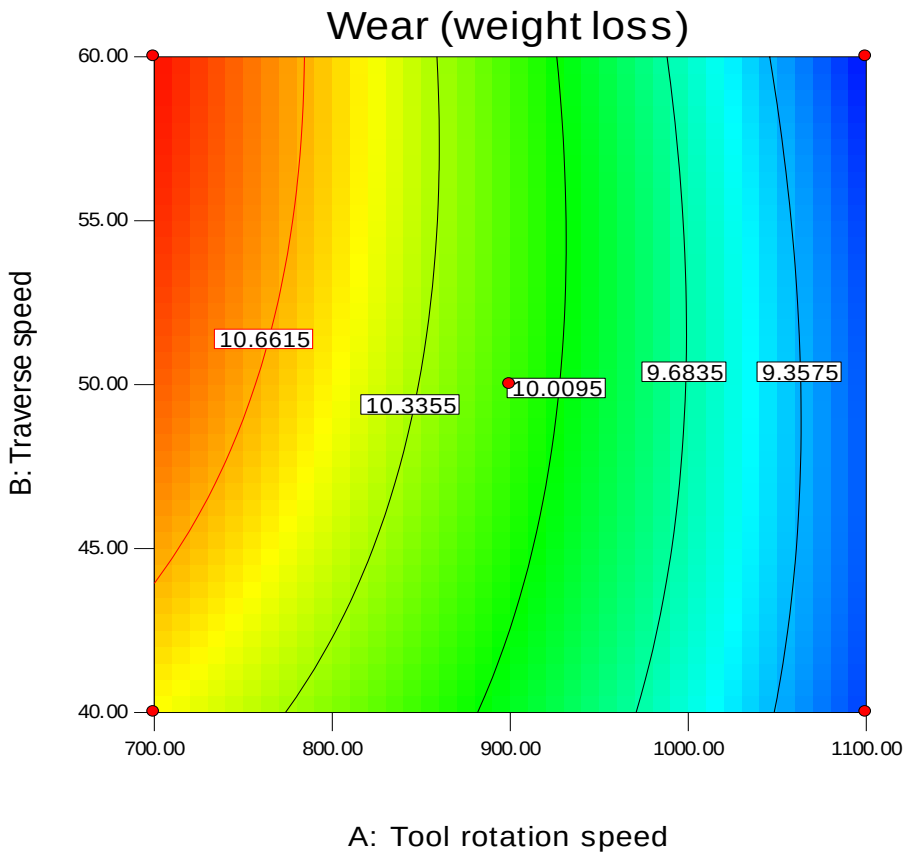
Wear (weight loss)
B: Traverse speed
60.00
55.00
50.00
45.00
40.00
10.6615
10.3355
10.0095
9.6835
9.3575
700.00
800.00
900.00
1000.00
1100.00
A: Tool rotation speed

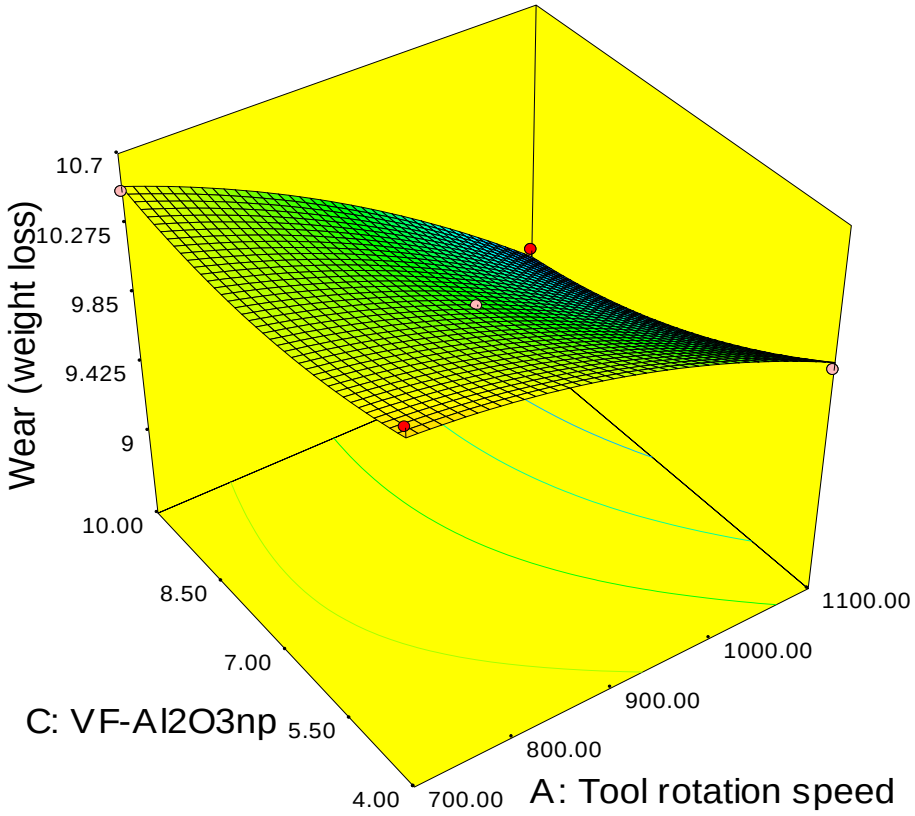
Wear (weight loss)
10.7
10.275
9.85
9.425
9
10.00
8.50
7.00
5.50
4.00
C: VF-Al2O3np
700.00
800.00
900.00
1000.00
1100.00
A: Tool rotation speed

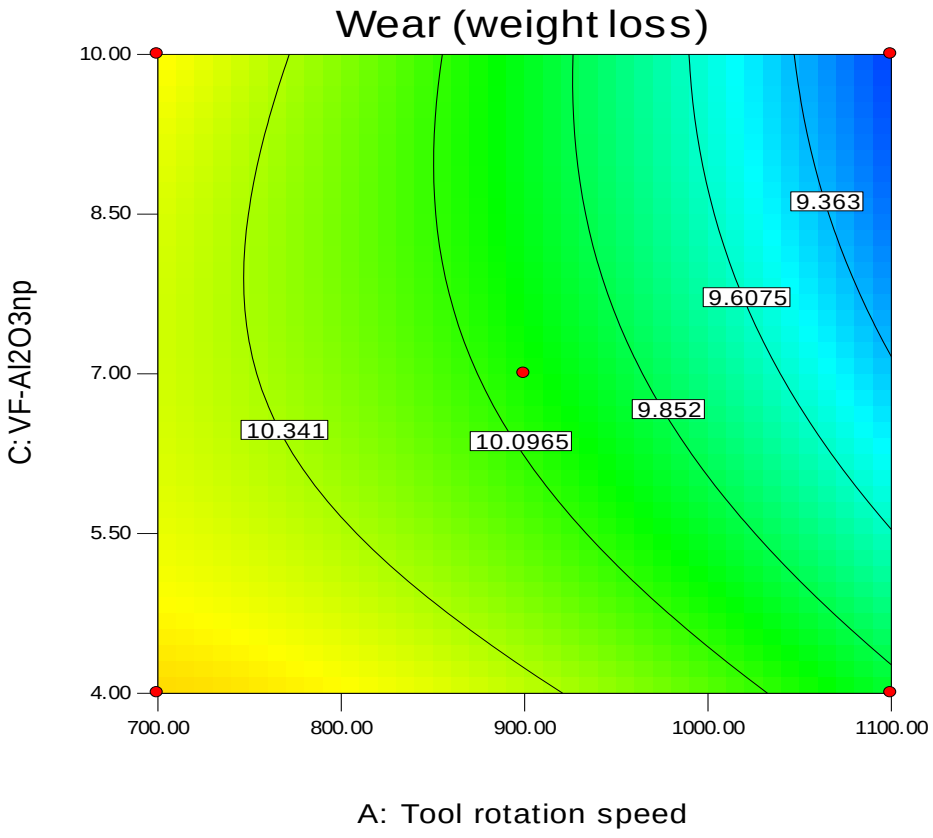
Wear (weight loss)
10.00
8.50
7.00
5.50
4.00
C: VF-Al2O3np
9.363
9.6075
9.852
10.0965
10.341
700.00
800.00
900.00
1000.00
1100.00
A: Tool rotation speed

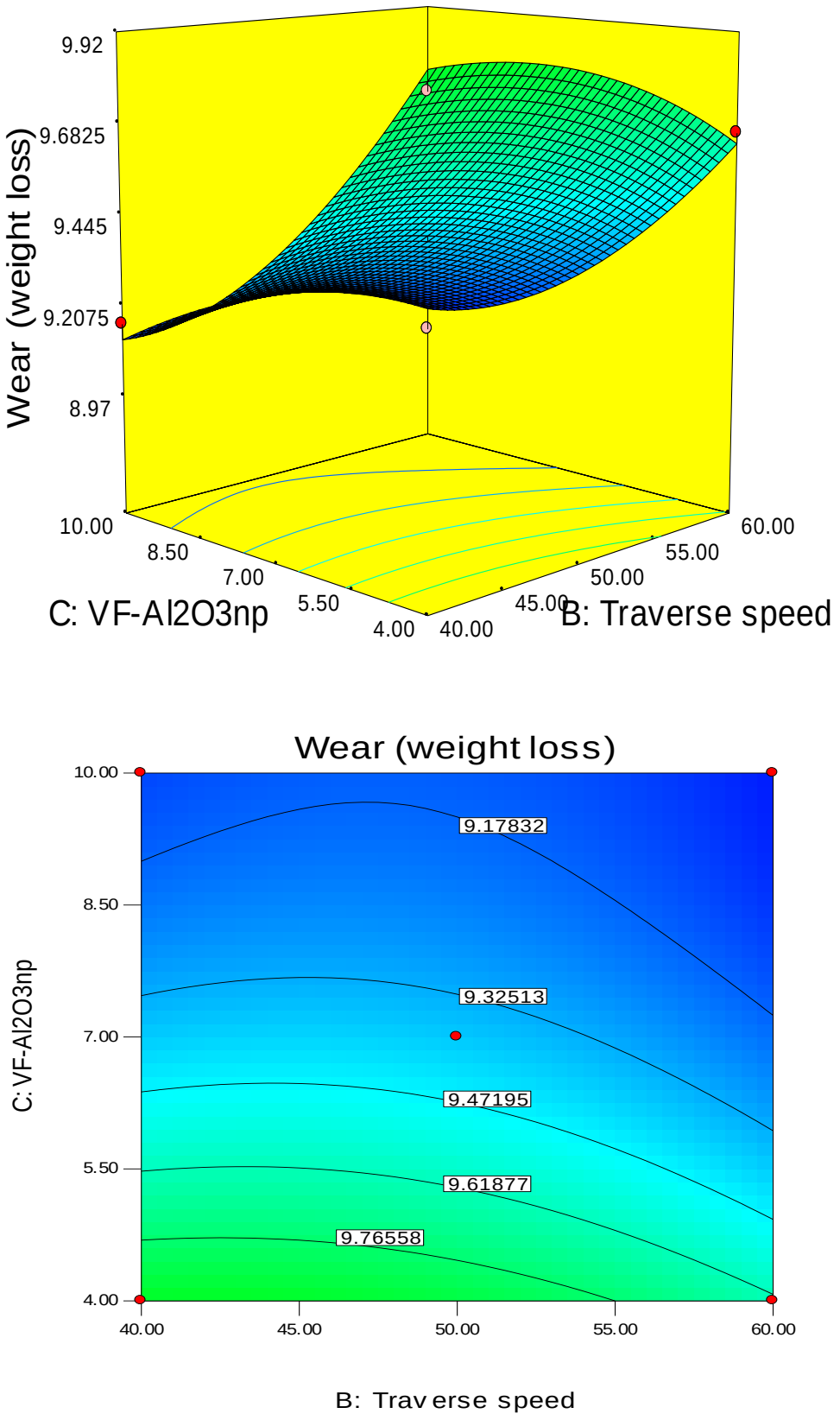

Figure 5.40: 3D response surface and contour plots of wear (weight loss) of composite joints incorporated with Al_2O_3np

The significance of grain refinement can be revealed by dynamic recrystallisation and pinning effect caused by Al_2O_3np. It can be observed that increasing tool rotation speed increases the tensile strength due to more uniform dispersion of speed Al_2O_3np resulting in enhanced pinning effect and reduced the grain size. As the traverse speed increases, tensile strength decreases. The minimum tensile strength of.171.70 MPa was observed at RS- 700 rpm, TS- 60 mm/min with 4% VF-Al_2O_3np due to unusual material mixing caused by inadequate tool stirring action. The highest tensile strength of 254.90 MPa was obtained at RS-1100 rpm, TS-40 mm/min with 10% VF-Al_2O_3np, when the traverses speed decreases, the tensile strength and micro-hardness increases. Improved material mixing in stir region was also observed at lower traverse speed leading to enhancement in tensile strength and micro-hardness of the composite joints as shown in Fig. (5.37-5.40).

5.7 MULTI RESPONSE OPTIMIZATION: DESIRABILITY

Desirability is a multiple response technique that Derringer and Suich [97] explain. It is a method for the optimization of several quality characteristic problems which is relevant to industry. The approach converts an estimated response into a scale-free value (di) termed desirability by using an objective function, D(X), known as the desirability function (utility transfer function). The weighted geometric mean of each response's individual desirability is known as the composite desirability. The ideal parameter circumstances are regarded to be the factor settings that have the highest overall desirability. The optimization is carried through using:

(i) Determining each response's specific desirability (d);

(ii) Obtained the composite desirability (D) by combining the specific desirability and;

(iii) Identifying the optimal settings by maximizing the obtained composite desirability.

In the present investigation, desirability function is employed to obtained the optimal parameters for FSPed composite joints to optimize tensile strength, % elongation, microhardness and wear behavior. In order to determine the best combination of variables and levels for the friction stir processing of AA6061 and AA7075, a second order CCD with three variables (tool rotation speed, traverse speed, and volume % of

Al_2O_3np) each at three levels was utilized. The desirability function was used to achieve the multi-response optimization.

5.7.1 Multi response optimization

To effectively assess the effect of each response on overall desirability, limits and goals for each response were specified. Weights are applied in order to highlight a goal value, the upper or lower boundaries, or both. According to the particular industry, importance is allocated. Importance varies 1 to 3, 1 is allocated for the least important and 3 to the most important.

The goals and importance of input parameters like tool rotation speed, traverse speed and volume fraction of Al_2O_3np, and the response parameters like tensile strength, micro-hardness, % elongation and wear behaviour are given in Table 5.22. Tensile strength, micro-hardness, %elongation and wear behavior all have been assigned with an importance of 3, lower and upper weight for UTS, % elongation, micro-hardness and wear behaviour is to be assigned 1. Finding an optimal set of conditions that will meet all the goals is the major objective of the optimization process. The value of desirability does not mandatory to be 1 as if the any one response is increases then the other decreases. In other words, the value depends solely on how nearly the lower and upper limits are selected in relation to the actual optimum. For the given design space constraints, seven optimal solutions are derived as tabulated in Table 5.23. The set of optimal parameters having higher desirability required for get the desired response parameters within the constraints is tabulated in Table 5.23.

Table 5.22: Range and importance of Input and Response Parameters

Name	Goal	Lower Limit	Upper Limit	Lower Weight	Upper Weight	Importance
Tool rotation speed	is in range	700	1100	1	1	3
Traverse speed	is in range	40	60	1	1	3
VF-Al_2O_3np	is in range	4	10	1	1	3
Tensile strength	is in range	171.7	254.9	1	1	3
%Elongation	is in range	18.1	26.6	1	1	3
Microhardness	is in range	114.8	169.1	1	1	3
Wear (wt. loss)	is in range	8.97	11.03	1	1	3

Table 5.23: Set of Optimal Solutions

Number	RS	TS	VF-Al_2O_3np	Tensile strength	%El	Micro-hardness	Wear (weight Loss)	Desirability	
1	1089.4	58.09	8.74	240.45	24.95	157.89	9.17	1	Selected
2	895.64	52.8	9.96	210.21	22.09	139.53	10.17	1	
3	851.36	56.18	7.01	196.47	20.73	131.51	10.34	1	
4	989.96	57.55	5.64	206.85	21.68	137.48	9.91	1	
5	731.32	50.62	7.22	183.64	19.61	124.16	10.64	1	
6	705.92	56.47	9.87	192.87	20.43	128.92	10.92	1	
7	843.12	48.47	9.42	201.67	21.32	134.89	10.31	1	

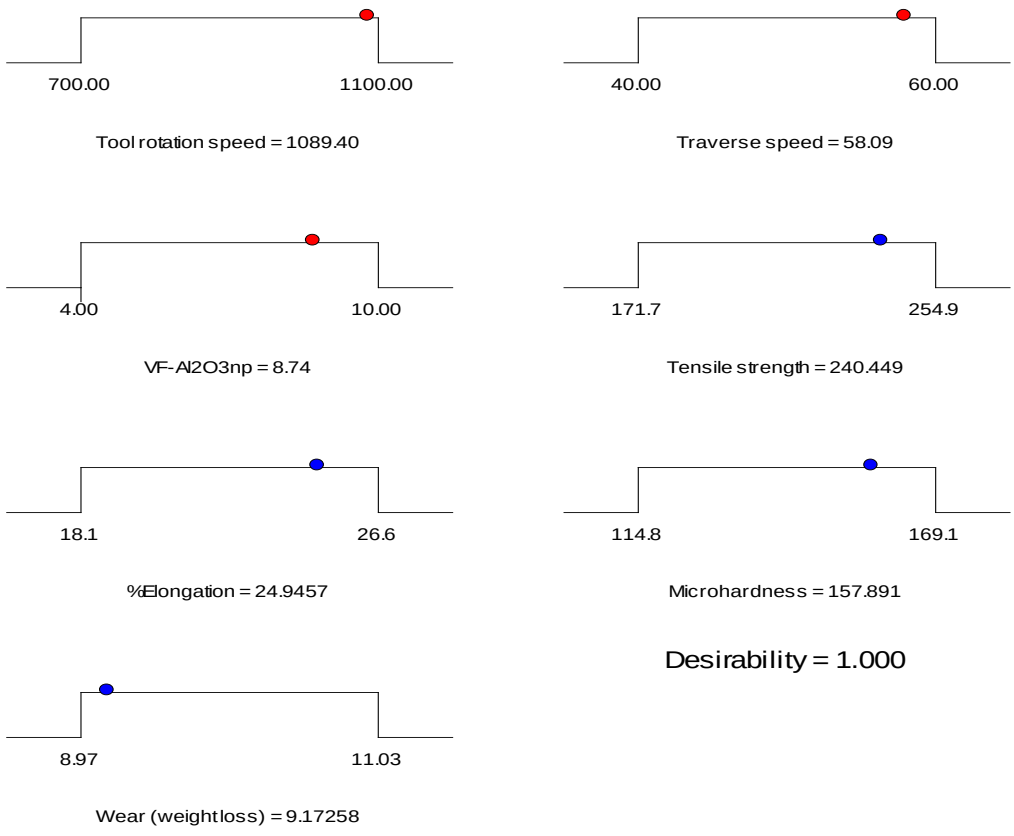

Figure 5.41: Ramp function graph for optimization of input and multi response parameters for FSPed composite joints incorporated with Al_2O_3np

The ramp function graph (Figures 5.41) derived from Design Expert (7) software, demonstrates the desirability for tensile strength, %elongation, microhardness and wear. Each ramp's dot indicates the response characteristic's factor setting or response

prediction. The height of the dot indicates how desired it is. Since the weight for each parameter was set to 1, a linear ramp function was established between the low value and the goal or the high value and the goal.

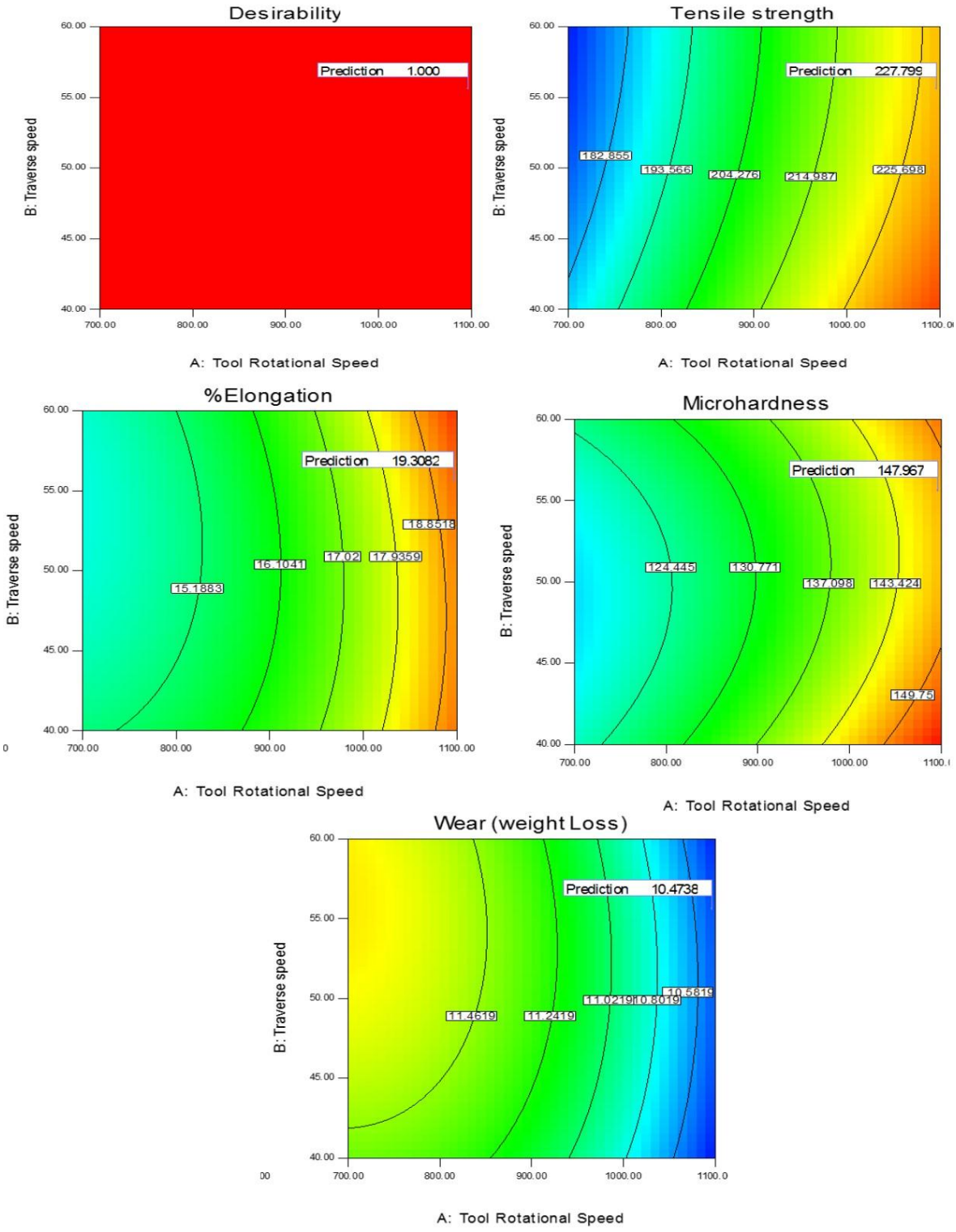

Figure 5.42: Optimized out responses of FSPed composite joints incorporated with Al_2O_3np

The range of desirability, ranging 0 to 1, depends on how closely the response comes to achieving the target. Employing this technology, several objective functions may be optimized. The desirable value for the optimized input and responses parameters is 1. The optimal value of tensile strength, %elongation, micro-hardness at stir zone and wear (weight loss) at stir zone are 240.45 MPa, 24.95%, 157.89 HV, and 9.17 mg, respectively, whereas the optimized value of rotational speed, traverse speed and VF-Al_2O_3np are 1089.40 rpm, 58.09 mm/min, and 8.74% VF-Al_2O_3np respectively as shown Fig. 5.41.

3D-plots for desirability were first derived with keeping input and responses parameters in range. Fig. 5.42 shows the desirability plots of desired responses for AA6061/AA7075, according to tool rotation speed, traverse speed and volume fraction of Al_2O_3 particles. It can be shown that overall desirability is increasing with increasing the tool rotation speed, desirability value is 1 for the high tool rotation speed level 3 (1100 RPM). As the traverse speed decreases the desirability increases as shown in Fig. 5.42.

5.7.2 Results of confirmation test

The confirmation experiment was performed to confirm the adequacy of the developed mathematical models for each response at optimal levels of the processing parameters. The average values of the characteristics were obtained and compared with the predicted values. The results of the test are presented in Table 5.24 which clearly shows that the developed models are adequate to predict the responses.

Table 5.24: Results of Confirmation test

Performance Measures/ Response parameters	Optimal set of parameters	Predicted optimal value	Experimental Value	% Error
Tensile strength (MPa)	RS=1089 rpm; TS= 58.09 mm/min; VF-Al_2O_3mp = 8.74%	240.45	251.38	4.55
% elongation (%)		24.95	24.02	-3.72
Micro-hardness (HV)		157.89	161.56	2.32
Wear weight loss (mg)		9.17	8.92	-2.72

5.8 MICROSTRUCTURE ANALYSIS OF FSPED COMPOSITE JOINTS INCORPORATED WITH AL_2O_3 NANOPARTICLES

The microstructure images of FSPed composite joints of AA 6061 and AA7075 incorporated with Al_2O_3np were taken from stir zone with different processing conditions. These were compared to each other on the basic dispersion pattern of Al_2O_3np and grain size.

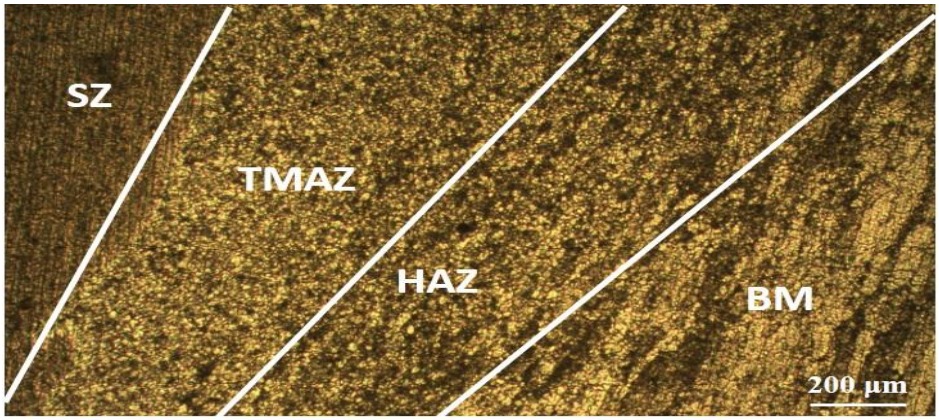

Figure 5. 43: Optical micrograph of various zone for FSPed composite joint of AA7075 and AA6061

The mechanical properties of FSPed composite joints is mainly influenced by grain refinement, pinning effect produced by Al_2O_3 particles and bonding between Al_2O_3 particles and metal-matrix. As a result of the higher grain refinement due to pinning effect of the uniformly distributed Al_2O_3 particles, composite joints exhibit the finer grains resulting in improved mechanical properties. Fig. 4.3 (a, c) depicts the optical micrograph of parent metal AA7075 and AA6061 with the granularity sizes of ~47 and ~ 36 µm, respectively. The weld zone of the FSPed composite joints includes stir zone (SZ), thermo-mechanical affected zone (TMAZ) and Heat affected zone (HAZ). The grain size in the weld zone is further found to decrease from HAZ to TMAZ and then to SZ as depicted in Fig. 5.43. This is due to the severe plastic deformation induced via the stirring action of tool in SZ causes dynamic recrystallization (DRX), results in the nucleation of refined grains [151,152]. The degree of refinement of fine and equiaxed recrystallized grains in the SZ also depends on the temperature grade. Higher value of rotational speed and lower value of traverse speed exhibit higher temperature and vice-versa [153]. Different microstructures of FSPed composite joint subjected to various process parameters conditions were produced, as depicted in Fig. 5.44 a-d. Compared

with other FSPed composite joints, the joint (specimen no-15) produced at the higher rotational speed of 1100 rpm and lower traverse speed of 40mm/min with 10% Al_2O_3 particles addition showed the best particle distribution at the joint, as shown in Fig. 5.44 d.

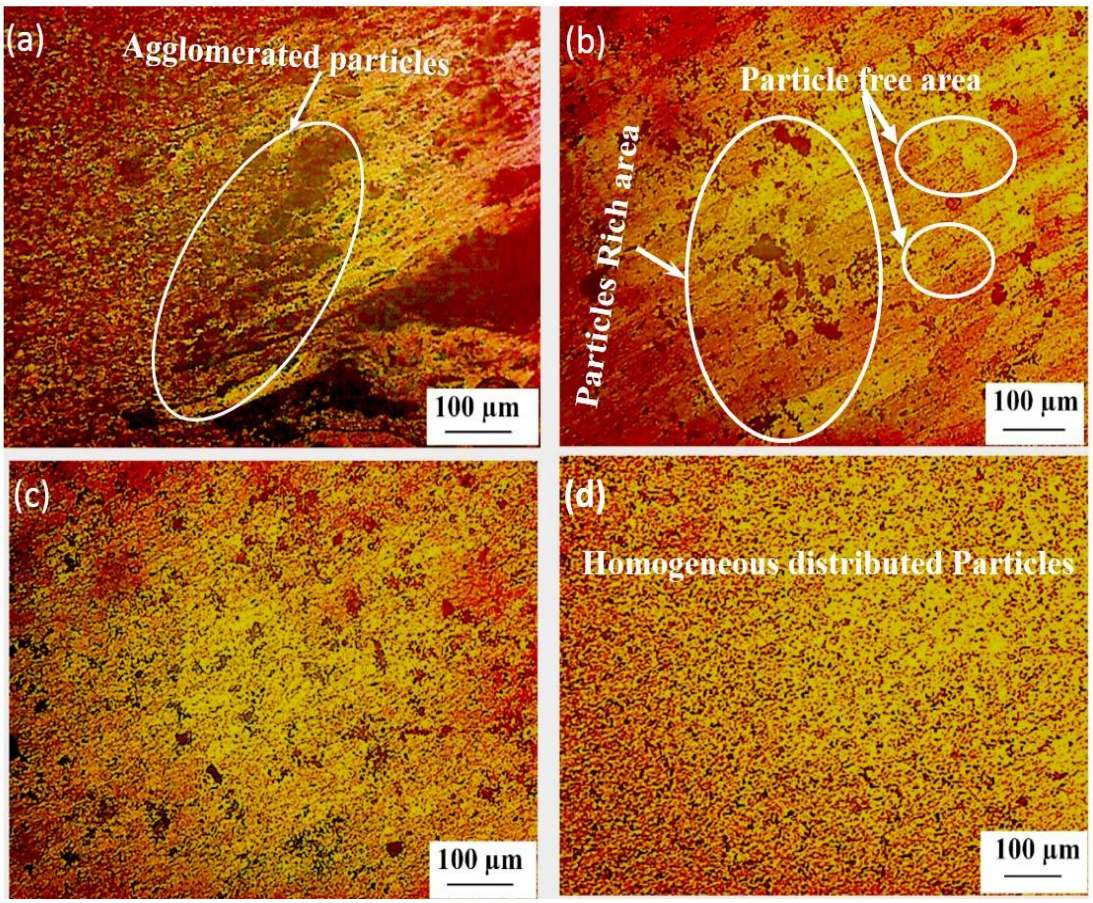

Figure 5.44: (a-d) micrographs of FSPed composite joints incorporated with Al_2O_3np, (a) specimen no-6, (b) Specimen no-9, (c) Specimen no-10, (d) Specimen no-15.

It can be attributed to the stirring action of tool that enhances the material flow and fragments the bigger particles into smaller particles. Dispersion of particles and grain refinement shown in Fig. 5.44 (a-d) were also evident from SEM images Fig. 5. 45 (a-f). Agglomeration of particles accompanied by poor bonding with surrounded metal matrix was observed in the FSPed composite joints produced at the rotational speed and traverse speed of 700 rpm and 60mm/min, respectively with 4 and 10 % Al_2O_3 volume fractions, as depicted in Fig. 5.45 a and b, respectively. The FSPed composite joints produced at the rotational speed of 900 rpm and traverse speed of 50 mm/min with 4 and 10% VF-Al_2O_3np (specimen no-16 and 9) characterized with particles rich area and particles free area. However, the FSPed joint with 4% VF-Al_2O_3 (specimen no-16) (Fig.

5.45 c) showed larger particles free area than that of the FSPed composite joint with 10% VF-Al_2O_3np (specimen no-16) (Fig. 5.45 d).

Hence, higher rotational speed and lower traverse speed were believed to produce improved mobility of the particles [130]. Fragmentation of particles also occurred owing to the enhanced stirring action of tool but adjudged to be less significant. Homogeneous dispersion with significant fragmentation of particles was achieved and agglomeration of particles was found absent in FSPed composite joints produced at the higher rotational speed of 1100 rpm and lower traverse speed of 40mm/min. Consequently, more Homogeneous dispersion and smaller particles in the SZ of the joint produced with 10% VF-Al_2O_3np (specimen no-15) (Fig. 5.45 f) were observed when comparing FSPed joint with 4% VF-Al_2O_3np (specimen no-10) (Fig. 5.45 e). The uniform dispersion of Al_2O_3 particles also results in creating a large number of aluminum matrix interfaces, which increases the pinning effect and further reduce the grain size (Fig. 5.45 f) [131]. It is also noticeable that there was no misconnection or gap between Al_2O_3np and the base metal, as depicted in Fig. 5.45 e.

The grain size in the stir zone was refined equiaxed grains throughout the stir zone, which was distinctly different to the TMAZ and HAZ. Optical micrograph also revealed the reduction in grain size in SZ, as compared with parent aluminum alloys. The reduction of grain size is attributed to the fragmentation of grains owing to heat input, dynamic recrystallization and pinning effect of incorporated Al_2O_3np. The mean grain size of specimen no-6 and 9 were observed as 17.1 µm and 11.4 µm, respectively due to low heat input and unusual dispersion of particles in the SZ. Specimen no-10 and 15 were produced at the same processing parameters and reinforced with 4 and 10% VF-Al_2O_3np, respectively. However, the mean grain size of specimen no- 10 and 15 was observed as 9.2 µm and 5.2 µm, respectively. The phenomenon of the smaller grain size in the SZ for specimen no-15 can be attributed to the existence of the higher volume fraction (10%) of Al_2O_3 nanoparticles because the processing parameters are the same. The grain size was associated with Zener- Holloman parameter [132]. The mean size of the grains was calculated as $R_c = \frac{4r}{3v_f}$, where Rc is a critical radius. So, it revealed that increasing the volume fraction of nanoparticles during FSP enhances the refinement to the existing grain's size in the SZ, as found in specimen no-15 comparing with

specimen no-10. The rate of grain growth during FSP using 2nd phase disperse nanoparticles is presented by eq. 5.21 [133].

$$\frac{dR_g}{dt} = (P_d - P_{zp})M_b = \left(\frac{g_c \gamma_{be}}{R_g} - \frac{3V_f \gamma_{be}}{2r_p}\right) M_b \qquad (5.21)$$

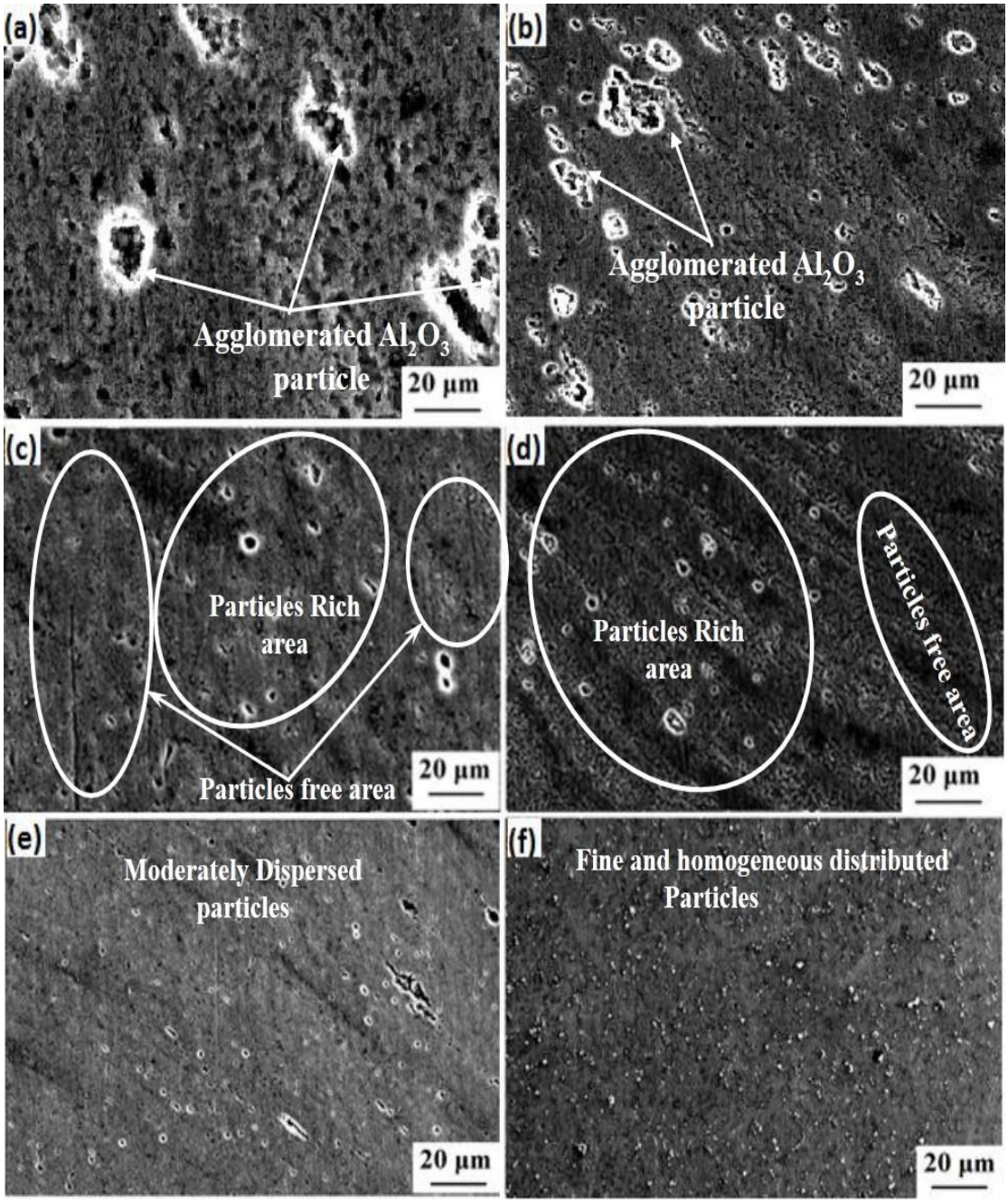

Figure 5.45: SEM micrographs reveal the dispersion of Al_2O_3 nanoparticles in SZ: (a, b) at RS 700 rpm and traverse speed 60 mm/min, (a) Specimen no-18 (4% Al_2O_3), (b) Specimen no-6 (10% Al_2O_3),; (c, d) at RS 900 rpm and traverse speed 50mm/min, (c) Specimen no-16 (4% Al_2O_3), (d) Specimen no-9(10% Al_2O_3); (e, f) at RS 1100 rpm and traverse speed 40mm/min,(e) Specimen no-10 (4% Al_2O_3), (f) Specimen no-15 (10% Al_2O_3)

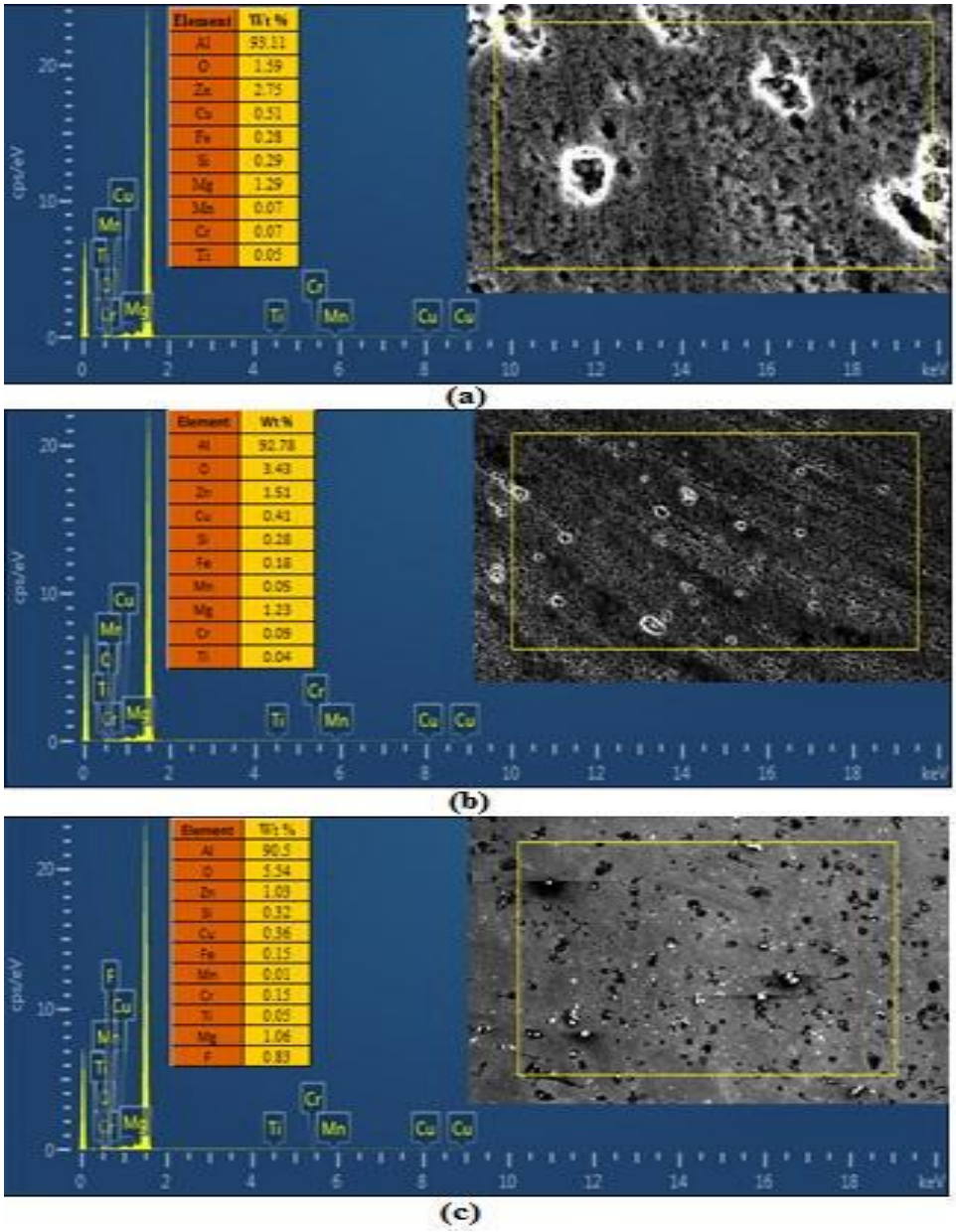

Figure 5. 46: EDS peak of FSPed composite joints at stir zone, (a) Specimen no.-18, (b) Specimen no.-9, (c) Specimen no.-15

Where M_b (m/s/J/m^2) is the mobility of boundary, R_g (µm) is the radius of grains, P_{zp} (MPa) is Zener pinning pressure, P_d (MPa) is driving pressure invented from the curvature of grains boundary, g_c is geometrical constant, V_f and r_p (µm) is the volume fraction and radius of 2nd phase particles, respectively. γ_{be} (mJ/m^2) is energy associated with grain boundary.

The grains growth will stop at $P_{zp} = P_d$

$$\frac{g_c \gamma_{be}}{R_g} = \frac{3V_f \gamma_{be}}{2r_p} \qquad (5.22)$$

If the curvature radius R_g (μm) is equivalent to the mean granularly radius D, then the Zener limiting grain size was observed (g_c = 1), then $D_{zl} = \frac{4r_p}{3V_f}$.

Consequently, it can be concluded that increasing value of rotational speed, decreasing value of traverse speed and higher volume fraction of Al_2O_3 nanoparticles reinforcement reduced the grain size in the SZ.

5.8.1 Fracture Surface analysis

The morphology of fractured surfaces of tensile samples of various composite joints was depicted in Fig. 5.47-5.50. Scanning electron microscopy was used to examine the fractured surface to understand the microstructure of the composite joint's failure pattern. Interestingly, all the composite specimens fractured outside the stir zone during tensile testing, indicating the well bond connection between the matrix and reinforcement particle (Al_2O_3np). The probability of achieving any matrix composite strengthening depends on transferring stress from the base metal to the nanoparticles. In the case of weak interfacial bonding, the interface may fail before transferring stress to the nanoparticle and no strengthening occurs [134]. The shear plane of the cup-cone shape was formed along the test specimens' periphery during the tensile loading. Micro voids' coalescence resulted in fine and equiaxed dimples at the fractured surface [137]. The fractured surface for specimen no- 15 showing tiny and equiaxed dimples, signifying fracture of ductile mode (Fig. 5.50) compared with that of specimen no. 18, 9 and 10 (Fig. 5.47-5.49).

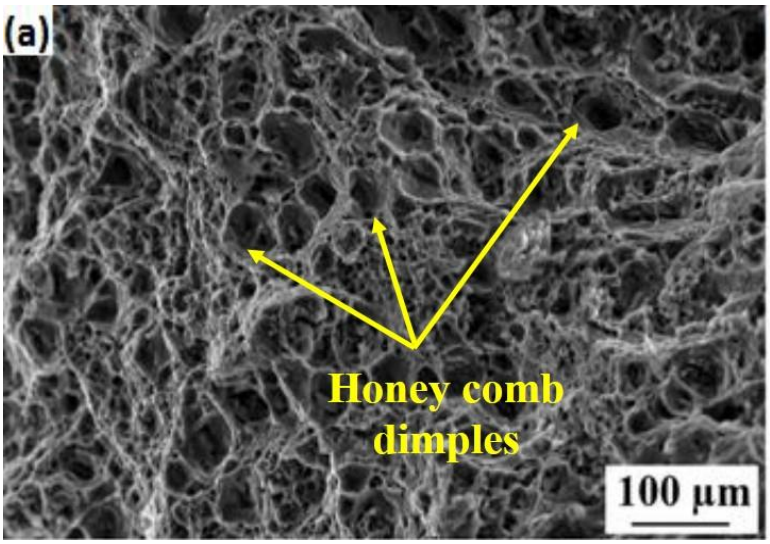

Figure 5.47: Fractured surface morphology of specimen no-6

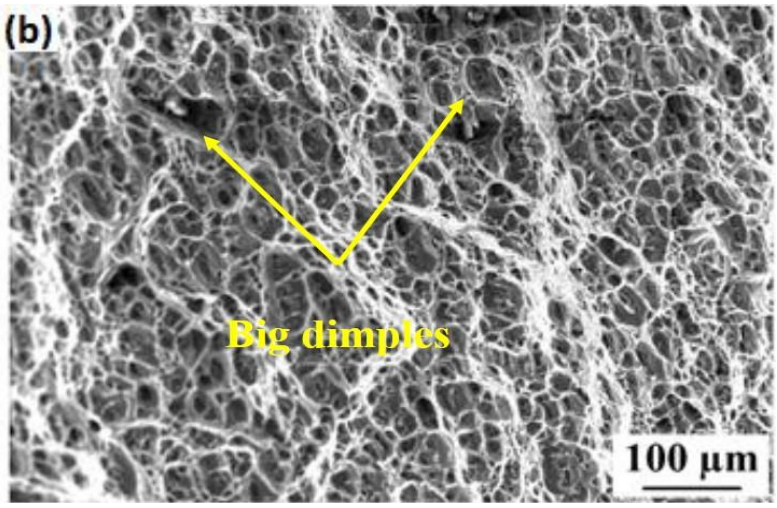

Figure 5.48: Fractured surface morphology of specimen no-9

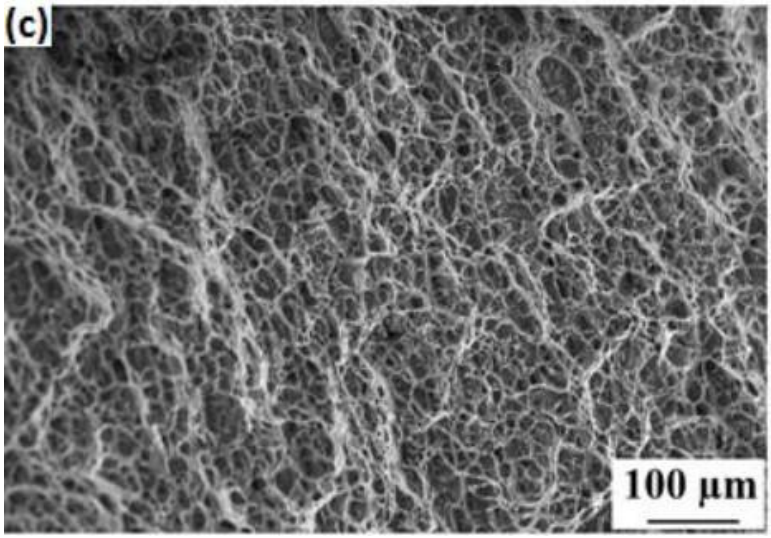

Figure 5.49: Fractured surface morphology of FSPed specimen no-10

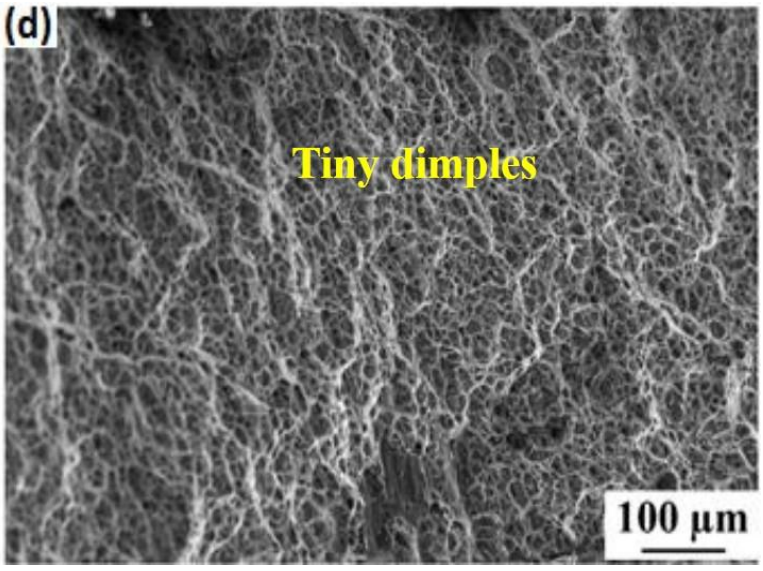

Figure 5. 50: Fractured surface morphology of specimen no-15

As depicted in Fig. 5.47, honeycomb dimples with a ductile fracture were observed in specimen no-18 and depicted the regularly separated features of cleavage and plastic deformation [154]. All the FSPed specimens were produced at various rotational and traverse speeds; thus, homogenous dispersion of reinforcing particles decreased the grain size, effectual material mixing, and fine and equiaxed dimples observed. Fractured metal matrix was identified in the HAZ due to softening of the material, confirmed by micro-hardness variation [155]. The examination of the fracture location of the joint is essential to enhance the mechanical properties of the FSP/Al_2O_3np.

When no reinforcing particles were utilized, grain refinement by DRX was the key determinant of the joint's mechanical characteristics. However, the mechanical properties of FSPed composite joints is mainly influenced by grain refinement, pinning effect produced by Al_2O_3 particles and bonding between Al_2O_3 particles and metal-matrix. As a result of the higher grain refinement due to pinning effect of the uniformly distributed AlO_3 particles, composite joints exhibit the finer grains resulting in improved mechanical properties [133,156].

The tensile strength of FSPed composite joints is mainly influenced by grain refinement, pinning effect produced by Al_2O_3 particles and bonding between Al_2O_3 particles and metal-matrix. As a result of the higher grain refinement due to pinning effect of the uniform distributed Al_2O_3 particles, composite joints exhibit the finer grains. Tensile strength is inversely proportional to grain’s size, as defined by Hall-patch relationship [157].

The FSP significantly refines the intermetallic particles and disperses them uniformly within the matrix. Decreasing the aspect ratio and increasing the particles number per unit area substantially lower the level of stress imposed on individual particles, thereby increases their resistance to breaking and/or detachment from the matrix giving rise to a better ductility [158-160].

The hardness of the SZ can also be ascribed to the grain refinement and distribution of Al_2O_3 particles resulting in pinning effect [116]. Smaller grain size exhibits higher hardness as per hall-patch relationship [117]. The microhardness of the composite joints embedded with reinforcement particles also enhanced due to the presence of hard Al_2O_3 particles.

Consequently, the specimen produced with higher RS, lower TS and higher volume fraction of Al_2O_3 particles exhibits homogeneous dispersion of particles and reduced grain size in the SZ. These results revealed that the improved mechanical properties could be achieved by the incorporation of reinforcing particles of Al_2O_3 particles in the SZ.

5.9 COMPARATIVE ANALYSIS BETWEEN Al_2O_3 MICRO AND NANO SIZED PARTICLES BASED COMPOSITE JOINTS

To evaluate the comparative analysis of FSPed composite joints incorporated with micro and nano sized Al_2O_3 particles, their maximum tensile strength, %elongation, microhardness and minimum wear weight loss were compared as tabulated in Table 5.25. The comparative analysis reveals that FSPed composite joints incorporated with Al_2O_3 nanoparticles shows higher maximum tensile strength, % elongation, microhardness and lower minimum wear weight loss as compared to those of the FSPed composite joints incorporated with Al_2O_3 micro particles.

Table 5.25: Comparative analysis between composite joints incorporated with Al_2O_3 micro and nano particles

Response parameters	Composite joints with Al_2O_3mp	Composite joints with Al_2O_3np	% improvement
Tensile strength (MPa)	241.4	254.9	5.59
%elongation (%)	20.3	26.6	31.03
Microhardness (HV)	157.5	169.1	7.37
Wear (wt. loss) (mg)	10.3	8.97	12.91

5.10 RESEARCH CONTRIBUTION

To investigate the effects of micro and nano sized Al_2O_3 particles on the weld quality of dissimilar AA6061/AA7075, the joint efficiency, %elongation and microhardness of FSPed composite joints were compared with those of previous studies and tabulated in Table 5.26. It was observed that the incorporation of micro and nano sized Al_2O_3

particles significantly improved the joint efficiency, %elongation and micro-hardness of dissimilar weld joint of AA6061/ AA7075.

Table 5.26: Comparison between present research work with previous research work

Parametric Condition	Weld joint	Joint efficiency	Micro-hardness-	%elongation	Author
RS-900 rpm TS-80,100,120,160 mm/min	AA6061/ AA7075	81.4%	20% higher than 6061	15% higher than AA6061	Bahemmat et al. [139]
RS-1200 rpm TS-2,3,5 m/s Force-6,6.1,6.6, 6.7,7 KN	AA6061/ AA7075	79%	Less than AA6061 and AA7075	33.3 % less than AA6061	J.F. Guo et al. [69]
RS- 800, 900, 1000 rpm TS- 90,100,110 mm/min PP- ST, TCT, TST	AA6061/ AA7075	67.68%	1.1 % higher than AA6061	-----	Ravikumar et al. [70]
RS-700,900,1100 TS- 40,50,60mm/min VF-Al_2O_3mp- 4,7 10%	AA6061/ AA7075	83.8%	60% higher than AA 6061	10.3 % higher than AA6061	Sumit Jain & R.S. Mishra [119]
RS-700,900,1100 TS- 40,50,60mm/min VF-Al_2O_3np- 4,7 10%	AA6061/ AA7075	88.5%	76.1% higher than AA6061	44.5 % higher than AA6061	Sumit Jain & R.S. Mishra [151]

5.11 RESEARCH BENEFITS TO SOCIETY

The FSP is a green fabrication process because it required less heat input and does not generate any kinds of dangerous fumes, gases, and rays during welding and processing.

These days a lot of research is going on the weld properties improvement. Improvement in the weld joint properties improves the performance and life of structural component. The increase in the life of component decreases its working cost.

5.12 ECONOMICAL ASPECT OF RESEARCH

FSP is a single step process, while other techniques require multiple steps which make FSP easier and less time consuming. In addition, FSP uses a simple inexpensive tool, and a readily available machine such as a milling machine can be used to conduct the process. Improvement in the weld joint properties improves the performance and life of structural component resulting in the enhancement in the components life. The increase in the life of component decreases its working cost.

5.13 LIMITATIONS OF THE RESEARCH CONDUCTED

Instead of a large number of advantages of friction stir processing for joining dissimilar aluminum alloys (AA7075/AA6061), there are few limitations of this research work. The limitation of the present study are as follows:

1. To Incorporate the reinforcing particles in the weld zone of the dissimilar aluminum alloys, the manufacturing of groove increases the efforts and time.

2. Cost of reinforcing particles.

CHAPTER-6

CONCLUSIONS

6.1 CONCLUSIONS

In the present study, fabrication of the composite joints of AA6061/AA7075 was carried out by imparting different volume fraction of Al_2O_3 micro and nano sized particles into the weld zone. The influence of rotational speed, traverse speed and different volume fraction of incorporated Al_2O_3 particles on mechanical and microstructural characteristics was investigated. The distribution of Al_2O_3 particles, dynamic recrystallization and pinning effect play a significant role in enhancing weld quality and microstructural characteristics. The major conclusions drawn from obtained results are mentioned below:

- Increasing rotational speed and decreasing traverse speed, leads to improving the dispersion pattern of Al_2O_3 particles (micro and nano) in the SZ of FSPed composite joints.
- The highest tensile strength (241.35 MPa), microhardness (157.5 HV) and minimum wear weight loss (10.3 mg) for FSPed composite joints incorporated with Al_2O_3 microparticles were observed at rotational speed of 1100 rpm, traverse speed of 40 mm/min with 10% volume fraction of Al_2O_3 microparticles.

- The maximum tensile strength (254.9 MPa) and microhardness (169.1 HV) for FSPed composite joint incorporated with Al_2O_3 nanoparticles were observed at rotational speed of 1100 rpm, traverse speed of 40 mm/min with 10% volume fraction of Al_2O_3 nanoparticles. Whereas, minimum wear weight loss (8.97 mg) was observed at the rotational speed of 1100 rpm, traverse speed of 60 mm/min with 10% volume fraction of Al_2O_3 nanoparticles.

- All the three parameters are found significant towards the variation in tensile strength, % elongation, microhardness and wear weight loss of FSPed composite joints of AA6061 and AA7075. Developed quadratic models for each response parameters are checked for their adequacy at 95 % confidence level by performing confirmatory experiments.

- The optimum value of tensile strength, % elongation, micro-hardness at the SZ and wear behavior (weight loss) at the SZ are 227.80 MPa, 19.31, 147.97 HV and 10.474 mg respectively, whereas the optimum value of rotational speed, traverse speed and VF-Al_2O_3-mp are 1096.76 rpm, 55.59 mm/min and 8.64 % respectively was found for Al_2O_3 microparticles

- The optimum value of tensile strength, % elongation, micro-hardness at the SZ and wear (weight loss) at the SZ are 240.45 MPa, 24.95%, 157.89 HV, and 9.17 mg, respectively, whereas the optimum value of rotational speed, traverse speed and VF-Al_2O_3np are 1089.40 rpm, 58.09 mm/min, and 8.74% VF-Al_2O_3np respectively was found for Al_2O_3 nanoparticles.

- The grains structure in the stir zone of FSPed composite joints was observed much finer than that of the base materials.

- The fractography of fractured tensile samples of FSP composite joints reveals that bigger dimples and quasi cleavage with a sharp edge were observed at lower rotational speed, whereas fine dimples were observed at higher rotational speed.

6.2 SCOPE OF FUTURE WORK

The present experimental work has been carried out to assess the influences of FSP processing parameters and volume fraction of micro and nano sized Al_2O_3 particles on the microstructural, mechanical and wear behaviour, and observed the optimum combination of input and output responses of dissimilar composite joints of AA6061 and AA7075. It is recommended that the following future work should be done.

- Influence of different reinforcements particles like TiB_2, SiC, B_4C etc. of different sizes (micro and nano) on mechanical and tribological properties can be investigated.
- Influence of mixture of two or three reinforcing particles with their different proportions on mechanical and tribological properties can be investigated.
- Effects of process parameters on considered alloys of different thicknesses can also be explored further.
- The influence of reinforcing particles on corrosion resistance, residual stress etc. of composite joints of considered alloys may be further explored.

- Effects of multi-pass FSP on the mechanical and tribological properties of composite joints can be explored.

REFERENCES

[1] W. M. Thomas, E. D. Nicholas, J. C. Needham, M. G. Nurch, P. Temple-Smith, and C. Dawes, Friction Stir Butt Welding, G. B. (1991).

[2] G. ¸Cam and G. Ipeko. glu, Recent developments in joining of aluminum alloys, Int. J. Adv. Manuf. Technol. 1–16 (2016).

[3] Gemme, F., Verreman, Y., Dubourg, L.& L., M. Numerical analysis of the dwell phase in friction stir welding and comparison with experimental data. Materials Science and Engineering, A, 527, (2010), 4152–4160.

[4] R. S. Mishra, M. W. Mahoney, S. X. McFadden, N. A. Mara, and A. K. Mukherjee, High strain rate superplasticity in a friction stir processed 7075 Al alloy, Scripta Materialia 42(2), 163–168 (1999).

[5] R. S. Mishra, Z. Y. Ma, and I. Charit, Friction stir processing: a novel technique for fabrication of surface composite, Mater. Sci. Eng.: A 341(1–2), 307–310 (2003).

[6] Y. Gan, D. Solomon, and M. Reinbolt, Friction stir processing of particle reinforced composite materials, Materials 3(1), 329 (2010).

[7] P. B. Berbon, W. H. Bingel, R. S. Mishra, C. C. Bampton, and M. W. Mahoney, Friction stir processing: a tool to homogenize nanocomposite aluminum alloys, Scripta Materialia 44(1), 61–66 (2001).

[8] G. R. Argade, K. Kandasamy, S. K. Panigrahi, and R. S. Mishra, Corrosion behavior of a friction stir processed rare-earth added magnesium alloy, Corros. Sci. 58, 321– 326 (2012).

[9] N. Sun and D. Apelian, Friction stir processing of aluminum cast alloys for high performance applications, JOM 63(11), 44–50 (2011).

[10] Y. Hangai, T. Utsunomiya, and M. Hasegawa, Effect of tool rotating rate on foaming properties of porous aluminum fabricated by using friction stir processing, J. Mater. Process. Technol. 210(2), 288–292 (2010).

[11] S. Rathee, S. Maheshwari, and A. N. Siddiquee, Issues and strategies in composite fabrication via friction stir processing: A review, Mater. Manuf. Process. 1–23 (2017).

[12] R. M. Miranda, T. G. Santos, J. Gandra, N. Lopes, and R. J. C. Silva, Reinforcement strategies for producing functionally graded materials by friction stir processing in aluminium alloys, J. Mater. Process. Technol. 213(9), 1609–1615 (2013).

[13] M. Yang, C. Xu, C. Wu, K. C. Lin, Y. Chao, and L. An, Fabrication of AA6061/Al2O3 nano ceramic particle reinforced composite coating by using friction stir processing, J. Mater. Sci. 45(16), 4431–4438 (2010).

[14] Y. Huang, T. Wang, W. Guo, L. Wan, and S. Lv, Microstructure and surface mechanical property of AZ31 Mg/SiCp surface composite fabricated by direct friction stir processing, Mater. Des. 59(0), 274–278 (2014).

[15] S. Rathee, S. Maheshwari, A. N. Siddiquee, and M. Srivastava, Effect of tool plunge depth on reinforcement particles distribution in surface composite fabrication via friction stir processing, Defen. Technol. 13(2), 86–91 (2017).

[16] H. R. Akramifard, M. Shamanian, M. Sabbaghian, and M. Esmailzadeh, Microstructure and mechanical properties of Cu/SiC metal matrix composite fabricated via friction stir processing, Mater. Des. 54(0), 838–844 (2014).

[17] S. Rathee, S. Maheshwari, and A. N. Siddiquee, Distribution of reinforcement particles in surface composite fabrication via friction stir processing: suitable strategy, Mater. Manuf. Process. 1–23 (2017). DOI:10.1080/ 10426914.2017.1303162.

[18] L. Karthikeyan, V. S. Senthilkumar, and K. A. Padmanabhan, On the role of process variables in the friction stir processing of cast aluminum A319 alloy, Mater. Des. 31 (2), 761–771 (2010).

[19] O. El-Kady and A. Fathy, Effect of SiC particle size on the physical and mechanical properties of extruded Al matrix nanocomposites, Mater. Des. 54, 348–353 (2014).

[20] S. A. Hosseini, K. Ranjbar, R. Dehmolaei, and A. R. Amirani, Fabrication of Al5083 surface composites reinforced by CNTs and cerium oxide nano particles via friction stir processing, J. Alloy Comp. 622, 725–733 (2015).

[21] A.P. Sannino and H. J. Rack, Dry sliding wear of discontinuously reinforced aluminum composites: review and discussion, Wear 189(1), 1–19 (1995).

[22] T. Y. Kosolapova, Carbides: Properties, Production, and Applications, Springer US, New York (2012).

[23] K. Kalaiselvan, N. Murugan, and S. Parameswaran, Production and characterization of AA6061–B4C stir cast composite, Mater. Des. 32(7), 4004–4009 (2011).

[24] R. G. Munro, Material properties of titanium diboride, J. Res. Nat. Instit. Stand. Technol. 105(5), 709–720 (2000).

[25] C. S. Ramesh, S. Pramod, and R. Keshavamurthy, A study on microstructure and mechanical properties of Al 6061– TiB2 in-situ composites, Mater. Sci. Eng.: A 528(12), 4125–4132 (2011).

[26] S. R. Bakshi, D. Lahiri, and A. Agarwal, Carbon nanotube reinforced metal matrix composites — a review, Int. Mater. Rev. 55(1), 41–64 (2010).

[27] Y. B. Li, B. Q. Wei, J. Liang, Q. Yu, and D. H. Wu, Transformation of carbon nanotubes to nanoparticles by ball milling process, Carbon 37(3), 493–497 (1999).

[28] Y. Morisada, H. Fujii, T. Nagaoka, and M. Fukusumi, MWCNTs/AZ31 surface composites fabricated by friction stir processing, Mater. Sci. Eng.: A 419(1–2), 344– 348 (2006).

[29] H. Izadi and A. P. Gerlich, Distribution and stability of carbon nanotubes during multi-pass friction stir processing of carbon nanotube/aluminum composites, Carbon 50(12), 4744–4749 (2012).

[30] Aziz, Z. Qi, and X. Min, Corrosion inhibition of SiCp/5A06 aluminum metal matrix composite by cerium conversion treatment, Chin. J. Aeronaut. 22(6), 670–676 (2009).

[31] P. M. Ashraf and S. M. A. Shibli, Development of cerium oxide and nickel oxide-incorporated aluminium matrix for marine applications, J. Alloy Compnd. 484(1–2), 477– 482 (2009).

[32] A. Shafiei-Zarghani, S. F. Kashani-Bozorg, and A. Zarei-Hanzaki, Microstructures and mechanical properties of Al/Al2O3 surface nano-composite layer produced by friction stir processing, Mater. Sci. Eng.: A 500(1–2), 84– 91 (2009).

[33] M. Raaft, T. S. Mahmoud, H. M. Zakaria, and T. A. Khalifa, Microstructural, mechanical and wear behavior of A390/graphite and A390/Al2O3 surface composites fabricated using FSP, Mater. Sci. Eng.: A 528(18), 5741– 5746 (2011).

[34] Prado, R.A., Murr, L.E., Soto, K.F. & McClure, J.C. (2002). Self-optimization in tool wear for friction-stir welding of Al 6061_/20% Al2O3 MMC. Materials Science and Engineering, A, 349, (2003), 156-/165.

[35] C.J. Dawes, P.L. Threadgill, E.J.R. Spurgin, and D.G. Staines, "Development of the New Friction Stir Technique for Welding Aluminum—Phase II," TWI member report 5651/35/95, Nov 1995.

[36] Christian B. Fuller, Friction Stir Tooling: Tool Materials and Designs , Friction Stir Welding and Processing, pp7-35, 2007. DOI:10.1361/fswp2007p007.

[37] L. Christodoulou, W. Palko, and C. Fuller, Equipment and Processing Variables Affecting Friction Stir Processing of NiAl Bronze, Friction Stir Welding and Processing III, K.V. Jata, M.W. Mahoney, R.S. Mishra, and T.J. Lienert, Ed., TMS, 2005, p 57–66 48.

[38] M.W. Mahoney, C.B. Fuller, W.H. Bingel, and M. Calabrese, "Friction Stir Processing of Cast NiAl Bronze," THERMEC 2006, July 4–8, 2006 (Vancover, Canada), TMS.

[39] M.W. Mahoney, W.H. Bingel, S.R. Sharma, and R.S. Mishra, Microstructural Modification and Resultant Properties of Friction Stir Processed Cast NiAl Bronze, Mater. Sci. Forum, Vol 426–432, 2003, p 2843–2848.

[40] Scialpi,A., De Filippis,L.A.C., Cavaliere,P.(2006). Influence of shoulder geometry on microstructure and mechanical properties of friction stir welded 6082 aluminium alloy. Materials and Design, 28, (2007),1124–1129.

[41] Patric B. Berdon, Willam H. Bingel, R.S Mishra, "Friction Stir Processing: A Tool to homogenize nano composite Al Alloy, Scripta mater, 44 (2001), 61-66.

[42] Z.Y.Ma, R.S Mishra, M.W. Mahoney," Super plastic deformation behavior of friction stir processed 7075Al alloy", Acta Materialia 50 (2002), 4419-4430.

[43] Indrajeet Charit, Rajiv S. Mishra, Murray W. Mahoney, "Multi sheet structure in 7475 aluminum by FSW in concert with post weld superplastic forming", Scripta Materialia 47 (2002) 631-636.

[44] Y.S. Sato, Y. Kurihara, S.H.C. Park, H. Kokawa, N. Tsuji , Friction stir welding of ultrafine grained Al alloy 1100 produced by accumulative roll-bonding, Scripta Materialia 50 (2004) 57–60.

[45] Moataz M. Attallah, Hanadi G. Salem, Friction stir welding parameters: a tool for controlling abnormal grain growth during subsequent heat treatment, Materials Science and Engineering A 391 (2005) 51–59.

[46] Su, T. Nelson and C. Sterling. "Friction stir processing of large-area bulk UFG aluminum alloys". Scripta Materialia 52 (2005) pp.135-140.

[47] Z.Y Ma, S.R Sharma, R.S Mishra, " Effect of Multipass Friction Stir Processing on Microstructure and tensile propeties of a Cast Al-Si Alloy", Scripta Materialia, 54 (2006) 1623-1626.

[48] G. Buffa, J.Hua, R. Shivpuri, L. Fratini, A continuum based fem model for friction stir welding—model development, Materials Science and Engineering A 419 (2006) 389–396.

[49] A. Barcellona, G. Buffa, L. Fratini, D. Palmeri, On microstructural phenomena occurring in friction stir welding of aluminum alloys, Journal of Materials Processing Technology 177 (2006) 340–343

[50] S.R. Ren, Z.Y. Ma and L.Q. Chen , Effect of welding parameters on tensile properties and fracture behavior of friction stir welded Al–Mg–Si alloy, Scripta Materialia 56 (2007) 69–72.

[51] Zhang & H. W. Zhang, Material behaviors and mechanical features in friction stir welding process International Journal of Advanced Manufacturing and Technology (2007) 35:86–100.

[52] R. Nandan, G.G. Roy, T.J. Lienert, T. Debroy Three-dimensional heat and material flow during friction stir welding of mild steel, Acta Materialia 55 (2007) 883–895.

[53] H.W. Zhang, Z. Zhang, J.T. Chen, 3D modeling of material flow in friction stir welding under different process parameters, Journal of Materials Processing Technology 183 (2007) 62–70.

[54] Y.Wang, X.L Shi, R.S mishra, T.J Watson, "Friction stir welding of devitrified AL-4.0Y-4.0Ni-0.9Co alloy produced by amorphose powder", Scripta Materialia 56 (2007) 971-974.

[55] A. Pirondi, L. Collini, D. Fersini, Fracture and fatigue crack growth behaviour of PMMC friction stir welded butt joints, Engineering Fracture Mechanics 75 (2008) 4333–4342.

[56] M. Maalekian, E. Kozeschnik, H.P. Brantner, H. Cerjak , Comparative analysis of heat generation in friction welding of steel bars, Acta Materialia 56 (2008) 2843–2855.

[57] Z. Zhang, H.W. Zhang, Numerical studies on controlling of process parameters in friction stir welding, journal of materials processing technology 209 (2009) 241–270

[58] Z.y.Ma, R.S Mishra, F.C Liu, “Super plastic behaviour of Micro-region in two pass friction stir processing 7075Al alloy”, Materialia Science and Engineering A 505 (2009) 70-78.

[59] Jerry Wong, Patricia Zambrano, Indira Escamilla, Bernardo Gonzalez, Victor Mucino, Rafael Colás, Friction stir linear welding of an aluminum alloy, Advanced Materials Research Vol. 68 (2009) pp 116-121.

[60] L. Commin, M. Dumont, J.-E. Masse, L. Barrallier, Friction stir welding of AZ31 magnesium alloy rolled sheets: Influence of processing parameters, Acta Materialia 57 (2009) 326–334.

[61] Olivier Lorrain, Véronique Favier, Hamid Zahrouni, Didier Lawrjaniec, Understanding the material flow path of friction stir welding process using unthreaded tools, Journal of Materials Processing Technology 210 (2010) 603–609.

[62] Mohamed Assidi, Lionel Fourment, Simon Guerdoux, Tracy Nelson, Friction model for friction stir welding process simulation: Calibrations from welding experiments, International Journal of Machine Tools & Manufacture 50 (2010) 143–155.

[63] D. Jacquin, B. de Meester, A. Simar, D. Deloison, F. Montheillet, C. Desrayaud, A simple Eulerian thermomechanical modeling of friction stir welding, Journal of Materials Processing Technology 211 (2011) 57–65.

[64] Jian Qing Su, T.W Nelson, T.R. McNelley, “Development of Nano crystalline structure in Cu during Friction Stir Processing”, Material Science and Engineering A, 525 (2011) 5458-5464.

[65] G. Buffa, A. Ducato, L. Fratini, Numerical procedure for residual stresses prediction in friction stir welding, Finite Elements in Analysis and Design 47 (2011) 470–476.

[66] Wang Kuai-she, WU Jia-lei, Wang Wen, ZHOU Long-hai, LIN Zhao-xia, KONG Liang, Underwater friction stir welding of ultrafine grained 2017 aluminum alloy, J. Cent. South Univ. (2012) 19: 2081-2085.

[67] Nilesh Kumar, R.S Mishra, " Ultrafined Grained Al-Mg-Sc Alloy via friction Stir Processing", Metallurgical and Materials Transaction, 44A (2013) 934-945.

[68] Jianqing Su, Jiye Wang, R.S Mishra, Ray Xu, " Microstructure and Mechanical Properties of Friction Stir Processing Ti-6Al-4V Alloy", Material Science and Engineering A 573 (2013) 67-74

[69] J.F. Guo, H.C. Chen, C.N. Sun, G. Bi, Z. Sun, J. Wei, Friction stir welding of dissimilar materials between AA6061 and AA7075 Al alloys effects of process parameters, Materials and Design 56 (2014) 185–192.

[70] Ravi kumar, Seshagiri Rao. V and Pranesh. R.V, Effect of welding parameters on macro and microstructure of friction stir welded dissimilar butt joints welded joints between AA7075 and AA6061 alloys, procedia materials science 5 (2014), 1726-1735.

[71] Dawood HI, Kahtan S. Mohammed, Azmi Rahmat, M. B. Uday, Effect of small tool pin profiles on microstructures and mechanical properties of 6061 aluminum alloy by friction stir welding, Trans. Nonferrous Met. Soc. China 25(2015) 2856−2865.

[72] M. Ilangovan, S. Rajendra Boopathy, V. Balasubramanian, Microstructure and tensile properties of friction stir welded dissimilar AA6061AA5086 aluminium alloy joints, Trans. Nonferrous Met. Soc. China 25 (2015) 1080-1090

[73] T. Srinivasa Rao, G. Madhusudhan Reddy, S. R. Koteswara Rao, Microstructure and mechanical properties of friction stir welded AA7075−T651 aluminum alloy thick plates, Trans. Nonferrous Met. Soc. China 25(2015) 1770−1778.

[74] Omar S. Salih, Hangan Ou, W.Sun, D.G McCartney, "A review of friction stir welding of aluminum matrix composite", Material and Design 86 (2015) 61-71

[75] Jamshidi Aval Hamed, Effect of welding heat input and post-weld aging time on microstructure and mechanical properties in dissimilar friction stir welded AA7075−AA5086, Trans. Nonferrous Met. Soc. China 27(2017) 1707−1715.

[76] Krishna Komerla, Andreas Naumov, Chris Mertin, Ulrich Prahl, Wolfgang Bleck, Investigation of microstructure and mechanical properties of friction stir welded AA6016-T4 and DC04 alloy joints, The International Journal of Advanced Manufacturing Technology, 94, 4209–4219 (2018).

[77] Narayanan, A.; Mathew, C.; Baby, V.Y.; Joseph, J. Influence of gas tungsten arc welding parameters in aluminium 5083 alloy. International Journal of Engineering Science and Innovative Technology (IJESIT) Volume 2, Issue 5, 269–277.

[78] Harish Suthar, Anirban Bhattacharya, Surajit Kumar Paul, Local deformation response and failure behavior of AA6061-AA6061 and AA6061-AA7075 friction stir welds, (2020), https://doi.org/10.1016/j.cirpj.2020.03.006

[79] Mahmoud Abbasi, Mohammad Givi and Behrouz Bagheri, New method to enhance the mechanical characteristics of Al-5052 alloy weldment produced by tungsten inert gas, Proc IMechE Part B: J Engineering Manufacture 1–9 DOI: 10.1177/0954405420929777.

[80] Khanna, N., Sharma, P., Bharati, M. et al. Friction stir welding of dissimilar aluminium alloys AA 6061-T6 and AA 8011-h14: a novel study. J Braz. Soc. Mech. Sci. Eng. 42, 7 (2020). https://doi.org/10.1007/s40430-019-2090-3.

[81] Sameer Mohammed & Anil Kumar Birru (2019) Friction Stir Welding of AA6082 Thin Aluminium Alloy Reinforced with Al2O3 Nanoparticles, Transactions of the Indian Ceramic Society, 78:3, 137-145, DOI: 10.1080/0371750X.2019.1635046

[82] Parumandla, N., Adepu, K. (2018). Effect of Al2O3 and SiC Nano Reinforcements on Microstructure, Mechanical and Wear Properties of Surface Nanocomposites Fabricated by Friction Stir Processing. Materials Science, 24(3), –. doi:10.5755/j01.ms.24.3.18220.

[83] Ahmadifard, S. Shahin, N., azghandi, M., Kazemi, S. (2021). Surface Hybrid Nanocomposite Produced by Friction Stir Processing : Microstructural Evolution , Mechanical Properties and Tribological Behavior, 1–16.

[84] Abdollahzadeh A, Shokuhfar A, Omidvar H, et al. (2019). Structural evaluation and mechanical properties of AZ31/SiC nano-composite produced by friction stir welding process at various welding speeds. Proceedings of the Institution of Mechanical Engineers, Part L: Journal of Materials: Design and Applications.;233(5):831-841.

[85] Bahrami, M., Farahmand Nikoo, M., & Besharati Givi, M. K. (2015). Microstructural and mechanical behaviors of nano-SiC-reinforced AA7075-O FSW joints prepared through two passes. Materials Science and Engineering A, 626, 220–228. https://doi.org/10.1016/j.msea.2014.12.009.

[86] Bozkurt Y, Uzun H, Salman S. (2011) Microstructure and mechanical properties of friction stir welded particulate reinforced AA2124/SiC/25p–T4 composite. Journal of Composite Materials.;45(21):2237-2245. doi:10.1177/0021998311401067.

[87] Cioffi, F.; Fernández, R.; Gesto, D.; Rey, P.; Verdera, D.; González-Doncel, G. (2013). Friction stir welding of thick plates of aluminum alloy matrix composite with a high volume fraction of ceramic reinforcement. Composites Part A: Applied Science and Manufacturing, 54(), 117–123. doi:10.1016/j.compositesa.2013.07.011

[88] Dragatogiannis, D. A.; Koumoulos, E. P.; Kartsonakis, I.; Pantelis, D. I.; Karakizis, P. N.; Charitidis, C. A. (2015). Dissimilar Friction Stir Welding Between 5083 and 6082 Al Alloys Reinforced with Tic Nanoparticles. Materials and Manufacturing Processes, (), 10426914.2015.1103856–. doi:10.1080/10426914.2015.1103856.

[89] Gopalakrishnan, S., Murugan, N. (2011). Prediction of tensile strength of friction stir welded aluminium matrix TiCp particulate reinforced composite. , 32(1), 462–467. doi:10.1016/j.matdes.2010.05.055.

[90] Kalaiselvan, K., Murugan. N., Parameswaran, S. (2011). Production and characterization of AA6061–B4C stir cast composite. , 32(7), 4004–4009. doi:10.1016/j.matdes.2011.03.018.

[91] Atul, K., Kaushik, P., Suhrit, M. (2017). Simultaneous improvement of mechanical strength, ductility and corrosion resistance of stir cast Al7075-2% SiC micro- and nanocomposites by friction stir processing. Journal of Manufacturing Processes, 30(), 1–13. doi:10.1016/j.jmapro.2017.09.005.

[92] Lee, S. J., Shin, S. E., Yufeng, S., Hidetoshi, F., Yongbum, P. (2018). Friction stir welding of multi-walled carbon nanotubes reinforced Al matrix composites. Materials Characterization, 145(), 653–663. doi:10.1016/j.matchar.2018.09.033.

[93] Kumar, R. A., Thansekhar, M.R. (2018). Reinforcement with alumina particles at the interface region of AA6101-T6 and AA1350 alloys during friction stir welding. Materials Research Express. doi:10.1088/2053-1591/aab8b5.

[94] Box, G.E.P., & Hunter, J.S. (1957). Multifactor experimental design, J. Ann. Math. Statistics. 28.

[95] Puri, A.B., Bhattacharyya, B. (2005). Modeling and analysis of white layer depth in a wire-cut EDM process through response surface methodology. Int J Adv Manuf Technol, 25, 301–307.

[96] Cochran, G., & Cox, G.M. (1962). Experimental design.Asia Publishing House, New Delhi.

[97] Hines, W.W., & Montgomery, D.C. (1990). Probability and statistics in engg. And management science. 3rd Edition, Wiley Publications.

[98] Peng, K.C. (1967).The design and analysis of scientific experiment. Addison-Wesley Publishing Company, London.

[99] Deringer, G. & Suich, R. (1980). Simultaneous optimization of several response Variables.Journal of Quality Technology, 12, 214-219.

[100] Mosneaga, V. A., Mizutani, T., Kobayashi, T. and Toda, H. (2002). Impact Toughness of Weldments in Al-Mg-Si Alloys. Mater. Trans. 43: 1381-1389.

[101] Çömez, N., and Durmuş, H. (March 11, 2019). "Cold Metal Transfer Welding of AA6061 to AA7075: Mechanical Properties and Corrosion." ASME. J. Eng. Mater. Technol. July 2019; 141(3): 031002.

[102] Pan, Shuaihang, Saso, Tomohiro, Yu, Ning, Sokoluk, Maximilian, Yao, Gongcheng, Umehara, Noritsugu, Li, Xiaochun (2020). New study on tribological performance of AA7075-TiB2 nanocomposites. Tribology International, (), 106565. doi: 10.1016/j.triboint.2020.106565.

[103] Dev, S., Aherwar, A. and Patnaik, A., 2020. Material selection for automotive piston component using entropy-VIKOR method. Silicon, 12(1), pp.155-169.

[104] M. Ilangovan, S. Rajendra Boopathy, V. Balasubramanian, Effect of tool pin profile on microstructure and tensile properties of friction stir welded dissimilar AA 6061eAA 5086 aluminium alloy joints, Defence Technology 11 (2015) 174-184.

[105] Mehdi, H, Mishra, RS. Microstructure and mechanical characterization of TIG-welded joint of AA6061 and AA7075 by friction stir processing. Proceedings of the Institution of Mechanical Engineers, Part L: Journal of Materials: Design and Applications 2021; 11: 2531-2546.

[106] Shanavas, S., & DHAS, J. E. R. (2017). Parametric optimization of friction stir welding parameters of marine grade aluminium alloy using response surface methodology. Transactions of Nonferrous Metals Society of China, 27(11), 2334-2344. 13.

[107] Rajakumar, S., & Balasubramanian, V. (2012). Establishing relationships between mechanical properties of aluminium alloys and optimised friction stir welding process parameters. Materials & Design, 40, 17-35.

[108] Koilraj M, Sundareswaran V, Vijayan S, Rao SRK. Friction stir welding of dissimilar aluminum alloys AA2219 to AA5083 – Optimization of process parameters using Taguchi technique. Mater Des 2012;42:1–7.

[109] Guo, J., Gougeon, P., Chen, X.G. (2012). Microstructure evolution and mechanical properties of dissimilar friction stir welded joints between AA1100-B4C MMC and AA6063 alloy, Mater. Sci. Eng. A553 149–156.

[110] Arora, A., Nandan, R., Reynolds, A. P., & DebRoy, T. (2009). Torque, Power Requirement and Stir Zone Geometry in Friction Stir Welding Through Modeling and Experiments. Scripta Materialia, 60 (1), 13-16.

[111] Nandan, R., Lienert, T. J. and DebRoy, T. (2008). "Toward reliable calculations of heat and plastic flow during friction stir welding of Ti-6Al-4V alloy" International Journal of Materials Research, 99, 4, 434-444.

[112] Arora, A., Zhang, Z., De, A., Debroy, T. (2009). Strains and Strain Rates during Friction Stir Welding. Scripta Materialia - SCRIPTA MATER. 61. 863-866.

[113] Smith, William F.; Hashemi, J. (2006). Foundations of Materials Science and Engineering (4th ed.), McGraw-Hill, ISBN 978-0-07-295358-9.

[114] Azizieh, M., Kokabi, A. H., & Abachi, P. (2011). Effect of rotational speed and probe profile on microstructure and hardness of AZ31/Al2O3 nanocomposites fabricated by friction stir processing. Materials & Design, 32(4), 2034–2041.

[115] Xu, W., Liu, J., Luan, G., Dong C. (2009). Temperature evolution, microstructure and mechanical properties of friction stir welded thick 2219-O aluminum alloy joints, Materials & Design, 30 1886-1893.

[116] Husain Mehdi, Arshad Mehmood, Ajay Chinchkar, Abdul Wahab Hashmi, Chandrabhanu Malla, Prabhujit Mohapatra. Optimization of process parameters on the mechanical properties of AA6061/Al2O3 nanocomposites fabricated by multi-pass friction stir processing, Materials Today: Proceedings, 2021, https://doi.org/10.1016/j.matpr.2021.11.333.

[117] V. Ebrahimzadeh, M. Paidar, M.A. Safarkhanian, O.O. Ojo, Orbital friction stir lap welding of AA5456-H321/AA5456-O aluminum alloys under varied parameters, Int. J. Adv. Manuf. Technol. 96 (2018) 1237–1254.

[118] Husain Mehdi, Mishra, R.S. (2020). Investigation of mechanical properties and heat transfer of welded joint of AA6061 and AA7075 using TIG+FSP welding approach. Journal of Advanced Joining Processes, 1, 100003, https://doi.org/10.1016/j.jajp.2020.100003.

[119] Jain, S., Mishra, R.S. (2022]). Influence of micro-sized Al2O3 particles on microstructure, mechanical and wear behaviour of dissimilar composite joint of AA6061/AA7075 by Friction stir processing/welding, Proceedings of the Institution of Mechanical Engineers, Part C: Journal of Mechanical Engineering Science, ISSN 0954-4062, DOI:10.1177/09544062221092334.

[120] Rejil CM, Dinaharan I, Vijay SJ, Murugan N. Microstructure and sliding wear behavior of AA6360/(TiC+B4C) hybrid surface composite layer synthesized by friction stir processing on aluminum substrate. Mater Sci Eng A, 2012; 552: 336–44.

[121] Alidokht, S.A., Abdollah-Zadeh, A., Soleymani, S., Saeid, T. (2012). Assadi Assadi H. Evaluation of microstructure and wear behavior of friction stir processed cast aluminum alloy.Mater Charact, 63: 90–7.

[122] Arbegast, W.J. (2003). Modeling Friction Stir Joining as a Metalworking Process, Miner, Metals Mater Soci.,313-330.

[123] Patel V.V., Badheka, V., Kumar, A. (2016). Influence of Friction Stir Processed Parameters on Superplasticity of Al-Zn-Mg-Cu Alloy. Mater Manuf Proce, 31:1573-1582.

[124] Kou, S. (2003). Welding Metallurgy, second ed., John Willy & Sons, New York, 2003.

[125] Srinivasu, R., Rao A.S., Reddy, G.M., Rao K.S. (2015). Friction stir surfacing of cast A356 aluminum silicon alloy with boron carbide and molybdenum disulphide powders. Defence Technology, 11:140-6.

[126] Mehdi, H., Mishra, R.S. (2021). Effect of Friction Stir Processing on Mechanical Properties and Wear Resistance of Tungsten Inert Gas Welded

Joint of Dissimilar Aluminum Alloys. J. of Materi Eng and Perform 30, 1926–1937.

[127] Mehdi, H., Mishra, R.S. (2021). Consequence of reinforced SiC particles on microstructural and mechanical properties of AA6061 surface composites by multi-pass FSP, Journal of Adhesion Science and Technology, DOI: 10.1080/01694243.2021.1964846.

[128] Mehdi, H., Mishra, R. (2021). Microstructure and mechanical characterization of tungsten inert gas-welded joint of AA6061 and AA7075 by friction stir processing. Proceedings of the Institution of Mechanical Engineers, Part L: Journal of Materials: Design and Applications.;235(11):2531-2546. doi:10.1177/14644207211007882.

[129] Chen, X.G., Silva, M.D. Gougeon, P., Georges, L.S. (2009). Microstructure and mechanical properties of friction stir welded AA6063–B4C metal matrix composites, Mater. Sci.Eng. A 518 (12) 174–184.

[130] Palanivel, R., Dinaharan, I., Laubscher, R.F., Paulo Davim, J.(2016). Influence of boron nitride nanoparticles on microstructure and wear behavior of AA6082/TiB_2 hybrid aluminum composites synthesized by friction stir processing. Mater Des; 106:195-204.

[131] Srivastava, M., Rathee, S., Siddiquee, A.N. et al. (2019). Investigation on the Effects of Silicon Carbide and Cooling Medium during Multi-Pass FSP of Al-Mg/ SiC Surface Composites. Silicon 11, 2149–2157.

[132] Chang, C. I., Lee, C. J., Huang, J. C. (2004). Relationship between grain size and Zener–Holloman parameter during friction stir processing in AZ31 Mg alloys, Scripta Mater. 51 509-514.

[133] Humphreys, F.J., Hatherly, M. (2004) Chapter 11 -grain growth following recrystallization, in: Recrystallization and Related Annealing Phenomena, Elsevier Ltd., 333–378.

[134] Lloyd, D. J. (1994). Particle reinforced aluminum and magnesium matrix composites, International Materials Reviews, 39 (1).

[135] Mehdi, H., Mishra, R.S. (2020). An experimental analysis and optimization of process parameters of AA6061 and AA7075 welded joint by TIG+FSP welding using RSM. Advances in Materials and Processing Technologies, 1–23. https://doi.org/10.1080/2374068X.2020.1829952.

[136] Salah, A. N., Mehdi, H., Mehmood, A., Hashmi, A.W. Malla, C., Kumar, R. (2021). Optimization of process parameters of friction stir welded joints of dissimilar aluminum alloys AA3003 and AA6061 by RSM, Materials Today: Proceedings,2021, https://doi.org/10.1016/j.matpr.2021.10.288

[137] Pandey, C., Saini, N., Mahapatra, M.M.. Kumar, P. (2017). Study of the fracture surface morphology of impact and tensile tested cast and forged (C&F) Grade 91 steel at room temperature for different heat treatment regimes, Eng. Fail. Analy, 71, p131-147.

[138] Liu, G., Xin, R., Li, J., Liu, D., Liu, Q. (2015). Fracture localisation in retreating side of friction stir welded magnesium alloy, Sci Tech Weld Join 378-384.

[139] Bahemmat, P., Haghpanahi, M., Besharati, M. K., Ahsanizadeh, S., & Rezaei, H. (2010). Study on mechanical, micro-, and macrostructural characteristics of dissimilar friction stir welding of AA6061-T6 and AA7075-T6. Proceedings of the Institution of Mechanical Engineers, Part B: Journal of Engineering Manufacture, 224(12),1854-1864.

[140] Strombeck, A.V., Santos, J.F.D., Torster, F., Laureano, P., Kocak, M. (1999). Fracture toughness behaviour of FSW joints on aluminum alloys. In: Proceedings of the first international symposium on friction stir welding.

[141] Khodabakhshi, F., Gerlich, A.P. (2018). Potentials and strategies of solid-state additive friction-stir manufacturing technology: a critical review. J. Manuf. Process, 36: 77–92.

[142] Gangil, N., Siddiquee, A.N., Maheshwari, S. (2017) Aluminum based in-situ composite fabrication through friction stir processing: a review. J. Alloys Compd 715: 91–104.

[143] Sharma, V, Prakash, U, Kumar, BVM. (2015). Surface composites by friction stir processing: a review. J. Mater. Process. Technol 224: 117–134.

[144] Sharma, DK, Patel, V, Badheka, V, et al. Fabrication of hybrid surface composites AA6061/(B 4 C+MoS) via friction stir processing. J. Tribology 2019; 141: 52201–52210.

[145] Ghangas, G, and Singhal, S. Modelling and optimization of process parameters for friction stir welding of armor alloy using RSM and GRA-PCA approach. Materials Research Express 2018; 6: 026553.

[146] Fuller, C.B., Mahoney, M.W., Calabrese, M., et al. (2010). Evolution of microstructure and mechanical properties in naturally aged 7050 and 7075 Al friction stir welds. Mater Sci Eng A, 527(9): 2233-2240.

[147] Liu, H.J., Fujii, H., Maeda, M., Nogi, K. (2003). Heterogeneity of mechanical properties of friction stir welded joints of 1050-H24 aluminum alloy. Mater Sci Lett, 22:441–4.

[148] Sato, Y.S., Kokawa, H. (2001). Distribution of tensile property and microstructure in friction stir weld of 6063 aluminum. Metall Mater Trans, 32A(12): 3023–31. 218.

[149] Aydın, H., Bayram, A., Uguz, A., Akay, K.S. (2009). Tensile properties of friction stir welded joints of 2024 aluminum alloys in different heat-treated-state, Materials and Design 30 2211–2221.

[150] Azimzadegan, T, Serajzadeh, S. (2010). An Investigation into microstructures and mechanical properties of AA7075-T6 during friction stir welding at relatively high rotational speeds. J. Mat. Eng. Perf. 19: 1256−1263.

[151] Jain, S., Mishra, R.S. Effect of Al2O3 nanoparticles on microstructure and mechanical properties of friction stir-welded dissimilar aluminum alloys AA7075-T6 and AA6061-T6, 2021, https://doi.org/10.1177/09544089211065534.

[152] Sharma, V.M., Sharma, S., Mewar, S.K., et al.(2018). Friction stir processing of Al6061-SiC-graphite hybrid surface composites. Mater. Manuf. Process, 33: 795–804.

[153] Patel, V., Li, W., Xu, Y. (2019). Stationary shoulder tool in friction stir processing: a novel low heat input tooling system for magnesium alloy. Mater. Manuf. Process, 34: 177–182.

[154] Heidarzadeh, A, Barenji, RV, Esmaily, M, et al. Tensile Properties of Friction Stir Welds of AA 7020 Aluminum Alloy. Trans Indian Inst Met 2015; 68: 757–767.

[155] Liu, HJ, Fujii, H, Maeda, M, et al. Tensile properties and fracture locations of friction-stir-welded joints of 2017-T351 aluminum alloy. J Mat. Proc. Technol 2013; 142: 692–696.

[156] Zhang, Z, Chen, DL. Consideration of Orowan strengthening effect in particulate-reinforced metal matrix nanocomposites: A model for predicting their yield strength Author links open overlay panel. Scripta Materialia 2006; 54: 1321-1326.

[157] Jamalian, HM, Ramezani, H, Ghobadi, H, Ansari, M, Yari, S, Givi, MKB, Processing–structure–property correlation in nano-SiC-reinforced friction stir welded aluminum joints, Journal of Manufacturing Processes, Volume 21,2016,Pages 180-189.

[158] Nouri, Z.; Taghiabadi, R.; Moazami-Goudarzi, M. (2020). Mechanical properties enhancement of cast Al-8.5Fe-1.3V-1.7Si (FVS0812) alloy by friction stir processing. Archives of Civil and Mechanical Engineering, 20(4), 102–. doi:10.1007/s43452-020-00106-1.

[159] Hannard, F.; Castin, S.; Maire, E.; Mokso, R.; Pardoen, T.; Simar, A. (2017). Ductilization of aluminium alloy 6056 by friction stir processing. Acta Materialia, 130(), 121–136. doi:10.1016/j.actamat.2017.01.047.

[160] Yang, Kang; Li, Wenya; Niu, Pengliang; Yang, Xiawei; Xu, Yaxin (2017). Cold sprayed AA2024/Al 2 O 3 metal matrix composites improved by friction

stir processing: Microstructure characterization, mechanical performance and strengthening mechanisms. Journal of Alloys and Compounds, (), S0925838817338902–. doi:10.1016/j.jallcom.2017.11.132.